Loughborough University

Phase change materials, systems and applications for low and medium temperature thermal energy storage

Center for Renewable Energy Systems Technology

By
© José Maria Paula Pinto Pereira da Cunha

Submitted in partial fulfillment of the requirements for the award of Doctor of Philosophy of Loughborough University

November 2018

Abstract

Determining the ideal size of compact thermal energy storage containers has been an issue for many building designers due to the difficulty of determining the transient performance of the thermal storage systems. Research and development of compact thermal energy storage systems has been ongoing for more than 80 years with phase change materials (PCMs) used to replace conventional water based thermal stores. PCMs have the potential to store larger amounts of energy when compared to water-based thermal stores over a narrow temperature range, providing a greater thermal storage capacity for the same available volume. This research was undertaken to investigate theoretically and experimentally the thermal behaviour of various PCMs and the overall decarbonisation potential when integrated into current heating and cooling systems. The overall aim was to develop algorithms that could determine optimal and cost effective compact thermal storage geometries and their system integration into the various heating and cooling applications studied. Three operating temperatures were selected based on the application: office space cooling (10 to 24°C), residential domestic hot water and space heating (40 to 65°C) and district heating (55 to 80°C). The algorithms developed predict the energy performance and CO_2 emissions reduction for each application with a latent heat thermal storage system compared to a reference (current system design) case in each application. Previous research has focused on the melting behaviour of the PCM within a specific geometry, modelling the heat transfer fluid (HTF) in a separate analysis. The algorithms developed focus on the modelling of these 2 elements simultaneously within the respective application. This provided a useful tool to evaluate the thermal performance of each storage technology compared to the reference case in each application studied. The levelized costs of energy (LCOE) in each application were compared. It was found that in all cases studied, the latent heat thermal energy storage system is an expensive solution, compared to the reference case in each application (72% more expensive in the office space cooling study, 69% more expensive in the domestic hot water and space heating study and 9% more expensive in the district heating study); although the obtained emission reductions are considerable (36% by shifting daily cooling loads, 57% by shifting domestic hot water and space heating loads and 11% by utilizing industrial waste heat via a compact portable thermal store). Further integration of renewable energy sources and the electrification of current heating and cooling applications with the possibility of shifting heating and cooling loads into periods with lower carbon emissions can significantly contribute to meet the UK's 80% carbon emissions reduction targets by 2050.

Acknowledgements

Thanks go to my supervisor, Philip Eames, for his assistance throughout the work and the range of opportunities he has made available to me throughout the PhD. I would like to acknowledge the funders of the work: Engineering and Physical Sciences Research Council, the interdisciplinary centre for Storage, Transformation and Upgrading of Thermal Energy and Loughborough University. I would also like to thank Paul Rowley for his insights on the economic feasibility studies undertook. Thanks to members of the Centre for Renewable Energy and Systems Technologies (CREST) at Loughborough University, past and present, for their support and advice and also providing distractions when required. Special mention to Ian Biggin and Rainer Busch whose efforts on collaborative projects fed into this work, and also to Georgina Fielding-Martin, who provided invaluable feedback on the thesis. Finally, I would like to give a special thanks to my family and friends, who have provided valuable moral support throughout the process.

"If I have seen further than others, it is by standing upon the shoulders of giants."

Sir Isaac Newton

Contents

List of Figures

List of Tables

List of Abbreviations

ASHP	Air Source Heat Pump
CAPEX	Capital Expenses [£]
CHP	Combined Heat and Power
COP	Coefficient of Performance
CREST	Centre for renewable energy and systems technologies
DH	District heating
DHW	Domestic hot water
DSC	Differential scanning calorimetry
EG	Expanded graphite
EOT	Equation of time $[min]$
GHA	Greenwich hour angle $[h]$
GDP	Gross domestic product
HA	Hour angle $[h]$
HDPE	High density polyethylene
HTF	Heat transfer fluid
HVAC	Heating, ventilation and air conditioning
LAT	Latitude [°]
LCOE	Levelized cost of energy $[£/MWh]$
LCOH	Levelized cost of heat $[£/MWh_{th}]$
LHTES	Latent heat thermal energy storage system
LONG	Longitude [°]
OPEX	Operational expenses $[£/year]$
PCM	Phase change material
ROI	Return on investment [%]
SH	Space heating
TDMA	Tri-dimensional matrix
TES	Thermal energy storage
TGA	Thermo-gravimetric analysis

List of Units

az, az_{surf}	Azimuth, surface azimuth [°]
C	Thermal capacitance $[kJ/K]$
Cwall/Cglass	Wall/ Glass thermal capacitance $[kJ/K]$
Croof/Cfloor	Roof/ Floor thermal capacitance $[kJ/K]$
Cp	Heat capacity $[kJ/kg.K]$
D_h	Hydraulic diameter $[m]$
$E_{density}$	Energy density $[kWh/m^3]$
g	Acceleration of gravity $[kg/m^2.s^2]$
Gr	Grasshof number
h_{cv}	Convection heat transfer coefficient $[W/m^2.K]$
h_{sol}	Daily solar height [°]
inc	Surface incidence [°]
L_{slab}	Slab length $[m]$
M_i	Molar mass $[g/mol]$
Nu	Nusselt number
Pr	Prandtl number
Ra	Rayleigh number
Re	Reynolds number
Rt_{cond}	Conduction resistance $[W/K]$
Rt_{conv}	Convection resistance $[W/K]$
Rt_{rad}	Radiation resistance $[W/K]$
St	Stefan number
T_m	Melting point $[°C]$
T_{sl}	Solid-liquid temperature region $[°C]$
V_{exp}	Volume expansion [%]
x_{mi}, z_{vi}, w_{mi}	Molar ratio; volumetric ratio; mass ratio
$\dot{I}_{dir}^{norm}$	Direct normal solar radiation $[W/m^2]$
$\dot{I}_{diff}^{hor}$	Diffuse horizontal solar radiation $[W/m^2]$
$\dot{I}_{glob}^{hor}$	Global horizontal solar radiation $[W/m^2]$
$\dot{Q}$	Heat flow $[W]$
$\dot{Q}_{fabric}$	Building fabric heat flow $[W]$
$\dot{q}_{cond}, \dot{q}_{conv}, \dot{q}_{rad}$	Conduction, convection and radiation specific heat flux $[W/m^2]$
$\dot{V}$	Volumetric flow rate $[m^3/s]$
α	Solar radiation absorption coefficient
β	Surface tilt angle towards horizon [°]
ϵ	Longwave emissivity coefficient
ρ	Density $[kg/m^3]$
ρ_g	Ground reflected solar radiation coefficient

δ	Solar yearly declination [°]
ΔT	Temperature gradient [$°C$]
ΔH_m	Latent heat enthalpy [kJ/kg]
σ	Stephan-Boltzmann constant [$W/m^2.K^4$]
λ	Thermal conductivity [$W/m/K$]
ζ	Kinematic viscosity [m^2/s]
τ	Solar radiation transmission coefficient [%]
μ	Dynamic viscosity [$Pa.s$]
Φ	Void fraction [%]

Chapter 1

Introduction

The main challenge that our society is facing today is the threat to the environment. The levels of carbon dioxide (CO_2) in the atmosphere have risen by more than 33% since the industrial revolution in the late 18^{th} century [32]. Initial global responses to this reality were taken in the 1992 United Nations Framework Convention on Climate Change (UNFCCC) in Kyoto [33], concluding that global warming was caused by human action mainly due to the amount of CO_2 emissions directly derived from the burning of fossil fuels. Emission targets were established based the development index for each country and GDP per capita, with currently 192 applicants already committed to the protocol.

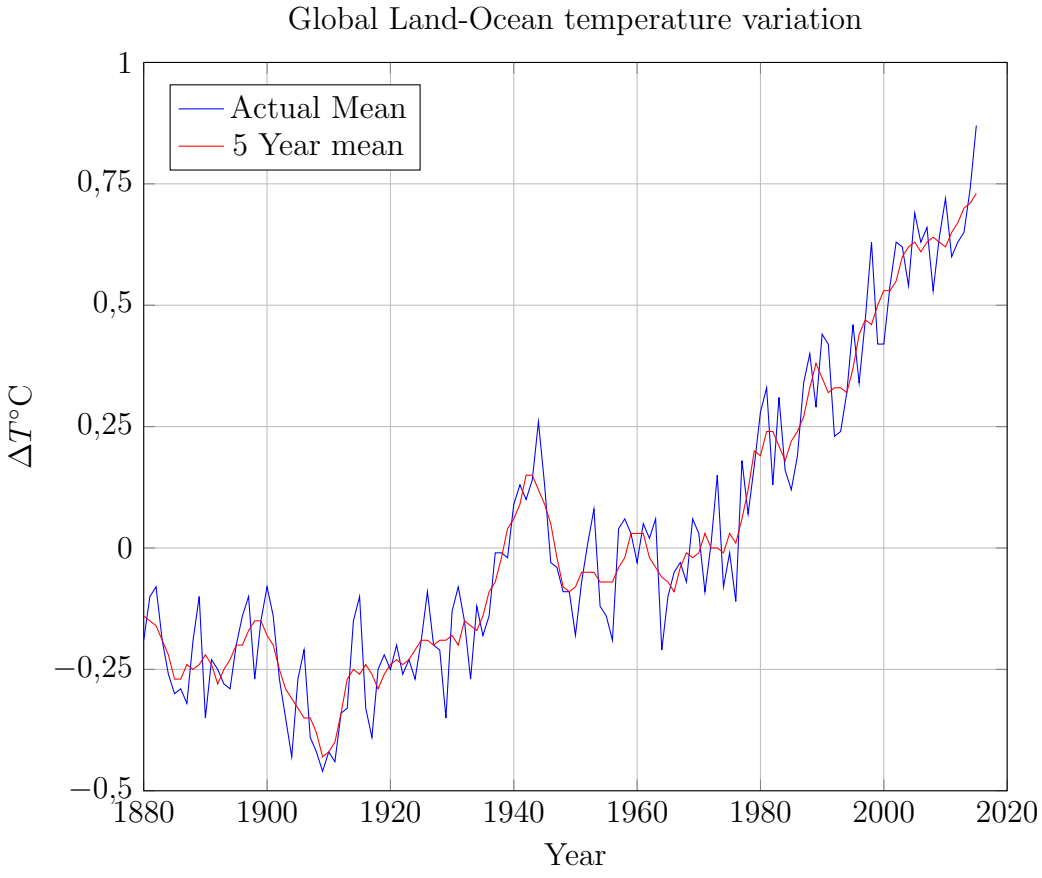

Figure 1.1: Average global surface temperatures from 1880 to 2015, data from [1]

Global measures adopted to stabilize global temperature rise below the 2°C target are considered to be insufficient [34], as seen in the upward trend presented by the red curve of figure 1.1 over the last 40 years. If this target is to be achieved, there must be an increased effort to decarbonize global energy consumption, still relying heavily on fossil fuel sources [35] either by the use of renewable sources of energy or by energy consumption reduction.

1.1 Global Energy Consumption

Since 1965, annual energy consumption worldwide has already increased by more than 350% reaching an estimated 14 186.6 million tonnes of oil equivalent (mtoe) by 2016 [2]. Figure 1.2 shows that approximately 86% of the total global primary energy consumption in 2016 was derived from fossil fuels (oil, natural gas and coal), whereas only 10% from renewable sources and 4% from nuclear energy.

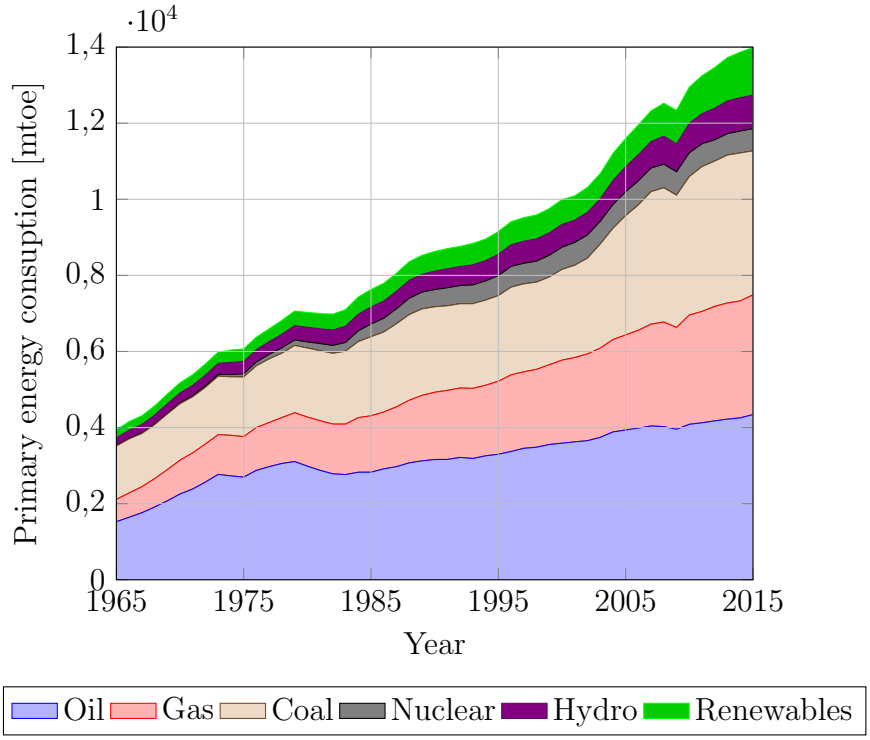

Figure 1.2: Estimated evolution of global primary energy consumption by fuel type from 1965 to 2016, data from [2]

In the UK, primary energy consumption has remained at around 200mtoe for the last 50 years, as seen in Figure 1.3, with its energy mix relying less on coal, turning to natural gas instead. With a population growth of 21% and a GDP growth of 2635% over the last 50 years, primary energy consumption in the UK has had an efficiency gain per capita of around 21% and of 96% per GDP [2].

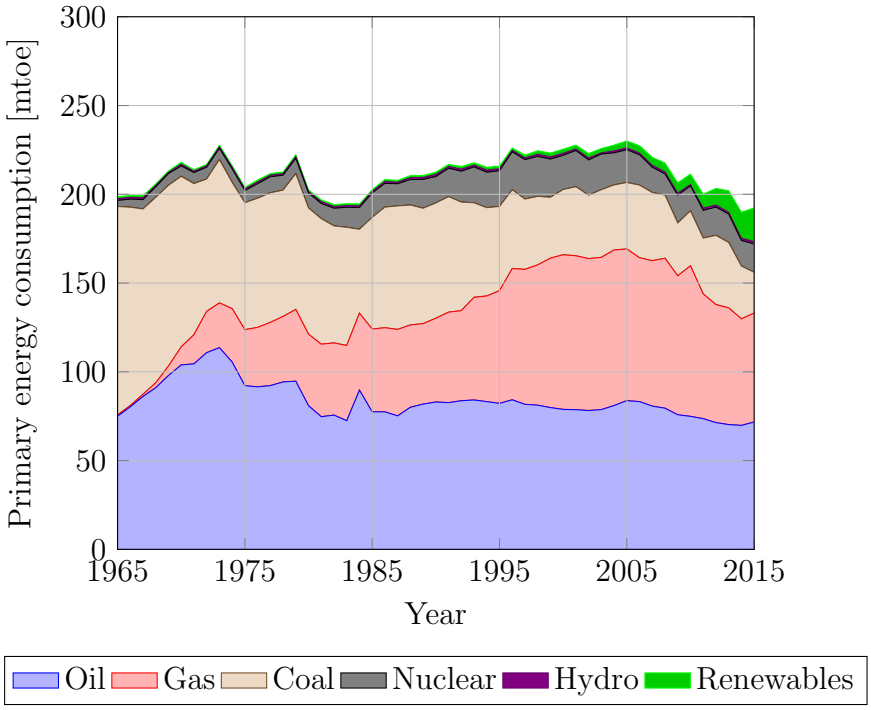

Figure 1.3: Estimated evolution of primary energy consumption by fuel type in the UK from 1965 to 2016, data from [2]

Although fossil fuels are currently the primary energy sources in the UK, Figure 1.3 shows that this fuel dependency has decreased from 98% in 1965 to 81% in 2016 [2]. Oil and gas in the UK had an estimated peak production in 1999 of approximately 226mtoe and of 84mtoe in 2016, a reduction of 63%. To be less dependent on fossil fuel sources there must be a strong focus on using renewable energy sources and improving energy efficiency in various sectors of the economy (buildings and services, transportation, supply chains, industry, etc.).

Main sources of renewable energy currently used are wind, hydro and solar photovoltaic due to their technological maturity and commercial acceptance. Global deployment and investment on these sources is steadily increasing, as can be seen from the literature [34, 2]. The trend towards decreasing costs of renewable energy generation, independence from fossil fuels and environmental considerations have been the main drivers for increasing the exploitation of the renewable energy potential during the last 5 decades [36]. In order to shift towards more renewable energy integration, energy storage needs to be addressed to reduce the mismatch between their intermittent supply and the energy demand.

Conventional heating and cooling in the domestic, commercial and public administration sectors had a combined natural gas and petroleum products consumption of around 22% of the final energy consumption in the UK in 2016 [3]. The distribution of fuel type in each sector is presented in figure 1.4.

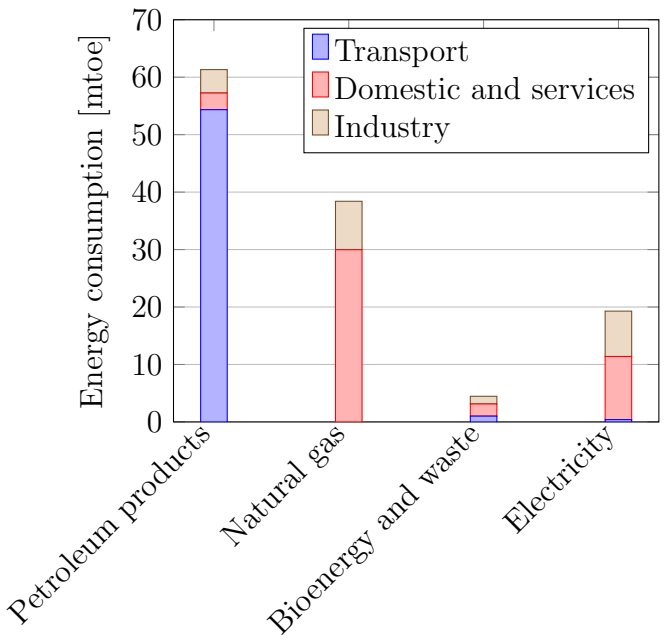

Figure 1.4: Final energy consumption in the UK in 2016 by fuel type in the Transport, Domestic and Services and Industry sectors, data from [3]

Due to their quoted low thermal hysteresis (temperature difference below 20°C) between charging and discharging processes, relatively low volume changes in the melting/solidification process and high storage density, latent heat storage systems in heating and cooling applications below 250°C can obtain greater $[CO_2]$ emissions reduction potential by replacing conventional heating and cooling applications in the domestic, commercial and public administration sectors with more energy efficient systems, such as heat pumps operating in specific off-peak periods of the electrical grid during the day using a thermal energy storage system to meet heating loads of peak periods [37].

1.2 Energy storage technologies

Energy storage is the capture of energy produced at one time for use at a later time. It can be characterized by the amount of energy stored measured in hours of use, the power rates able to be achieved and the energy lost by converting from and to the initial received energy form, also known as round trip efficiency. Proven storage technologies already on the market are pumped hydropower, compressed air, flywheels, electrochemical, hydrogen and thermal energy storage.

Pumped hydro energy storage (PHES) collects the energy potential of water between 2 distinct heights. It is one of the most mature energy storage systems [36] that offers a high round trip efficiency (70 to 80%), long lifespan and low operation and maintenance (OM) costs. Their usual storage capacity varies between hours to days, with nominal power outputs ranging from a few kW to 3GW. The investment cost is usually very high, due to the extended civil works required to build the water reservoirs/damns. It is currently the most used grid-scale energy storage technology with 129GW of installed capacity worldwide.

Compressed air energy storage (CAES) collects energy by compressing air into

an enclosed volume. The round trip efficiency is lower than pumped hydro storage (from 40 to 75%), and also has a lower quoted lifespan [38]. Technical constraints arise when designing large pressurized vessels over ground and requires considerable geological research to assess feasible underground caverns [39].

Flywheel energy storage collects energy in the revolution of high inertia masses that rest on very low friction bearings. Their usual power capacity is in the range of 100kW to 20MW, although their storage capacity ranges from seconds to minutes. It has limited time span due to the deterioration of its mechanical components, but a very fast response, suitable for frequency regulation and power quality applications [40].

Electrochemical batteries can be divided into three groups: solid-state, sodium-sulphur and redox batteries. Solid-state batteries such as the lead acid [41], nickel-cadmium or lithium-ion (Li-ion) [42], are used in the 100W to 2MW range, and their storage capacity ranges from 1 to 12 hours [41]. Sodium-sulphur batteries (Na-S), a type of molten salt battery, are more energy dense than solid state batteries, but require working temperatures between 300-350°C, usually in the same output and capacity range of solid-sate batteries. They are quoted to have a high round trip efficiency, but relatively high static heat losses due to the high temperatures involved [43]. Redox or flow batteries such as the vanadium battery (VRB) are potential energy storage systems where the chemical components with reduction potential are stored in separate tanks, permitting larger storage capacities [44]. Their charge and discharge operation is made via forced circulation of the chemical components and indirect contact via a a plate heat exchanger [45].

Table 1.1: Key parameters comparison of commercially available energy storage technologies.

Storage technology	Capacity range [h]	Power output range [MW]	Round trip efficiency [%]	Life-cycle expectancy [Years]	Cost [£]	
					/ kWh	/ kW
PHES [46]	4 - 72	0.1 - 3000	75 - 85	50	4 - 75	400 - 1500
CAES [46]	4 - 72	50 - 300	50 - 70	20-40	2 – 40	300 - 600
Flywheel ES [44]	2.7E-7 – 0.1	0.1 - 20	85 - 95	20	1E3 – 4E3	150 – 260
Lead acid [44]	0.001 - 72	0.1 - 20	70 - 90	20	150 - 300	200 - 400
Li – ion [44]	0.001 - 12	0.1 - 50	75 - 90	5 - 15	400 – 2E3	900 – 3E3
Na-S [44]	0.001 - 12	0.1 - 10	75 - 85	5 - 15	250 - 400	750 – 2E3
VRB [44]	4 - 96	0.1 - 3	65 -80	25 - 30	100 - 750	400- 1.2E3

1.2.1 Thermal energy storage

Thermal energy storage (TES) systems collect energy on the temperature differential of a large mass preferably with high heat capacity. It can be achieved through 3 distinct ways: sensible; latent or thermochemical heat storage. Sensible heat storage relies on the specific heat capacity of the material. Latent heat storage relies on the phase change enthalpy of the material to store heat within a narrow temperature range. It provides greater energy density $[kWh/m^3]$ than that achievable with sensible heat storage over the same temperature interval; however volumetric expansions during the melting process can reach 10 to 15% for some materials.

Thermochemical heat storage is more energy dense than latent heat storage and relies on adsorption / desorption or other chemical reactions. Reaction kinetics and reactor design significantly determine their actual performance, and require distinct charging and discharging temperatures [4] (usually between 100 and 300°C depend-

ing on the reaction), having potential interest for inter-seasonal storage applications. Figure 1.5 presents the heat storage capacity $[kWh/m^3]$ of water sensible heat storage and a PCM over a 20°C temperature interval; the PCM can store 2.9 times more energy than water over the same temperature range.

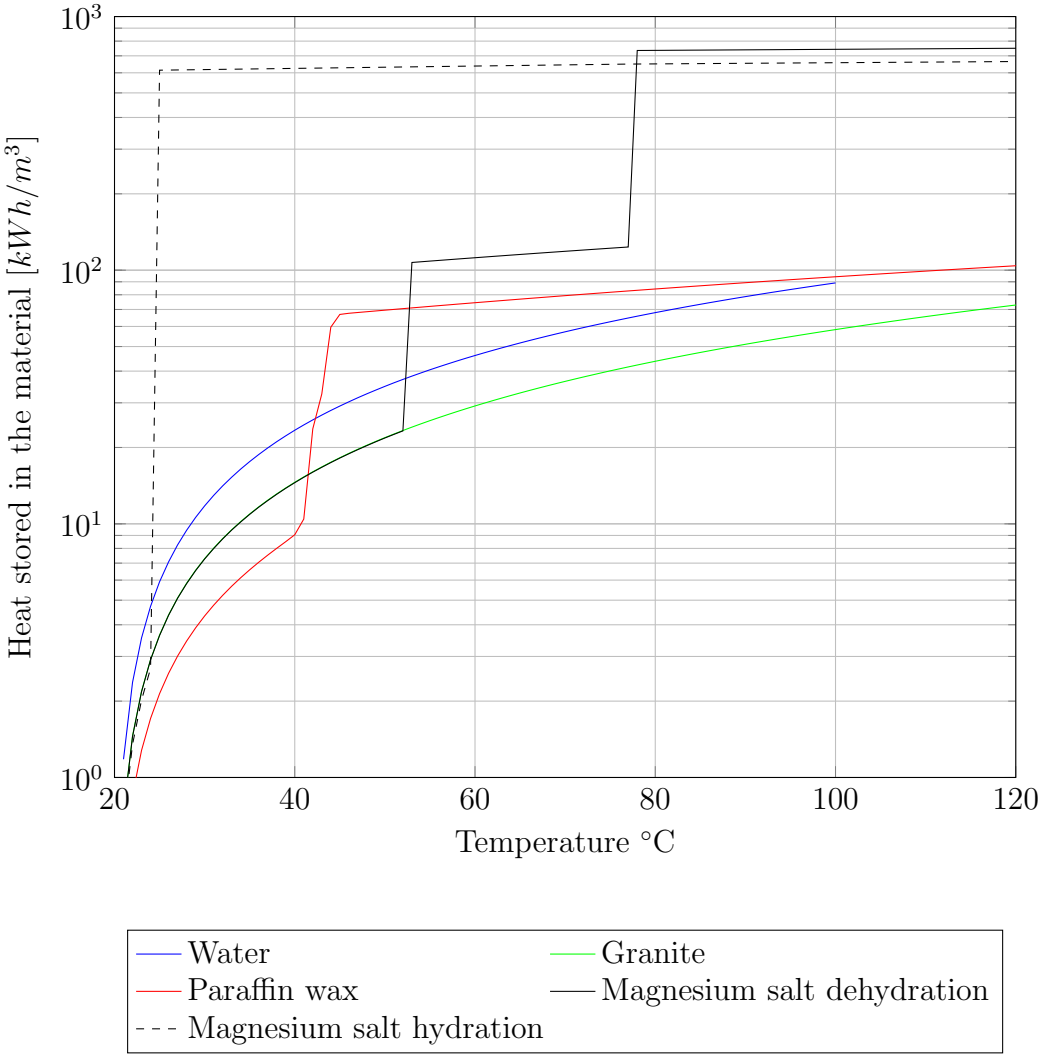

Figure 1.5: Heat stored vs. Temperature diagrams comparison of a paraffin wax, water, magnesium sulphate heptahydrate (data from [4]) and granite rock

1.3 Scope of research

The overall aim of this research is to develop a numerical model that would determine the optimum thermal storage geometry for the required storage capacity and heat transfer rates in the operational temperature range available for each application, as well as to determine potential energy savings and CO_2 emissions reductions. An economic comparison was also made for each application studied to assess their economic feasibility. The research work developed in this thesis is driven by the importance of shifting peak heating and cooling loads hence allowing further renewable energy integration into the grid, further increasing its stability and potentially reducing the need for backup ancillary services such as combined cycle gas turbines and coal. The objectives of the research are to:

- Review phase change materials and indirect heat exchanger designs for latent heat storage systems and thermal performance enhancement mechanisms for temperatures between 0 and 250°C.

- Review governing heat transfer mechanisms occurring within thermal energy storage containers and how the phase change process is numerically modelled and solved for each time step.

- Material properties characterization from a selection of 50 PCMs in the given temperature range to determine their latent heat of fusion, melting and crystallization point, solid and liquid heat capacities and degree of subcooling.

- Assess the integration of compact and encapsulated latent heat storage containers into domestic hot water and space heating systems to determine their energy savings, economic feasibility and decarbonisation potential.

- Assess the integration of encapsulated latent heat storage containers into an office space cooling system and determine their energy savings, economic feasibility and decarbonisation potential.

- Assess the integration of industrial waste heat into district heating networks via a continuous supply of portable latent heat storage containers and determine their energy savings, economic feasibility and decarbonisation potential.

In the 2^{nd} chapter, a comprehensive review of phase change materials (PCMs) with phase transition temperatures between 0 and 250°C is presented, followed by an assessment of indirect heat exchanger designs for latent heat storage systems and possible thermal performance enhancement mechanisms.

In the 3^{rd} chapter a comprehensive review is made of the heat transfer mechanisms occurring in a latent heat storage container when a fluid flow is circulated through it, how the phase change process is numerically modelled and solved for each time step.

In the 4^{th} chapter, a selection of 50 promising PCMs are characterized in the given temperature range using scanning calorimetry and thermogravimetric analysis to accurately determine their latent heat of fusion, melting and crystallization point and degree of subcooling of the materials.

In the 5^{th} chapter the thermal performance of four active cooling (cooling systems that require an energy input such as heat pumps and centrifugal fans) approaches to meet daytime office cooling requirements is assessed in an open plan office using London climate data using a developed Matlab finite-volume numerical model. The four cooling approaches simulated were: a conventional heating, ventilation and air conditioning (HVAC) system; the HVAC system with extra ventilation on demand; the HVAC system with a thermal store with a 15°C melting point wax charged with cool night time ambient air and the HVAC system with a thermal store with a 8°C melting point wax charged using night time off peak electricity. The aim was to evaluate the decarbonisation impact and economic feasibility of each solution compared to the reference HVAC only scenario by the reduction in the electrical consumption for space cooling.

In the 6^{th} chapter the decarbonisation potential of using latent heat storage systems in current domestic hot water systems in the UK is assessed. A performance

comparison is presented to four domestic space and hot water heating systems: conventional gas boiler, air source heat pump (ASHP) with water buffer tank, ASHP with a packed bed buffer tank and an ASHP with a smaller water tank and a compact latent heat store. All systems with ASHP were simulated with solar thermal collectors for a typical UK climate, to demonstrate the potential of phase change material based energy storage systems in domestic heating applications. An economic analysis to each system was then made to assess their economic feasibility and main constraints.

In the 7^{th} chapter the decarbonisation potential of using portable compact latent storage to provide industrial waste heat into a district heating network by reducing gas consumption in the gas boiler and gas engine units is assessed. The levelized cost of energy of the integration of 1 to 3 portable storage units operating simultaneously is compared to the reference scenario with no portable latent heat storage.

In the final chapter the conclusions of the decarbonisation potential of phase change materials into heating and cooling applications are presented, as well as the main limitations and promising areas to benefit from latent heat storage devices.

Chapter 2

Review of phase change materials and their potential applications

In order to assess the potential of latent heat storage applications, a comprehensive review of the PCMs physical properties during phase change is critical. This chapter details a comprehensive review of phase change materials (PCMs) with phase transition temperatures between 0 and 250°C is presented. From the literature review made, promising PCMs were presented based on their latent heat of fusion and bulk price. For the comparative economic evaluation, market prices for industrial grade materials were used to provide a common approach. The aim of this literature review is to assess active heating and cooling systems that will be further studied in the next chapters. PCMs for passive heating and cooling applications are prominent in the building environment increasing the thermal mass of plaster walls, trombe walls and other building components [47, 48], although the approaches later developed in this thesis are for higher power applications (relying on forced fluid flows passing through them).

Practical indirect heat exchanger designs for latent heat storage systems were also assessed and feasible heat enhancement mechanisms reviewed. The focus on this temperature range is due to the potential CO_2 emissions reduction that can be achieved by replacing conventional gas heating applications in the domestic, commercial and public administration sectors (comprising a fifth of the UK's final energy consumption in 2016 [3]), with heat pumps operating on a selective electricity tariff [37], using phase change materials to develop more compact buffer tanks to meet the heating loads of the building during peak times. Other potential applications for compact thermal energy storage systems is buffering cooling loads with night time ambient cooling [49] and buffering district heating loads with hot water tanks [50].

2.1 Organic PCMs

Organic compounds, characterized by having carbon-hydrogen bonds in their molecular structure, generally have low thermal conductivity (0.1 to 0.5W/m.K), hence requiring enhancing mechanisms to achieve reasonable heat transfer rates. Table 2.1 presents the thermophysical properties of the organic compounds identified as promising for thermal energy storage based on their relative low price, stability in their molten state and enthalpy of phase change. The organic compounds reviewed that appeared to be promising in this temperature range are some of the saturated

fatty acids [51], sugar alcohols [52, 53], carboxylic acids [54], amides [55] and alkanes [18]. Urea [56], not a promising compound in its pure state due to its instability in the liquid state [57], has some eutectic mixtures with suitable properties for latent heat storage systems, details shown in Table 2.1. The economical comparison was based on a market evaluation made through the Alibaba online platform [58].

Table 2.1: Thermophysical properties of selected organic compounds.

Compound	T_m	ΔH_m	Cp_{s-l}	λ_{s-l}	ρ_s	V_{exp}	$E_{density}$	Price		Ref.
	°C	kJ/kg	$kJ/kg.K$	$W/m.K$	kg/m^3	%	kWh/m^3	£/m^3	£/kWh	
Formic Acid	8	277	1 – 1.17	0.3 – 0.27	1227	12	96	255	4.2	[59, 60]
Acetic Acid	17	192	1.33 – 2.04	0.26 – 0.19	1214	13.5	71	327	7.2	[59, 61]
Lauric acid	44	212	2.02 – 2.15	0.22 – 0.15	1007	13.6	66	276	6.5	[59, 61]
Stearic acid	54	157	1.76 – 2.27	0.29 – 0.17	940	9.9	49	345	11	[57, 60, 62, 63]
Palmitic acid	61	222	1.69 – 2.2	0.21 – 0.17	989	14.1	67	354	8.3	[59, 62, 64, 65]
Paraffin Wax	0 - 90	150 -250	3 – 2	0.2	880-950	12 – 14	50 – 70	400 – 800	7.1 – 9.5	[59, 66, 20]
Acetamide	82	260	2 – 3	0.4 – 0.25	1160	13.9	93	1318	22.2	[59, 67]
Erythritol	117	340	2.25 – 2.61	0.73 – 0.33	1450	10.3	148	1287	13.6	[52, 57, 68]
HDPE	130	255	2.6 – 2.15	0.48 – 0.44	952		80	463	9	[59, 69]
Phthalic anhydride	131	160	1.85 – 2.2		1530		85	2042	37.4	[70]
Urea	134	250	1.8 – 2.11	0.8 – 0.6	1320	16.7	97	189	3	[70]
Maleic acid	141	385	1.17 – 2.08		1590		184	1059	9	[70]
2-Chlorobenzoic acid	142	164	1.3 – 1.6		1544		83	1861	35.1	[71]
Adipic acid	152	275	1.87 – 2.72		1360	20.2	109	584	8.4	[72]
d-Mannitol	165	300	1.31 – 2.36	0.19 – 0.11	1490		139	1027	11.5	[52, 73, 74, 75]
Hydroquinone	172	258	1.59 – 1.64		1300		105	3415	50.9	[59, 76]
Oxalic acid	190	356	1.62 – 2.73		1900		211	524	3.9	[54, 77]

2.2 Salt hydrates

Salt hydrates, formed by water absorption of an anhydrous salt at ambient temperature and atmospheric pressure, have their phase change temperature below 120°C, low bulk prices and a relatively high storage density [78]. Subcooling during crystallization [79], phase segregation [80] and corrosion with commonly used metals (copper, aluminum, stainless steel) [59], are the main issues inhibiting their use in latent heat energy storage systems. Table 2.2 presents the thermophysical properties for a selection of salt hydrates.

Table 2.2: Thermophysical properties of selected salt hydrates.

Compound	T_m	ΔH_m	Cp_{s-l}	λ_{s-l}	ρ_s	V_{exp}	$E_{density}$	Price		Ref.
	$°C$	kJ/kg	$kJ/kg.K$	$W/m.K$	kg/m^3	%	kWh/m^3	£/m^3	£/kWh	
Water	0	333	3.3 – 4.18	1.6 – 0.61	1000	-8.7	109	0	0	[59, 81]
Calcium chloride hexahydrate	30	125	1.42 – 2.2	1.09 – 0.53	1700	11	64	93	2	[59, 66, 82, 83]
Sodium sulphate decahydrate	32	180	1.93 – 2.8	0.56 – 0.45	1463	4	82	48	1	[59, 66, 82]
Calcium nitrate tetrahydrate	43	139	1.58 – 1.92	0.43 – 0.34	1750	2.9	104	343	4	[84]
Sodium thiosulfate pentahydrate	46	210	1.46 – 2.39	0.76 – 0.38	1750	6	103	199	3	[59, 69, 85]
Sodium acetate trihydrate	58	266	1.68 – 2.37	0.43 – 0.34	1450	3	113	233	3	[59, 86, 87]
Barium hydroxide octahydrate	78	280	1.34 – 2.44	1.26 – 0.66	2180	11	171	422	4	[59, 88, 89]
Magnesium nitrate hexahydrate	89	140	2.5 – 3.1	0.65 – 0.5	1640	5	74	131	3	[59, 66, 79]
Oxalic acid dihydrate	105	264	2.11 – 2.89	0.9 – 0.7	1653	0	133	339	4	[57, 77]
Magnesium chloride hexahydrate	117	150	2 – 2.4	0.7 – 0.63	1570	8	72	56	1	[59, 79, 90]

2.2.1 Phase separation

Water separation, related to poor molecular bonding between water and the salt hydrate [80, 90] is the main factor determining thermal stability in the molten phase. Suitable encapsulation could help reduce the effects of water segregation, by preventing the release of partially evaporated water. Other technique would be the use of gelling agents, which will be further discussed in the thermal performance techniques section.

2.2.2 Subcooling

The onset of solidification can occur at a significantly lower temperature than the melting point of the salt, remaining in some cases in its meta-stable liquid form until activated [64]. Adding higher melting point salts with similar crystal structures has already proven to supress this limitation, although there is no scientific evidence as to why the additives are effective [79]. Table 2.3 presents a review on nucleating agents already used and successfully tested by the authors [79, 91, 92, 77, 90].

Table 2.3: Used nucleating agents for each salt hydrate.

Compound	T_m / °C	Subcooling	Nucleator	$\%W_t$	Subcooling with agent / °C	Ref.
Calcium chloride hexahydrate	30	22.5	Strontium chloride hexahydrate	1	0	[79]
			Barium iodide hexahydrate	0.5	0	
			Barium hydroxide	0.5	0	
Sodium sulphate decahydrate	32	25	Sodium tetraborate decahydrate	3	5	[91]
Calcium nitrate tetrahydrate	43	30	Barium hydroxide octahydrate	5		[92]
Magnesium nitrate hexahydrate	89	11	Magnesium sulphate tetrahydrate	0.5	0	[77]
			Magnesium hydroxide	0.1	0.17	
			Magnesium oxide	0.1	0.12	
Magnesium chloride hexahydrate	117	36.8	Strontium carbonate	0.5	1.2	[90]
			Strontium hydroxide	0.5	0.1	

2.3 Eutectic PCMs

Binary (two component) and ternary (three component) mixtures of inorganic salts have been widely studied for thermal storage applications. Nitrate, chloride and sulphate salts of alkali and alkaline metals, such as lithium, sodium, potassium, magnesium and calcium, are the main compounds used to produce medium temperature eutectic mixtures [93]. Due to their higher density and stability in their liquid state, they have been widely used as ionic liquids in high-temperature sensible thermal storage systems such as concentrated solar thermal power [94, 95, 96].

Due to the lack of experimental data for some of the thermophysical properties of eutectic mixtures, weighting methods were used to predict the missing thermophysical properties, namely heat capacity (Cp), density (ρ), thermal conductivity (λ) and melting enthalpy (ΔH_m), based on the correlations used by Yanping [97], Rowlinson [98] and Mehling [99]; presented in equations 2.1 to 2.6.

$$w_{mi} = x_{mi} \cdot M_i (\sum_i x_{mi} \cdot M_i)^{-1} \tag{2.1}$$

$$z_{vi} = \frac{w_{mi}}{\rho_i} \cdot (\sum_i \frac{w_{mi}}{\rho_i})^{-1} \tag{2.2}$$

$$Cp_{eut} = \sum_i Cp_i \cdot w_{mi} \tag{2.3}$$

$$\rho_{eut} = \sum_i \rho_i \cdot z_{vi} \tag{2.4}$$

$$\lambda_{eut} = \prod_i \lambda_i^{z_{vi}} \tag{2.5}$$

$$\Delta H_{eut} = Tm_{eut} \cdot \sum_i \frac{\Delta H_i \cdot w_{mi}}{Tm_i} \tag{2.6}$$

These correlations use available properties of the mixture and its constituents, molar ratio (x_{mi}), mass ratio (w_{mi}) volumetric ratio (z_{vi}) and their melting point (T_m) to predict the unknown values. A comparison was made with some eutectic salts for which experimental data was available the difference between predictions and measurements was less than 10%. Table 2.4 presents the physical properties of the selected eutectic compounds in the 0-250°C range, with the predicted latent heat values shown in bold.

Table 2.4: Thermophysical properties of selected eutectic compounds.

Eutectic compound	Mass ratio	T_m	ΔH_m	$Cp_{s/l}$	$\lambda_{s/l}$	$E_{density}$	Price		Ref.
		$°C$	kJ/kg	$kJ/kg.K$	$W/m.K$	kWh/m^3	$£/m^3$	$£/kWh$	
$CaCl_2.(H_2O)_6$ - $MgCl_2.(H_2O)_6$	67-33	25	127	1.62-1.27	0.93-0.55	57	80	1.4	[59, 69]
Urea - $CH_3COONa.(H_2O)_3$	60-40	30	**200**	**1.75-2.21**	0.63 – 0.48	74	206	2.8	[69, 100]
$Mg(NO_3)_2.(H_2O)_6$ - NH_4NO_3	61-39	52	125	2.13-2.67	0.59-0.5	58	188	3.3	[69, 100]
Urea – Acetamide	38-62	53	224	1.92-2.66	0.51-0.34	73	924	13	[83]
Stearic acid - Palmitic acid	36-64	53	182	1.72-2.23	0.23-0.17	46	351	8	[101]
$Mg(NO_3)_2.(H_2O)_6$ - $MgCl_2.(H_2O)_6$	59-41	59	132	2.29-2.81	0.67-0.53	58	99	1.7	[59, 69]
Stearic Acid - Acetamide	83-17	65	213	1.8-2.4	0.3-0.18	56	485	8.6	
$LiNO_3$ - $MgNO_3.(H_2O)_6$	14-86	72	180	2.38-2.9	0.7-0.51	84	718	8.5	
Urea - $LiNO_3$	82-18	76	**218**	**1.77-2.02**	**0.85-0.6**	84	851	10.1	[100]
Urea - $NaNO_3$	71-29	83	**187**	**1.6-2.03**	**0.75-0.59**	76	220	2.9	
Urea - NH_4Cl	85-15	102	**214**	**1.77-2.09**	**0.76-0.58**	77	174	2.3	
Urea – K_2CO_3	15-85	102	**206**	**1.66-2.02**	**0.78-0.58**	78	269	3.4	
Urea - KNO_3	77-23	109	**195**	**1.6-1.91**	**0.81-0.58**	74	255	3.4	
Urea – NaCl	90-10	112	**230**	**1.72-2.02**	**0.82-0.6**	85	180	2.1	
Urea - KCl	89-11	115	**227**	**1.69-1.96**	**0.83-0.6**	83	197	2.4	
$LiNO_3$ - $NaNO_3$ - KNO_3	30-18-52	123	140	1.17-1.44	0.79-0.53	79	1979	25	[102, 103]
$LiNO_3$ - KNO_3	34-66	133	150	1.17-1.35	0.96-0.52	82	2167	26	[102, 104]
KNO_3 - $NaNO_2$	56-44	141	97	1.18-1.74	0.73-0.57	52	504	9.7	[105]
KNO_3 - $NaNO_3$ - $NaNO_2$	53-6-41	142	110	1.17-1.73	0.72-0.57	60	497	8.3	[59, 105]
KNO_2 - $NaNO_3$	48-52	149	**124**	**1.05-1.63**	**0.58-0.52**	70	994	14	[105]
$LiNO_3$ - $NaNO_2$	62-38	156	**233**	**1.57-1.91**	**1.12-0.66**	143	3816	27	
$LiNO_3$ – KCl	58-42	160	**272**	**1.26-1.35**	**1.31-0.59**	161	3409	21	[59, 106]
$LiNO_3$ - $NaNO_3$ – KCl	45-50-5	160	**266**	**1.32-1.69**	**0.88-0.59**	166	2852	17	
HCOONa – HCOOK	45-55	176	**175**	**1.15-0.93**	**0.63-0.43**	92	421	4.6	[107]
$LiOH$ - $LiNO_3$	19-81	183	**352**	**1.6-2**	**1.33-0.69**	202	5165	26	[105]
$LiNO_3$ - $NaNO_3$	49-51	194	262	1.35-1.72	0.87-0.59	165	3084	19	[59, 105]
$LiNO_3$ - $NaCl$	87-13	208	369	1.54-1.56	1.35-0.63	235	5254	22	[59, 106, 108]
KNO_3 - KOH	80-20	214	**83**	**1.03-1.35**	**0.88-0.54**	43	611	14	[59]
KNO_3 - $NaNO_3$	55-45	222	**110**	**1.01-1.49**	**0.73-0.51**	61	482	8	
$LiBr$ - $LiNO_3$	27-73	228	**279**	**1.34-1.38**	**1.14-0.57**	196	6134	31	[105, 109]
$LiOH$ - $NaNO_3$ – $NaOH$	6-67-27	230	**184**	**1.3-2**	**0.78-0.67**	107	538	5	
$NaNO_2$ - $NaNO_3$	55-45	233	163	1.31-2.13	0.59-0.64	97	382	3.9	
$CaCl_2$ - $LiNO_3$	13-87	238	317	1.5-1.53	1.37-0.69	204	5325	26	
$LiCl$ - $LiNO_3$	10-90	244	342	1.58-1.61	1.37-0.64	218	6019	28	
$NaNO_3$ – $NaOH$	86-14	250	**160**	**1.19-1.86**	**0.66-0.6**	97	339	3.5	[59]

2.4 Performance enhancement methods

Most PCMs have low thermal conductivity, which can seriously affect the storage system charge and discharge heat transfer rates. To address this limitation, extended metal surfaces [7], conductive powders [5] or conductive matrices [6] have proven to be effective in increasing the PCMs heat transport properties, leading to a more uniform temperature distribution within the PCM and consequently better charge and discharge performances for the latent heat storage container/system. Other thermal enhancement solutions improve heat transfer between the flow and the PCM through direct contact between the PCM and their respective heat transfer fluid, allowing higher convective currents within the solid PCM whilst preventing flow mixing in the molten PCM due to different densities [110].

Another technique could be shape stabilization through the use of polymeric adsorbents such as polyethylene or polystyrene [111], that would prevent leakage of molten PCM. On the case of salt hydrates, the use of inorganic adsorbents, such as

diatomaceous earths containing silica [69], could prevent water separation from the inorganic salt, maintaining its phase change enthalpy.

2.4.1 Heat transfer enhancement using extended metal surfaces

One of the most widely used heat transfer enhancement techniques is the addition of extended metal surfaces, fins, to increase the heat exchange area between the PCM and the flow. Numerous studies on modelling the phase change process with different fin geometries have already been made [112, 113]. Agyenim [66] tested a compact horizontal tube in tube container with erythritol as the PCM, using longitudinal fins to enhance heat transfer.

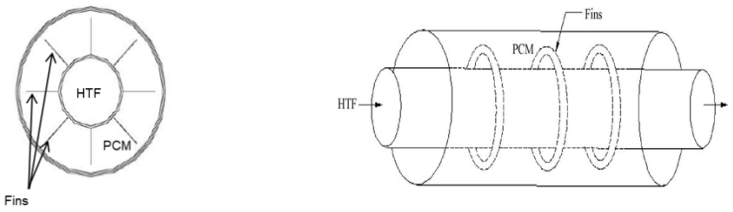

(a) longitudinal fins [66] (b) annular fins [5]

Figure 2.1: Schematic representation of extended metal surfaces in a tube in tube.

They concluded that the system with longitudinal fins had an adequate melting/solidifying process that could provide the required heat flux suitable to act as the heat source for driving Li-Br absorption cooling systems. Figure 2.1a and 2.1b illustrates two common fin geometries widely used in the literature [5].

2.4.2 Heat transfer enhancement using carbon

Exfoliated graphite, also known as expanded graphite (EG) is presented in figure 2.2a, 2.2b and 2.2c. It has a thermal conductivity ranging from 24 to 470 W/m.K depending on the measuring direction, with the potential to increase thermal conductivity within the PCM [88] using low volume ratios (usually around 10-15% [59]). EG is generally obtained from the corrosion of natural graphite with a mixture of nitric and sulphuric acid, followed by drying and rapid heating in a furnace at 800 to $900^{c}ircC$ to obtain the desired volumetric expansion. To produce EG/PCM composites, the PCM is impregnated into the EG in vacuum to suppress the formation of air gaps within the composite material [69, 5]. This technique is the most effective procedure currently used to enhance the PCM thermal conductivity [94]. It could also provide a shape-stabilized (SS) form to the PCM since pore cavities can withstand the thermal expansion typical during phase change and prevent leakage of molten PCM [69].

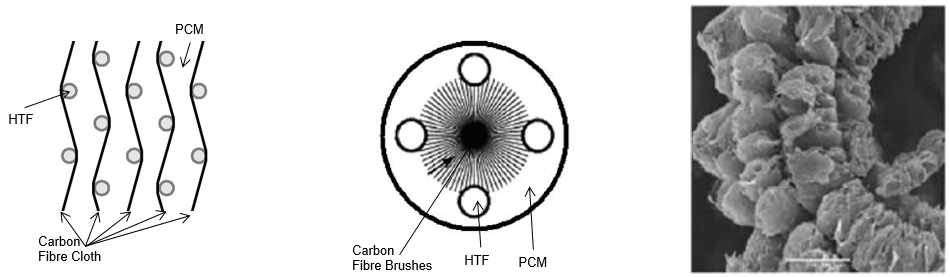

(a) carbon fiber cloth (b) carbon fibre brush (c) Expanded graphite

Figure 2.2: Three examples of heat transfer enhancement using carbon [5]

The container studied by Nakaso [6] presented in figure 2.3 was predicted to double its heat output (from 25 to 50kWth) if a carbon fibre cloth comprising 0.8% of the storage volume was incorporated into the system. The system would then provide a nearly constant heat output of 50kW for around 10h and 20 minutes.

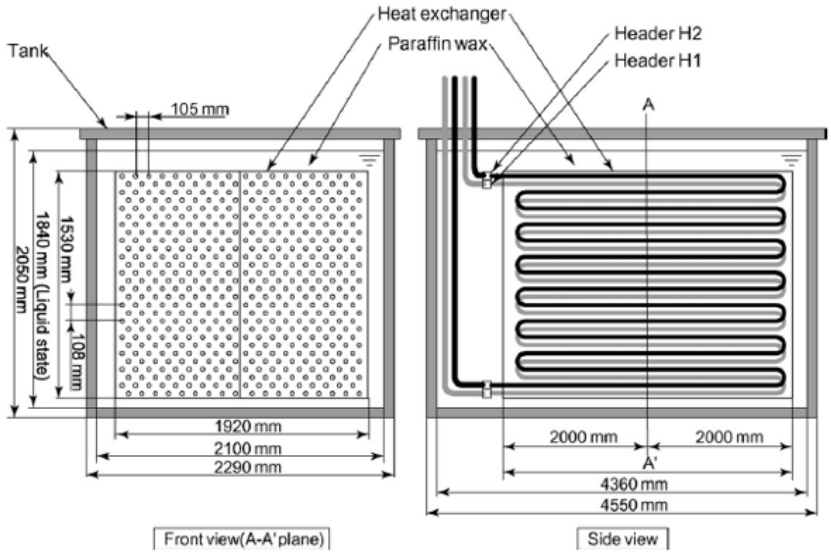

Figure 2.3: A schematic diagram of the 18 770L compact latent heat storage unit designed by Nakaso [6], comprised of 18 parallel 28mm copper tubes, each having 14 passes through the PCM volume.

2.4.3 Heat transfer enhancement using metal matrices

Using sparse metal matrices is another way to increase thermal conductivity within the bulk PCM, providing also multiple nucleation points. The impregnation of a PCM medium with steel wool can be more cost effective than using EG, although the potential risk of thermal gaps due to poor contact between conductive surfaces can reduce their thermal conductivity improvement. Due being a sparse matrix and not a rigid and porous foam as expanded graphite, it would not provide shape stabilization of the molten PCM.

Including small percentages by volume of metallic particles such as lessing rings, presented in figure 2.4a and 2.4b, could increase thermal diffusion within low thermal conductivity PCMs [5], would have the benefit of increasing the number of nucleation points, potentially enhancing crystallization within the PCM. However, the risk of thermal gaps would be even higher than using steel wool, due to their sparse distribution and also the conductive material could lose its miscibility when the PCM is in its molten state due to differences in density, separating from the storage material and sinking to the base of the container. This could be prevented by including gelling agents in the PCM [69], with a consequent reduction in the PCM volume ratio.

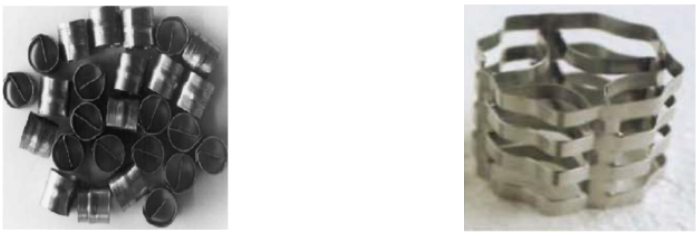

(a) aluminum lessing rings (b) stainless steel lessing rings

Figure 2.4: Two examples of metal matrices, from Agyenim [7]

2.4.4 Direct heat transfer techniques

Another technique to improve heat transfer is to provide direct contact between the heat transfer fluid and the PCM. It effectively increases heat transfer during the melting process due to the additional flow mixing between the heat transfer fluid and molten PCM, increasing the convective heat transfer on the solid-liquid PCM interface [8]. Weilong [114] studied the performance of a direct contact latent heat storage container using erythritol and a heat transfer oil, seen in figure 2.5a to 2.5c, concluding that at the beginning of the melting process the oil has a low flow rate due to the blockage of solid erythritol, the top surface of the PCM melts faster than the bottom due to the higher heat transfer rate and the melting time varies significantly with the oil flow rate.

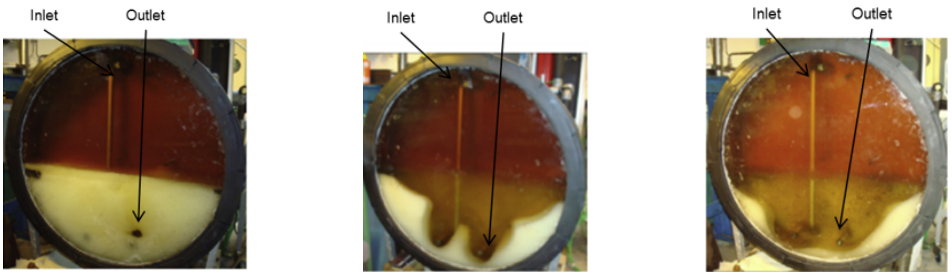

(a) initial stage (b) middle stage (c) final stage

Figure 2.5: A temporal variation of the melting process in a direct contact heat transfer container using erythritol as PCM and oil as heat transfer fluid, from Weilong [8].

To overcome the initial blocking of the fluid flow path when the PCM is in the solid state, Shaopeng [9] studied the insertion of electric heaters, seen in figure 2.6, and concluded that the overall energy spent on melting the initial flow pathways was 5% of the total thermal energy stored.

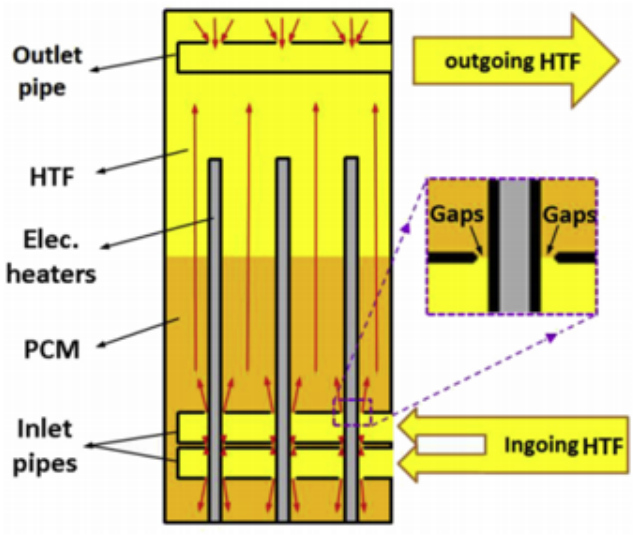

Figure 2.6: Schematic cross section showing the locations of the inlet pipes electric heaters, studied by Shaopeng [9]

2.4.5 Shape stabilization

Shape-stabilized PCMs are obtained adsorbing the molten PCM into the structure of a porous adsorbent. Common inorganic adsorbents such as some diatomaceous earths containing silica (SiO_2) are generally used to adsorb salt hydrates due to their affinity with water [65]; however their maximum adsorption capability is usually below 50% of its weight. Organic polymeric adsorbents such as high-density polyethylene, polystyrene [111] and polyvinyl chloride (PVC) are generally used to adsorb paraffin waxes, fatty acids and their blends and can generally adsorb up to 80% of its weight [115].

Alkan [116] prepared shape stabilized fatty acid PCMs by blending them with solutions of Poly(methyl methacrylate) (PMMA) in chloroform. They concluded that the composite PCM could maintain its shape up to 80%wt of PCM and that they could be considered as candidates for latent heat storage systems integrated into underfloor space heating applications.

2.5 Potential applications for indirect latent heat storage containers

The integration of latent heat storage containers into specific heating or cooling applications is dependent on the heat transfer fluid used: gas or liquid. Using water as the heat transfer fluid, latent heat storage containers could be integrated into conventional domestic central heating systems with common water radiators, ideal when retrofitting gas boilers for heat pumps [117], as illustrated in figure 2.7a. Due to their higher storage capacity when compared to sensible water storage, they would allow the heat pump to be operated during off-peak times preventing the overload of the local electrical grid demand [37]. Using air as the heat transfer fluid, latent heat storage containers could be integrated into centralized ventilation systems, typical in large office areas and commercial buildings [118], as illustrated in figure 2.7b.

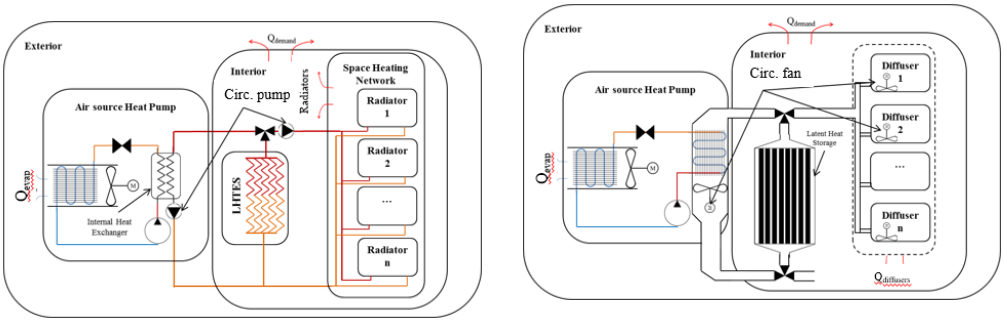

(a) into a domestic space heating system

(b) into a ventilated heating and cooling system system

Figure 2.7: Simplified diagrams of the integration of LHTES into two different heating systems

Most latent heat storage containers can be divided into two groups: compact and encapsulated. In compact latent heat storage containers, the PCM is enclosed within a large container with an embedded heat exchanger [7], a general configuration used is the shell and tube type, presented in figure 2.8a.

Encapsulated latent heat storage containers are those in which the PCM is encapsulated within small containers, over which the heat transfer fluid flows, leading to a heat storage system that contains a greater component of sensible heat storage than compact latent heat storage systems over the same temperature range [119], due to the larger volumetric ratio of heat transfer fluid. Such encapsulated designs have the versatility to be integrated with both air and water heating networks, due to their shape versatility and leak proof construction. Figure 2.8b and 2.8c present the simplified cross sections of 2 different types of encapsulated latent heat storage containers.

It is imperative that a void fraction is included in the design of any PCM storage container to allow for thermal expansion that occurs during the melting process.

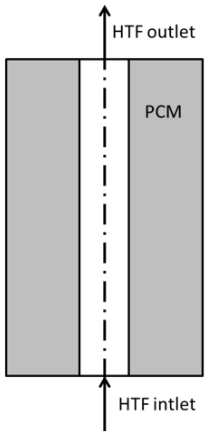

(a) compact tube in tube

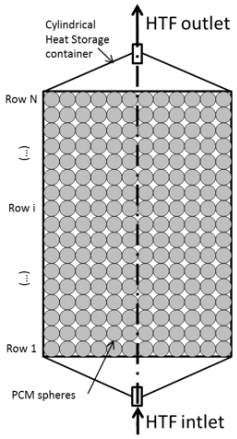

(b) encapsulated packed bed

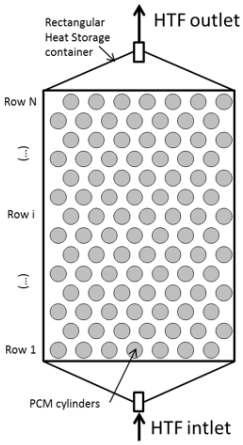

(c) encapsulated staggered cylinders

Figure 2.8: Cross sections of three geometries used in latent heat storage containers

2.5.1 Compact latent heat storage systems

Compact latent heat storage systems can have higher PCM volumetric ratios than encapsulated latent heat systems $[m^3_{PCM}/m^3_{Container}]$, theoretically providing longer isothermal outputs; however low rates of thermal diffusion within the bulk PCM can limit their heat transfer rate [120].

For domestic and small district water heating requirements, characterized by

heating rates typically below 50kW, more complex heat exchanger configurations can be used to obtain higher inlet-outlet temperature differentials, since flow head losses are not the main challenge. Figure 2.3 presents a schematic diagram of an 18 770L PCM container modeled by Nakaso [6], with a predicted thermal storage capacity of $516.7kWh_{th}$, using a paraffin wax with a melting point of 49°C (discharged from 53°C to 40°C). Nakaso [6] predicted numerically that without any thermal enhancement, the system could provide a constant 25kW thermal power output for 80% of its total capacity, around 16h and 32 minutes.

For larger process heating applications, large parallel arrays of tubes should be used, to overcome the heat transfer limitation imposed by the PCMs low thermal conductivity [50], rather than using complex heat exchanging geometries [6]. Large parallel tube bundles can reduce fluid flow passing through a single tube and their inherent frictional head losses, maintaining a high power output through the bundle combination, multiplying the flow passing through a single tube by the total number of tubes in the bundle. Figure 2.9a illustrates the longitudinal cross section of a storage container with 100 tubes running in parallel for the heat transfer fluid. The illustrated storage system could contain up to 827L of PCM within a container 2m high, with a square cross section of 800mmx800mm.

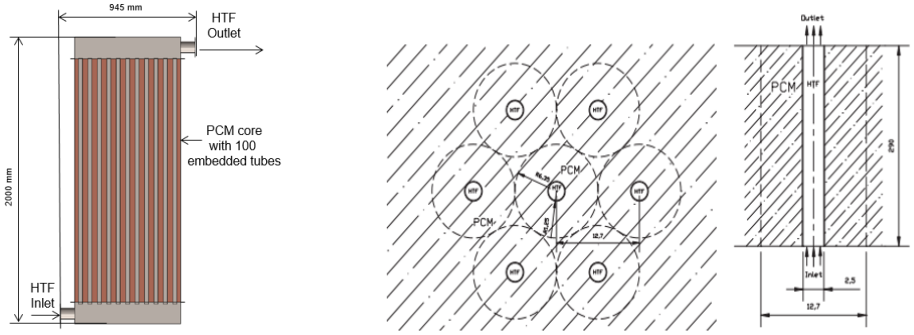

(a) cross-section of 827L thermal store

(b) top and cross section view of thermal store studied by Colella [50]

Figure 2.9: Schematic representations of compact thermal store geometries for district heating applications

Latent heat storage for use with district heating networks has been studied by Colella [50], and compared to traditional water storage which is commonly used in many district heating systems. Colella studied numerically the use of the commercial wax RT100 from Rubitherm [20] in a 15x15 matrix of 25mm copper pipes 2.9m length, theoretically storing 446kWhth from 65°C to 120°C, the tube bundle arrangement is displayed schematically in Figure 2.9b. The study concluded that the LHTES unit could be capable of covering a 130kW–400kW heat request depending on the operating conditions, charged during the night and discharged in daytime operation.

Due to the high energy density of latent heat storage systems, portable containers charged from industrial waste heat streams could be of potential interest in providing heat to the nearby district heating networks. Figure 2.10 presents the design of a prototype thermal storage system for use with a district heating system housed in a 20 foot long cargo container tested by Deckert [10]. The system stored a maximum capacity of $1758kWh_{th}$, using sodium acetate trihydrate between 90 and

25°C; supplied by a biogas plant located 6km from the district heat network with the charged store being physically transported between locations. Limiting the practical storage capacity to 80%, the compact latent heat storage system could provide 40kW of nearly constant thermal output over a discharge time of 38h. Chapter 7 will further study this storage approach.

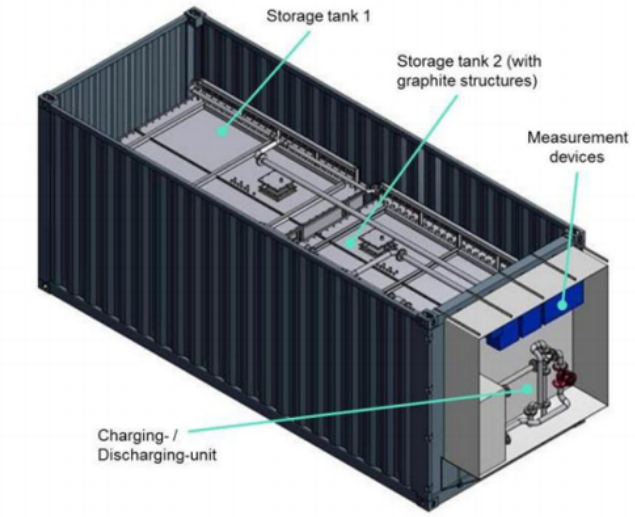

Figure 2.10: Structure of the prototype storage system developed by Deckert [10] to meet the heat demands of a district heating network.

2.5.2 Encapsulated latent heat storage systems

Systems using encapsulated PCMs generally offer higher heat transfer area per storage material volume [$m^2_{HT_{area}}/m^3_{PCM}$], but present lower PCM volumetric ratios [m^3_{PCM}/m^3_{Store}]. Another advantage is the ease of obtaining leak-proof solutions [40], suitable for volatile materials. Their geometrical flexibility provides them with easiness of integration into any given storage container, regardless of size; hence their popularity [119, 121].

The geometries used vary significantly with the application, but they commonly have cylindrical or spherically shaped capsules, which can be inserted into off the shelf storage containers. Cabeza [11] undertook a study in which 2 to 6 small cylinders containing a mixture of 90% sodium acetate trihydrate with 10% graphite as the PCM, were inserted in the upper part of a domestic hot water tank, making good use of the water tank thermal stratification, seen in figure 2.11. The study concluded that the addition of 2% by volume of PCM (2 tubes) to the top region of the store could increase 40% of a 146L water tank thermal storage capacity over a temperature difference of 1°C around the PCM solidification point (around 54°C).

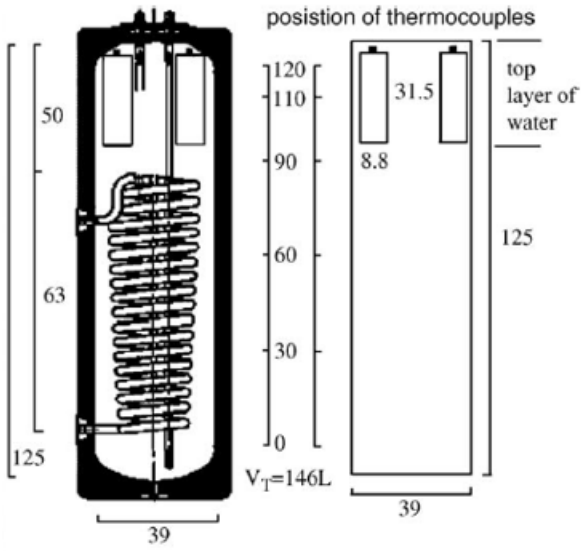

Figure 2.11: Schematic representation illustrating the location of the encapsulated PCM modules inside the water tank of the experimental work undertaken by Cabeza et al. [11].

Encapsulating a PCM into spherical capsules, seen in figure 2.12a and 2.12b, provides closer packing within the storage system [106] and higher heat transfer fluid flow mixing, consequently obtaining better convective heat transfer coefficients [119] than vertical cylinders, illustrated in figure 2.11. However, lower rates of thermal diffusion within the spherical capsules can reduce their effectiveness in exchanging heat to and from the heat transfer fluid [12].

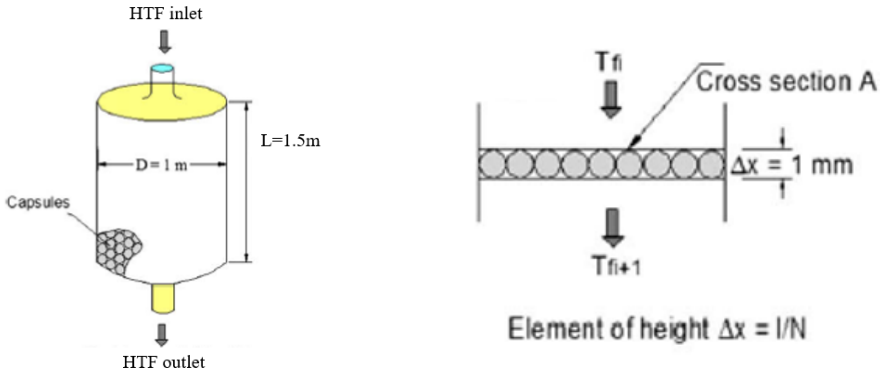

(a) modeled container (b) cross section view of a node

Figure 2.12: Simplified representation of the packed bed model studied by Regin [12].

Direct space cooling applications in which the thermal store charging occurs during the night and discharging during the day (from 10.00 to 18.00) to provide space cooling in office areas have been studied by Mosaffa [13] and Jiao [122]. Using air as the heat transfer fluid, a thermal store was made with rectangular slabs containing $CaCl_2.6H_2O$ as PCM_1 and RT25 [20] as PCM_2. Figure 2.13a and 2.13b illustrate the system studied by Mosaffa with a PCM store in an office air duct. The

storage unit was composed by 80 rectangular slabs with 10mm thickness, 500mm width, and 1.3m length, with air gaps of 3.2mm thickness. The modeling results demonstrated that the system could provide a constant cooling rate between 2.5kW and 5kW, with the air flow varying from $800m^3/h$ to $1600m^3/h$ respectively; for an inlet air temperature of 36°C, the calculated coefficient of performance of the system was around 7.

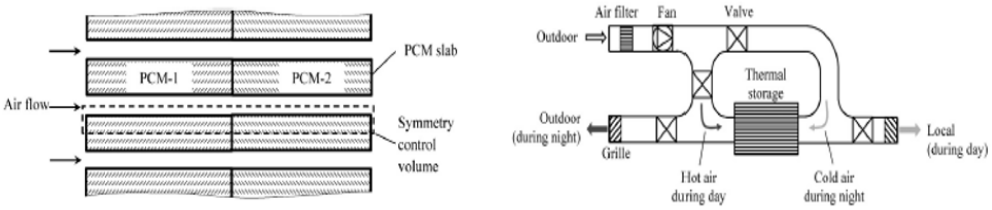

(a) cross-section view

(b) store integration

Figure 2.13: Schematic representation of the ventilated thermal store studied by Mosaffa [13].

Another possible application for an encapsulated latent heat storage system was studied by Reyes [123] and is illustrated in figure 2.14a and 2.14b. Heat from solar thermal collectors is absorbed by a 10x30 matrix of black aluminum soda cans filled with paraffin wax, and then air is used as the heat transfer fluid to discharge the $5.267kWh_{th}$ latent heat store (from 80°C to 20°C). Due to poor convective heat transfer from the outer shell and poor thermal diffusivity of the wax within the can, aluminum strips were used between the soda cans and within the wax, obstructing the air flow and providing multiple thermal bridges within the soda can, increasing the overall heat transfer area and providing a substantial increase in the latent heat storage system effectiveness and global solar collector system efficiency.

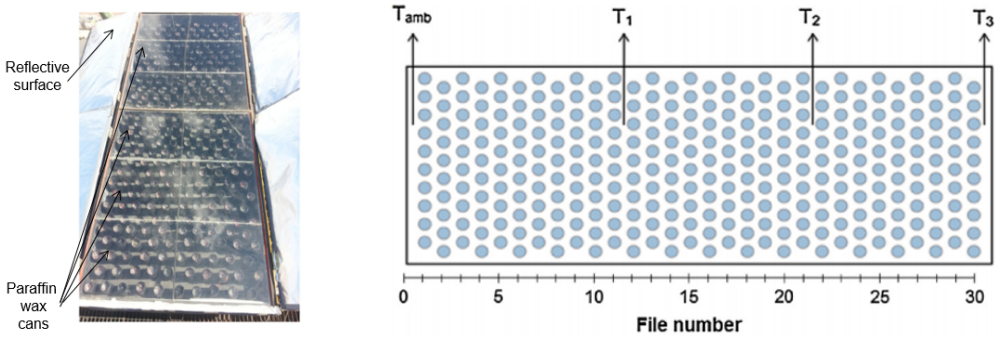

(a) store top view picture

(b) schematic top view

Figure 2.14: Schematic representation of the solar collector developed by Reyes [110].

Micro-encapsulation

Microcapsules with a diameter varying from around $1 - 1000\mu m$ [59] offer another effective method to encapsulate PCMs. Such microcapsules when introduced into a liquid form a slurry, effectively increasing the thermal storage capacity of the working fluid and potentially its convective heat transfer properties.

Current production methods for microencapsulated PCMs are coacervation, suspension and emulsion polymerization, poly-condensation and poly-addition. Huang [124] undertook a study in which a cylindrical container filled with a PCM slurry was heated and cooled using a helical coil heat exchanger. The slurry varied between 25, 35 and 50% composition by volume of PCM capsules to the carrier fluid. It was concluded that higher volumetric ratios (50% respectively) reduced natural convection heat transfer within the storage container.

Another disadvantage of using PCM filled microcapsules is the low PCM volumetric ratios per capsule, normally around 50%, which when accounting the slurry total volume leads to a very low PCM volumetric ratio, suppressing the typical heat capacity increase obtained when using PCMs [78, 84].

2.6 Discussion and conclusions from the review of phase change materials and their potential applications

This literature review has laid out the framework to assess suitable PCMs according to the operational temperature range and also showcased the most quoted techniques to improve the performance of active latent heat storage systems. With this information, the active integration of PCMs three different applications will be studied and their potential energy savings and CO_2 emissions reductions will be assessed.

Phase change materials have the potential to store large amounts of energy within a smaller temperature range when compared to common sensible heat storage materials. Due to the low thermal conductivity of many PCMs, poor rates of thermal diffusion within the PCM can seriously affect the storage system charge and discharge rates that can be achieved.

A comprehensive review of PCMs melting between 0 and 250°C has been made and the relevant properties of promising phase change materials presented. Below 100°C, organic compounds and salt hydrates are the most promising materials. Eutectic mixtures with Urea seem promising around 100°C, and in the range from 130°C up to 250°C eutectic mixtures of inorganic salts appear to be the most promising PCMs.

A review of potential indirect latent heat storage containers and systems suitable for integration with various process heating and cooling networks is also reported. Due to its geometrical versatility, encapsulated systems seem more feasible since they can be integrated to any existing system without major technical constraints, although they have lower PCM volume ratios. Compact systems can offer larger periods of constant temperature due to their higher PCM volume ratios.

For active heating/cooling applications where higher power outputs are required, heat transfer enhancement among the PCM is imperative to achieve reasonable heating and cooling outputs, since PCMs low thermal conductivity can be a major constraint.

Chapter 3

Review of heat transfer processes and mathematical procedures to model thermal energy storage containers

Thermal energy storage (TES) systems can store heat or cold to be later released, under a given temperature differential and fluid flow. TES systems are divided in three types already described in the previous chapter: sensible heat, latent heat, and thermochemical [125]. In general TES refers to the process of storing enthalpy in a specified thermal gradient of a given mass with a given heat capacity, as it is presented in equation 3.1. The amount of stored heat is directly proportional to all the thermophysical properties referred above.

$$E(\rho, V, Cp, \Delta T) = \rho \cdot V \cdot Cp \cdot \Delta T; [J] \tag{3.1}$$

3.1 Modes of heat transfer

To obtain the desired heat transfer rates, the storage heat transportation methods must also be taken into account, all dependent on the thermal gradient that the heat storage system can provide to the end user. Those can be conduction, convection, advection, and radiation heat transfer.

Conduction heat transfer refers to the enthalpy transfer in a static material, where there is no macroscopic movement of particles, also known as diffusion heat transfer. This heat flux is related to the random translation movement, and also the internal rotation and vibration movements of its molecules [126], and can be calculated using Fourier's Law, equation 3.2.

$$\dot{q}_{cond} = -\lambda \cdot \frac{dT}{dx}; [{}^{W}/_{m^2}] \tag{3.2}$$

Convection heat transfer is a superficial phenomenon and refers to the heat flux driven by the macroscopic movement of particles next to a surface, equation 3.3. Such fluid movement is associated to, at any given moment, a considerable number of molecules moving collectively or as an aggregate [126]. Conduction heat transfer still occurs within the fluid inter-molecular movements; however, the fluid global

movement is imposed as the ruling heat transfer mechanism. The Nusselt number [127] is the adimensional coefficient used to quantify the ratio between convection and conduction heat transfer, presented in equation 3.4.

$$\dot{q}_{cv} = h_{cv}(T_{surf} - T_{\infty}); [^{W}/_{m^2}] \tag{3.3}$$

$$Nu = h_{cv} \cdot \frac{L_c}{\lambda} \tag{3.4}$$

Advection heat transfer refers to the heat transfer process imposed by the macroscopic movement of particles, a flow. It differs from convection heat transfer since it relates to a heat flux in the bulk of a material, similar to conduction, not surface related, presented in equation 3.5.

$$\dot{q}_{adv} = \rho \cdot \frac{\dot{V}}{A} \cdot Cp \cdot \frac{dT}{dx}; [^{W}/_{m^2}] \tag{3.5}$$

Radiation heat transfer refers to the heat flux obtained when a temperature difference exists between 2 surfaces in sights of each other, equation 3.6 (the temperatures in the equation are in Kelvins). The radiative emitting limit is defined by Stefan-Boltzmann constant (σ), and the emission coefficient (ϵ) is to account the inefficiencies of non-black bodies in emitting and absorbing electromagnetic radiation, photons.

$$\dot{q}_{rad} = \epsilon \cdot \sigma(T_{surf}^4 - T_{env}^4); [^{W}/_{m^2}] \tag{3.6}$$

3.1.1 Analogy with electrical circuits

There is an analogy between thermal and electrical circuits, and it can be useful to expose the heat transfer problem more schematically. Comparing the voltage driving potential to a temperature differential, the resistance to the heat flux would be given by the inverse of the heat transfer coefficients, demonstrated in equation 3.7.

$$Re = \frac{\Delta V}{I}[^{V}/_{A}] \equiv \begin{cases} Rt_{cond} = \frac{\Delta T}{\dot{Q}_{cond}} = \frac{dx}{\lambda \cdot A}; [^{K}/_{W}] \\ Rt_{conv} = \frac{\Delta T}{\dot{Q}_{conv}} = \frac{1}{\alpha_{conv} \cdot A}; [^{K}/_{W}] \\ Rt_{rad} = \frac{\Delta T}{\dot{Q}_{rad}} = \frac{1}{\epsilon \cdot \sigma \cdot (T_{surf}^2 + T_{env}^2) \cdot (T_{surf} + T_{env}) \cdot A}; [^{K}/_{W}] \end{cases} \tag{3.7}$$

As it has been previously said thermal energy storage is related to the temporal variation of enthalpy in a given mass, it is therefore a transient problem. The following section describes the transient mode of transportation in the bulk of a phase change material.

3.2 Transient methods to account phase change

In order to predict and optimize latent heat systems, reliable modelling solutions are required. Melting or solidification of a material accounts for several different mechanisms. Those involve heat, often also mass transfer, possible subcooling, absorption or release of latent heat and changes in the thermophysical properties of

the storage material [128]. Phase change is described by a particular kind of moving boundary, where the phase process is occurring. This problem was initially studied by Clapeyron and Lame in 1831 when analyzing the cooling process in the formation of the crust of the Earth [129]. Nevertheless, the variable that characterizes the speed of a melting/solidification front, the Stefan number (equation 3.8), is named after Jozef Stefan, the Slovene physicist who introduced the general class of such problems in 1889 when studying the problem of ice formation [130].

$$St = \frac{Cp \cdot (T_m - T_{wall})}{\Delta H_m}; \tag{3.8}$$

3.2.1 Governing equations

Any given stationary liquid with buoyancy driven forces, can be assumed incompressible, with constant physical properties, laminar and with no viscous dissipation [131]. Thus, the equations describing the overall balance of a given volume are usually the conservation of mass and the Navier Stokes equations of momentum, as reported in [132].

Those governing equations require a velocity field for each spatial coordinate and a scalar Pressure dependent field, where buoyancy forces are assumed to act in the z-direction following a linear density-temperature relation known as the Boussinesq approximation [131]. After determining the velocity profiles for each spacial coordinate (to determine convection and advection heat transfer), the energy balance of each spacial coordinate can be determined, presented in equations 3.9 and 3.10. The source term S is to account for heat generation within the control volume [14].

- In cartesian coordinates

$$\rho \cdot V \cdot C_p \cdot \left(\frac{\partial T}{\partial t} + u\frac{\partial T}{\partial x} + v\frac{\partial T}{\partial y} + w\frac{\partial T}{\partial z} \right) = \lambda \cdot \left(\frac{\partial^2 T}{\partial x^2} + \frac{\partial^2 T}{\partial y^2} + \frac{\partial^2 T}{\partial z^2} \right) + S \tag{3.9}$$

- In cylindrical coordinates

$$\begin{aligned} &\rho \cdot V \cdot Cp \cdot \left(\frac{\partial T}{\partial t} + u_r\frac{\partial T}{\partial r} + \frac{u_\theta}{r}\frac{\partial T}{\partial \theta} + u_z\frac{\partial T}{\partial z} \right) \\ &= \lambda \cdot \left(\frac{\frac{1}{r}\partial}{\partial r}\left(r\frac{\partial T}{\partial r} \right) + \frac{1}{r^2}\frac{\partial^2 T}{\partial \theta^2} + \frac{\partial^2 T}{\partial z^2} \right) + S \end{aligned} \tag{3.10}$$

3.3 Numerical methods to solve partial differential equations

The governing set of coupled partial differential equations, with three distinct velocity directions, pressure and temperature components possess a major computational challenge due to the non-linearity of the convective terms and the moving melting front. Since the focus of this research is the overall performance of heat storage systems and their subsequent integration into practical applications, only thermal diffusion models will be developed (known as enthalpy methods), reducing the governing equations for each control volume to one (equation 3.9 for Cartesian

coordinates and equation 3.10 for cylindrical coordinates). the initial step is to divide the physical domain into a matrix to later assign an unknown to each cell and solve it for each time step.

To account phase change, the heat capacity terms in the left part of the equation 3.10 are considered dependent of its nodal temperature (Cp(T), demonstrated in equation set 3.11) [133, 134, 135], and its integration between a specified temperature interval above and below its melting point totals its latent heat of fusion [133]:

$$Cp\,(T) = \begin{cases} Cp_s & : T < T_m - T_{sl}/2 \\ \frac{Cp_s + Cp_l}{2} + \frac{H_l}{T_{sl}} & : T_m - T_{sl}/2 \leq T \leq T_m + T_{sl}/2 \\ Cp_l & : T > T_m + T_{sl}/2 \end{cases} \tag{3.11}$$

3.3.1 Spatial discretization

In order to divide the physical domain, two types of grids can be used: steady and transient. Steady grids maintain their spatial discretization over time; whereas transient grids deform themselves to follow the solid-liquid interface [133]. Transient grids use two independent domains to describe solid and liquid phases [136], being the interface speed and direction calculated using the Stefan condition [134], described in equation 3.12.

$$\rho_s \cdot V \cdot \Delta H_m \cdot \vec{n_n} = \lambda_s \left\{ \frac{\partial T}{\partial n} \right\}_s - \lambda_l \left\{ \frac{\partial T}{\partial n} \right\}_l \tag{3.12}$$

Besides the time constraint, grids can be structured and unstructured. Structured grids are those where the spatial discretization has orthogonal axes, and can easily be implemented in the matrix form. Examples of those are the Cartesian, Cylindrical (figure 3.1a) and Spherical grid systems. For more complex geometries, transformation techniques are commonly used to shape the grid into the physical domain [136].

Unstructured grids (figure 3.1b) are often used in finite element techniques [133], using elements such as the tetrahedron, the cube and the hexahedron; where the number of nodes for each element defines the mesh complexity.

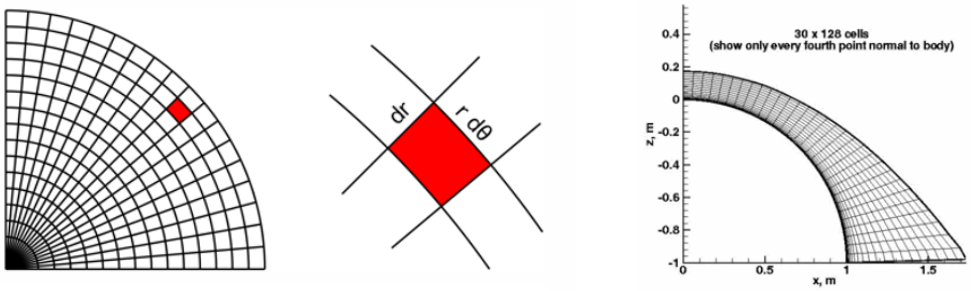

(a) 2D cylindrical grid (b) 2D unstructured grid

Figure 3.1: Simplified diagrams of a structured and unstructured grid, from [].

The algorithms developed in this thesis consider only structured grids with Cartesian, Cylindrical and spherical coordinates, depending on the geometry.

3.3.2 Domain boundaries

The physical boundaries of a heat transfer model can have 3 types of interaction. The Drichilet or 1^{st} order boundary condition (figure 3.2a) is considering constant the value of a transient scalar variable (a temperature imposition). Newman or 2^{nd} order boundary condition (figure 3.2b) [133] defines the surface interaction with a heat flux, constant or transient in time.

Third order or convective surface border condition (figure 3.2c) defines a convection interaction with another domain, being able to represent a transient boundary condition interacting with both domains. The algorithms developed in this thesis utilize this type of interaction to model the fluid flow passing through the heat storage material surface considering a convective heat transfer coefficient determined according to the flow geometry and Reynolds number (laminar, transient or turbulent flows).

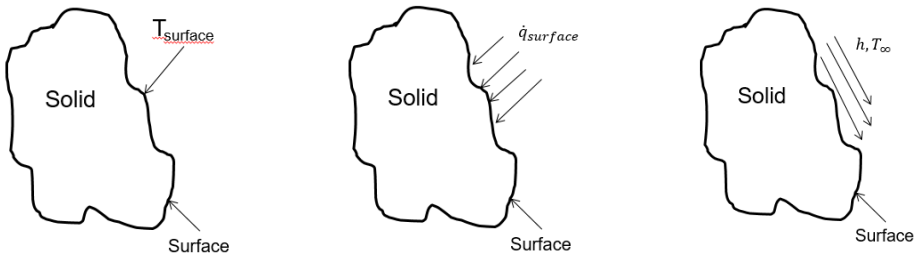

(a) drichilet (b) neumann (c) 3^{rd} order boundary

Figure 3.2: Simplified diagrams of the three available types of boundary conditions, from [14].

3.3.3 Model computation

After defining the spatial discretization and physical boundaries of our problem, the 2 most common techniques to solve numerically the partial differential equations are the finite difference method and the finite element method. The algorithms developed on this thesis were based on the finite difference method, although a general description of the finite element method will be made as well.

Finite element method

When complex geometrical constraints appear in the physical model, a nodal approach can provide greater versatility (figure 3.3a). The finite element method relies on having non-overlapping elements with nodal interactions with other elements, being those elements easily deformed to the desired shape.

The initial process is to discretize the solution domain, dividing it into a finite number of sub domains (elements) of simple geometry such as triangles or quadrilaterals, figure 3.3a and 3.3b) obtaining the finite element mesh. The mesh will later be refined until a desirable accuracy is achieved.

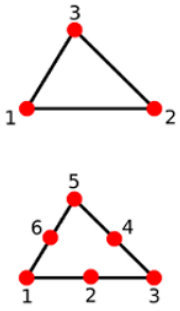

(a) 3 and 6 nodes triangular element

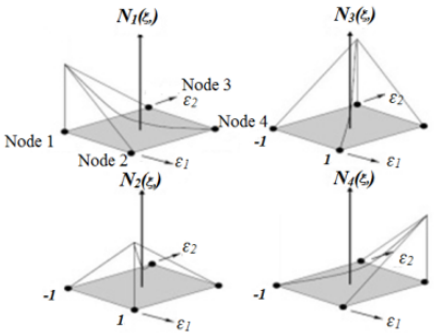

(b) weighting method in quadrilateral element

Figure 3.3: Simplified diagrams of two different elements.

The following procedure is to develop an integral formulation for the governing equations, either by the method of weighted residuals or the variational method. The method of weighted residuals is based on the minimization of a residual term R by approximating the integral formulation to the governing equation. The variational formulation relies on a minimization obtained through a variational form of the governing equation. Both methods use classical variational method of approximations to solve the integral equations [132].

After selecting the integral formulation, an approximation function is chosen to develop equations to approximate the solutions for each element. The appropriate function with unknown coefficients is chosen to approximate the solution; usually a polynomial [14].

With all the polynomials selected accounting the nodal percentage of in each element, figure 3.3b, an element characteristics equation is formed. The direct substitution of the approximation function in the integral form of the governing equation of the element results in individual characteristics equation for each element. After having the characteristics equation for each element, all elements are assembled into the general stiffness matrix, $[K^e]$, displayed in equation 3.13. The assembly process is governed by the concept of continuity, where neighbouring elements with common nodes must have equivalent unknown values or its derivative values.

$$[K^e]\{\Phi\} = \{f^e\} \tag{3.13}$$

Then, the boundary conditions are imposed; the system of equations is solved for each time step minimizing its round-off error due to the truncation of the partial differential equations. Finally, a post processing of the solved data allows us to determine relevant parameters such as total heat transfer rate, energy stored, etc.

Finite difference method

Such algorithms use Taylor's polynomial expansions to numerically approximate the partial differential equations [132]. The computational method involves a 2 step process. Initially, appropriate finite difference formulas are selected according to the physical process described by governing equation; afterwards, these formulas are replaced in the governing equation to obtain the discretized equation.

The algorithms developed in the thesis rely on the finite volume method (figure 3.4), where the domain is divided into a finite number of non-overlapping cells, and

in each cell the governing diffusivity equation is discretized using Taylor polynomial expansions [132]. To accurately model the storage material enclosure, the boundary nodes with the enclosure would have half the control volume so that the change in domain is accurately represented (as shown in figure 3.4).

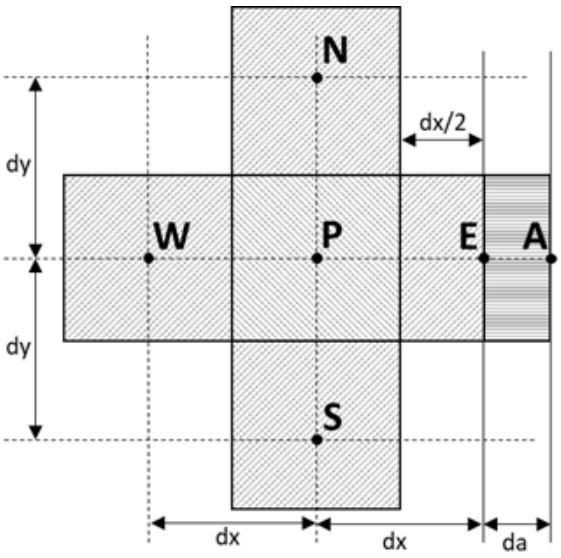

Figure 3.4: 2D finite volume method using Cartesian coordinates detailing the spatial discretization near the boundary between the storage material and enclosure

By suppressing the convective velocity terms in governing equation 3.9, the energy balance of a control volume in its Cartesian coordinates is detailed in equation 3.14. The capacitance term C [J/K] is the multiplication of the control volume density, volume and specific heat capacity.

$$C \cdot \frac{\partial T}{\partial t} = \frac{\partial}{\partial x}\left(\lambda_x \cdot \frac{\partial T}{\partial x}\right) + \frac{\partial}{\partial y}\left(\lambda_y \cdot \frac{\partial T}{\partial y}\right) + \frac{\partial}{\partial z}\left(\lambda_z \cdot \frac{\partial T}{\partial z}\right) \tag{3.14}$$

There are three common techniques to solve the partial difference in time presented in equation 3.14. Acknowledging that time is a one-way coordinate [132]; its integration can either be using an explicit, implicit or the Crank-Nicholson method. Figure 3.5 presents a simplified comparison between these 3 time integration procedures.

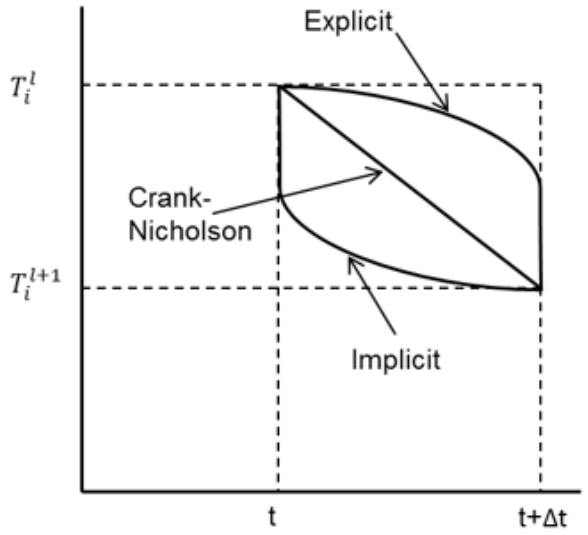

Figure 3.5: Graphical comparison between the different time approximation schemes, from [14].

The explicit method considers that the value of the dependent variable of the next time step will only be function of the previous values. The implicit method considers the dependent variable value only function of its values in the next time step, and the Crank Nicholson considers that the solution will account the previous and next time step values.

Solving equation 3.14 over the control volume using Taylor's polynomial expressions, gives equation 3.15. The tri-dimensional problem then inherits a fourth dimension, time (spatial dimensions i,j,k and time dimension l presented in equation 3.15). For simplification purposes, the models developed in this thesis accounted heat propagation on 2 directions only (transversal and axial to the fluid flow).

$$\begin{aligned} C\frac{T_{i,j,k}^{l+1}-T_{i,j,k}^{l}}{\Delta t} = \lambda_x \Bigg(& f\frac{T_{i+1,j,k}^{l+1}+T_{i-1,j,k}^{l+1}-2T_{i,j,k}^{l+1}}{\Delta x} \\ & + (1-f)\frac{T_{i+1,j,k}^{l}+T_{i-1,j,k}^{l}-2T_{i,j,k}^{l}}{\Delta x}\Bigg)\Delta y\Delta z \\ + \lambda_y \Bigg(& f\frac{T_{i,j+1,k}^{l+1}+T_{i,j-1,k}^{l+1}-2T_{i,j,k}^{l+1}}{\Delta y} \\ & + (1-f)\frac{T_{i,j+1,k}^{l}+T_{i,j-1,k}^{l}-2T_{i,j,k}^{l}}{\Delta y}\Bigg)\Delta x\Delta z \\ + \lambda_z \Bigg(& f\frac{T_{i,j,k+1}^{l+1}+T_{i,j,k-1}^{l+1}-2T_{i,j,k}^{l+1}}{\Delta z} \\ & + (1-f)\frac{T_{i,j,k+1}^{l}+T_{i,j,k-1}^{l}-2T_{i,j,k}^{l}}{\Delta z}\Bigg)\Delta x\Delta y \end{aligned} \tag{3.15}$$

Re-arranging equation 3.15, the governing energy balance equation for node (i,j,k), it can be expressed in a single algebraic equation function of the bordering control volumes from the current and future time step. The solution for each time step will be a vector with all the unknown variables [14]. The solving procedure

presented in equation 3.16, considers a transport matrix [Γ] that will account all nodal heat transfers (heat conduction within the bulk material, conduction between the storage material and the encapsulant and convection between the encapsulant and fluid flow), a capacitance matrix [C] that accounts all the variables thermal capacitance (the multiplication of volume, mass and specific heat capacity), and the vector $\{S\}$ to account all nodal external interactions (such as the thermal storage system heat losses to ambient). A brief explanation of possible solvers will be described further below.

$$\begin{cases} [\Gamma_2] = f \cdot [\Gamma_1] + [C] \\ \{m\} = (1-f) \cdot \left\{[\Gamma_1] \cdot \{\Phi^l\}\right\} + [C] \cdot \{\Phi^l\} + \{S\} \\ [\Gamma_2] \cdot \{\Phi^{l+1}\} = \{m\} \end{cases} \tag{3.16}$$

3.3.4 Numerical solvers

Observing the last equation of the set 3.16, the equation can be re-arranged to $[A] \cdot \{x\} = \{b\}$ where the unknown values are the temperatures of each control volume in the next time step $\{\Phi^{l+1}\}$.

That means that the entire problem can be expressed by a system of linear algebraic equations, solved at each time step. In the following sections it will be briefly explained the direct and iterative methods commonly used to solve large system of equations [14].

Iterative methods

Iterative methods rely on successive iterations from an initial guess solution until the specified tolerance limit has been reached. The most common solver is the Gauss-Seidel algorithm [132] that converges to the solution by solving each variable using the former values for the indexes above i and the already calculated values for the indexes below i. Equation 3.17 describes the general formula.

$$x_i^{k+1} = \frac{c_i - \sum_{j=1}^{i-1} a_{i,j} \cdot x_j^{k+1} - \sum_{j=i+1}^{n} a_{i,j} \cdot x_j^k}{a_{i,j}} \tag{3.17}$$

The solution is computed until the Euclidean norm, equation 3.18, is below a pre-defined tolerance limit, usually below 0.1% [14].

$$\frac{\|x_i^{k+1} - x_i^k\|_e}{\|x_i^{k+1}\|_e} \leq \epsilon_s \tag{3.18}$$

Sometimes the convergence process requires various iterations to achieve an acceptable tolerance limit. In such cases a coefficient can be used to weight the computed solution, named the successive over-relaxation, equation 3.19

$$x_i^{k+1} = \Lambda \left[\frac{c_i - \sum_{j=1}^{i-1} a_{i,j} \cdot x_j^{k+1} - \sum_{j=1}^{n} a_{i,j} \cdot x_j^k}{a_{i,j}} \right] + (1-\Lambda)\, x_i^k \tag{3.19}$$

Direct methods

Direct methods perform a finite number of steps to obtain the solution. One of the most used is the Gaussian elimination method. Gaussian elimination aims to reduce

the system of equations into an upper triangular matrix. That is achieved by combining equations until all the lower triangular coefficients are eliminated. Equation 3.20 presents a generalized formula for the elimination process [14]. Special consideration must be undertaken if the denominator coefficient is zero. In those cases, pivoting that equation into a lower place in the matrix might solve the problem, however making the solving process more complex.

$$a_{i,j}^{k} = a_{i,j}^{k-1} - \frac{a_{k,j}^{k-1}}{a_{k,k}^{k-1}} a_{i,k}^{k}; \quad fork + 1 \leq j \leq m; \quad k + 1 \leq I \leq n; \quad m = n + 1 \tag{3.20}$$

Once the upper triangular system of equations is defined, a back substitution process will numerically solve each unknown; according to the generalized equation presented in 3.21.

$$x_i = \frac{a_{i,m}^{i} - \sum_{j=i+1}^{n} a_{i,j}^{x-1} \cdot x_j}{a_{i,j}^{x-1}} \tag{3.21}$$

A more common solver used in 2D and 3D heat transfer problems is the LU factorization method [132], which decomposes the matrix $[A]$ into the product of a lower triangular and a upper triangular matrices ($[A] = [L][U]$). After decomposing the matrix, the solution of $[L] \cdot [U] \cdot \{x\} = \{b\}$ is made by two steps. Initially, $[U] \cdot \{x\}$ is expressed as a new vector of variables $\{y\}$ obtained by solving the lower triangular matrix $[L] \cdot \{y\} = \{b\}$ by forward substitution. The vector of variables $\{x\}$ is then obtained by solving the upper triangular matrix $[U] \cdot \{x\} = \{y\}$ by backward substitution [14].

The algorithms developed in this thesis in Matlab used their "linsolve" code (which uses the LU factorization method) to obtain the unknown temperatures in each time step. The construction of matrix $[A]$ varied according to the geometry of the thermal energy storage system, explained in the next chapters (chapter 5, 6 and 7) for each case studied.

3.4 Discussion and conclusions from the review of heat transfer processes and mathematical procedures to model thermal energy storage containers

A review of heat transfer processes involved in thermal energy store systems has been made, followed by the review of computational methods to model transient heat transfer problems.

Regarding the computational methods, the control volume approach approximates its governing equations by a point wise discretization scheme, where derivatives are replaced by finite difference formulas that involve the unknown values at the nodal points. The finite element method also provide the discretization of the solution domain by assembling simply shaped sub-regions, the finite elements. The approximate function is derived over each finite element by a linear combination of interpolation functions. Its actual approximation is then obtained by minimizing the weighted residual of the problem over each element.

Phase change materials have usually low thermal conductivity, which limits the storage containers nominal heat transfer rate. This problem is usually tackled using the thermal performance enhancement techniques discussed in the previous chapter. However, focusing on the containers geometry and fluid flow arrangement can minimize the impact of the PCMs low thermal conductivity, leading to a higher utilization of the latent heat stage.

Chapter 4

Thermal analysis of phase change materials

Fifty phase change materials (PCMs) with phase transition temperatures between 0 and 250°C have been analyzed using differential scanning calorimetry (DSC) and thermogravimetric analysis (TGA) to assess their thermal stability above the melting point and measure their latent heat of fusion. The two main reasons for this material characterization was to verify if some of the PCMs quoted in the literature had a freezing point with relatively low subcooling (or a freezing point at all) and to use the measured heat capacity diagrams in the developed enthalpy models.

The materials analyzed can be classified into organic compounds, salt hydrates, and eutectic mixtures. They were evaluated based on their phase change enthalpy, thermal stability above the melting point, and a low degree of subcooling.

From the thermal analysis made, 11 potential candidates were shortlisted based on their working temperature range, low bulk price and relatively low degree of subcooling; and subjected to a slow DSC scan (1°C/min) to obtain a more accurate thermal response on their phase change. A brief explanation on the theoretical background of the thermal analysis devices commonly used, followed by a description of the experimental procedure employed will be made in the next 2 sections.

4.1 Thermal analysis measurement devices

4.1.1 Calorimetric analysis

Differential scanning calorimetry

Standard DSC analysis, also known as heat flux DSC, measure a temperature differential between a pan with the sample and an empty pan. The heat flux is then calculated at each instant through the relation presented in equation 4.1. Q is the sample heat flow, ΔT the temperature difference between the sample and the reference and R the thermal resistance from the sample mass to the sample holder.

$$Q = \frac{\Delta T}{R}; in \left[\frac{W}{m^2}\right] \tag{4.1}$$

Current measuring techniques do not use such a simplistic approach due to potential errors obtained from the transient behaviour of the sample, the difference between the sample and reference capacitances (Cs and Cr) and possible differences

in the thermal resistance between the sample and reference sensors (Rs, Rr). Equation 4.2 presents the current formulation used to calculate the instantaneous heat flow.

$$Q = -\frac{\Delta T}{R} + \Delta T_0 \cdot \left(R_r - \frac{R_s}{R_r \cdot R_s}\right) + (C_r - C_s) \cdot \frac{dT_s}{dt} - C_r \cdot \frac{d\Delta T}{dt} \tag{4.2}$$

T-history method

One of the main disadvantages of the DSC analysis is that they measure low mass samples (usually lower than 10 mg) and if the liquid PCM does not crystallize readily at temperatures just below its melting point, a more energetic reaction takes place when the nucleation eventually occurs at lower temperatures, also known as subcooling. When there is enough energy to start the solidification process, the subcooled PCM tends to increase its temperature to near its melting point, leading to a peak heat flow in the measured signal. One of the main techniques used to prevent this excessive subcooling is the T-History method.

The T-history method, first developed by Yinping [15], determines the crystallization temperature more accurately due to the higher mass of the sample, schematized in figure 4.1. The procedure consists in heating the tubes above the PCM melting temperature followed by a rapid cooling in a controlled environment with high convective heat transfer to obtain a homogeneous temperature.

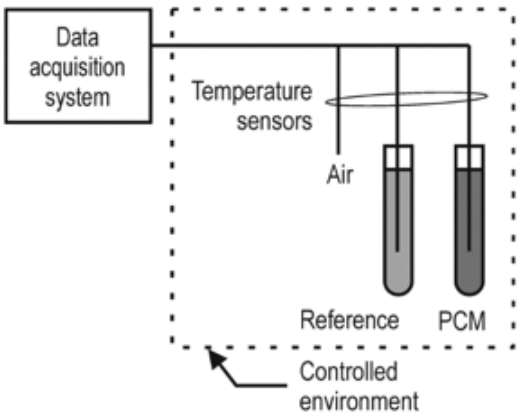

Figure 4.1: Schematic diagram of a T-History method comparison between the PCM and a reference, usually a material with know properties, from [15].

By recording the temperature drop of both tubes in the controlled environment, as presented in figure 4.2a to 4.2c, knowing the tube and reference mass and heat capacities, it is possible to obtain the heat capacity and melting enthalpy of the PCM.

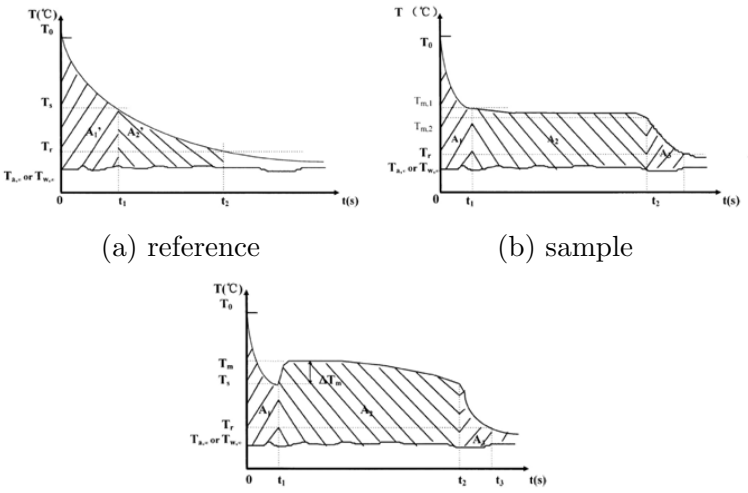

(a) reference (b) sample

(c) sample with subcooling

Figure 4.2: T-History method typical temperature recordings, from [15].

An energy balance is made for the 3 different regions, liquid state, the melting area and solid state, and in each the following equations are applied:

$$h_i = \frac{Cp_w \cdot m_w + Cp_t \cdot m_t}{A_c \cdot A_i'} \cdot (T_{i-1} - T_i); \left[\frac{W}{m^2 \cdot K}\right] \tag{4.3}$$

$$\begin{cases} (m_t \cdot Cp_t + m_p \cdot Cp_l) \cdot (T_0 - Tm_1) = h_1 \cdot A_c \cdot A_1'; \\ (m_t \cdot Cp_t + m_p \cdot \Delta H_m) \cdot (Tm_1 - Tm_2) = h_2 \cdot A_c \cdot A_2'; \\ (m_t \cdot Cp_t + m_p \cdot Cp_s) \cdot (Tm_2 - T_r) = h_3 \cdot A_c \cdot A_3'; \end{cases} \tag{4.4}$$

The first step is to obtain the respective heat transfer coefficient with the reference material for the specific temperature band (graph A), expressed in equation4.3. With that heat transfer coefficient and knowing the heat transfer area and mass of the PCM, its heat capacity is determined for the specific temperature band, as expressed in equation 4.4. It is therefore important that both the reference and PCM temperature readings have a similar ending time, usually meaning that the reference has a higher mass.

4.1.2 Thermogravimetric analysis

TGA analysis measure the weight loss of a material sample with temperature by using a precise mass balance to measure the difference between the pan with the material and an empty pan.

The device uses platinum pans, presented in figure 4.3a and 4.3b, to hold the sample and an infrared oven coated with graphite give a precise thermal response.

(a) available pans (b) balance system

Figure 4.3: Pans used and balance relative weighting method of the TGA.

4.1.3 Thermal conductivity measurements

In any thermal management application, the material thermal diffusivity is a key parameter to determine the system nominal heat transfer rates. Thermal conductivity can be measured through steady state techniques and transient techniques. Steady state techniques have the advantage of simplicity in the analysis of the measured signal, although they require longer periods of time to take measurements.

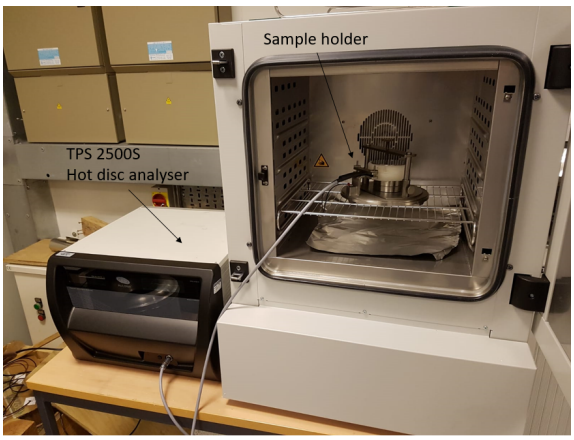

Figure 4.4: Overview of the TPS 2500s device and its customized sample holder [16].

The transient plane source technique, presented in figure 4.4, is based on the measurement of the temporal evolution of a sample being heated in its bulk. It is composed by a nickel spiral 20µm thick sandwiched between 2 Kapton films 25 µm thick to protect the nickel film and provide electrical insulation. The sensor acts both as the heating element and as the resistance temperature detector (RTD).

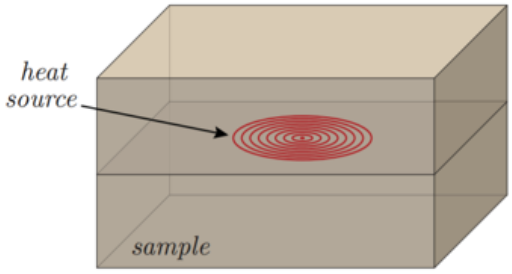

Figure 4.5: Basic principle of Transient plane source method, from [17].

The average sensor temperature is measured with the RTD and it is expected to follow the transient variation [137] described in equation 4.5. P is the heating power input, r the sensor radius, and the shape function D is dependent of the adimensional time, τ

$$T(\tau) = \frac{P}{\pi^{1.5} r \lambda} D(\tau); \tag{4.5}$$

The adimensional time is obtained with equation 4.6. The characteristic time Θ is obtained through equation 4.7; where (a) is the thermal diffusivity of the material.

$$\tau = \sqrt{\frac{t}{\Theta}}; \tag{4.6}$$

$$\Theta = \frac{r^2}{a}; \tag{4.7}$$

4.2 Experimental method

The experimental procedure taken started by measuring the thermal stability of each PCM in the TGA, followed by a heating ramp in the DSC. If the PCM showed no decomposition when the temperature was increased to at least 20°C above their melting point, the subsequent DSC cycling test would use normal aluminum lids on the DSC sample holder. If the material showed some degree of vaporization above its melting point, hermetic aluminum lids would be used to prevent the loss of the volatile gases from the test sample. After the selection of the appropriate DSC sample holder lid, 20 heating and cooling cycles were performed in the DSC cycling to at least 20°C above the PCM melting point and 20°C below their crystallization point at a ramp rate of 5°C/min. By measuring the difference in enthalpy between the 1^{st} and the 20^{th} cycle, the stability and reversibility of phase change for each tested PCM could be assessed.

After shortlisting the most promising PCMs, another DSC test using 2 different ramp rates (a 5°C/min and a 1°C/min), determined the melting point more precisely and subsequently the heat capacity thermogram for the melting and freezing process.

In order to obtain comparable results for different PCMs, reagent grade quality materials were purchased from [138] and [139]. The costs of the materials purchased in bulk were obtained from a price assessment using Alibaba for industrial grade PCM materials, with no geographical preference, similar to the method employed in chapter 2 [140].

The latent heat of each PCM was obtained by integrating the area between the endothermic peak curve and a baseline between the solid and liquid normalized heat flow curve, then multiplied by a coefficient determined by prior calibration using Indium. The TA software used, TRIOS, has a sigmoidal baseline curve that integrates a phase change accurately, accounting for the difference in the solid and liquid heat capacities of the tested material. For an estimation of the total heat stored, the temperature range selected was +/-20°C around its melting point. For the commercial PCMs tested [20, 19], the specified temperature range by the manufacturer was used.

To determine the thermal behaviour of a material, the 2 most used techniques are the differential scanning calorimetry (DSC) and thermogravimetric analysis (TGA) [141], presented in figure 4.6.

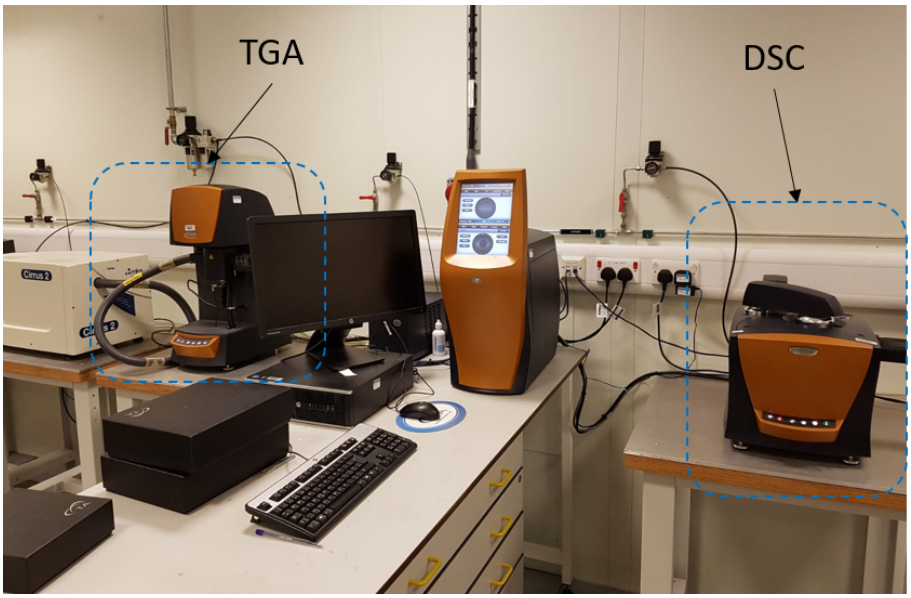

Figure 4.6: Discovery TGA (left apparatus on the image) and DSC (right apparatus on the image), from CREST thermal analysis laboratory.

4.3 Thermal property measurements

4.3.1 Measured thermal properties of selected organic PCMs

The organic compounds selected were alkanes (pentadecane, hexadecane, octadecane, and high-density polyethylene), sugar alcohols (xylitol, sorbitol, erythritol and mannitol), fatty acids (stearic and palmitic acid), dicarboxylic acids (maleic and adipic acid), benzoic acid, phthalic anhydride and 2-chlorobenzoic acid. The selection criteria was based on the economic analysis performed by the authors [140]. All the alkanes and fatty acids demonstrated good stability near their melting point, usually being in a stable molten form with little weight loss for at least 50°C above their melting point, as seen in Figure 4.7.

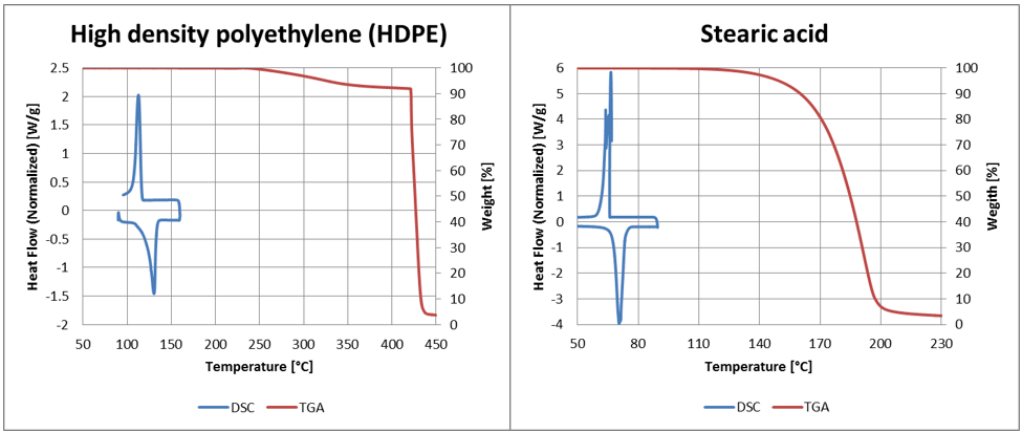

Figure 4.7: Overlay of the DSC and TGA measurement results for HDPE and Stearic acid.

The sugar alcohols analyzed seen in figure 4.8, present a smaller stability plateau above their melting point, slowly losing weight. They also possess larger subcooling than the alkane and fatty acid seen in the previous image. Measuring the enthalpy of solidification in materials that exhibit a considerable degree of subcooling (the difference between the exothermic and endothermic peaks shown in figure 4.8) can be challenging due to the sudden increase of the sample temperature, as can be seen in figure 4.8.

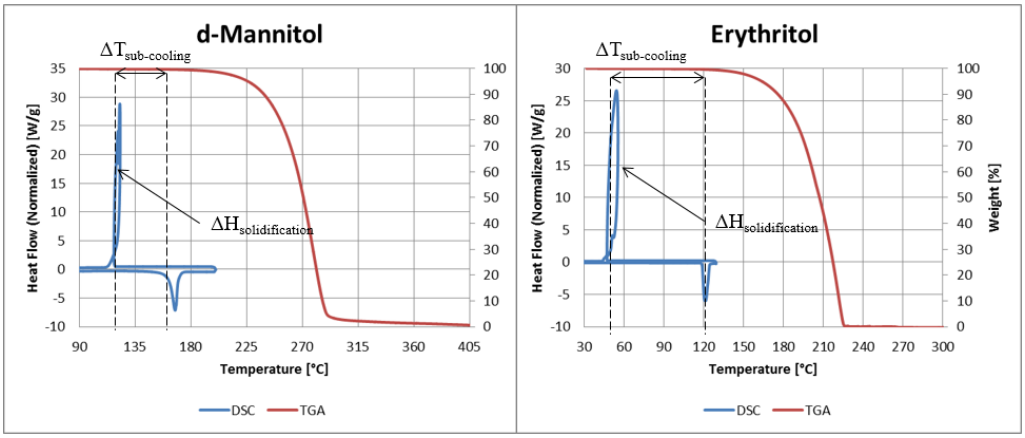

Figure 4.8: Overlay of the DSC and TGA measurements for d-Mannitol and Erythritol.

Besides sugar alcohols and HDPE, all the organic PCMs melting above 100°C were unstable in their molten state. Figure 4.9 presents the overlay of the TGA and DSC results for benzoic acid and adipic acid.

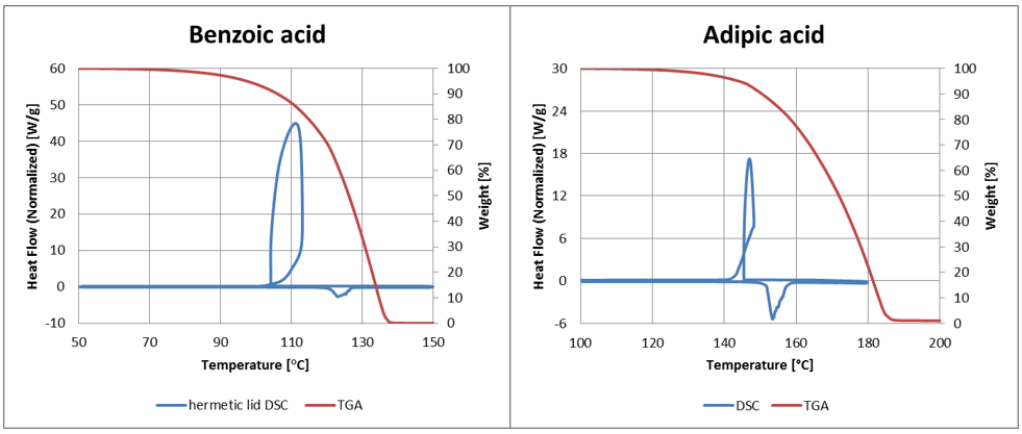

Figure 4.9: Overlay of the DSC and TGA measurement results for Benzoic acid and Adipic acid.

Benzoic acid evaporated completely at 150°C, having lost almost 50% of its mass below its melting point. Adipic acid demonstrated better thermal stability than benzoic acid, slowly evaporating with increasing temperature in its molten state. Both components also presented subcooling, with a large exothermic peak in Benzoic acid (around 45W/g).

Thermal cycling

Presented in figure 4.10 are the two fatty acids tested that melted below 100°C, stearic and palmitic acid, which demonstrated good cycle repeatability (the 1^{st} and 20^{th} cycle curves are very similar in figure 4.10), with no apparent enthalpy losses over 20 cycles and little subcooling (around 3 to 5°C). The latent heat measured of stearic acid was 199kJ/kg with a melting point of 69°C, values that were 20kJ/kg less energy dense and a melting point 5°C higher than the experimental measurements reported by Sharma [142] Palmitic acid melted at 63°C absorbing 200kJ/kg during its phase change.

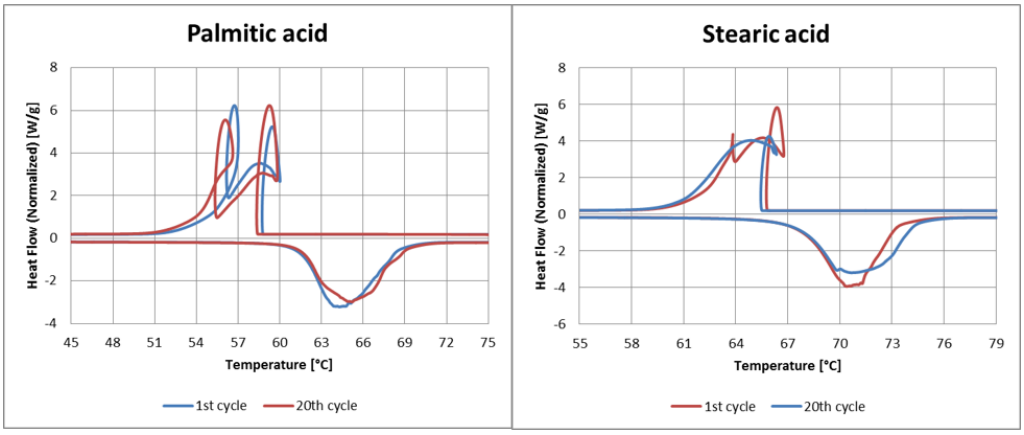

Figure 4.10: DSC thermal cycling measurements for Palmitic and Stearic acid.

Both components demonstrated subcooling, and Palmitic acid presented 2 peaks in its solidification process, possibly indicating the presence of a solid-solid phase change prior to its melting point.

The DSC thermal cycling measurements for the two sugar alcohols melting below 100°C, xylitol and sorbitol are presented in figure 4.11. These materials did not crystallize during the DSC thermal cycling tests, a partial crystallization was measured to occur at a temperature of approximately -20°C, but no reversible phase change was observed at its reported melting point. The measured latent heat values for both sugar alcohols were similar to those obtained by Tong [143] (5kJ/kg lower for xylitol and 9kJ/kg lower for sorbitol).

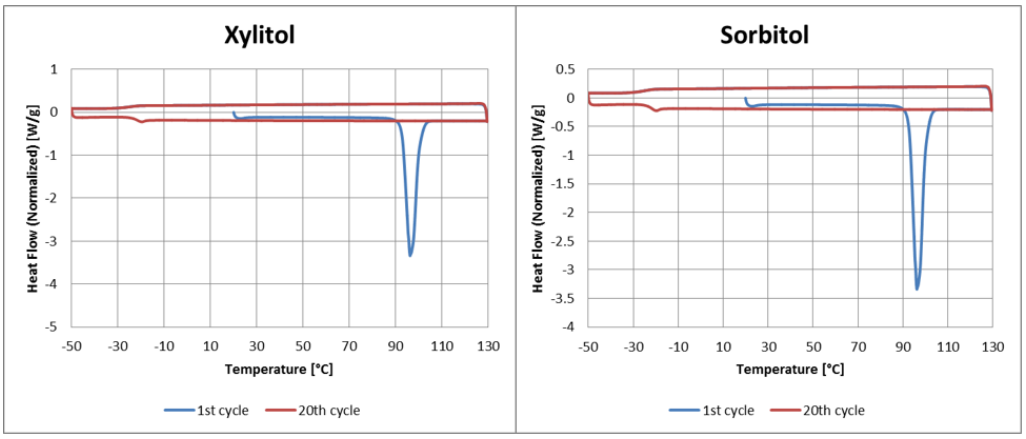

Figure 4.11: DSC thermal cycling measurements for Xylitol and Sorbitol.

Table 4.1 presents an analysis of the DSC measurements. For the economic comparison, the enthalpy values obtained were measured between the T_{max} and T_{min} temperature range. Nearly all the measured organic compounds with a melting point below 100°C were stable in their molten state, with the exception of Acetamide.

Table 4.1: Key parameters from the DSC thermal cycling analysis for the organic PCMs with a melting point below 100°C.

Organic PCMs	Enclosure	T_{melt}	Subcooling	T_{min}	T_{max}	ΔH_m	ΔH_{tot}		$\Delta H_{loss}^{20cycles}$	Price	
		°C				kJ/kg		kWh/m^3	%	$£/m^3$	$£/kWh$
Pentadecane	Normal	8	0.1	0	15	143	179	38	0	2000	52
Hexadecane	Normal	17	2.5	-5	28	202	271	58	0	2027	35
Octadecane	Normal	27	3.5	10	35	205	258	56	0	3757	68
Palmitic acid	Normal	63	4	35	75	200	300	70	0.6	650	9.2
Stearic acid	Normal	69	3	40	80	207	308	81	0.1	488	6.1
Acetamide	Hermetic	74	29	60	100	245	348	106	10	1859	17
Xylitol	Normal	93		75	115	241	327	138	100	2261	16
Sorbitol	Normal	95		75	115	149	216	89	100	1198	13.4

As stated previously, most organic materials with a phase change above 100°C required hermetic encapsulation to ensure no loss of mass in their molten state. The measurements from the DSC cycling experiments for benzoic acid and erythritol are presented in figure 4.12. Benzoic acid demonstrated good stability and reversibility during the cycling experiment, having almost no change in melting enthalpy from the 1st to the 20^{th} cycle, with its latent heat in accordance with those reported by Maki [49]. The measured latent heat of fusion of Erythritol in the 100-130°C temperature range was 321kJ/kg, with a melting point of 119°C in its first cycle. After the initial cycle, the measured melting point reduced to approximately 107°C and its measured latent heat of fusion decreased by nearly 5% over the remaining 20 cycles, 6kJ/kg lower than the values reported by Tong [68].

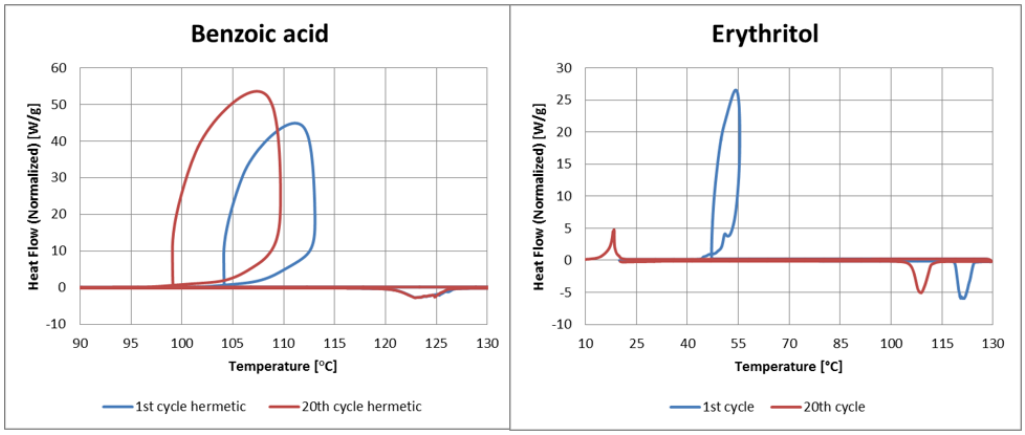

Figure 4.12: DSC thermal cycling measurement for Benzoic acid in a hermetic enclosure and Erythritol in a normal enclosure.

The DSC cycling measurements for HDPE and Phthalic anhydride are presented in figure 4.13. Both PCMs demonstrated good cycling stability, with no apparent loss in their melting enthalpy or change in their melting point. Phthalic anhydride had an increase in the degree of subcooling, 15°C for the ^{1st} cycle and 28°C for the 20^{th} cycle. High-density polyethylene did not demonstrate any subcooling, but with a wide range of phase change. Comparing the measured properties with those from the literature, the phase change enthalpy of Phthalic anhydride was 7kJ/kg less than that reported by Lorz [70].

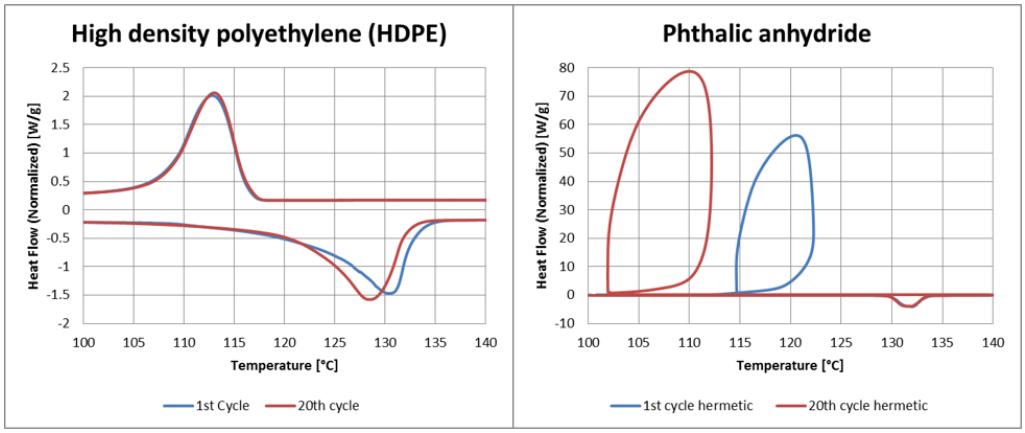

Figure 4.13: DSC thermal cycling measurements for HDPE in a normal enclosure and Phthalic anhydride in a hermetic enclosure.

Figure 4.14 presents the DSC thermal cycling measurements for maleic and 2-chlorobenzoic acid. The measured enthalpy of 2-Chlorobenzoic acid reduced approximately 18% after 20 cycles, indicating some irreversibility in its phase change. It also had the least subcooling of the tested organic compounds, measured to be between 2 and 4°C. From the measurements of maleic acid, in 20 cycles its enthalpy of phase change reduced 86% while the melting temperature continuously reduced, indicating cycle instability and unsuitability for use as a phase change material.

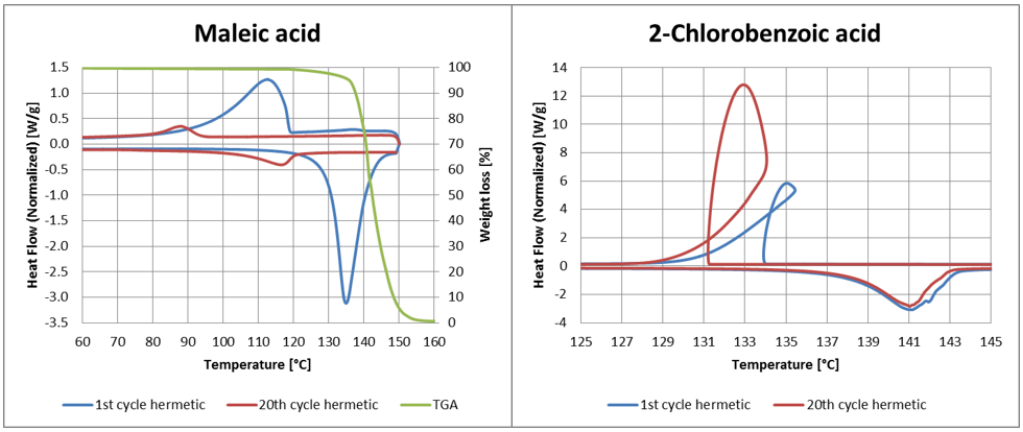

Figure 4.14: DSC thermal cycling measurements for Maleic acid and 2-chlorobenzoic acid in hermetic enclosures.

Figure 4.15 presents the DSC cycling measurements for Mannitol and Adipic acid. Mannitol had around 45°C of subcooling and lost 2% of its initial melting enthalpy in 20 cycles, while adipic acid had only 6°C of subcooling and no apparent change in enthalpy. Compared to the values reported by Barreneche [144], the measured phase change enthalpy for mannitol was 26kJ/kg lower. The measured phase change enthalpy for adipic acid was 5kJ/kg lower than that reported by Haillot [57].

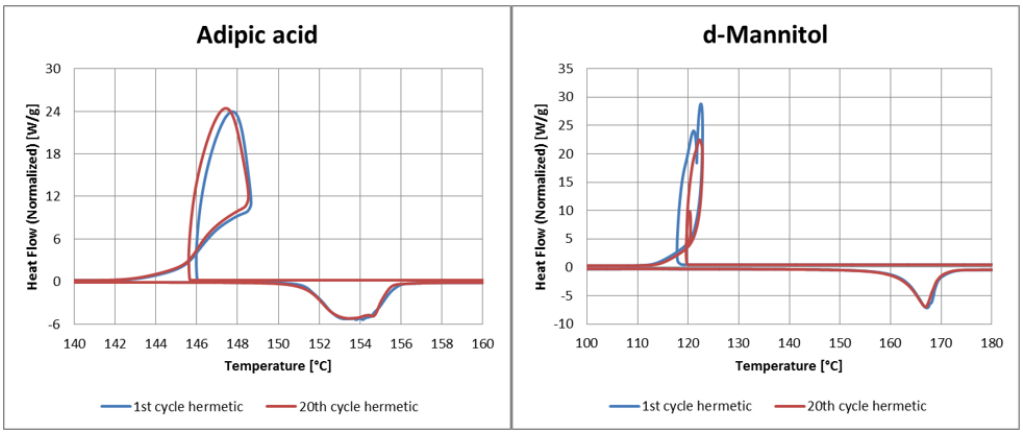

Figure 4.15: DSC cycling measurements for Mannitol and Adipic acid in hermetic enclosures.

Table 4.2 presents a summary of the key parameters obtained from the DSC thermal cycling analysis. The economic comparison used the same procedure described in chapter 2.

Table 4.2: Key parameters from the DSC thermal cycling analysis for the organic PCMs with a melting point above 100°C.

Organic PCMs	Enclosure	T_{melt}	T_{cryst}	Subcooling	T_{min}	T_{max}	ΔH_m	ΔH_{tot}		$\Delta H_{loss}^{20cycles}$	Price	
		°C					kJ/kg		kWh/m^3	%	$£/m^3$	$£/kWh$
Erythritol	Normal	119	54	65	90	130	334	412	166	4.7	4726	28.45
Benzoic acid	Hermetic	123	104	19	95	135	142	219	77	0.5	1469	19.04
HDPE	Normal	130	113	17	100	140	146	280	74	0.6	755	10.2
Phthalic anhydride	Hermetic	130	115	15	100	140	152	211	90	0.7	2880	32.066
Maleic acid	Hermetic	130	118	12	110	150	306	395	175	86	1728	9.9
(2-Chlorobenzoic acid)	Hermetic	136	134	2	105	145	146	218	93	17.8	3035	32.47
Adipic Acid	Hermetic	151	146	5	120	160	245	320	121	0.8	961	7.94
d-Mannitol	Normal	155	118	37	140	180	274	378	156	2	3575	22.85

Almost all the organic compounds required some degree of subcooling to initiate crystallization, leading to exothermic peaks increasing with the PCMs subcooling. Only HDPE had a smooth crystallization, with no exothermic reaction in its solidification process. 2-Chlorobenzoic acid showed the lowest level of subcooling, but also had a lower phase change enthalpy.

4.3.2 Measured thermal properties of selected salt hydrates

The overlay of the TGA results and DSC results for magnesium nitrate hexahydrate and magnesium chloride hexahydrate are presented in figure 4.16. It can be seen from the TGA curves that these salt hydrates undertake a continuous dehydration process; hence requiring hermetic enclosures for the DSC cycling tests.

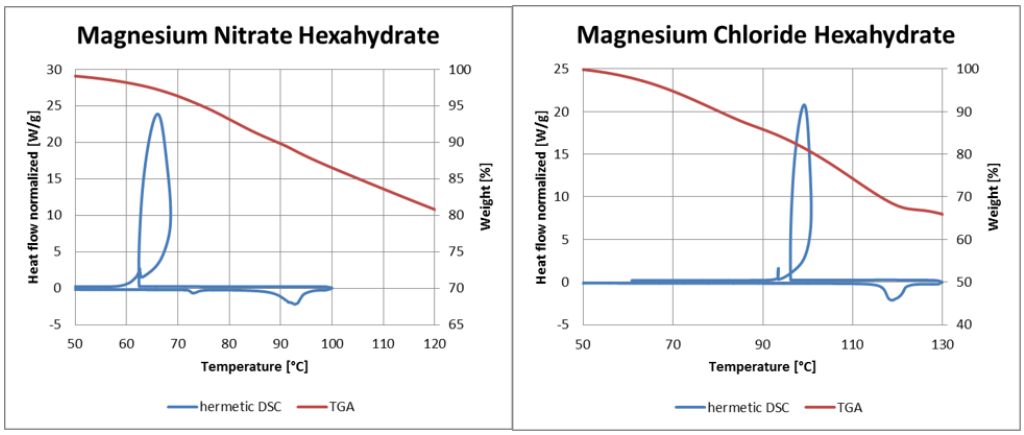

Figure 4.16: Overlay of the TGA and DSC measurements for magnesium nitrate and magnesium chloride hexahydrates.

Thermal cycling

The DSC cycling measurements for tap water and Glauber's salt in hermetic containers are shown in figure 4.17. The DSC measurements for tap water showed that it subcooled by 15°C before crystallizing. Sodium sulfate decahydrate demonstrated good cycle repeatability, no loss of its initial melting enthalpy was evident and the level of subcooling was approximately 18°C.

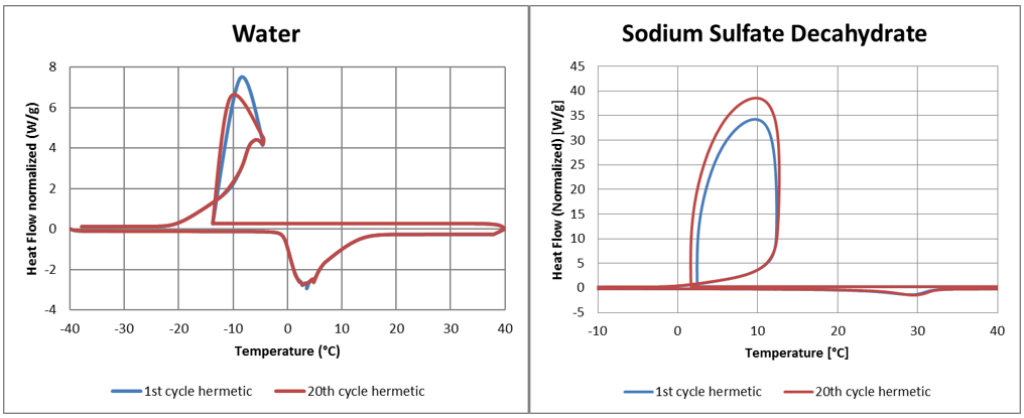

Figure 4.17: DSC cycling measurements for tap water and Glauber's salt in hermetic enclosures.

The DSC measurements for calcium chloride hexahydrate and calcium nitrate tetrahydrate are presented in figure 4.18. Between the 1^{st} and 20^{th} cycles calcium chloride hexahydrate lost approximately 4% of its melting enthalpy (138kJ/kg in the 1st cycle) values that were 27kJ/kg less than that reported by Jankowsky [59]. It had a subcooling of 54°C, with 2 distinct exothermic peaks in their solidification process, as seen in figure 4.18. Calcium nitrate tetrahydrate had a measured latent heat of 144kJ/kg, 7kJ/kg less than the value reported by Jankowsky [59]; and did not recrystallize within the limits of the DSC, which can ramp down the temperature up to -80°C. The salt hydrate had a phase change at -57°C, but not as energetic as the initial melting.

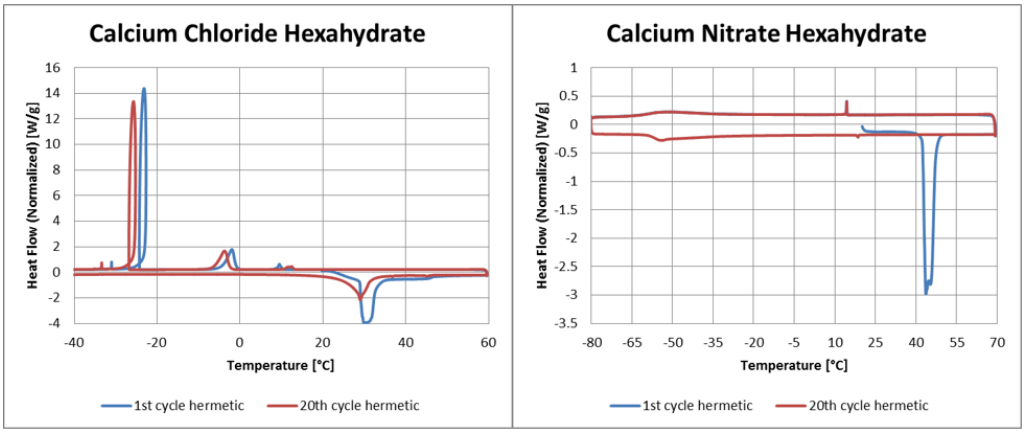

Figure 4.18: DSC thermal cycling measurements for calcium chloride hexahydrate and calcium nitrate tetrahydrate in hermetic enclosures.

The DSC cycling measurements for the hydrated salts of sodium acetate and sodium thiosulfate in hermetic containers are presented in figure 4.19. Sodium thiosulfate pentahydrate subcooled 69°C, and its melting point shifted after the first cycle from 49 to 34°C, with a 16.9% decrease in its latent heat. Sodium acetate trihydrate did not crystallize within the temperature range used, similar to the previous calcium nitrate tetrahydrate. The measured values for latent heat capacity were 8kJ/kg less for both materials compared to values reported in the literature [85].

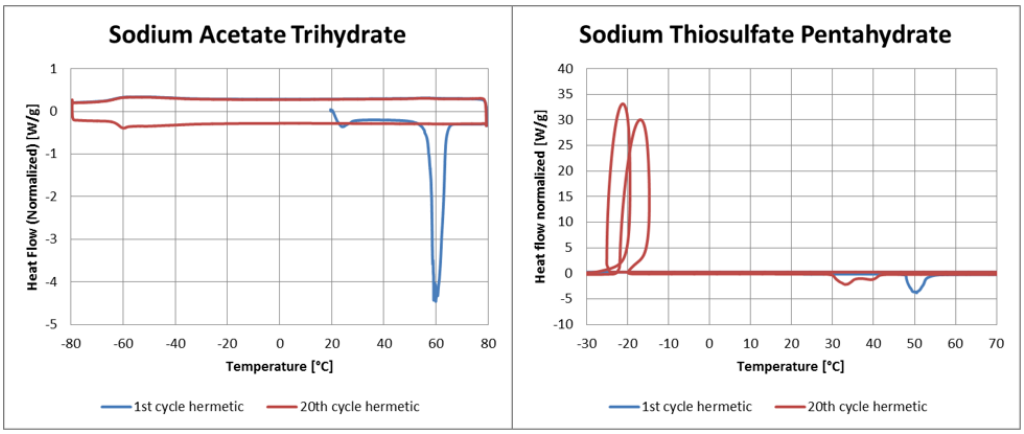

Figure 4.19: DSC thermal cycling measurements for sodium acetate trihydrate and sodium thiosulfate pentahydrate in hermetic containers.

Figure 4.20 shows the thermal cycling measurements for magnesium nitrate hexahydrate and magnesium chloride hexahydrates. Magnesium nitrate hexahydrate demonstrated good cycling properties with no loss in melting enthalpy, its subcooling reducing from 26 to 23°C between the 1^{st} and 20^{th} cycles. There was a 15% reduction in melting enthalpy between the 1st and 20th cycles for magnesium chloride hexahydrate, and subcooling increased from 20 to 22°C. Comparing its measured latent heat values with those in the literature, the value measured for magnesium chloride hexahydrate was 36kJ/kg lower than that from El-Sebaii [145] and magnesium nitrate hexahydrate 29kJ/kg lower than that measured from Nagano [146].

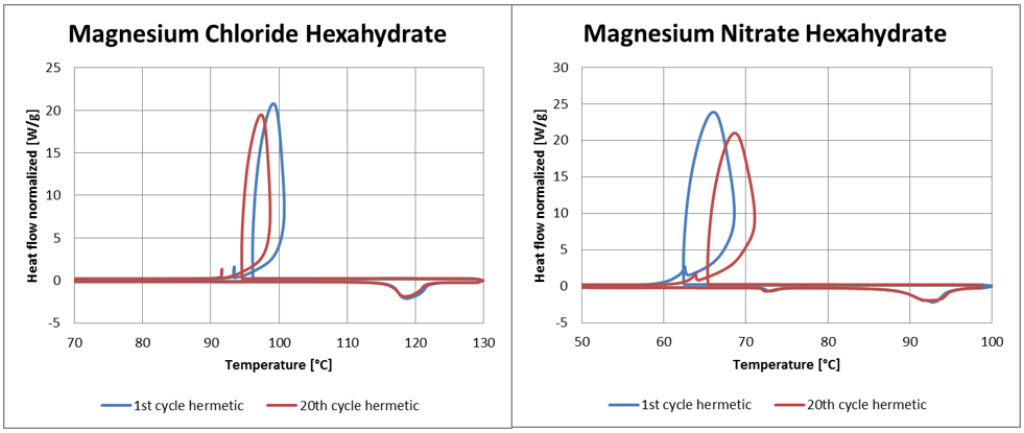

Figure 4.20: DSC thermal cycling measurements for magnesium chloride hexahydrate and magnesium nitrate hexahydrate in hermetic enclosures.

The DSC measurements for barium hydroxide octahydrate and oxalic acid dihydrate are presented in figure 4.21. Barium hydroxide octahydrate lost all of its melting enthalpy between the 1^{st} and 20^{th} cycle, proving that it is unsuitable for use as a thermal energy storage material. Oxalic acid dihydrate demonstrated a slight reduction in its melting point and a 36% reduction in melting enthalpy between the 1^{st} to the 20^{th} cycle. The level of subcooling for both the 1^{st} and 20^{th} cycle remained at 12°C. The non-linearity of the freezing curve is related to the temperature increase in the measuring sample due to the reaction taken during its freezing process, trying to reach its melting point.

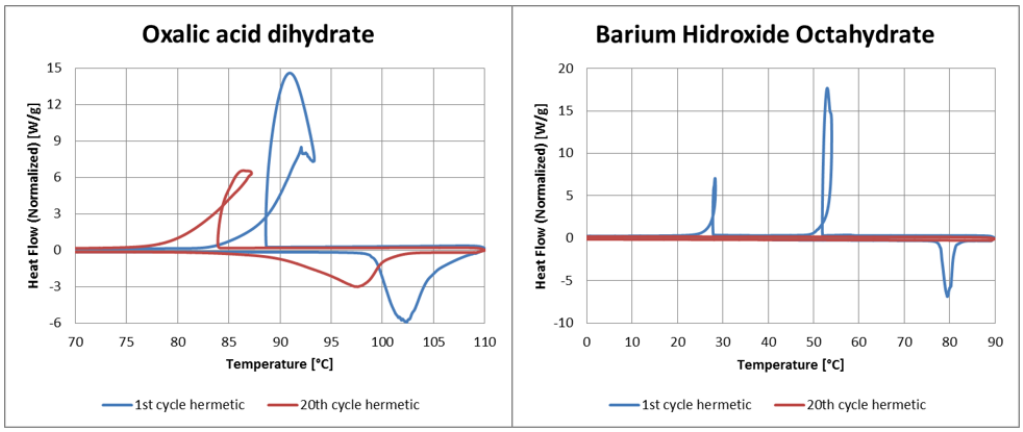

Figure 4.21: DSC thermal cycling measurements for oxalic acid dihydrate and barium hydroxide octahydrate in hermetic containers.

The subcooling that occurred for all salt hydrates tested was in agreement with previous studies reported in the literature [56, 61, 62]. Adding specified salts has been proven to reduce the subcooling of some salt hydrates [79], as reported in chapter 2. Table 4.3 reports the measured enthalpy values of the selected salt hydrates.

Table 4.3: Key parameters from the DSC thermal cycling analysis for the salt hydrates tested in hermetic enclosures.

Salt hydrates	T_{melt}	T_{cryst}	Subcooling	T_{min}	T_{max}	ΔH_m	ΔH_{tot}		$\Delta H_{loss}^{20cycles}$	Price	
	°C					kJ/kg		kWh/m^3	%	$£/m^3$	$£/kWh$
H_2O	0	-15	15	-20	20	333	458	127	3.6	0	0
$Na_2SO_4.10(H_2O)$	23	3	20	0	40	126	234	97	2.4	91	0.94
$CaCl_2.6(H_2O$	29	-25	54	10	50	144	148	70	4	185	2.64
$Ca(NO_3)_2.4(H_2O)	43			20	60	145	219	115		425	3.69
$Na_2SO_3.5(H_2O)$	49	-20	69	25	65	207	296	137	16.9	324	2.36
$CH_3COONa.3(H_2O)$	59			35	75	254	368	148		381	2.57
$BaOH.8(H_2O)$	78	52	26	50	90	232	379	229	100	757	3.3
$Mg(NO_3)_2.6(H_2O)$	89	63	27	60	100	121	232	105	0.2	192	1.82
Oxalic acid dihydrate	102	88	14	70	110	405	491	225	35.4	718	3.18
$MgCl_2.6(H_2O)$	117	96	21	85	125	108	203	88	15	86	0.97

4.3.3 Measured thermal properties of selected eutectic and non-eutectic mixtures

The selected eutectic mixtures were prepared by combining the required mass ratios of the compounds in the mixture, then gently heating to a temperature slightly above their melting point and stirring until a homogeneous melt was observed. The molten PCM was then poured into a mortar to solidify after which it was ground to a fine powder and inserted into the appropriate pans/containers for the DSC or TGA analysis.

Eutectic and non-eutectic mixtures melting below 100°C

Eutectic mixtures of fatty acids due to their low subcooling and relatively affordable bulk prices are attractive for use as PCMs. The DSC measurements of a commercial PCM developed by Croda [19] for ambient temperature control applications are presented in Figure 4.22. The DSC measurement results of Crodatherm 21 indicated

its melting point at 19°C, with a total enthalpy between 10 and 25°C of 199 kJ/kg, corresponding to a volumetric storage capacity of 48kWh/m3. The eutectic mixture of hexadecane and octadecane had a melting point of 13.5°C, storing 204kJ/kg between 5 and 20°C, a similar value to Croda21, however with a lower melting point.

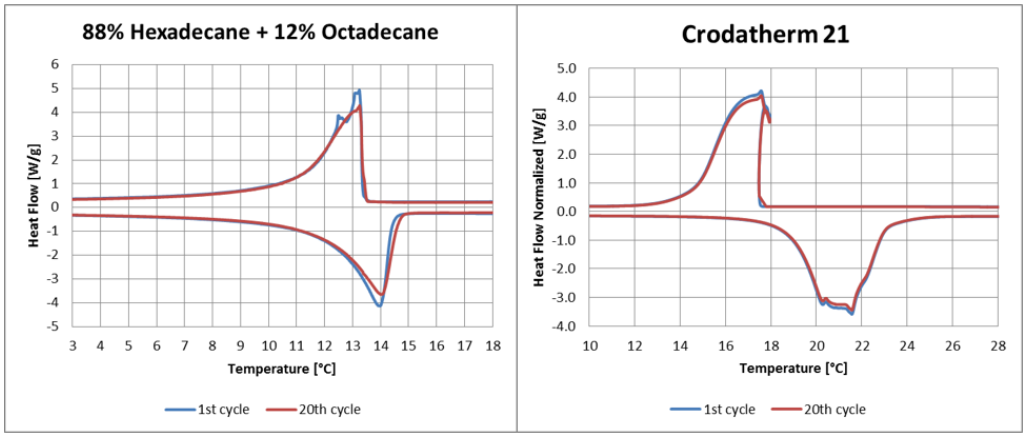

Figure 4.22: DSC measurement for the eutectic mixture of hexadecane and octadecane (88/12) [18] and Crodatherm 21 [19] in normal enclosures.

Other organic PCM mixtures widely studied are the paraffin waxes. The DSC measurements for 2 commercial paraffin waxes tested supplied by Rubitherm [20] are presented in figure 4.23. Both waxes have two crystallization peaks. For RT42, Rubitherm defines its working temperature range around the highest peak, from 33 to 50°C; while for the RT44HC, their chosen temperature range, from 35 to 55°C, covers both peaks. Comparing the measured total enthalpy values with the commercial data sheets available, RT 42 measured 15kJ/kg less enthalpy while RT44HC measured enthalpy were according to the values reported by Rubitherm.

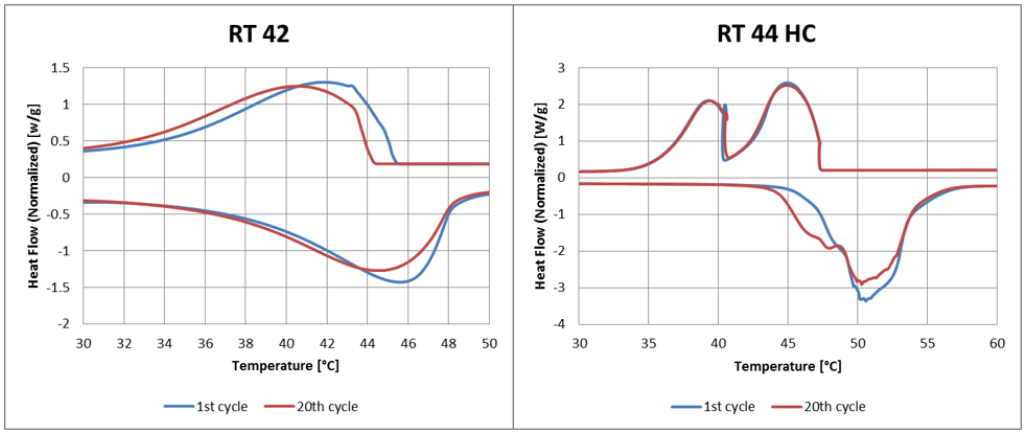

Figure 4.23: DSC measurements for two paraffin wax blends; RT42 and RT44HC [20].

The DSC thermal cycling measurements for the eutectic mixtures of magnesium nitrate hexahydrate with ammonium nitrate and stearic acid with palmitic acid are presented in figure 4.24. The ammonium nitrate mixture, studied by Griffith [147],

subcooled by approximately 17°C, with no significant change in melting enthalpy between the 1^{st} and 20^{th} cycles. The eutectic mixture of stearic acid and palmitic acid had no subcooling, no enthalpy loss and its measured enthalpy values were in accordance with the experimental work performed by Baran [101].

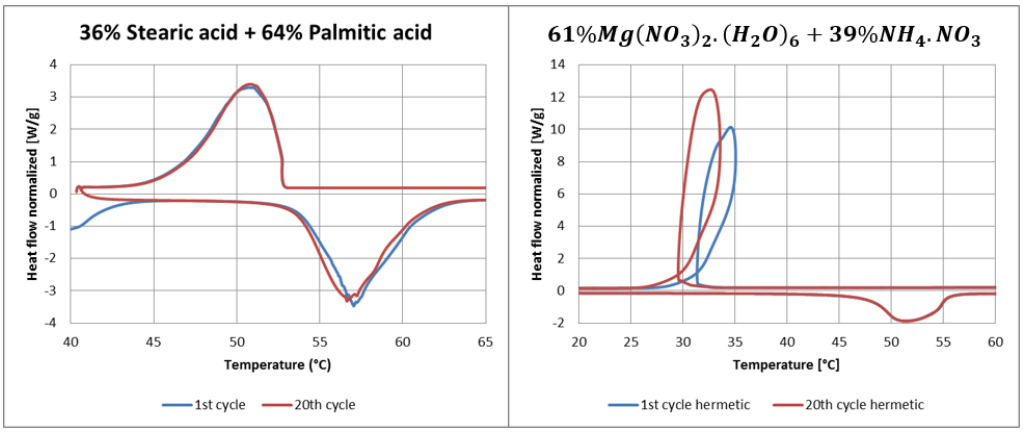

Figure 4.24: DSC thermal cycling measurements for the eutectic mixtures of stearic acid and palmitic acid (36/64) in the normal enclosure and $Mg(NO_3)_2.(H_2O)_6$ – NH_4NO_3 (61/39) in a hermetic enclosure.

Figure 4.25 shows the DSC measurements for eutectic mixtures of magnesium nitrate hexahydrate with magnesium chloride hexahydrate and lithium nitrate. Both eutectic mixtures had a high melting enthalpy and low subcooling (being around 3°C with lithium nitrate, taking the inflection of the solidification curve as the reference point). Being relatively dense compared to other PCMs tested, they have higher volumetric energy density, one of their main advantages when compared with organic PCMs. Comparing the measured latent heat with the values reported by Jankowski [59]; both the eutectic mixtures were in accordance with the published results by author.

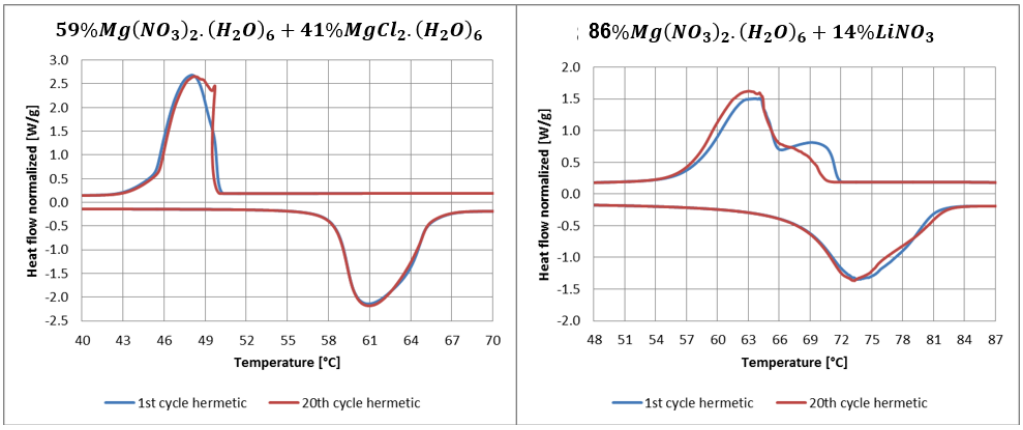

Figure 4.25: DSC thermal cycling measurements for $Mg(NO_3)_2.(H_2O)_6$ - $MgCl_2.(H_2O)_6$ (59/41) and $Mg(NO_3)_2.(H_2O)_6$ - $LiNO_3$ (86/14) eutectic mixtures in hermetic enclosures.

DSC thermal cycling measurements of urea eutectic mixtures with sodium and lithium nitrate are presented in figure 4.26. The mixture with sodium nitrate seemed

stable in the molten state with a loss of only 1.8% of its initial melting enthalpy in 20 cycles; the degree of subcooling was approximately 42°C. There was also a continuous increase in the melting peak heat flow in the 20 cycles. The mixture with lithium nitrate had its melting enthalpy decreased by around 43kJ/kg in the 20 cycles performed, with no significant endothermic peak evident by the 20^{th} cycle during the melting process, making it unsuitable to be used as a PCM.

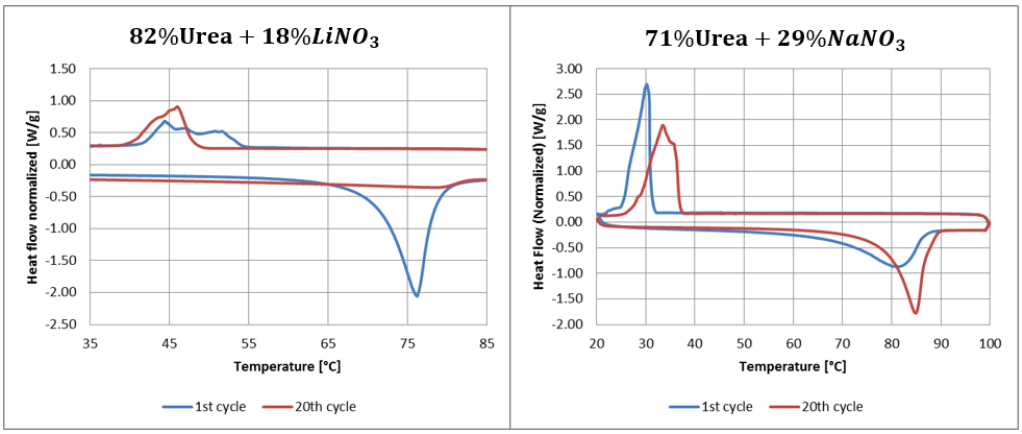

Figure 4.26: DSC thermal cycling measurements for Urea $-LiNO_3$ (82/18) and Urea - $NaNO_3$ (71/29) eutectic mixtures in hermetic enclosures.

A summary of the measurements from the DSC analysis made of eutectic PCMs with a melting point below 100°C is presented in table 4.4. It is important to notice that the salt hydrate mixtures have the highest volumetric thermal energy storage capacity below 100°C mainly due to their higher density. From the measurements made, the PCMs likely to have potential for process heat applications are Crodatherm 21, RT42 and 44HC and the two eutectic mixtures of magnesium nitrate hexahydrate with lithium nitrate and magnesium chloride hexahydrate due to the low hysteresis between their melting and solidification temperatures and their relatively low bulk prices.

Table 4.4: Key parameters from the DSC thermal cycling analysis for Eutectic PCMs melting below 100°C.

PCM mixtures melting below 100°C	T_{melt} °C	T_{cryst} °C	Subcooling °C	T_{min} °C	T_{max} °C	ΔH_m kJ/kg	ΔH_{tot} kJ/kg	ΔH_{tot} kWh/m^3	$\Delta H_{loss}^{20cycles}$ %	Price $£/m^3$	Price $£/kWh$
88% Hexadecane +12% Octadecane	13.5	13.5	0	5	20	123	204	44	0	2017	45.9
Crodatherm 21	19	18	1	10	25	161	199	48		2463	51.8
paraffin wax (RT42)	42	42	0	35	50	109	150	36		813	22.9
Paraffin wax (RT 44 HC)	47	47	0	35	50	232	255	59		813	13.7
$61\%Mg(NO_3)_2.(H_2O)_6 + 39\%NH_4NO_3$	48	37	11	20	60	131	217	101	0	265	2.63
36% Stearic acid + 64% Palmitic acid	54	53	1	25	65	192	285	77	0.6	589	7.66
$59\%Mg(NO_3)_2.(H_2O)_6 + 41\%MgCl_2.(H_2O)_6$	61	48	13	30	70	137	214	96	0.3	147	1.54
$86\%Mg(NO_3)_2.(H_2O)_6 + 14\%LiNO_3$	70	67	3	50	90	143	236	112	0.3	1151	10.2
82% Urea +18%$LiNO_3$	72	52	20	45	85	175	321	128	42.6	1388	10.8
71% Urea +29%$NaNO_3$	79	37	42	55	95	153	228	95	1.8	359	3.78

Eutectic mixtures melting above 100°C

Most eutectics mixtures melting above 100°C are mainly composed of inorganic materials, some of which are widely used in their liquid state as molten salts [37–39] to store sensible heat in concentrated solar power systems. Due to their known

thermal stability in the molten state, their DSC measurements demonstrated excellent thermal cycling properties. To represent and compare the different eutectic mixtures of inorganic salts, only one cycle is represented for each mixture in their respective graphs. Other eutectics melting above 100°C are the eutectic mixtures of urea with nitrates, chlorides and carbonates; and the eutectic mixture of sodium and potassium formate.

DSC thermal cycling measurements of urea eutectic mixtures with ammonium chloride and potassium carbonate are presented in figure 4.27. The mixture with ammonium chloride had a high latent heat of fusion (185kJ/kg), with 5°C of subcooling and lost 19% of its initial melting enthalpy in the 20 cycles made, indicating poor cycling properties; although cycling in hermetic pans could improve thermal stability. The eutectic mixture of Urea with potassium chloride lost 8% of its initial melting enthalpy in 20 cycles and subcooled 32°C.

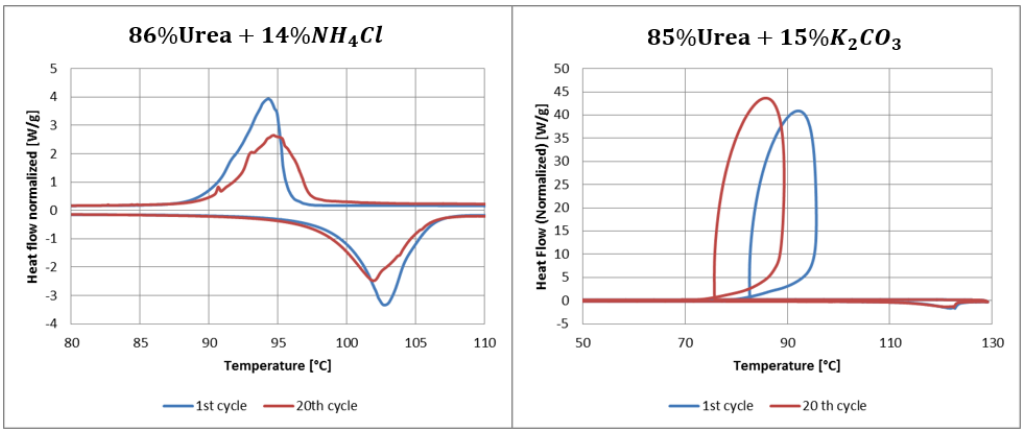

Figure 4.27: DSC thermal cycling measurements for Urea - NH_4Cl (86/14) and Urea - K_2CO_3 (85/15) eutectic mixtures in normal enclosures.

Figure 4.28 presents the DSC thermal cycling measurements of urea eutectic mixtures with potassium nitrate and potassium chloride. The mixture with potassium chloride measured high latent heat values (193kJ/kg) and exhibited a reduction in subcooling from 26 to 22°C in 20 cycles, however losing nearly 6% of its initial melting enthalpy. The mixture with potassium nitrate had no considerable loss in its melting enthalpy in 20 cycles and demonstrated subcooling of around 37°C.

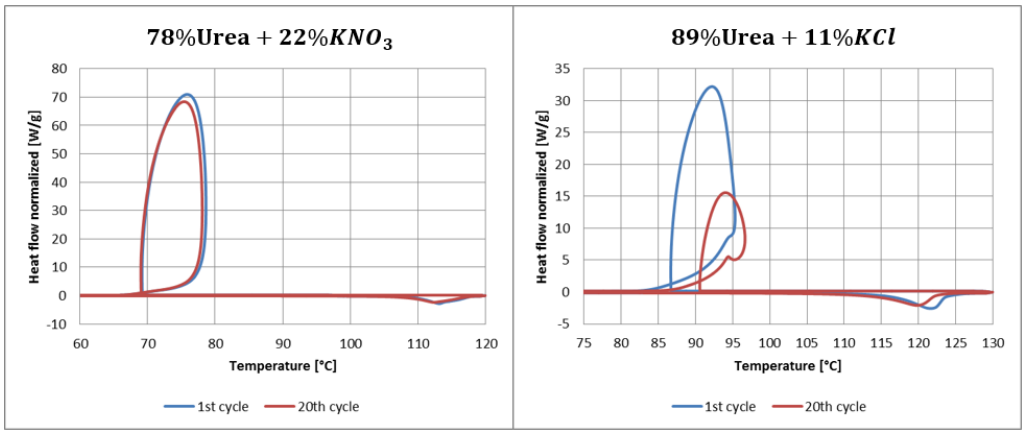

Figure 4.28: DSC thermal cycling measurements for Urea - KNO_3 (78/22) and Urea - KCl (89/11) in non-hermetic pans.

Figure 4.29 presents an overlay of the DSC measurements for two nitrate eutectic mixtures [103, 148] melting below 150°C. The binary eutectic mixture of lithium and potassium nitrate (34/66) had a subcooling of approximately 19°C and a melting point around 125°C with a volumetric thermal energy storage capacity from 105 to 145°C of approximately $108 kWh/m^3$. The measured latent heat capacity was 24kJ/kg less than that reported by Roget [80]. The ternary eutectic mixture of lithium, sodium and potassium nitrates (30/18/52) subcooled by 15°C, had a melting point of approximately 112°C and a volumetric storage capacity of $101 kWh/m^3$ between 92 and 132°C. Its measured latent heat capacity was 32kJ/kg lower than that obtained by Roget [103].

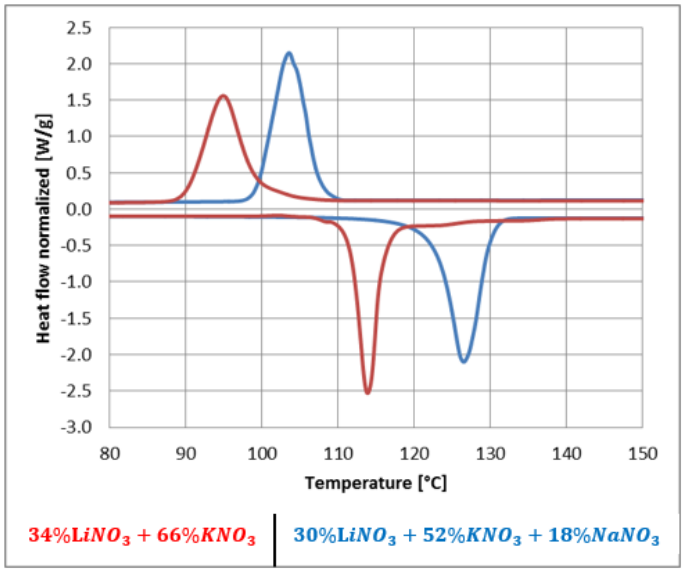

Figure 4.29: DSC measurements for $LiNO_3$ - KNO_3 (33/66) eutectic and $LiNO_3$ - $NaNO_3$ - KNO_3 (30/18/52) ternary eutectic mixtures in normal enclosures.

The DSC measurements for Hitec salt [21], a mixture melting below 150°C, are presented in figure 4.30. The mixture has a melting point around 142°C with negligible subcooling; its measured latent heat of 64kJ/kg is 46kJ/kg less than the value reported by Wang [21]. The mixture had much lower melting enthalpy than

other eutectic mixtures of lithium tested, with a volumetric thermal storage capacity of $78kWh/m^3$ between 122 and 162°C; however, it was less hydrophilic and had lower bulk prices than the other lithium mixtures. The binary eutectic mixture of sodium nitrite with potassium nitrate (44/56) had a similar melting point to Hitec salt with 3°C of subcooling and was 8kJ/kg less energy dense.

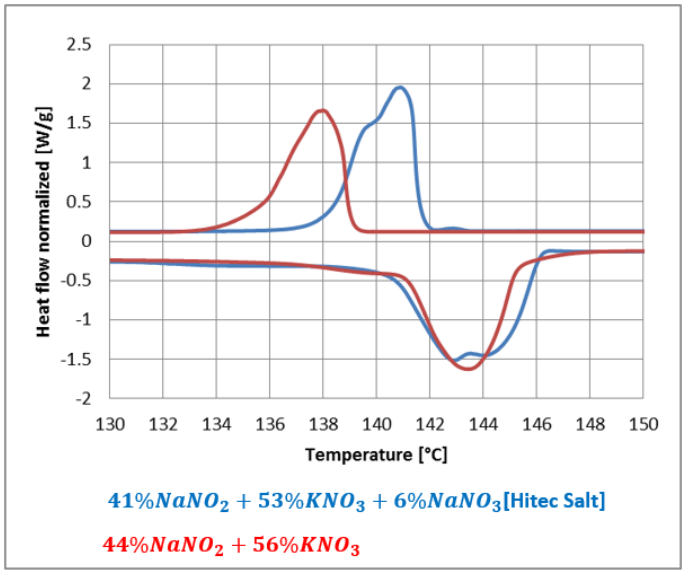

Figure 4.30: DSC measurements for the Hitec salt [21] and $NaNO_2$ - KNO_3 (44/56) eutectic mixtures in normal enclosures.

Figure 4.31 presents the DSC measurements for a eutectic mixture of sodium and potassium formate (55/45) which had the highest melting point of the organic eutectic mixtures tested. The mixture had a melting point of 164°C, subcooled 44°C and lost 1% of its initial melting enthalpy in 20 cycles with a normal enclosure, indicating some thermally stability.

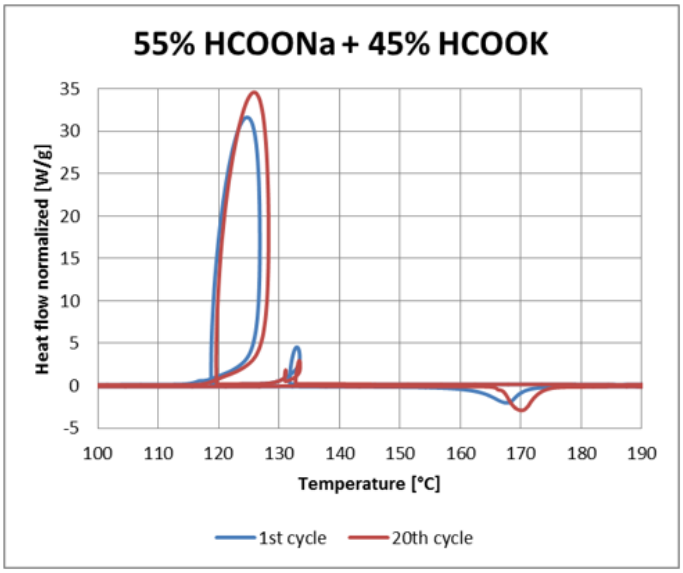

Figure 4.31: DSC thermal cycling measurements for a eutectic mixture of sodium formate - potassium formate (55/45) in the normal enclosure.

From figure 4.32 the lithium nitrate/ potassium chloride eutectic mixture (52/48) had a melting point of 165°C with 9°C of subcooling. The mixture could store up to $144kWh/m^3$ of heat between 140 and 180°C. The lithium nitrate/sodium nitrate eutectic mixture (53/47) tested had a melting point of 195°C with 3°C of subcooling. This material could store up to $208kWh/m^3$ of heat between 175 and 215°C. The main disadvantage of these materials is their high bulk material prices.

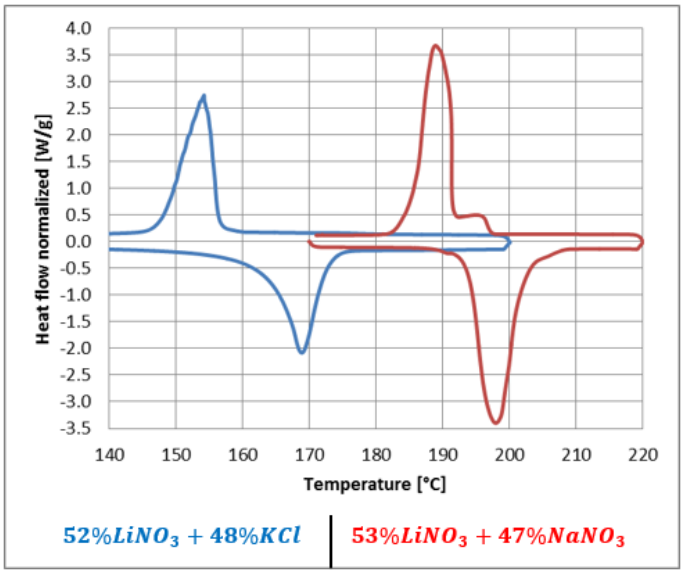

Figure 4.32: DSC measurements for $LiNO_3$ - KCl (52/48) eutectic and $LiNO_3$ - $NaNO_3$ (53/47) eutectic in normal enclosures.

Figure 4.33 presents the DSC measurements for three eutectic mixtures melting above 200°C. The image on the left allows the comparison of solar salt [93], a mixture of sodium and potassium nitrate (41/59) with the eutectic mixture of lithium nitrate and sodium chloride (87/13); and the image on the right compares solar salt with the eutectic mixture of sodium nitrate and sodium nitrite (59/41). It can be seen from figure 4.33 that solar salt had a melting point of approximately 223°C and no subcooling; its measured latent heat (73kJ/kg) was 22kJ/kg less than that reported by Kenisarin [108]. The eutectic mixture of lithium nitrate with sodium chloride, melting at 227°C had 7°C of subcooling and a measured latent heat of 422kJ/kg, 63kJ/kg more than that reported by Gasanaliev [106]. The eutectic mixture of sodium nitrite with sodium nitrate, detailed in Gamataeva [104], melted at 226°C, 4°C above solar salt with a latent heat 50kJ/kg higher than solar salt.

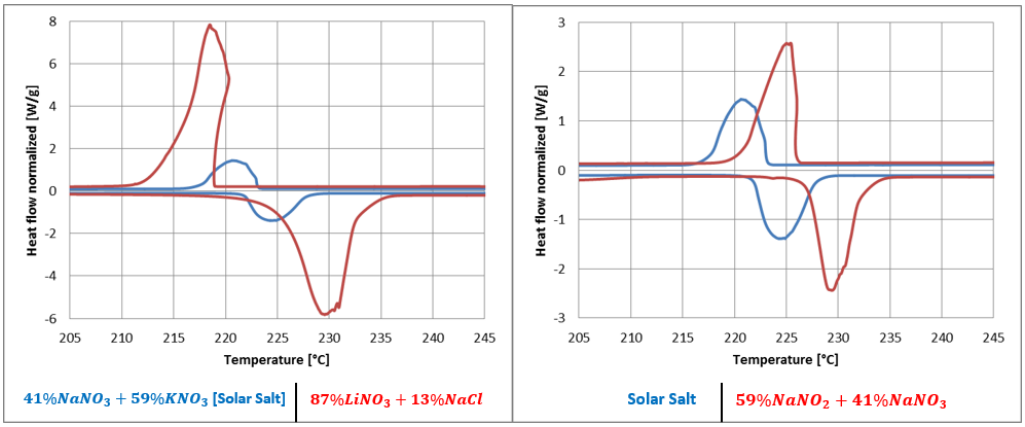

Figure 4.33: Overlays comparing the DSC measurements for solar salt $NaNO_3$ - KNO_3 (41/59) with those of $LiNO_3$ - $NaCl$ (87/13) and $NaNO_2$ - $NaNO_3$ (59/41) eutectic mixtures in normal enclosures.

A summary of the thermal properties obtained from the DSC analysis of eutectic mixtures melting above 100°C is presented in table 4.5. All the inorganic eutectic mixtures analysed have their melting and solidification point within a narrow temperature range (less than 30°C). Their relatively high bulk material costs are their main disadvantage. The urea eutectic mixtures, with high enthalpy values and low bulk material costs, may be cost effective options; most eutectics however still require research into potential nucleating agents to reduce their high levels of subcooling. The eutectic mixture of urea with ammonium chloride (86/14) appears to be the only suitable candidate for process heating applications, although it will require encapsulation. The eutectic mixtures of sodium and potassium formate had high measured values of enthalpy, but their excessive subcooling still needs to be addressed.

Table 4.5: Key parameters from the DSC measurements for eutectic PCMs melting above 100°C.

PCM mixtures melting above 100°C	T_{melt} °C	T_{cryst}	Subcooling	T_{min}	T_{max}	ΔH_m kJ/kg	ΔH_{tot}	kWh/m^3	Price $£/m^3$	$£/kWh$
86% Urea + 14%NH_4Cl	103	94	9	70	110	185	268	100	285	2.84
85%$Urea$ + 15%K_2CO_3	113	81	32	90	130	124	226	89	438	4.92
78%$Urea$ + 22%KNO_3	107	69	38	80	120	171	239	94	416	4.42
89%$Urea$ + 11%KCl	117	87	30	90	130	193	267	102	321	3.15
30%$LiNO_3$ + 52%KNO_3 + 18%$NaNO_3$	112	97	15	92	132	123	176	101	3229	31.9
34%$LiNO_3$ + 66%KNO_3	125	106	19	105	145	138	193	108	3535	32.7
41%$NaNO_2$ + 53%KNO_3 + 6%$NaNO_3$ (Hitec salt)	142	142	0	122	162	64	142	79	811	10.3
44%$NaNO_2$ + 56%KNO_3	142	139	3	122	162	77	137	76	822	10.8
55%$HCOONa$ + 45%$HCOOK$	164	120	44	144	184	189	249	132	687	5.2
52%$LiNO_3$ + 48%KCl	165	156	9	145	185	176	237	145	5562	38.5
53%$LiNO_3$ + 47%$NaNO_3$	195	192	3	175	215	261	323	208	5461	26.2
41%$NaNO_3$ + 59%KNO_3 (Solar salt)	223	223	0	203	243	73	125	70	798	11.4
59%$NaNO_2$ + 41%$NaNO_3$	227	226	1	207	247	117	186	114	627	5.49
87%$LiNO_3$ + 13%$NaCl$	227	219	8	207	247	422	514	336	8571	25.5

4.4 Material screening and characterization

Based on the measurements made, a selection of the most promising PCMs in the temperature range from 0 to 250°C is presented in table 4.6. The selection was firstly based on their stability, secondly their subcooling (less than 30°C) and thirdly their

bulk price. The PCMs marked in bold are those requiring encapsulation to ensure thermal stability.

Table 4.6: Key parameters from the DSC measurements for selection of most suitable candidate PCMs in the temperature range from 0 to 250°C.

Material ($\%_{wt}$	T_{min}	T_{max}	ΔH_{tot}		Cp_s	Cp_l	Price	
	°C		kJ/kg	kWh/m^3	kJ/kg.K		$£/m^3$	$£/kWh$
H_2O	-20	20	423	117	1.94	4.18	0	0
Crodatherm 21	10	25	170	41	1.83	2.15	2463	60.6
RT 44 HC	35	50	261	58	2.04	2.62	813	14
$59\%Mg(NO_3)_2.(H_2O)_6 + 41\%MgCl_2.(H_2O)_6$	30	70	190	85	1.65	2.28	147	1.73
Stearic acid	40	80	291	76	2.4	2.25	488	6.4
$86\%Urea + 14\%NH_4Cl$	70	110	263	99	1.85	2.1	285	2.89
$34\%LiNO_3 + 66\%KNO_3$	95	135	189	106	1.18	1.48	3535	33.3
$41\%NaNO_2 + 53\%KNO_3 + 6\%NaNO_3$ (Hitec salt)	120	160	126	70	2.22	1.52	811	11.6
$52\%LiNO_3 + 48\%KCl$	140	180	249	152	1.45	1.5	5562	36.7
$53\%LiNO_3 + 47\%NaNO_3$	175	215	311	201	1.33	1.69	5461	27.2
$59\%NaNO_2 + 41\%NaNO_3$	205	245	153	94	1.62	1.74	627	6.7

Extended calorimetric analysis to promising PCMs

Following the previous calorimetric analysis made, 11 PCMs were subjected to another DSC analysis at a lower ramp rate (1°C/min), to obtain a more precise thermal response [148] and their subsequent heat storage thermograms, presented in figure 4.34 and figure 4.35.

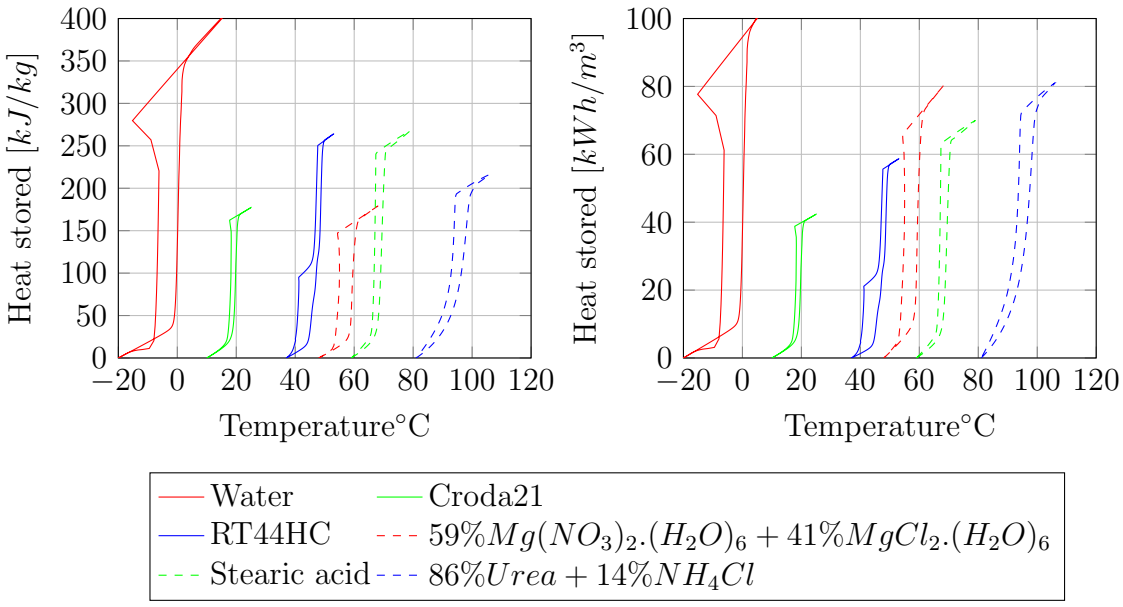

Figure 4.34: Measured thermograms of promising PCMs melting below 100°C.

It can be seen that most of the organic compounds and their mixtures presented higher enthalpy properties when compared per kg to inorganic PCMs and lower (or no) subcooling. Their lower bulk density provides them with lower volumetric enthalpy (kWh/m^3) and higher specific enthalpy (kJ/kg), when compared to inorganic PCMs.

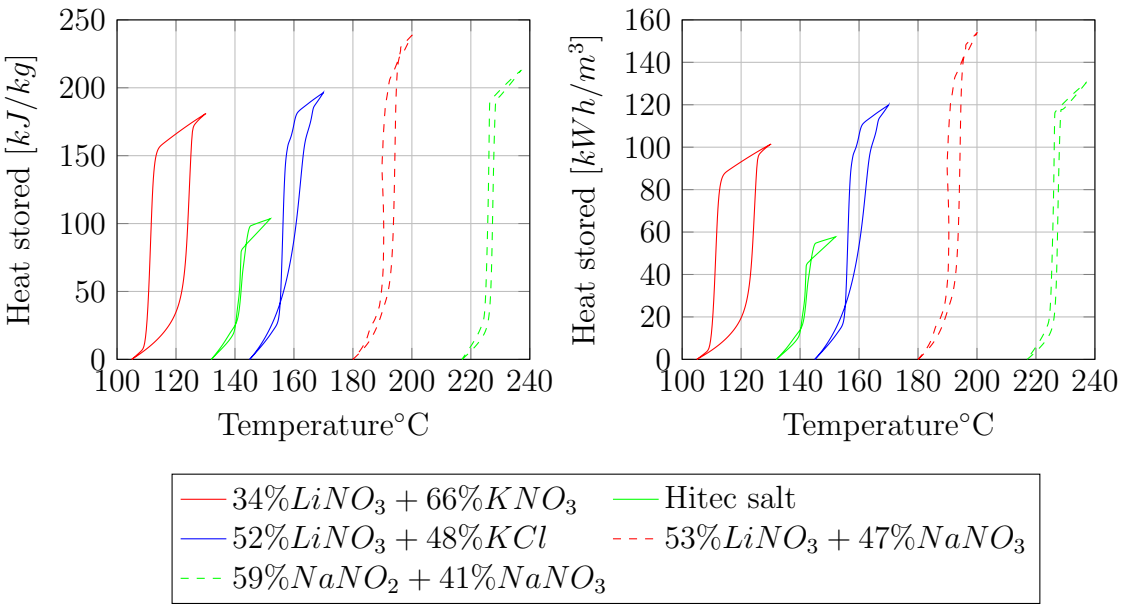

Figure 4.35: Measured thermograms of promising PCMs melting above 100°C.

4.5 Discussion and conclusions from the thermal analysis performed of phase change materials with melting points between 0 and 250°C

From the thermal analysis made of 50 potential PCMs with a solid to liquid phase change in the 0 to 250°C temperature range, 11 were identified to have promising properties based on their thermal stability, low subcooling tendency, operating temperatures and relatively low bulk price, making them suitable for thermal storage applications.

Despite that DSC analyses provide a rapid way to screen and characterize a large selection of PCMs, they cannot provide an accurate representation of the PCM solidification behavior if the compound demonstrates subcooling, since nucleation effects are volume dependent [149]. For such determinations, T-history tests or similar larger sample based methods should be the adopted analysis technique.

For space cooling applications, Crodatherm 21 appears to be an appropriate material, being able to store $41kWh/m^3$ in the temperature range from 10 to 25°C. Candidate materials for space heating applications identified are the paraffin wax RT44HC and the mixture of magnesium nitrate hexahydrate with magnesium chloride hexahydrate (61/39) which have little subcooling and relatively high latent heat of fusion of 190kJ/kg.

Stearic acid and a mixture of urea with ammonium chloride (86/14) can be used at temperatures up to 110°C making them candidates for higher temperature applications such as district heating networks. The urea mixture can store nearly $100kWh/m^3$ of heat between 70 and 110°C.

For thermal storage at temperatures above 100°C, suitable for process heat applications, only ionic liquids appear to be suitable, since all the organic materials tested demonstrated high levels of subcooling with the exception of HDPE and adipic acid.

A eutectic mixture of lithium nitrate with potassium nitrate (34/66) which can store up to $106kWh/m^3$ in the temperature range from 95 to 135°C, can be a promising storage material for solar cooling when using Li-Br absorption systems. The main disadvantage of this material is its relatively high bulk price.

Using the measured DSC diagrams, the potential of integrating latent heat storage systems into the space cooling, domestic heating and district heating sectors was numerically studied. That would enable a more accurate prediction of the thermal performance of each developed thermal store.

Chapter 5

The potential of phase change energy storage for office cooling load shifting in the UK

In light of the global warming threat, the demand for space cooling is rapidly growing worldwide [150]. Currently, it is estimated that 40 to 45% of the EU total energy demand [151] is used in buildings. Of this consumption in buildings, around 3% is used for cooling and humidification, as seen in figure 5.1a. According to the European Union approved directive 91 in 2002 [152] and ratified in 2010, all new buildings in the EU are expected to reduce or consume "nearly zero" energy after 2020 [150]. Although currently minimal, the energy used for cooling and humidification is expected to grow [150] and efforts should be made to reduce its associated emissions.

From the UK 2016 final energy use [3], electrical consumption in the public administration and commercial sectors accounted for 8mtoe, around 6% of the total energy used, according to the report made by the Department of Business, Energy and Industrial Strategy [22]. From [22], it is estimated that 3.3% of the energy used in buildings was consumed for cooling and humidification mostly in offices. For offices, cooling and humidification represented 8% of the total energy consumed in the sector, seen in figure 5.1b.

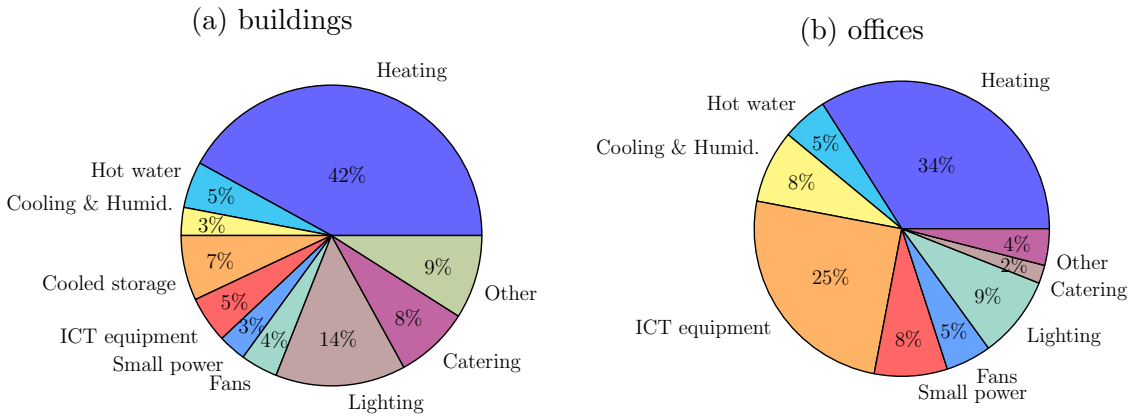

Figure 5.1: Energy consumption by end use in all buildings (A) and in offices (B), from [22].

A total of 58% of CO_2 emissions associated with cooling & humidification in buildings is in retail and office buildings with combined emissions of $1.3 MtCO_2/_{year}$, as seen in figure 5.2. The emission values were determined based on the marginal emissions factors of the UK grid in 2015, based on the study made by Hawkes [25].

Shifting the energy required for cooling and humidification in offices during the day to the night by storing that required daily cooling in a compact latent heat storage system with the benefit of using cold nigh time ambient air could potentially reduce those emissions.

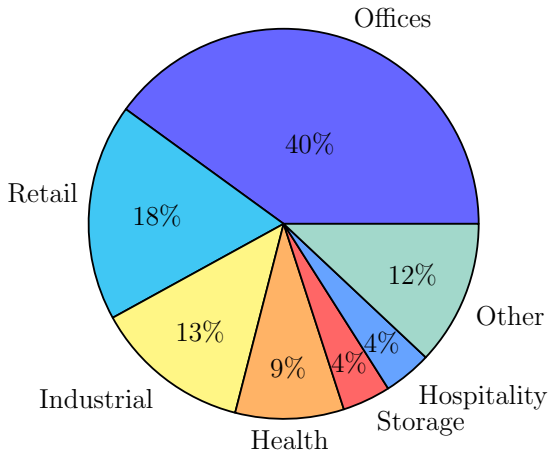

Figure 5.2: CO_2 emissions associated with electrical consumption for cooling and humidification, from [22].

This chapter will focus on 3 cooling approaches (charging a thermal store with cool night time air, charging a store using off peak night time electricity or using mechanical ventilation on demand), comparing them with a standard heating, ventilation and air conditioning (HVAC) system [23].

The CIBSE guide [153] categorizes office buildings into 4 types: naturally ventilated cellular, naturally ventilated open-plan offices, air-conditioned standard and prestige buildings. This study focuses on open plan office buildings, since they usually have standard HVAC systems installed in a centralized air distribution system. Additionally, for these medium or highly glazed buildings, improving building fabric to reduce winter heating demand [154] can significantly increase summer cooling loads.

5.1 Building thermal model

To assess the potential reduction in CO_2 emissions achievable with the integration of a compact latent heat storage unit into a building space cooling network, a typical open plan office was chosen, based on the study made by Korolija [23]. The office building is a three-storey full building with a 32 by 16 meter footprint, and a floor-to-ceiling height of 3.5 meters and is shown schematically in figure 5.3a. Each floor is divided in 2 zones: zone 1 is the open-office area and zone 2 comprises the common areas (kitchen, corridors, toilets, etc.). The proposed heating and cooling system is a centralized air distribution system, with a thermal store, heat pump and centrifugal blower installed on the building rooftop, as illustrated in figure 5.3b.

For the conventional approach, the thermal store and the extra centrifugal fan are removed, retaining the heat pump to supply the required heating and cooling needed.

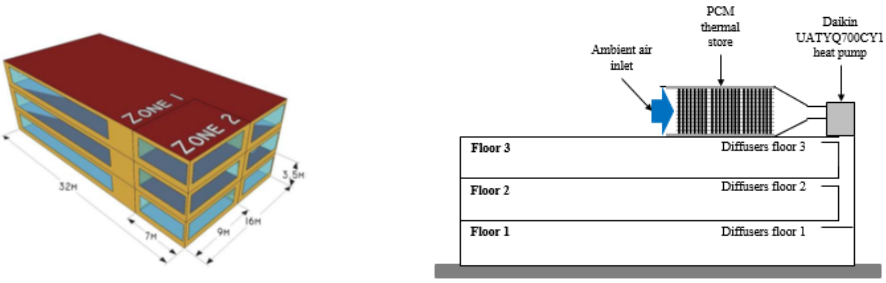

(a) 3-storey building (b) system integration

Figure 5.3: Schematic drawing of the studied 3-storey building, from [23] and representation of the thermal store integration in the rooftop.

Table 5.1 presents the standard values for compliance with the building regulation appraisal document L for 1990 (building fabric 1) and the new best practice values, in compliance with the building regulations appraisal document L2 for 2010 (building fabric 2) [155]. Using the new best practice values made the building more insulated and consequently more prone to overheating due to internal and solar gains [23].

Table 5.1: Building fabric U-values $[W/m^2.K]$, from [23].

Building components	Building fabric 1 $[W/m^2.K]$	Building fabric 2 $[W/m^2.K]$
Cavity wall	0.53	0.25
Flat roof	0.45	0.15
Ground floor	0.84	0.15
Glazing	3.21	1.98

The building indoor temperature was considered uniform with no stratification, the heat exchanging with the external environment was calculated using the "building fabric 2" U-values expressed in table 5.1. The building yearly energy consumption results were verified with the model of the same building studied by Korolija [154] using the EnergyPlus software [24]. The heat balance calculation for each floor was based on equation 5.1. A fresh air ventilation rate of 10 l/s per person was required to meet the building ventilation standards. The auxiliary heat input ($\dot{Q}_{aux}$) will be positive or negative according to the required auxiliary energy to achieve the set point temperature.

$$\begin{aligned}\dot{Q}_{indoor} = \rho_{air} \cdot Cp_{air} \cdot (F_{air} + V_{person} \cdot N_{person}) \\ \cdot (T_{amb} - T_{indoor}) + \dot{Q}_{gain} + \dot{Q}_{LHS} + \dot{Q}_{aux} + \dot{Q}_{fabrics}\end{aligned} \tag{5.1}$$

Climate data for Gatwick; available from the open access weather data files in the EnergyPlus software [24] was used in the simulation. Adopting the recommended values from the CIBSE guides [153], the building indoor temperature was either

heated to 20°C or cooled to 24°C during the occupied hours (from 07.00 to 19.00) [23], with the indoor temperature maintained between 12 and 28°C during unoccupied hours. The casual gains from office appliances and lighting were assumed to be $27W/m^2$, the casual gains were 108W/person with an occupant for each $9m^2$ of floor area was considered, in line with the CIBSE guide recommendations [153].

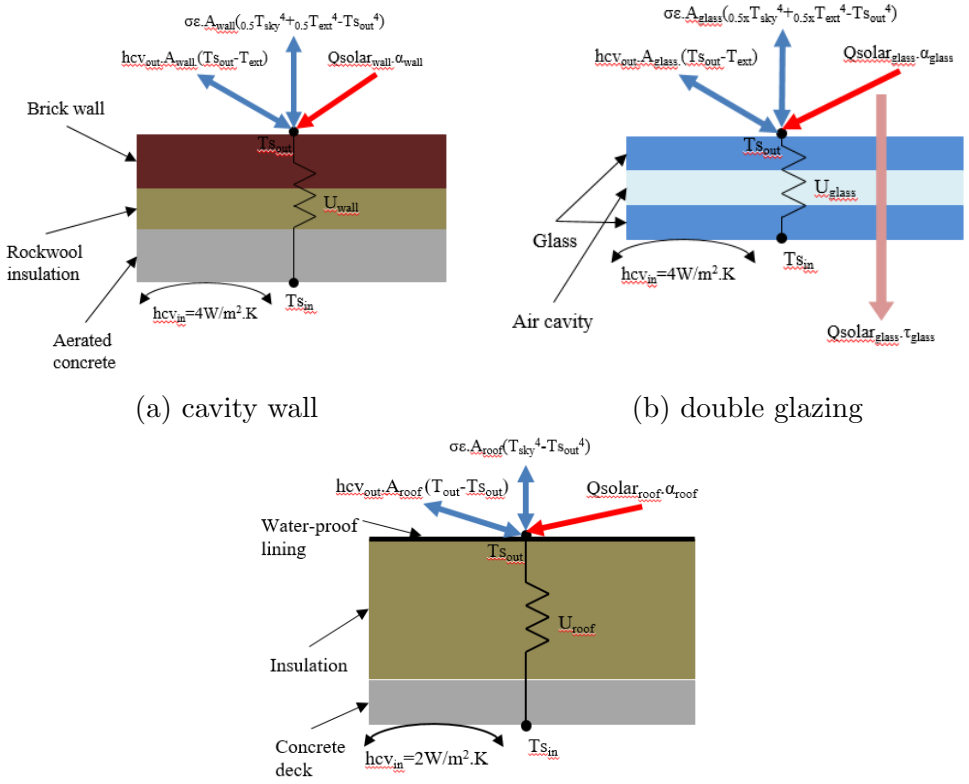

(a) cavity wall

(b) double glazing

(c) flat roof

Figure 5.4: Simplified energy balance of each building component used.

A simplified energy balance was made for each building component, as shown in figure 5.4a to 5.4c. The total heat transfer through the building fabric to the indoor air ($\dot{Q}_{fabrics}$) is expressed in equation 5.2.

$$\begin{aligned}\dot{Q}_{fabrics} = [3 \cdot Area_1 \cdot (T_{wall,N}(k) + T_{wall,S}(k) + T_{glass,N}(k) + T_{glass,S}(k)) + 3 \cdot Area_2 \\ \cdot (T_{wall,E}(k) + T_{wall,W}(k) + T_{glass,E}(k) + T_{glass,W}(k)) - 12 \cdot T_{indoor}(k) \\ \cdot (Area_1 + Area_2)] \cdot U_{int,vert} \\ + [Area_{space} \cdot (T_{roof}(k) + T_{floor}(k) + 4 \cdot T_{deck}(k) + 3 \cdot k_{solid} \cdot T_{solid}(k)) \\ - T_{indoor}(k) \cdot A_{space} \cdot (6 + 3 \cdot k_{solid})] \cdot U_{int,hor}\end{aligned} \tag{5.2}$$

All the exterior building surface temperatures were calculated assuming an instantaneous heat balance between the absorbed solar radiation and ambient air at each surface, using the simple combined external convective heat transfer correlation from EnergyPlus engineering reference handbook [156], expressed in equation 5.3. Coefficients D, E and F varied according to the external surface material and surface roughness (detailed in [156]) and V_z is the local wind speed.

$$h_{cv} = D + E + F \cdot V_z^2 \tag{5.3}$$

Table 5.2 summarizes the assumptions made and the building characteristics assumed. To calculate the respective thermal mass of each building component exchanging heat with the indoor zone temperature, as expressed in equation 5.2. The materials used were aerated concrete for the inner wall leaf, concrete slabs for the floor and roof and a single layer of glass for the double glazing. The internal convective heat transfer was assumed to be $4W/m^2.K$ for all vertical and $2W/m^2.K$ for all horizontal surfaces, based on the EnergyPlus engineering reference [156]. Radiative heat transfer from the indoor building components to the indoor ambient temperature were considered negligible since the temperature difference is not significant.

To account for the extra thermal mass added by office appliances (tables, desks, chairs, etc.) a solid mass was included for each floor, representing 2% of the air volume of each floor. The total building thermal mass (the indoor air volume combined with all of the building fabric in direct contact with the indoor volume) was calculated to be 517 514kJ/K.

Table 5.2: Modelled building thermal characteristics.

Cavity wall height [m]	1.75	Floor area [m^2]	512
Glass height [m]	1.75	Floor air volume [m^3]	1750
Brick thickness [mm]	103	Glazing percentage [%]	50
Rockwool insulation thickness [mm]	210	C wall N/S [kJ/K]/floor	2 792
Aerated concrete thickness [mm]	100	C wall E/W [kJ/K]/floor	1 396
Glass thickness [mm]	6	C glass N/S [kJ/K]/floor	2 116
Glass cavity thickness [mm]	6	C glass E/W [kJ/K]/floor	1 058
EPS insulation thickness [mm]	250	C roof [kJ/K]	96 829
Concrete slab thickness [mm]	80	C floor [kJ/K]	96 829
Brick thermal conductivity [W/m.K]	0.77	C solid [kJ/K]/floor	28 672
Aerated concrete thermal conductivity [W/m.K]	0.11	N occupants per floor	57
Rockwool thermal conductivity [W/m.K]	0.04	Air infiltration rate [m^3/s]	0.149
EPS thermal conductivity [W/m.K]	0.04	Ventilation rate [m^3/s]	0.57
Concrete slab thermal conductivity [W/m.K]	0.8	Q appliances [W]	13 824
U intvert [$W/m^2.K$]	2	Q occupants [W]	6 156
U inthor [$W/m^2.K$]	4		
U wallint [$W/m^2.K$]	0.152	α wall [%]	80
U glassint [$W/m^2.K$]	2.37	α glass [%] [157]	7
U roofint [$W/m^2.K$]	0.152	α roof [%]	90
U floorint [$W/m^2.K$]	0.152	τ glass [%]	66

Passive solar gains were determined in each floor calculating the transmitted radiation through each glass area and then absorbed by the respective floor. Each wall had a specific angle of incidence with the sun calculated according to the set of equations 5.4, from [158]. For obtaining each wall azimuth, it was considered that each wall was facing a cardinal direction; the longer walls to north and south and shorter walls east and west. Each surface azimuth (az_{surf}) was the relative azimuth angle towards south.

$$\begin{cases} HA = \left(GHA + \frac{EOT}{60} + \frac{Long}{15} - 12\right) \cdot 15 \\ EOT = 229,18 \cdot (7,5E^{-5} + 1,87E^{-3}cos(\gamma) - 3,2E^{-2}sin(\gamma) - 1,45E^{-2}cos(2\gamma) - 4,08E^{-2}sin(2\gamma)) \\ \gamma = \frac{2\pi}{365}(day - 1) \\ \delta 23,45 \cdot sin\left(\frac{360}{365}(day - 81)\right) \\ h_{sol} = asin\left(sin(\delta) \cdot sin(Lat) + cos(\delta) \cdot cos(Lat) \cdot cos(HA)\right) az = acos\left(\frac{sin(h_{sol}) \cdot sin(Lat) - sin(\delta)}{cos(h_{sol}) \cdot cos(Lat)}\right) \\ inc = acos\left[sin(h_{sol}) \cdot cos(\beta_{surf}) + cos(h_{sol}) \cdot sin(\beta_{surf}) \cdot cos(az_{surf} - az)\right] \\ \dot{Q}_{solar} = \sum_{k=1}^{4} A_{surf}\left[\dot{I}_{dir,n} \cdot \frac{cos(inc_k)}{sih(h)} + \dot{I}_{diff,hor} \cdot \frac{1-cos(\beta_{surf})}{2} + I_{glob,hor} \cdot \rho_g \cdot \frac{1+cos(\beta_{surf})}{2}\right] \end{cases} \tag{5.4}$$

Considering the building properties presented in table 5.2, the calculated yearly cooling loads with the conventional HVAC system were considerably higher than its heating loads, as presented in table 5.3, in accordance with the values obtained with the EnergyPlus software in the study of Korolija et al. [23]. It can be seen that the highest cooling loads were obtained during the Summer and Autumn months and the bulk of the yearly heating demands occurred during the winter months.

Table 5.3 presents the average daily heating and cooling demand for each month. The cooling demand, peaks in August and is almost non-existent during winter months. In order to meet the base load during the cooling season (when the daily cooling load surpasses its heating demand), from April to October, an average of 349kWh/day of cooling is required.

Table 5.3: Calculated open office daily heating and cooling loads for each month.

Month	Jan	Feb	Mar	Apr	May	Jun	Jul	Aug	Sep	Oct	Nov	Dec
Cooling load [kWh/day]	6	0	11	91	309	403	577	594	340	110	13	0
Heating load [kWh/day]	223	249	140	62	10	2	0	1	4	35	106	236

Figure 5.5 presents the average daily profiles of external ambient temperature and building cooling demand in each season. The average daily cooling required to maintain CIBSE comfort values [153], vary considerably between spring and autumn to summer months. The rooftop heat pump chosen provided 72.6kW of cooling and 69.8kW of heating [159]. To charge a thermal store using economy 7 tariff times, the total charging time available would be 7 hours, consequently limiting the maximum storage capacity to 508kWh with the selected heat pump.

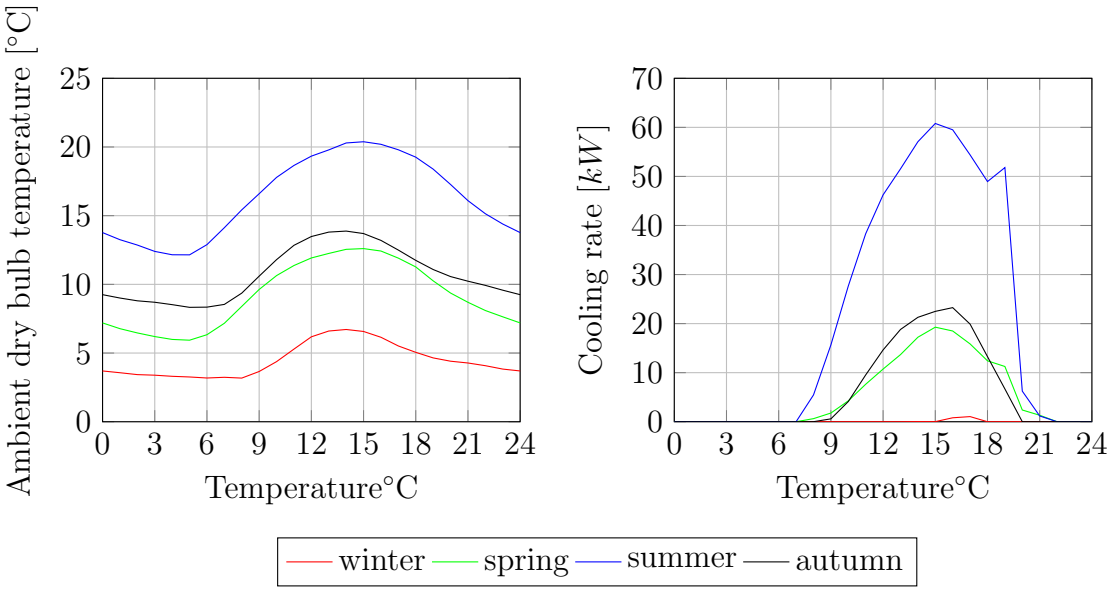

Figure 5.5: Average daily profiles of dry bulb ambient temperature for London-Gatwick climate data [24] and building cooling demand for each season.

Two thermal energy storage system capacities were designed and simulated with the aim of reducing the building cooling loads: 1) using cold night time air temperatures (with a thermal storage capacity of 349kWh between 8 and 24°C using PCM RT15), and 2) using cold night time air temperatures with off-peak electrical cooling (with a thermal storage capacity of 508kWh between 1 and 24°C using PCM RT8HC) operating during economy 7 electricity tariff times [160]. Both thermal stores were designed to be fully charged in 7h and discharged in 10h, leading to a charging/discharging cooling rates of 50/35kW for the store using RT15 and a 73/51kW for the store using RT8HC.

5.2 Numerical models developed

Two finite volume models were developed in Matlab to simulate the impact of the thermal stores in an office cooling system. They assumed pure diffusion, with no volume changes during the melting process and isotropic heat propagation within the PCM. The 2 geometries modelled were parallel slab and staggered cylinder. These algorithms were then added to the lumped capacitance thermal model developed based on the EnergyPlus engineering reference [156].

5.2.1 Parallel slab thermal model

The parallel slab model simulated an air flow through a rectangular duct containing PCM on its outer walls. Its side walls contained half of a rectangular PCM slab and it was insulated on the top and bottom walls. Figure 5.6a and 5.6b presents a simplified diagram of the heat transfer mechanism and top view of the air flow distribution.

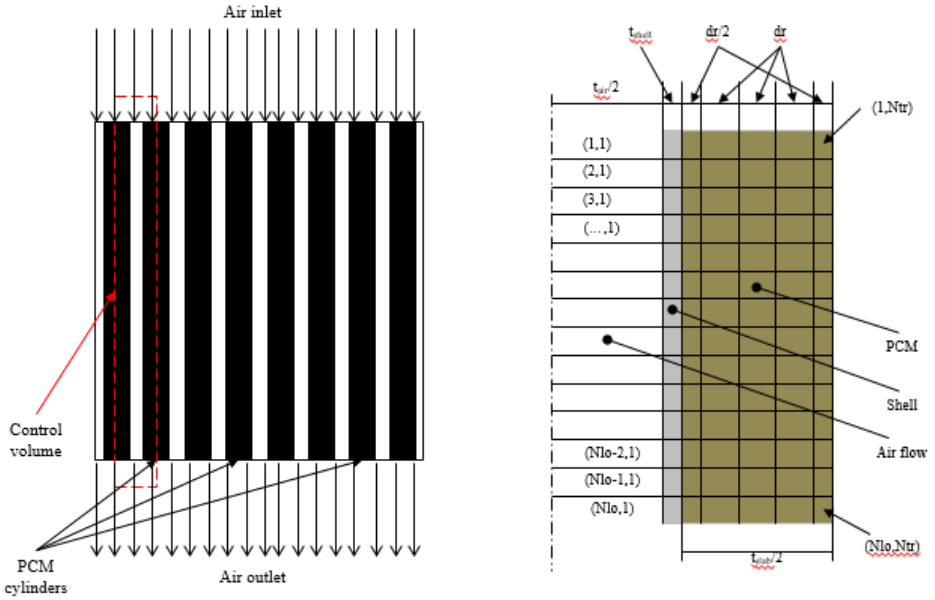

(a) air flow distribution (b) model discretization

Figure 5.6: Schematic diagram of the thermal store top view and air flow distribution and the spatial discretization employed for simulation.

The air flow Reynolds number was calculated using the hydraulic diameter of the air gap between slabs ($D_h = (\frac{4 \cdot A_{section}}{P_{section}})$. The laminar Nusselt number was calculated using equation 5.5, retrieved from VDI heat atlas [161]. For turbulent flow regimes, the Gnielinski's expression was used [161] for turbulent pipe flow, expressed in equation 5.6, and assuming the "pipe" diameter to be the hydraulic diameter expressed above.

$$Nu_{lam} = \sqrt[3]{4,861^3 + \left(1,841 \cdot \sqrt[3]{Re \cdot Pr \cdot \frac{D_h}{L_{slab}}}\right)^3 + \left(\frac{2}{1 + 22 \cdot Tr}^{\frac{1}{6}} \cdot \sqrt{Re \cdot Pr \cdot \frac{D_h}{L_{slab}}}\right)^3} \quad (5.5)$$

$$Nu_{turb} = \frac{0,125 \cdot \zeta \cdot Re \cdot Pr}{1 + 12,7 \cdot \sqrt{0,125 \cdot \zeta \cdot \left(Pr^{\frac{2}{3}} - 1\right)}} \left(1 + \left(\frac{D_h}{L_{slab}}\right)^{\frac{2}{3}}\right) \quad (5.6)$$

5.2.2 Staggered cylinder model

The model for the staggered cylinder thermal stores developed simulated an air flow passing through a staggered arrangement of PCM cylinders, with unidirectional radial propagation among the PCM, as shown in figure 5.7a to 5.7c.

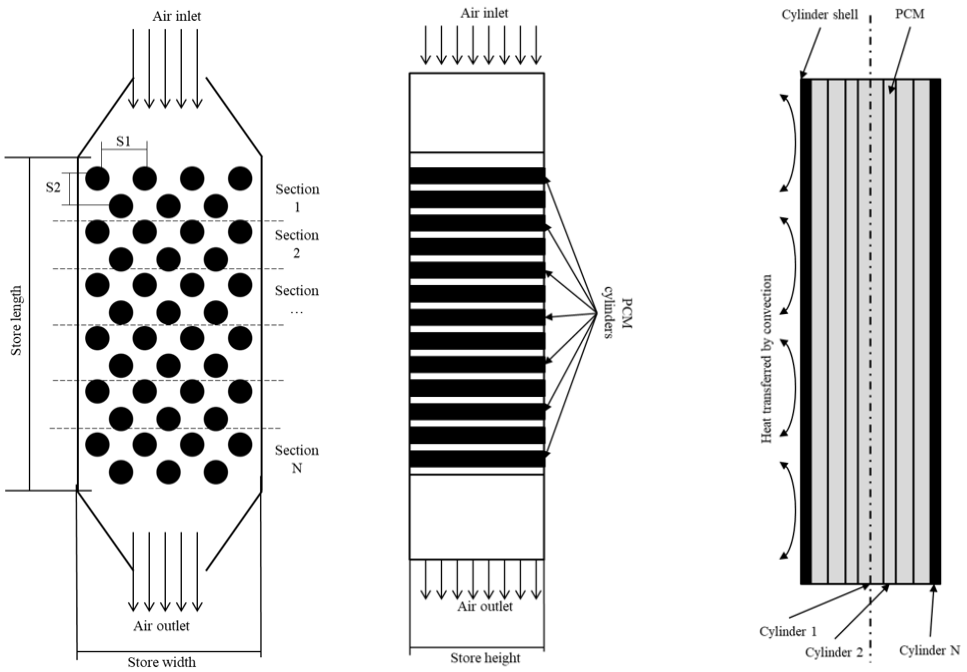

(a) top view (b) side view (c) PCM cylinder

Figure 5.7: Modelled staggered cylinder thermal store top view, side view and radial heat propagation within each PCM cylinder.

The air flow Reynolds number was calculated considering the streamlined flow passing a single tube (half of the perimeter of one cylinder), accounting for the store void fraction as presented in equation 5.7. Coefficients a and b are transversal and longitudinal tube spacing ratios based on the cylinder diameter, expressed in equation 5.8. The Nusselt number was calculated based on the correlation presented in [161], all expressed in equations 5.9 to 5.11.

$$Re = \frac{V \cdot d_{cylinder} \cdot \pi}{2 \cdot \Psi \cdot \nu} \tag{5.7}$$

$$\begin{cases} a = \frac{S_1}{d_{cylinder}}; & b = \frac{S_2}{d_{cylinder}} \\ \Psi = 1 - \frac{\pi}{4 \cdot a}; & if b \leq 1; \\ \Psi = 1 - \frac{\pi}{4 \cdot a \cdot b}; & if b < 1; \end{cases} \tag{5.8}$$

$$Nu_{lam} = 0,664 \cdot \sqrt{Re} \cdot \sqrt[3]{Pr} \tag{5.9}$$

$$Nu_{turb} = \frac{0,037 \cdot Re^{0,8} \cdot Pr}{1 + 2,443 \cdot Re^{-1} \left(Pr^{\frac{2}{3}} - 1\right)} \tag{5.10}$$

$$Nu_{bundle} = \left(1 + \frac{2}{3b}\right) \cdot \left(0,3 + \sqrt{Nu_{lam}^2 + Nu_{turb}^2}\right) \tag{5.11}$$

5.3 Experiments undertaken to validate the numerical models

To determine the accuracy of the numerical models developed, a ventilated open-loop experimental rig was assembled to test the 2 thermal stores developed. The

temperature of the rig was controlled via an adapted shell and tube heat exchanger by circulating a silicon oil on the shell side, controlled by a Huber Tango temperature control unit. A centrifugal fan mounted on the air inlet blower air through the shell and tube heat exchanger, delivering the required air flow to the thermal store, as shown in figure 5.8.

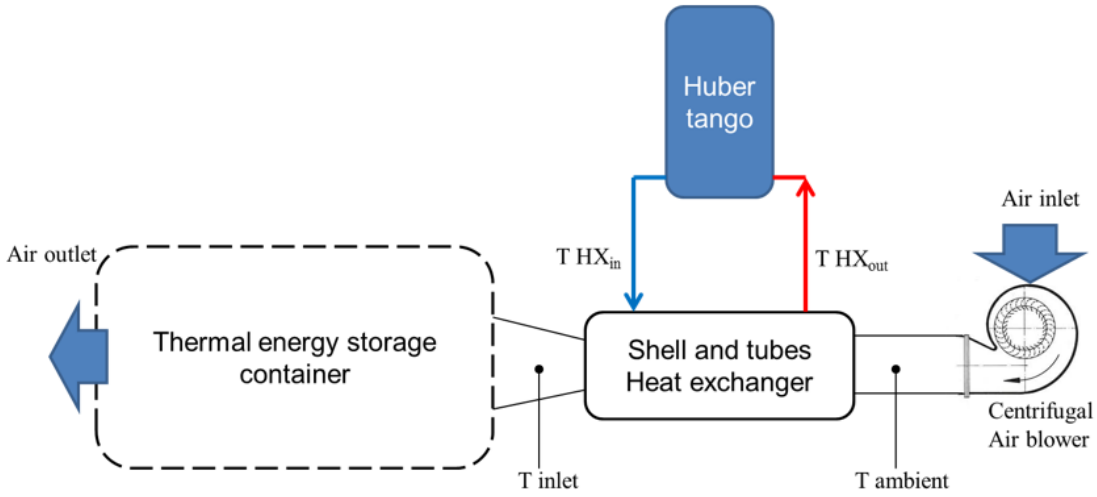

Figure 5.8: Simplified representation of the rig assembled to test ventilated thermal st res.

5.3.1 Shape stabilized PCM produced

A shape stabilized PCM composite was prepared in situ by blending Croda 21, an organic esters mixture developed by Crodatherm [19] with a 18°C melting point, with an enhanced polymeric adsorbent. The polymeric adsorbent consisted of a mixture of graphite powder, a hydrogenated styrene block copolymer and a diatomaceous earth developed by Phase Energy Ltd [162]. The enhanced composite had a higher thermal conductivity and an extra 10J/g enthalpy compared to the base mixture of Croda21 with the block copolymer only. This resulted from the higher density provided by the diatomaceous earth as seen in table 5.4.

Table 5.4: Material properties of the selected PCMs used in the experiment.

Material ($\%_{wt}$)	$T_{min} - T_{max}$	ΔH_{stored}	λ_{solid}	λ_{liquid}	Price	
	°C	kWh/m^3	W/m.K		$£/kg$	$£/kWh$
Croda 21	12-24	53	0.18	0.15	4	69.7
Croda 21/adsorbent (80/20)		40	0.2	0.18	4.02	91.9
Croda 21/composite adsorbent (77/23)		43	0.47	0.35	3.5	81.1

5.3.2 Uncertainty measurement

The experimental rigs developed measures the temperature difference between the inlet and outlet air passing through the heat storage system and flowrate. According to [163], the combination of errors from a sum or multiplication of two measured variables can be calculated according to equation 5.12.

$$\begin{cases} a = b - c; & (\Delta a)^2 = (\Delta b)^2 + (\Delta c)^2 \\ a = bc; & \left(\frac{\Delta a}{a}\right)^2 = \left(\frac{\Delta b}{b}\right)^2 + \left(\frac{\Delta c}{c}\right)^2 \end{cases} \tag{5.12}$$

The relative error on the measured heat transfer rate passing through the latent heat storage system is then calculated according to equation 5.13. It can be seen that the measured uncertainty will increase for low temperature differences and low measured air flow velocities.

$$\begin{cases} \Delta T = T_{in} - T_{out}; & \Delta T_{err} = \sqrt{(Tin_{err})^2 + (Tout_{err})^2} \\ Q = \rho \frac{V_{flow}}{A} Cp \Delta T; & \frac{Q_{err}}{Q} = \sqrt{\left(\frac{\Delta T_{err}}{\Delta T}\right)^2 + \left(\frac{Vflow_{err}}{V_{flow}}\right)^2} \end{cases} \tag{5.13}$$

The temperature measurement is made with T-type thermocouples (with an absolute measured error of +-0.5°C) and the the air flow is calculated multiplying the section area of the outlet duct by the measured air velocity (using a hot wire anemometer with an absolute measurement error of +-0.1m/s). To minimize the measurement error, the thermocouples were calibrated using an oil bath controlled with a Pt100 reducing the error to +-0.01°C (the resolution of the DAQ reader) and the hot wire anemometer through the calibration sheet provided by the manufacturer.

5.3.3 Numerical models developed

Two PCM stores were developed to verify the accuracy of the algorithms developed. For the parallel slab model, a thermal store was built using 1mm thick HDPE sheet and wooden bars. Figure 5.9a and 5.9b represents schematically the parallel slab store constructed. It consisted of 5 PCM slabs 9mm thick of 1000x1000 mm dimensions and 12mm air gaps between them, it was able to contain 40L of PCM. Wooden spacers were inserted between the PCM slabs to ensure a 12mm air gap was maintained and enabled the 1000mm long air flow pass to be extended to 5 times this length, as seen in figure 5.9a and 5.9b.

(a) thermal store section view (b) air gap

Figure 5.9: Cross-section drawing of the parallel slab store developed and detailed view of the air gap/slab construction.

Figure 5.10a and 5.10b shows photographs of the empty store and the store filled with 3 PCM slabs. In the filling process, the shape stabilized PCM was produced

separately and allowed to naturally cool down to ambient temperature on a casting plate. When the slab temperature was near ambient, it was removed from the casting plate, weighed, and placed into the respective slot of the store. When a full layer was complete, another HDPE sheet was inserted; this was followed by filling the next layer.

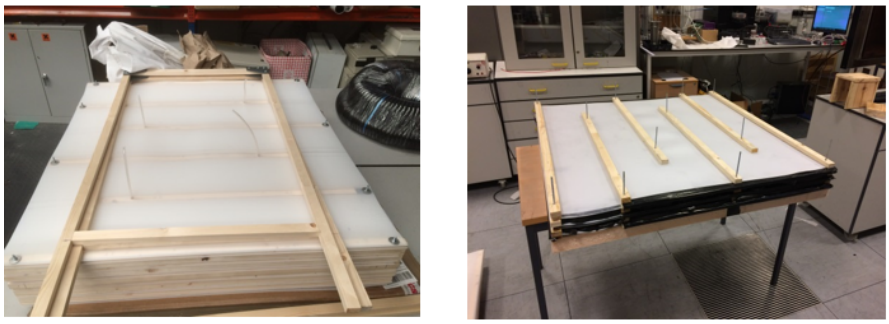

(a) empty store (b) filled with 3 PCM slabs

Figure 5.10: General view of the empty parallel slab store and with 3 PCM slabs filled.

When all 5 PCM layers were complete, the store was sealed with duct tape and calibrated T-type thermocouples were placed in the locations presented in figure 5.11a and 5.11b. Using a Huber tango to control the shell and tubes heat exchanger, the store inlet air temperature was regulated from 5 to 30°C to fully charge and discharge the PCM.

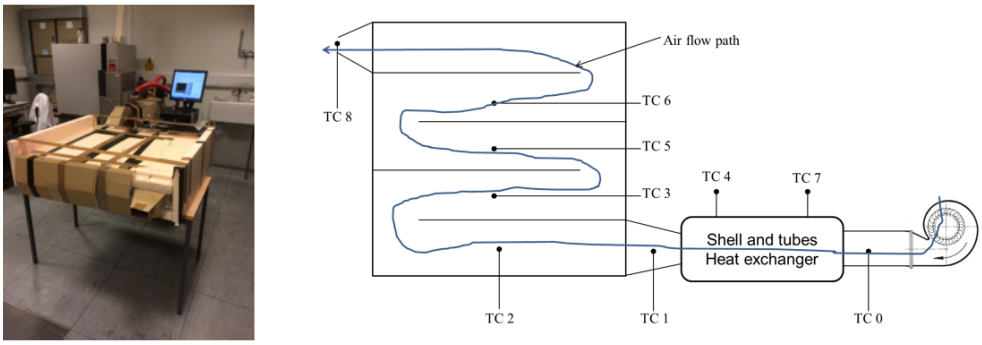

(a) view of the rig (b) air flow path

Figure 5.11: General view of the assembled parallel slab store and a schematic diagram showing the thermocouples location in the test rig.

The shape stabilized PCM produced could store up to 173.2J/g in the temperature range between 6 and 24°C, corresponding to a volumetric storage capacity of $45kWh/m^3$. The thermal store developed had a storage capacity of 1.89kWh for the same temperature range, as seen in table 5.5.

Table 5.5: Geometric and heat transfer properties of the constructed parallel slab thermal store.

Store height $[mm]$	1000	HTF:	
Store length $[mm]$	1000	Flow rate (predicted/actual) $[m^3/h]$	75.4/45.8
Store width $[mm]$	117	Re (predicted/actual)	3277/3490
PCM slab width $[mm]$	9	hcv $[W/m^2.K]$	9.22/25
		ΔP store $[Pa]$	328
Number of PCM slabs	5	Experimental results obtained:	
Number of air passings	5	Fan efficiency $(at 45.8m^3/h)[\%]$	8
		Fan cons. $(at 45.8m^3/h)[W]$	54.9
PCM fraction [%]	39	Charging time $[h]$	21
Store Volume $[m^3]$	0.103	Thermal energy charging $[kWh]$	2.092
PCM volume $[m^3]$	0.04	Diff. to experimental result [%]	-3.91
		Discharging time $[h]$	25
Total store capacity from 6 to 24°C $[kWh]$	1.89	Thermal energy discharging $[kWh]$	1.666
Specific HT area $[m^2/m^3_{PCM}]$	222	Diff. to experimental result [%]	-4.66
Insulation thickness $[mm]$	0.05	Cycle efficiency [%]	79.6
λ insulation $[W/m.K]$	0.04	System COP	0.66
Charging kWh_{th} uncertainty [%]	3.24	Discharging kWh_{th} uncertainty [%]	3.25

Figure 5.12 presents the experimental results obtained and the simulation predictions. The obtained simulation results are in good agreement with the experimental results obtained (both charging and discharging enthalpy measured a relative difference less than 5%), with a slight variation in the heat transfer rate during the charging process (freezing of the PCM). This might be due to dimensional changes not considered during the freezing of the shape stabilized PCM slab (contraction of the storage material allowing the formation of air gaps within the PCM slabs).

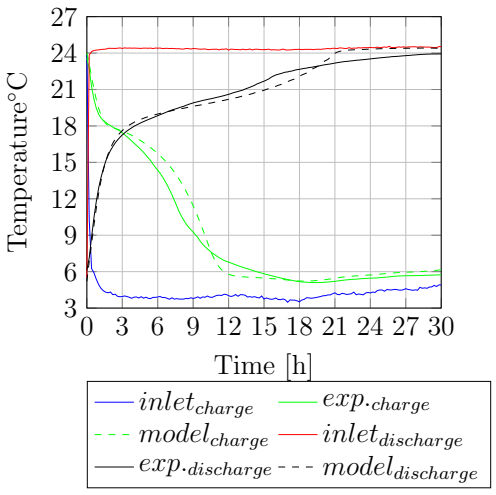

(a) temperature readings

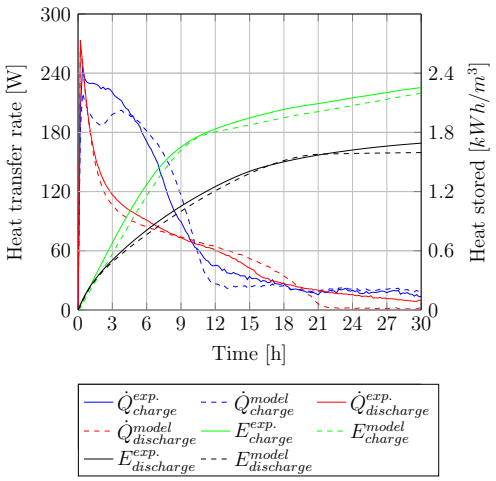

(b) heat transfer rate and storage capacity

Figure 5.12: Experimental results and simulation predictions for the parallel slab store outlet temperature, heat transfer rate and storage capacity.

To verify the accuracy of the developed numerical model for the staggered cylinder store, a thermal store containing 80L of PCM was constructed. The proposed geometry was a staggered arrangement of cylinders similar to a shell-and-tube heat exchanger, as seen in figure 5.13a and 5.13b. It consisted of 42 cylinders with 40mm OD and 2m length, distributed in 3 concentric rings and displaced 50mm from each

other. The inner ring had 8 cylinders, the middle ring 12 and the outer ring 20 cylinders. The chosen geometry was considering the air flow to propagate radially, passing through 3 rows of PCM cylinders between each air division, as shown in figure 5.13a. The selection of the chosen geometry was to maximize the air passing through each PCM cylinder to provide an outlet temperature closer to the PCM temperature.

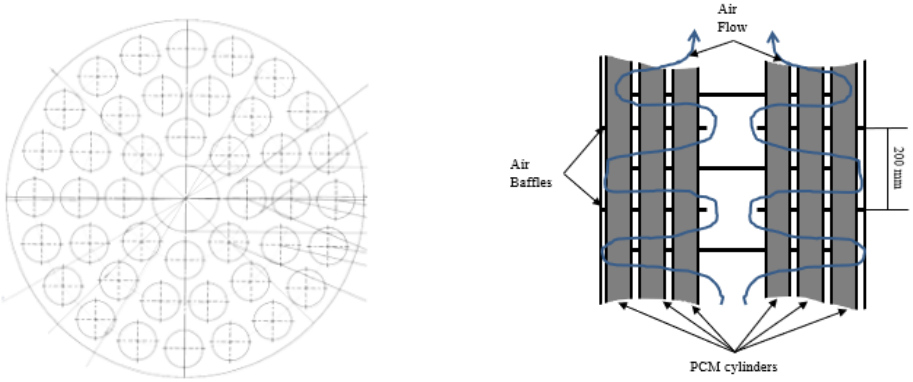

(a) air baffle (b) flow distribution

Figure 5.13: Top view of the air baffles and detailed view of the air flow distribution within the thermal store.

Figure 5.14a to 5.14c presents a general view of the store constructed. The baffles and outer shell were made of 1mm thick HDPE sheet, the 40mm diameter cylinders were fabricated from general purpose plastic pipes. The numerical model developed predicted no significant differences in using higher conductivity construction materials such as aluminum or steel compared to the plastic used due to the flow length provided by the 20 baffles spaced at 100mm. The optimized flow distribution provided by the baffles ensured an acceptable effectiveness between the outer air flow and the PCM used.

(a) empty store (b) cylinder distribution (c) insulated store

Figure 5.14: General view of the staggered cylinder store constructed, the cylinder distribution and thermal store with 50mm of Rock-wool insulation.

The shape stabilized PCM produced could store up to 161J/g in the temperature range between 12 and 28°C, corresponding to a volumetric storage capacity of $43kWh/m^3$. The staggered cylinder thermal store developed had a storage capacity of 3.45kWh for the same temperature range, as seen in table 5.6.

Table 5.6: Geometrical and heat transfer properties of the constructed staggered cylinder thermal store.

Cylinder length $[mm]$	2000	HTF:	
Cylinder outer diameter $[mm]$	40	Flow rate (predicted/actual) $[m^3/h]$	75.4/45.8
Cylinder wall thickness $[mm]$	2.4	Re (predicted/actual)	5742/3490
Transversal spacing (S1) $[mm]$	52.36	hcv $[W/m^2.K]$	33/25
Longitudinal spacing (S2) $[mm]$	52.36	ΔP store $[Pa]$	335
Number of cylinders	40	Experimental results obtained:	
Number of rows	3	Fan efficiency $(at 45.8m^3/h)[\%]$	8
Number of baffles	20	Fan cons. $(at 45.8m^3/h)[W]$	54.9
		Charging time $[h]$	43
PCM fraction [%]	35	Thermal energy charging $[kWh]$	4.46
Store Volume $[m^3]$	0.231	Diff. to experimental result [%]	-0.33
PCM volume $[m^3]$	0.080	Discharging time $[h]$	30
Total store capacity from 6 to 24°C $[kWh]$	3.45	Thermal energy discharging $[kWh]$	3.33
Specific HT area $[m^2/m^3_{PCM}]$	126	Diff. to experimental result [%]	3.1
Insulation thickness $[mm]$	0.05	Cycle efficiency [%]	74.7
λ insulation $[W/m.K]$	0.04	System COP	0.83
Charging kWh_{th} uncertainty [%]	5.94	Discharging kWh_{th} uncertainty [%]	5.95

The simulated results obtained from the numerical model using the actual experimental flow rate were in good agreement with the experimental measurements (both charging and discharging enthalpy measured a relative difference of less than 5%), as seen from the predicted and measured air outlet temperature presented in figure 5.15. The measurement uncertainty on the results obtained is higher than the parallel slab thermal store due to the longer measurement duration of the staggered cylinder thermal store.

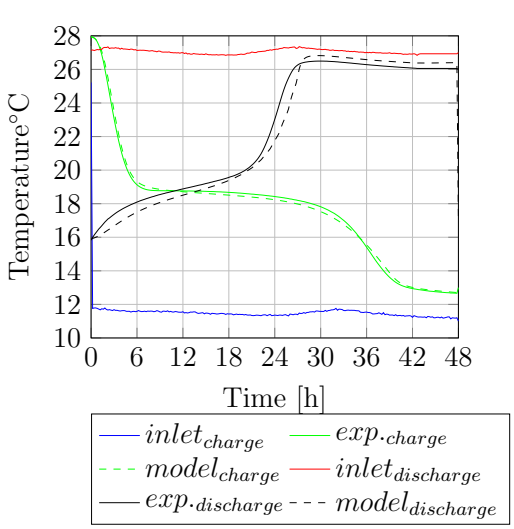

(a) temperature readings

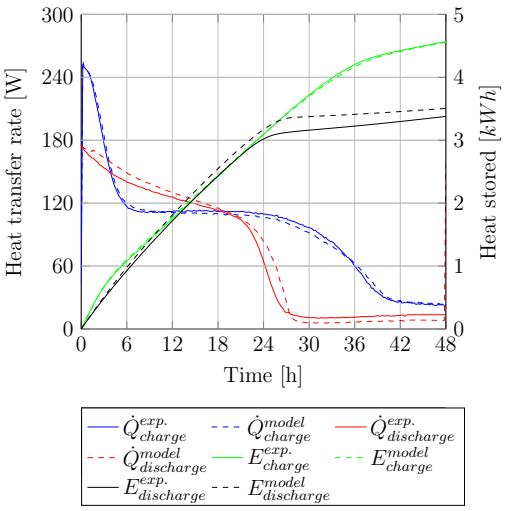

(b) heat transfer rate and storage capacity

Figure 5.15: Experimental measurements and model predictions for the inlet and outlet temperature; storage capacity and heat transfer rate of the staggered cylinder thermal store.

The 3.45 kWh storage container had an average charging rate of 104W and a slightly higher discharging rate of 111W, requiring 43h to fully charge and 30h

to discharge. The extended charge-discharge cycle duration of 73h and the low centrifugal fan efficiency lead to a system COP of 0.83, as detailed in table 5.6.

Using the fan from the suction side, the air flow could be increased by 65% (to 75.4 m^3/h) also increasing the blower efficiency from 8% to 12.1%. This would reduce the charging and discharging times to 22h and 18h respectively, leading to a system COP of 1.65, assuming that the charging temperature was 12°C and the discharging temperature 28°C. The restrictions to the air flow due to the baffles restricted the air flow within the thermal store, limiting its heat transfer rates.

5.4 Thermal stores optimization

For cooling the studied office building, higher heat transfer rates are needed hence larger flow rates are required, leading to thermal stores with no baffles in the air flow, thus eliminating air flow obstructions, as seen schematically in figure 5.16a and 5.16c. Two sets of simulations were carried out for each proposed geometry testing the day time cooling reduction potential of using free night cooling with the RT15 [41] composite. The possibility of shifting cooling load with night time charging was simulated with RT8HC. The models were used to simulate a scenario in which each latent heat store was fully utilized. In regard to the operational temperature range, the store filled with RT8HC was charged at 1°C and the store filled with RT15 charged at 7°C; both were discharged at 24°C.

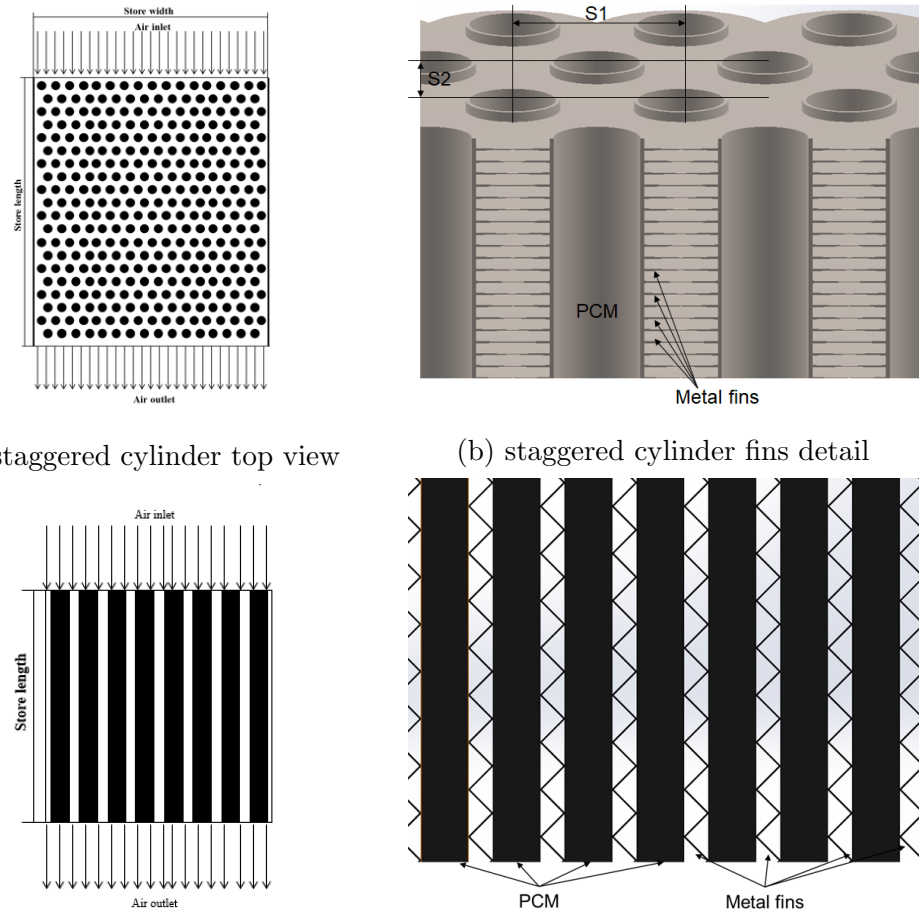

(a) staggered cylinder top view

(b) staggered cylinder fins detail

(c) parallel slab top view

(d) parallel slab side view

Figure 5.16: Simplified diagrams of the staggered cylinder and parallel slab thermal stores geometry and detailed view of the proposed fins.

To obtain higher heat outputs, the admissible flow rates need to be considerably higher, leading to a staggered arrangement of cylinders with no baffles. The heat transfer area can be increased by adding fins transversal to the flow path. Two thermal store designs were then optimized for the two cooling approaches: using night time cold air (using RT15) and using night time load shifting (using RT8HC) charged during economy 7 tariff times. Table 5.7 presents the designed parallel slab store geometrical parameters for each PCM.

Table 5.7: Geometric properties of the 2 optimized parallel slab thermal stores.

Parameter	Using RT8HC	Using RT15
Store length $[m]$	1.48	
Store width $[m]$	7.814	7.562
Store height $[m]$	2	
Air gap $[mm]$	20	
PCM slab thickness $[mm]$		
Enclosure thickness $[mm]$	1	
Number of fins per gap	400 (in figure 5.16c and 5.16d)	
Specific HT area $[m^2/m^3_{PCM}]$	806	
Area increase with fins [%]	910	
Number of slabs	186	180
Store Volume $[m^3]$	23.124	22.378
PCM volume $[m^3]$	11.011	10.045
PCM fraction [%]	47.62	
Insulation conductivity $[W/m.K]$	0.04	
Insulation thickness $[mm]$	200	

Figure 5.17 presents the simulated results for the parallel slab optimized stores with and without fins. The model simulated a full utilization scenario for each latent heat store. The store using RT8HC was charged at 1°C and at 7°C using RT15; both discharged at 24°C. Both stores were designed to provide 10 hours of cooling at a constant rate of 50.8kW for the store filled with RT8HC and 34.9kW for the store filled with RT15. Both stores were charged in 7 hours, the predicted charging rates were 72.6kW for the store filled with RT8HC and 49.86kW for the store filled with RT15.

The centrifugal fan flow rate was controlled between 50% and 150% of the nominal flow rate, according to the heat demand needed. Both stores with fins allowed higher charging rates and longer periods of constant cooling rates during the discharge, taking advantage of nearly all the storage capacity over the 10h discharging time.

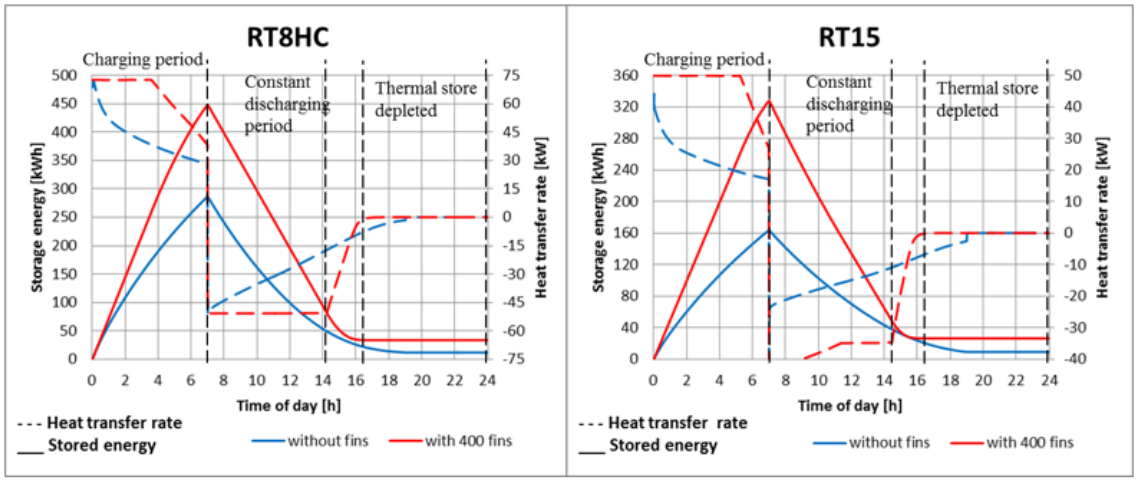

Figure 5.17: Simulation predictions for the optimized parallel slab thermal store with RT8HC and for the thermal store with RT15 with and without fins.

Table 5.8 presents the designed staggered cylinder store geometrical parameters for each PCM. It can be seen that the PCM fraction is much smaller than in the parallel slab stores, leading to a greater heat transfer area increase when fins are included. The main consequence is the larger area occupied by the store if sized to meet the storage capacity required.

Table 5.8: Geometric and heat transfer properties of the 2 optimized staggered cylinder thermal stores.

Parameter	Using RT8HC	Using RT15
Store length $[m]$	10.71	10.3
Store width $[m]$	25.23	
Store height $[m]$	2	
Transversal spacing (S1) $[mm]$	238	
Longitudinal spacing (S2) $[mm]$	206	
Cylinder outer diameter $[mm]$	38.1	
Enclosure thickness $[mm]$	1.6	
Number of fins per gap	400	
Specific HT area $[m^2/m^3_{PCM}]$	125	
Area increase with fins [%]	16 103	
Cylinders per row	211	210
Number of cylinders	5 486	5 250
Store Volume $[m^3]$	540.48	519.7
PCM volume $[m^3]$	10.496	10.045
PCM fraction [%]	2	
Insulation conductivity $[W/m.K]$	0.04	
Insulation thickness $[mm]$	200	

Figure 5.18 presents the simulated results for the staggered cylinder optimized thermal stores with and without fins. The variation between the store with and without fins is smaller than for the parallel slab geometry, but a clear performance increase is still noted with the use of fins.

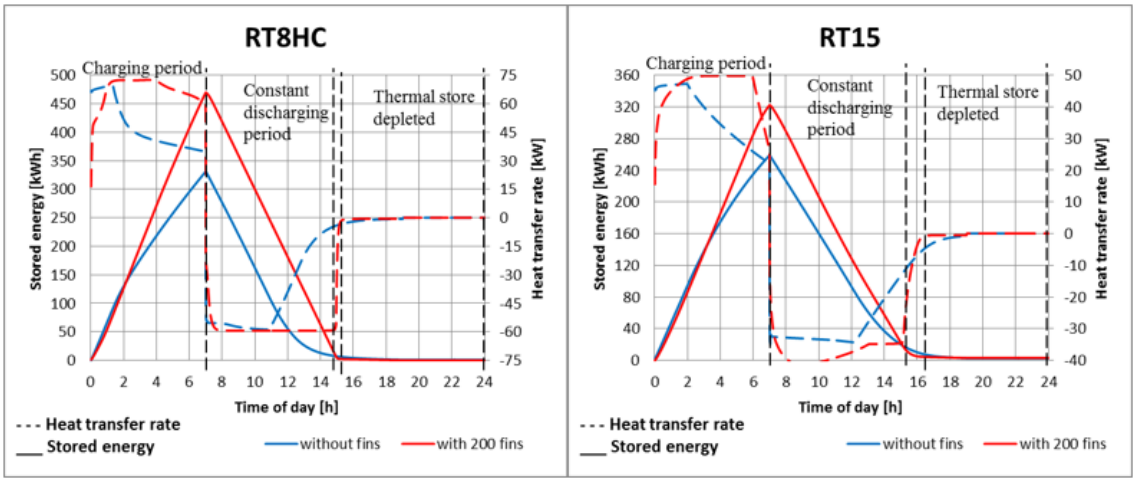

Figure 5.18: Simulation predictions for the optimized staggered cylinder thermal store with RT8HC and for the thermal store with RT15 with and without fins.

Industrial-scale centrifugal fans can obtain an isentropic efficiency of up to 70% [164], significantly increasing the COP of the system when compared to the tested thermal stores, as seen in table 5.9. By adding 400 fins to each tube spaced 5mm and with 10mm length increased the heat transfer area by 16 103%, as detailed in table 5.9. The optimized thermal stores were integrated in the developed building model, charged during economy 7 [167] off peak times (00.00 to 07.00) and discharged during office working hours from 07.00 to 19.00. The designed thermal storage capacity of the thermal store with RT8HC (from 1 to 24°C) is equivalent to 15.5% of the total building thermal mass, while the store using RT15 (from 7 to 24°C) is only equivalent to 14.3% of the building thermal mass.

Table 5.9: Heat transfer properties for the 4 thermal stores modelled.

PCM	Using RT8HC		Using RT15	
Geometry	Parallel slab	Staggered cyl	Parallel slab	Staggered cyl
Storage capacity $[kWh]$	508		349	
Nominal air flow rate $[m^3/h]$	16 509		13 522	
Air velocity $[m/s]$	0.62	0.091	0.52	0.074
Reynolds number of the air flow	1683	265	1425	217
Air h_{cv} $[W/m^2.K]$	3.86	5.01	3.08	4.53
Charging efficiency (w/fins) [%]	88	92	94	92
Fan consumption (w/fins) $[kWh]$	54.6	51.4	52.8	52.69
System COP	8.21	9.14	6.2	6.12
C_{avg} $[kJ/K]$	80 296		73 906	
λ_{solid} $[W/m.K]$	0.45			
λ_{liquid} $[W/m.K]$	0.178			

5.5 Yearly results

Using London Gatwick climate data and the building design parameters specified in table 5.2, simulations were performed with HVAC systems and thermal stores for a whole year to determine potential enhancements in the daily performance and consequently reductions in yearly energy requirements with each approach. Four cases with extra fresh air provision were compared to the conventional HVAC system (A): on demand (B), using a store filled with RT15 (C) and using a store filled with RT8HC and with electrical night cooling (D). The modelled space cooling network is schematically illustrated in figure 5.19a.

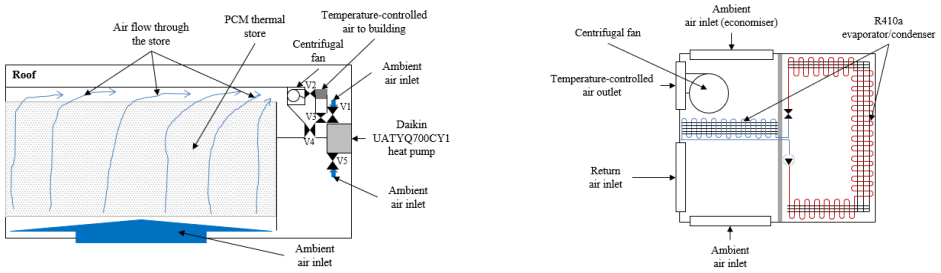

(a) thermal store rooftop integration (b) detailed view of heat pump

Figure 5.19: Schematic representation of the staggered cylinder latent heat storage system integration into the building model and detailed view of the rooftop heat pump.

All cooling systems modelled were activated during daytime office hours when the indoor air temperatures were above 22.5°C. The heat pump was activated only if the indoor air temperature increased above 24°C. The coefficient of performance (COP), used for the heat pump during office working hours was 3 [159]. For the simulation using extra ventilation on demand, valve V2 would open (shown in figure 5.19a) and the centrifugal fan activated when indoor temperature increased above 22.5°C, allowing colder outdoor air to be introduced reducing the building cooling load during office working hours.

For the simulation with a thermal store filled with RT15, during the night valve V1 and V4 would open, directing the outside ambient air flow to cool/charge the thermal store. During office working hours (from 07.00 to 18.00), if the indoor temperature increased above 22.5°C valve V4 closes, V2 and V3 open and the centrifugal fan is activated, reversing the air flow through the store and consequently discharging it to provide space cooling to the office building, as shown schematically in figure 5.19a. The air flow from the centrifugal fan could vary between 50% and 150% of its nominal flow-rate.

For the simulations using the heat store filled with RT8HC, the heat pump was assumed to charge the latent heat store with a COP of 4.5, based on the Daikin UATYQ-CY1 rooftop air conditioners service manual [159]. During store charging, valve V5 and V4 are open, allowing the ambient air flow to be cooled by the heat pump if the ambient air temperature is above the required cooling temperature of 1°C. To effectively work and improve energy efficiency, all the specified cooling systems are only operated if their COP, calculated according to equation 5.14, is above 3.5. Using the centrifugal fan specifications from SODECA [165], the 3kW

electrical input to the fan had an estimated 65% efficiency reported at 15 $000 m^3/s$ (varying its flow-rate and electrical consumption according to the required cooling demand), meaning the designed cooling systems were only activated for cooling loads above 16kW.

$$COP(t) = \frac{\rho \cdot \dot{V}_{fan}(t) \cdot Cp \cdot (T^{out}_{store}(t) - T_{indoor}(t)) \cdot \eta_{fan}(t)}{\Delta P_{fan}(t)} \tag{5.14}$$

Figure 5.20 presents the aggregated yearly results for each studied case. The obtained reduction in electricity use for cooling by using only extra air circulation can reach up to 34%. Using RT15 with ambient night time cooling gave slightly better results, 36% for the staggered cylinder store and 39% in the parallel slab store. Shifting daily cooling loads with RT8HC did not reduce the yearly electricity consumption for cooling with the staggered cylinder store and a 15% reduction was achieved with the parallel slab store. The poor performance values are due to the parasitic heat gains from ambient occurring when the thermal store is not being used.

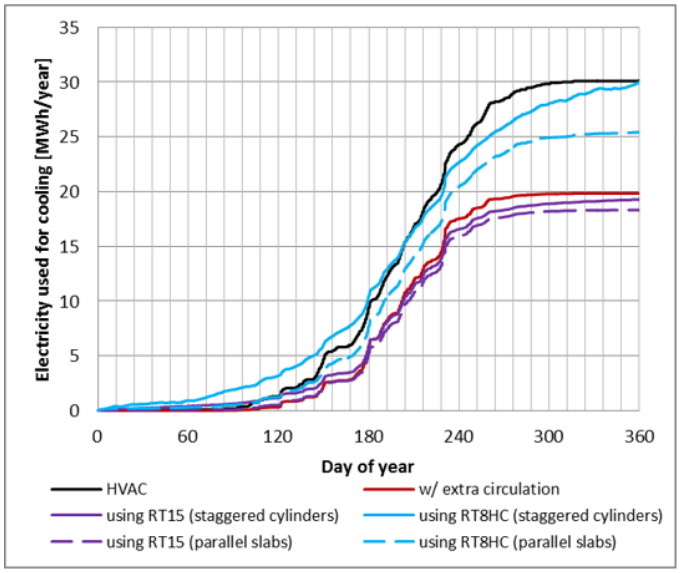

Figure 5.20: Aggregated electricity consumed for cooling in the building for all the cases studied over a year period.

Figure 5.21 presents the daily cooling load for each season and for each simulated cooling approach. The most significant levels of energy reduction with the extra ambient fresh air provision on demand are predicted mainly during the spring and autumn months and the reductions are minimal in summer months due to the higher ambient temperature. The reduction in the cooling load during office working hours in summer is larger using a store filled with RT15 with free night cooling; however, the overall gain is reduced by the additional energy required for the fan to charge the store during the night.

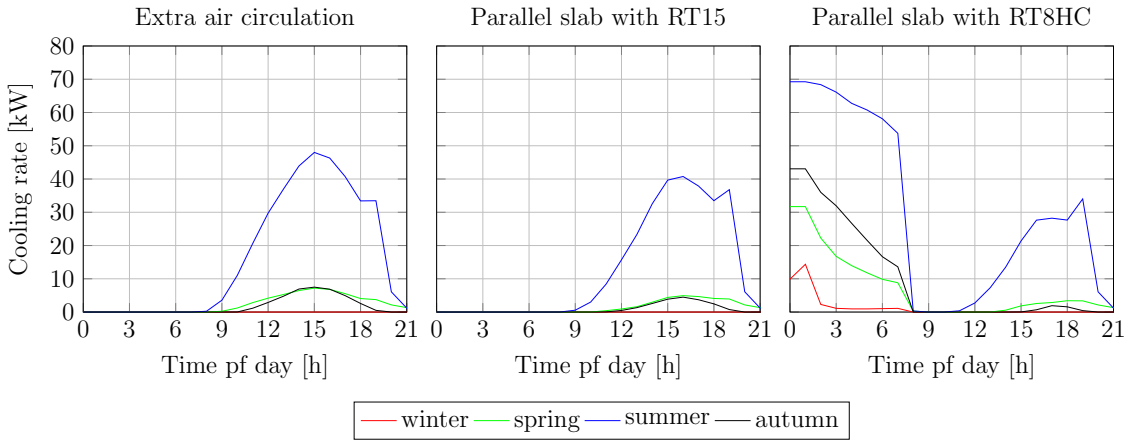

Figure 5.21: Seasonal results for daily cooling loads with extra air circulation, for the parallel slab thermal stores with RT15 and with RT8HC.

The predicted energy used for cooling in the system with RT8HC charged during the night with the heat pump presented in figure 5.21, successfully enabled daily cooling loads to be shifted into off peak times in both Spring and Autumn months and significantly reduced the cooling load during the Summer months, shifting the Summer peak cooling load to 19.00 (when the thermal energy storage system is nearly depleted).

Figure 5.22 presents the instantaneous coefficient of performance (COP) for each modelled system, calculated according to equation 5.14. For the extra ambient fresh air provision on demand system, no thermal energy storage is used and extra ambient air is ventilated through the building is the exterior temperature is lower than the indoor temperature.

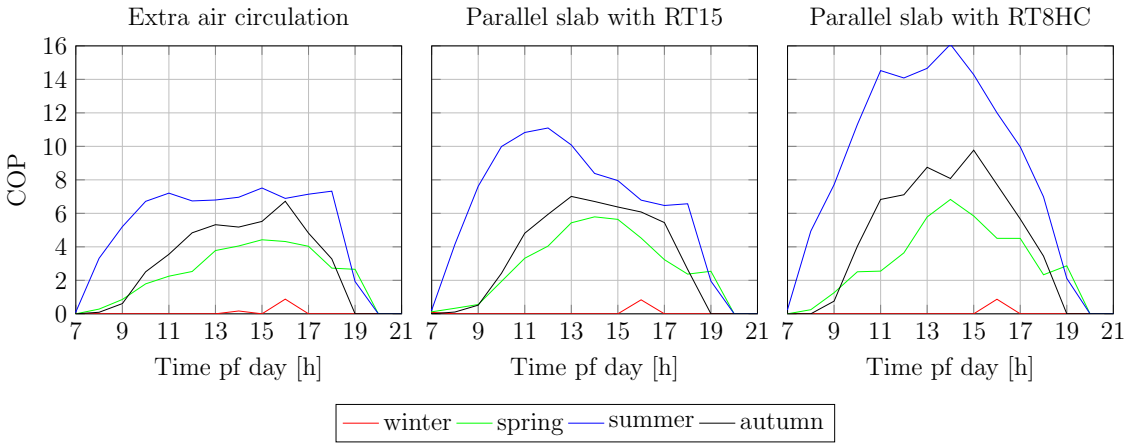

Figure 5.22: Seasonal results for the system instantaneous COP with extra air circulation, for the parallel slab thermal stores with RT15 and with RT8HC.

The increase in predicted COP for the thermal storage system using RT15 compared to the extra ambient fresh air provision on demand system was more pronounced during summer months and only slightly higher during spring and autumn months. The predicted daily profile for the COP for the storage system with RT8HC was very similar to that of the system with RT15 during spring and autumn months.

The predicted COPs are considerably higher during summer months where the systems predicted gains in efficiency were more pronounced due to the higher required cooling power, making more use of the thermal energy storage system.

Figure 5.23 presents the average daily profiles for each season predictions of the electrical consumption for the three systems. The lower values predicted from 08.00 to 10.00 are the result of simulating a variable speed centrifugal fan to provide the ventilation, with the fan electricity consumption regulated to meet the required cooling load. At the start of the daily cooling cycle (07.00), the latent heat stores were charged, hence the temperature difference was at its maximum value, with lower flow rates required to achieve the cooling output.

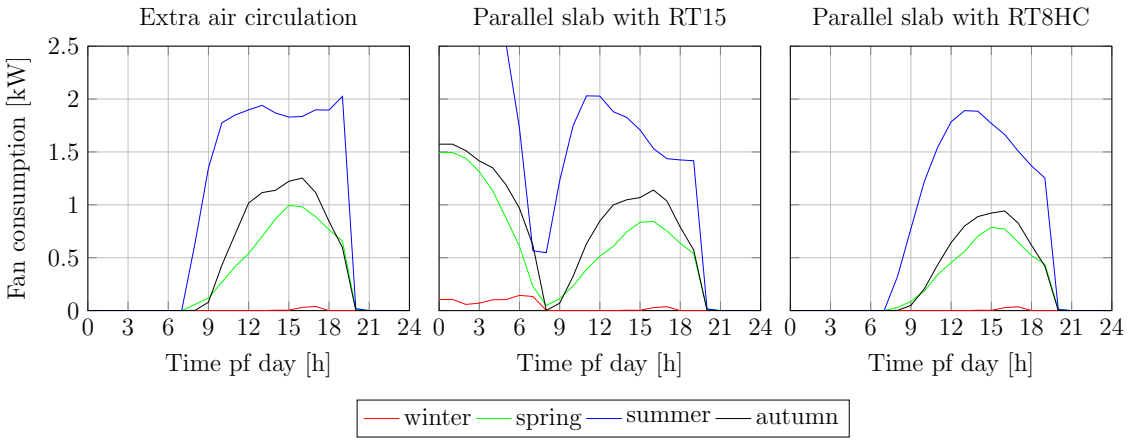

Figure 5.23: Seasonal daily profiles of the fan electrical consumption for the system with extra air circulation, with RT15 and using RT8HC with night cooling.

The thermal store filled with RT8HC shifted daily cooling loads into off peak periods of electrical tariffs for Spring and Autumn months effectively. Full load shifting during summer months was prevented by the thermal capacity of the selected heat pump (due to restricted charging period, the maximum energy able to be charged was $7h \cdot 16.13kW \cdot 4.5 = 508kWh$, less than the maximum required in summer months, 594kWh).

Table 5.10 presents the predicted electrical consumption for heating and cooling for each season and the calculated value for a year for the three systems simulated and the case using a conventional HVAC system approach. The thermal storage system with RT8HC and night time cooling provided the greatest reduction in electricity use during peak times due to its ability to effectively shift the building cooling load, although greatly increasing electricity consumption during off peak times.

Table 5.10: Seasonal electricity used for heating and cooling during peak time and off-peak times in each modelled system.

Electricity used $[kWh]$			**Winter**	**Spring**	**Summer**	**Autumn**	**Yearly**
Conventional		**Off peak**	0	0	0	0	**0**
		Peak time	8527	7671	19390	7360	**42 948**
+ extra circulation		**Off peak**	0	0	0	0	**0**
		Peak time	8464	5178	15051	3994	**32 687**
Storage system with RT15 (ambient cooling)	**Staggered cylinder thermal stores**	**Off peak**	598	1002	1581	976	**4 157**
		Peak time	8464	4354	11977	3242	**28 037**
	Parallel slab thermal stores	**Off peak**	89	653	1523	785	**3 050**
		Peak time	8463	4357	12080	3236	**28 137**
Storage system with RT8HC (electric night cooling)	**Staggered cylinder thermal stores**	**Off peak**	1662	4133	9389	5727	**20 912**
		Peak time	8464	3838	7292	2527	**22 121**
	Parallel slab thermal stores	**Off peak**	455	2361	8997	3825	**15 638**
		Peak time	8463	3806	7879	2531	**22 679**

5.6 Economic comparison of all modelled systems

A general financial assessment was made to assess the three approaches described and compared with the conventional HVAC system. Each systems component costs and operation and maintenance costs were compared with the reference scenario of using the heat pump only.

Table 5.11 presents the initial capital expense (CAPEX) and operational expense (OPEX) costs for the 4 cases studied. For the heat pump system, Daikin UATYQ700MCY1 [159] was selected due to meeting the heating and cooling required. An industrial-scale centrifugal fan [164] with a nominal flow rate of 15 $000 m^3/h$ was selected from SODECA [165].

For the finned cylinder thermal stores, market research indicated a price of $3.8£/m$, commonly found for stainless steel condenser tubes [166]. For the parallel slab thermal stores, assuming that the shape-stabilized PCM would not leak through the rectangular slab and the galvanized steel sheets enclosing that slab would be compressed with the corrugated sheets serving as fins in the rectangular air gaps (as seen schematically in figure 5.16d), a cost of $650£/ton$ was considered [167] as a reference for the metal.

Due to the larger size of the designed systems, the whole system installation costs were assumed to be 5% of the initial CAPEX [168]. The cylinder costs were the largest capital component in the staggered cylinder, representing 37% of the total system cost for both thermal stores. In the parallel slab thermal stores, the composite PCM was the largest capital component, representing 53% of the initial CAPEX. Operation and maintenance costs were assumed to be $0.9£/m^2$ of office space, in accordance with [169]. The waxes used were assumed to have an indicative price of $4£/kg$ [20] and the composite adsorbent material developed by [162] an indicative price of $2.65£/kg$, both mixed with a 80/20 mass ratio, providing a composite storage material cost of $3.73£/kg$.

For the standard electricity tariff, Npower provided a price of $0.1664£/kWh$ with a standing charge of $55.1£/year$. Using economy 7 electrical tariffs, Npower provided a peak tariff of $0.2131£/kWh$ and an off-peak tariff of $0.0765£/kWh$, with the same standing charge. The levelized cost of energy (LCOE) for each system was calculated using equation 5.15, from [170].

$$LCOE = \frac{\left(\frac{CAPEX \cdot r}{1-(1+r)^{-n}} + OPEX + E_{used} + E_{tariff}\right) \cdot n}{W_{produced} \cdot n} \left[\frac{£}{kWh}\right]; \quad (5.15)$$

Table 5.11: CAPEX and OPEX costs comparison for the systems studied.

Component		HVAC (heat pump only)	+ extra circulation	Staggered Cylinder		Parallel Slab		Ref.
				With RT15	With RT8HC	With RT15	With RT8HC	
Thermal store cost [£]	Insulation +structure			11 953	12 356	1 057	1 089	[171]
	PCM enclosure			39 900	41 694	6 317	6 527	[167]
	PCM + composite			31 669	32 929	32 474	33 556	[20]
	Centrifugal fan		3 142					[165]
Heat pump cost [£]		17 305						[172]
Installation costs [£]		865	1 022	5 198	5 371	3015	3081	[168]
CAPEX [£]		18 170	21 469	109 167	112 797	63 310	64 700	
Yearly system maintenance [£/year]		1 382						[169]
Yearly electricity used [kWh]		7 206	5 504	5 412	6 371 (econ 7)	5 245	6 087 (econ 7)	-
OPEX [£/year]		8 588	6 886	6 794	7 753	6 627	7 469	
LCOE [£/MWh]		97.17	84.45	166.75	179.11	120.77	129.89	

For a 20-year life cycle with an annual interest rate of 8%, the LCOE calculated for each system is presented in table 5.11. The system with extra air circulation presents the lowest LCOE due to the reduction in the energy required to meet the cooling load achieved with ambient air cooling for a typical London Gatwick climate. Due to the high CAPEX costs of the thermal stores, their yearly reduction in electricity costs compared to the conventional system were not enough to provide a more economical cost of energy. The parallel slab thermal stores offered lower LCOE than the staggered cylinder stores due to their higher PCM fraction (requiring less area to be insulated) and the cost-effective steel enclosure.

In order to obtain the same LCOE as the conventional HVAC system, a CAPEX reduction in the staggered cylinder thermal stores of 77% would be required for the store with RT8HC and 67% for the store with RT15. The parallel slab thermal stores would require lower cost reductions: 40% for the store using RT15 and 54% for the store using RT8HC

5.7 Conclusions from the analysis of 2 systems integrating PCMs into centralized ventilation systems

Medium to highly glazed buildings with lower U-value building fabric such as the building simulated, generally consume more energy for cooling than for heating due to the high solar gains transmitted through the glazing, high occupancy and

electronic devices emitting heat. From the three approaches numerically simulated, the use of extra mechanical ventilation can have a significant positive impact for a typical UK climate, since the ambient temperature during office working hours is mostly below 24°C, (97% for the London Gatwick IWEC climate data).

When compared to extra fresh ambient air provision on demand, making use of colder night air does not achieve major reductions in electricity use, because the extra free cooling obtained during working hours is off set by the energy required to charge the stores during the night.

Using a thermal store filled with RT8HC with off peak electrical cooling with a COP of 4.5 successfully shifted office daily cooling loads into off peak electrical tariffs during Spring and Autumn months. The staggered cylinder thermal store did not obtain any yearly electricity reductions due to the greater external surface area of the thermal stores, increasing its parasitic heat gains. The parallel slab thermal store reduced yearly electricity consumption by 15% compared to the reference HVAC approach, although still less than using extra mechanical ventilation only. Shifting daily cooling loads to Summer months in economy 7 electrical tariffs is capped by the capacity of the heat pump used.

Using extra air ventilation or night time ambient cooling can contribute to the decarbonisation of current office HVAC systems through electricity consumption reduction, that reduction being more attractive with night time ambient cooling. Shifting daily cooling loads with electrical off peak cooling has a lower decarbonisation potential with the parallel slab thermal store and no effect for the staggered cylinder thermal store, although it successfully shifted 67% of the daily electrical demand for cooling to off peak times.

From the economic analysis, the high capital costs of installing the thermal stores reduce significantly their economic benefit, with the lowest price of energy obtained by using extra ambient fresh air provision on demand, $84.45£/MWh$, for a 20-year life cycle with an annual interest rate of 8%.

Shifting daily electrical peak loads into off peak times can have a significant decarbonization impact by allowing the consumption of low carbon electricity (such as wind and hydro) to be made in off peak times, potentially reducing the need for backup ancillary services such as combined cycle gas turbines and coal.

Chapter 6

The potential of phase change energy storage to reduce peak electrical demands for space and water heating in domestic sector in the UK

6.1 Daily demand on the UK National electricity grid

In line with the increasing global concern about climate change, the Kyoto Protocol [33] established greenhouse gas emissions baseline to be that of 1990 of each country, and proposed a reduction in CO_2 emissions by 12.5% for the UK. This objective was achieved in 2008, when the UK government introduced a new reduction goal of 80% by 2050, with the climate change act [173]. It is estimated that 45% of CO_2 emissions are attributed to the building sector [174].

In 2015, 22% of the final energy consumption in the UK was used for domestic hot water and space heating applications using natural gas and petroleum products [3]. In order to decarbonize the sector, the use of renewable heat sources such as solar thermal could be implemented, backed up by either heat pumps or gas boilers. Heat pump operation should, where possible, be restricted to off peak times to prevent an increase in the peak electrical grid demand [117].

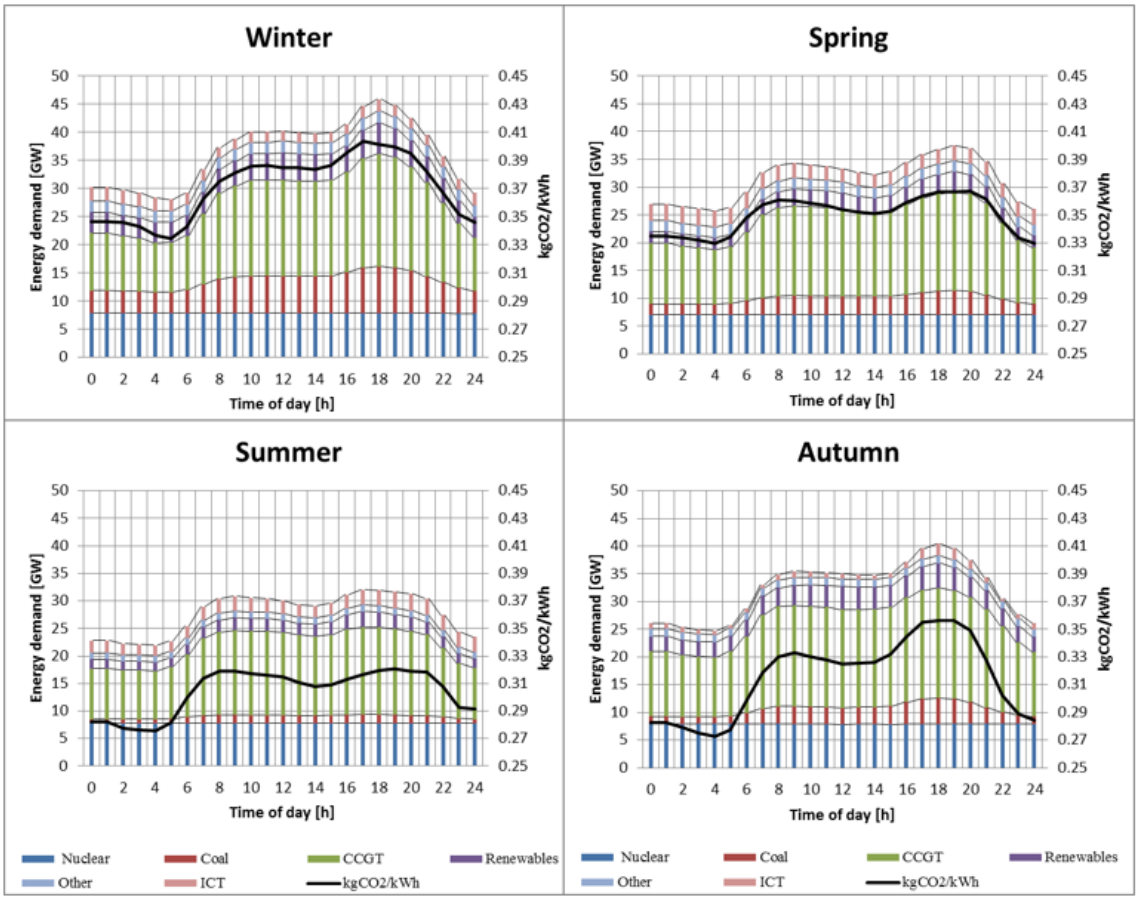

Figure 6.1: Daily variation of CO_2 emissions in each season associated with each electricity source supplied by the UK national grid in 2016 [25, 26].

The daily variation of CO_2 emissions in each season in the UK are presented in figure 6.1. Values were obtained from the generation mix for the UK national grid with CO_2 marginal emission factors applied similar to those estimated by Hawkes [25].

To achieve 80% emissions reduction in this sector, heat pump CO_2 emissions should be less than the currently emitted by conventional gas burning domestic heating systems (around $204 gCO_2/kWh_{th}$ [25, 37]), operation during off peak electrical load times will minimize both carbon emissions and peak electrical load. This can be achieved if heat pumps are operated using either economy 10 or economy 7 electricity tariffs [37], with hot water buffer tanks used to store the required heat load during peak times, offsetting the electrical load while meeting the heat demand required.

The higher CO_2 grid emissions during the winter months are mainly due to the higher consumption of coal and natural gas, a consequence of a greater electrical demand in this season in the UK. It can be seen in figure 6.1 that the lowest CO_2 daily emission period is from 23.00-05.00 and that a small reduction in the marginal emissions curve occurs from 12.00-16.00 in all seasons.

6.2 English housing stock

Of the estimated 23.5 million households in England in 2015, the vast majority are owner occupiers (63%), although this share has been reducing from the maximum of 71% reached in 2003.The share of buildings with an efficiency rating of A-C has also significantly increased [175], representing 28% of the total housing stock, with a higher share (48%) in the social rented sector. The dwelling types in which this study focused on terraced, semi-detached and detached houses. The reason for selecting these types of dwellings is due to their importance, since they represent 70% of the total British housing stock in 2015, around 16.7 million dwellings, based on the English housing survey report made by the Department for Communities and Local Government [27], as presented in figure 6.2.

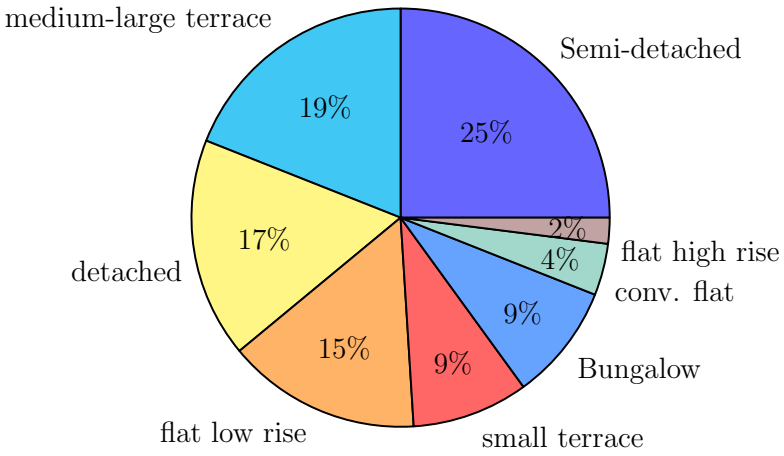

Figure 6.2: Dwellings by type, from the UK English housing survey report of 2015 [27].

6.2.1 Reference household consumption model

Using the building parameters and domestic hot water flow consumption from the high resolution stochastic integrated thermal and electrical domestic demand model developed by Mckenna [176], the daily variation of heat demand in the three selected dwelling types was simulated and analyzed for the equinox and solstice days assuming that they were in Leicester. Figure 6.3 shows a schematic diagram of the simulated gas boiler domestic hot water and space heating system used as the reference system.

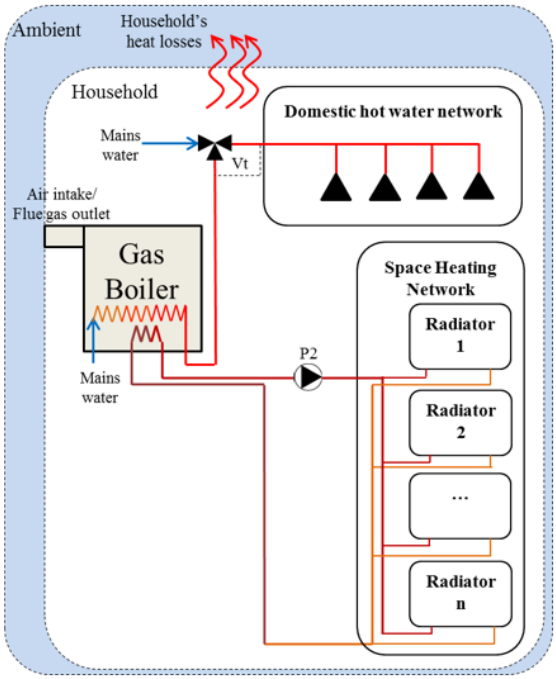

Figure 6.3: Simplified diagram of the gas boiler hot water and space heating system used as reference.

Each modelled dwelling thermal properties assumed were based on CREST demand model building specifications [31], as seen in table 6.1. The minutely-resolution domestic hot water consumption profiles and daily climate data generated by the stochastic model [31] were also used. All dwellings were considered to have been previously insulated to meet A grade efficiency standards [155].

Table 6.1: Thermal properties of each modelled building and daily heat consumption in each season.

Building type	**Terraced**	**Semi-detached**	**Detached**	**Units**
Season	**(Winter/Spring/Summer/Autumn)**			
Daily SH demand	15.40/16.71/0.00/1.85	25.37/16.14/2.57/2.64	26.40/18.25/0.00/6.53	**kWh**
Daily DHW demand	9.52/6.14/11.14/10.62	5.16/23.17/8.58/5.26	11.48/10.88/8.62/12.29	
Yearly total gas demand	7287 ($729m^3$ of gas)	9903 ($990m^3$ of gas)	7436 ($744m^3$ of gas)	
Daily DHW cons.	0.223/0.144/0.261/0.249	0.121/0.543/0.201/0.116	0.269/0.255/0.202/0.288	m^3
$UA_{value}/m^2_{floorarea}$	1.297	1.031	0.909	$W/m^2.K$
Building thermal capacitance	492.5	530.7	917.3	**kJ/K**
Floor area	58	87	136	m^2
Heat emitters total water volume	0.0296	0.0424	0.0503	m^3
Heat emitters total surf. area	34.71	49.72	58.99	m^2

The yearly energy use for each system was then obtained by multiplying the values of each day by 91.25 and summing them (assuming a typical year with 365 days, divided by 4 gives 91.25 days in each season). The gas boiler was then replaced in the model with a heat pump and 3 thermal energy storage systems were studied,

two with phase change materials (one using compact modules and one using a packed bed with encapsulated PCM spheres) and one with a water buffer tank. All the savings obtained for the storage systems studied were compared with to the reference case.

6.3 PCM screening for DHW applications

Hot water buffer tanks have constant heat capacity over the working temperature range used for conventional space heating of 40 to 65°C [175], hence requiring a considerable volume to meet 8h of domestic space heating load. Phase change materials with a phase transition temperature between 40 and 65°C can effectively increase the storage capacity within this narrow temperature range, hence reducing the required buffer tank water volume, allowing more heat to be stored for a given volume.

Organic PCMs melting in this temperature range are the paraffin waxes (RT54HC [20]) and fatty acids, as the eutectic mixture studied by Baran [101]. Other candidate PCMs working in this temperature range are salt hydrates, but their high subcooling usually prevents their use in hot water and space heating applications; however, the eutectic mixture of magnesium chloride hexahydrate with magnesium nitrate hexahydrate previously tested, presented low levels of subcooling and a high phase change enthalpy. Figure 6.4 presents the thermogram curves for the salt hydrate eutectic mixture and the candidate organic PCM materials measured in the DSC as reported in Chapter 4.

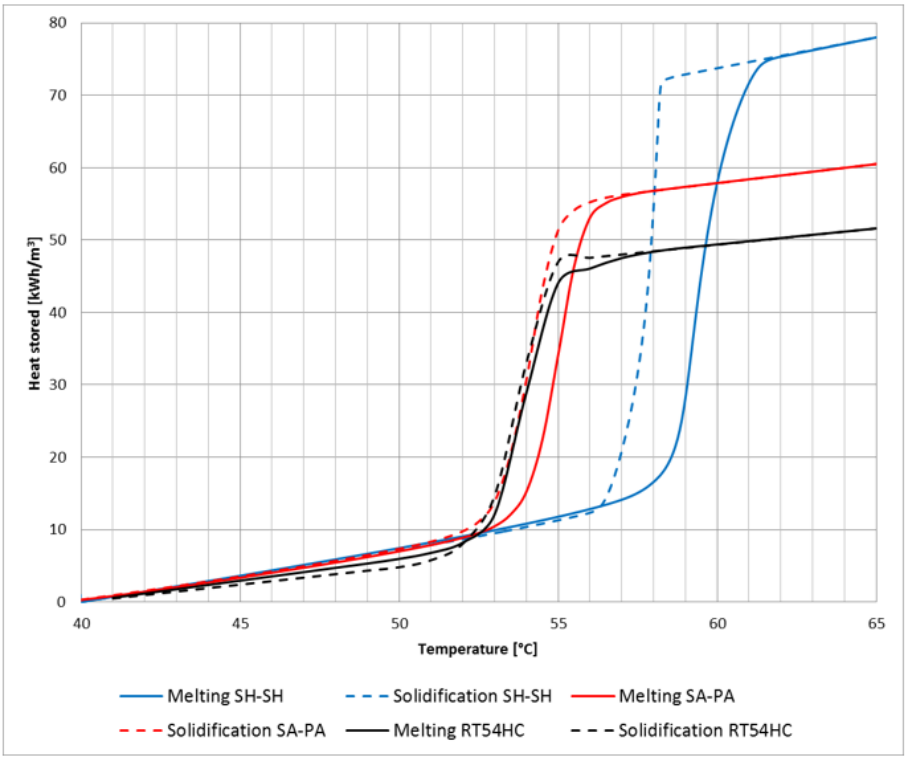

Figure 6.4: Measured heat capacity thermograms for the three candidate PCMs selected for domestic hot water and space heating applications.

It can be seen from figure 6.4 that the salt hydrate eutectic mixture has higher

volumetric storage capacity for the given temperature range. Table 6.2 presents the properties of the three candidate materials, and the salt hydrate eutectic mixture is nearly 3 times more energy dense than water, within the 40 to 65°C working temperature range.

Table 6.2: Thermal storage properties of the three selected PCMs.

PCM candidates	Temp. range °C		ΔH_{stored} kWh/m^3	$\Delta H/\Delta H_{H2O}$	λ_{solid} W/m.K	λ_{liquid}	Price $£/kg$	$£/kWh$	Ref.
$41\%MgCl_2.(H_2O)_6$ + $59\%Mg(NO_3)_2.(H_2O)_6$ (SH-SH)	40	65	78	2.72	0.6	0.606	0.061	1.19	[146, 177]
36% stearic acid + 64% palmitic acid (SA-PA) [101]			61	2.11	0.288	0.168	0.381	5.72	[61, 178]
RT 54HC [20]			52	1.8	0.215	0.165	0.51	7.63	[179, 180]

6.4 Household space heating models

According to the survey made by the Department of Energy and Climate Change (DECC) [28], domestic space heating in the UK is generally restricted to 6 months, with most households operating their heating systems between October and April, as can be seen in the histogram of figure 6.5.

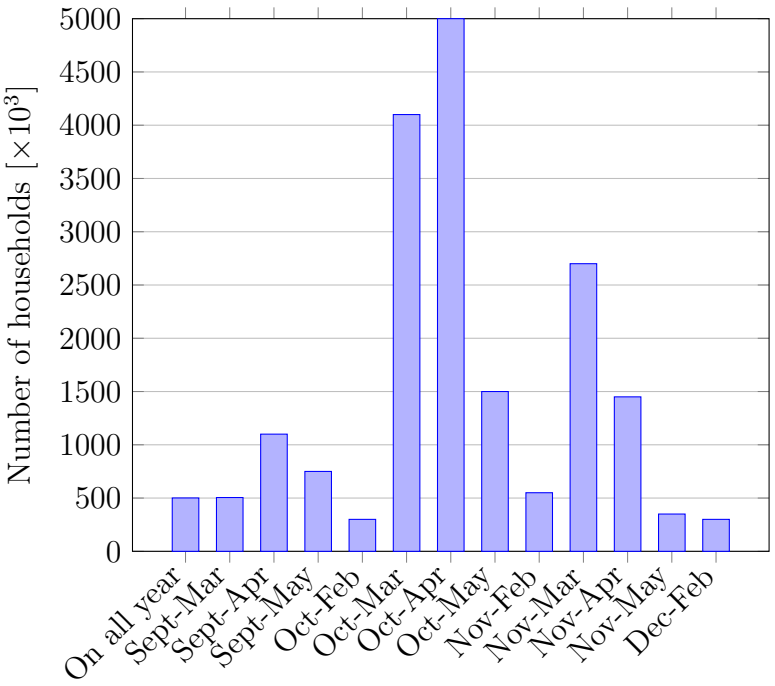

Figure 6.5: Results from DECC survey of the duration of the heating period [28].

Each latent heat storage system was designed to meet the highest 8 hour heat demand during the whole yearly simulation for each dwelling, using the salt hydrate eutectic mixture as PCM. The properties of the thermal stores are presented in table 6.3. The highest heat demand occurred during the winter months. The thermal

energy store system was sized to meet these heat demands, being oversized for the remaining months.

Table 6.3: Key properties of the thermal stores modelled (A-Buffer tank; B-Packed bed and C-Compact LHS).

Dwelling	Terraced			Semi-detached			Detached		
System	A	B	C	A	B	C	A	B	C
Store capacity $[kWh]$	18.72			24.53			18.68		
Water tank vol $[L]$	653	354	125	856	461	210	652	353	210
H/D ratio	3		1	3		1	3		1
PCM vol $[L]$		181	185		238	227		180	155
Z PCM $[\%]$		51	55.2		51.5	48.4		51	40.1
$Specific_{HTarea}$ $[m^2/m^3_{PCM}]$		127	38.63		115	38.63		127	39.72
Q_{PCM} $[kWh]$		14.1	14.46		18.54	17.67		14.06	12.08
$Q_{water+encapsulant}$ $[kWh]$	18.72	4.63	4.27	24.53	6	6.86	18.68	4.62	6.6

Packed beds have higher specific heat transfer areas compared to the compact systems, as seen in table 6.3. The PCM fraction of each modelled compact latent heat store is reduced by the additional DHW tank required to meet high heat demands from hot water appliances, this effect is more evident in the smallest system for the terraced house.

The hot water buffer tank storage system presented schematically in figure 6.6, was initially compared to the conventional gas boiler system. Daikin Altherma V high temperature air source heat pump [181], operating during off peak hours based on economy 10 electricity tariffs (00.00-05.00/13.00-16.00) [37], was used in the simulation, coupled with a solar thermal collector array, as seen in figure 6.6 and 6.7.

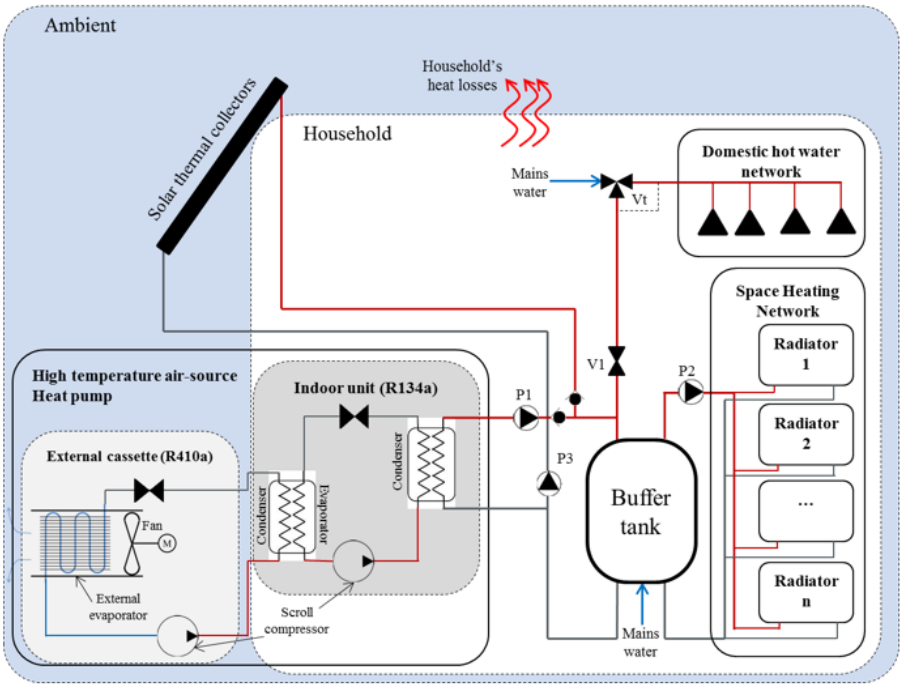

Figure 6.6: Simplified diagram showing the integration of a hot water buffer tank into a domestic hot water and space heating system using an air-source heat pump and solar thermal collectors.

In the model, circulation pump (P1) transferred heat from the heat pump water heat exchanger to charge the store, with a maximum flow of 20l/min which was adjusted based on the building needs and the store capacity. Pump (P2) transferred heat from the buffer tank to the building heat emitters, with a water flow-rate of 12l/min, controlling the inside building air in the temperature band between 19.5 and 20.5°C from 07.00 to 22.00 and 15.5 to 16.5°C in the remaining hours.

Pump (P3) transferred heat from the solar collectors (1 considered for the terraced dwelling and 2 thermal collectors for the semi-detached and detached dwellings) to the thermal store at a constant water flow of 2 l/min and an absorber area of $2m^2$ per solar collector [158], having its operation given priority over the heat pump. The pump (P3) would be turned on whenever the solar thermal collector water temperature was higher than the top temperature of the buffer tank. Whenever a hot water appliance was activated, valve V1 would open and the thermostatic valve Vt would regulate the hot water flow coming from the buffer tank to maintain a constant 52°C temperature output to the hot water appliances.

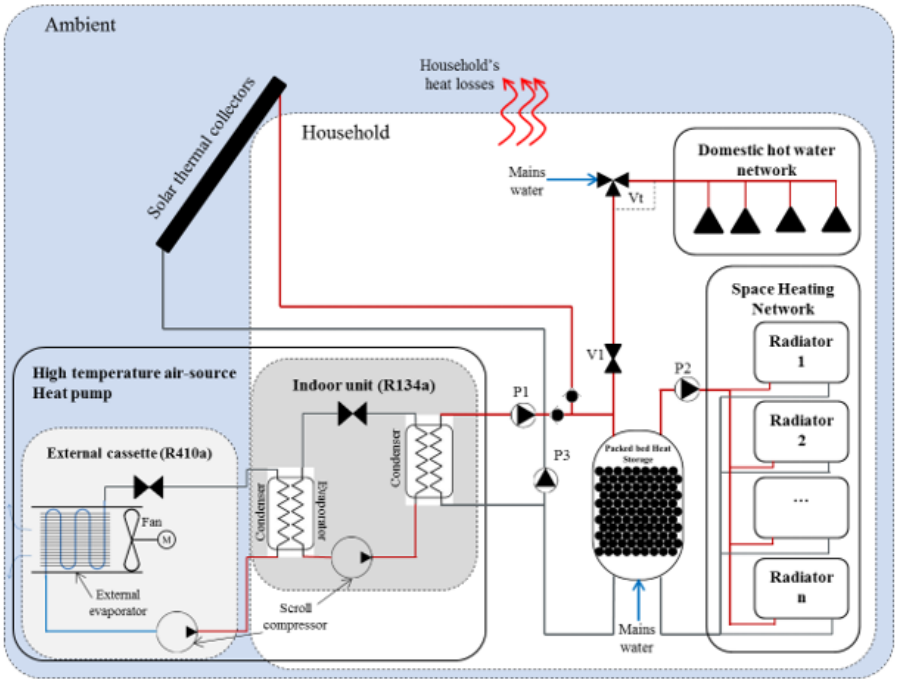

Figure 6.7: Simplified diagram showing the integration of a packed bed latent heat store into a domestic hot water and space heating system using an air-source heat pump and solar thermal collectors.

Figure 6.7 presents the integration of a packed bed latent heat store into the hot water and space heating system of a domestic building. The thermal store integration to the hot water and space heating system is the same as the hot water buffer tank shown in figure 6.6. The main difference is the volume reduction (reference case shown in table 6.8 and buffer tank system shown in table 6.10) of the buffer tank due the higher thermal storage from the PCM spheres.

The integration of a compact latent heat store into a domestic hot water and space heating system with an air source heat pump is shown in figure 6.8. The integration of the latent heat store into the building heating system is made on the coldest zone of the heat network of the dwelling to promote a higher thermal strati-

fication between the hot water tank outlet and the cold-water inlet from the mains. The reason for using a small hot water tank is to compensate for the temperature drop of the latent heat store in periods of high heat demand, a consequence of having a low water volume within the compact latent heat store.

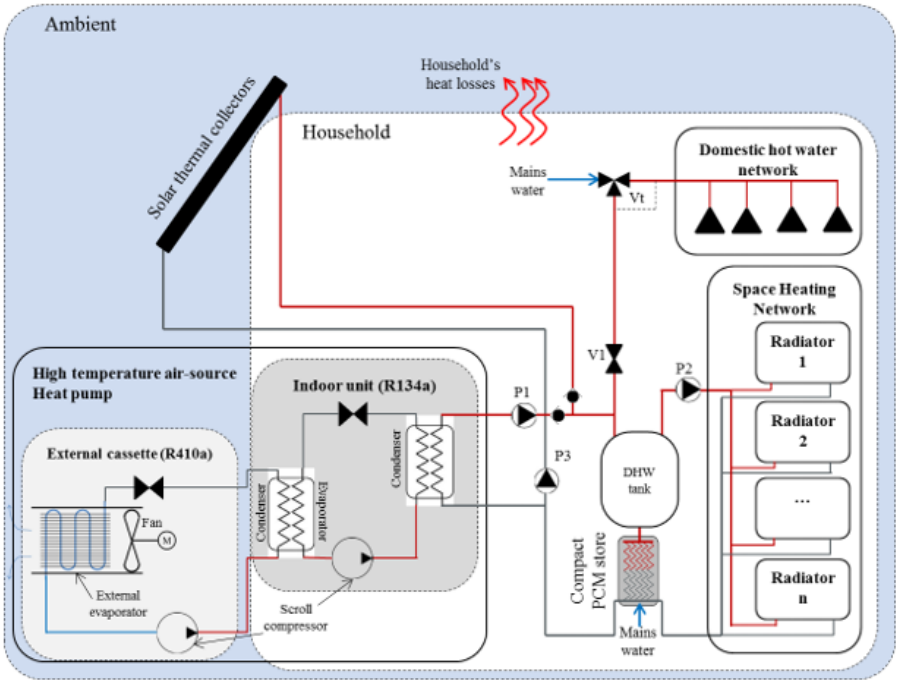

Figure 6.8: Simplified diagram showing the integration of a compact latent heat store into a domestic hot water and space heating system using an air-source heat pump and solar thermal collectors.

The compact latent heat store, comprising from 62% to 77% of the total system thermal storage capacity from 40 to 65°C depending on the dwelling type (values presented in table 6.3), would be connected with the heat emitter cold loop and the mains, to maintain the highest thermal stratification possible, as seen in figure 6.8.

The convective heat transfer coefficient of the heat emitters (equation 6.3) was determined during each time step by calculating the Rayleigh number (equation 6.1) and Nusselt coefficient for a vertical surface (equation 6.2) using the instantaneous emitter-ambient temperature difference, and considering a typical emitter height of 600mm [175]. The radiative heat transfer coefficient, assuming the heat emitter area much smaller than the walls of the building and a surface infrared emissivity of 0.9 [182], can be calculated according to equation 6.4 using also the instantaneous emitter-ambient temperature, from [161]. The emitter global heat transfer coefficient would be the sum of the 2 coefficients, seen in equation 6.5. The convective heat transfer coefficient is multiplied by 4 since convection occurs on the 2 sides of each heat emitting surface, considering a double panel convector radiator [175].

$$Ra_{(t)} = \frac{g \cdot \beta \cdot h_3 \cdot (T_{amb}(t) - T_{em}(t))}{\zeta^2} \cdot Pr_{air} \tag{6.1}$$

$$Nu_{Ra} = \left(0,825 + 0,387 \cdot \left(Ra\left(1 + \left(\frac{0,492}{Pr}\right)^{\frac{9}{16}}\right)^{-\frac{16}{9}}\right)^{\frac{1}{6}}\right)^{2} \tag{6.2}$$

$$h_{cv} = \frac{Nu \cdot \lambda_{air}}{L_{emitter}} \tag{6.3}$$

$$h_{rad} = \sigma \cdot \epsilon_{emitter} \cdot \left(T_{amb}^2 + T_{emitter}^2\right) \cdot \left(T_{amb} + T_{emitter}\right) \tag{6.4}$$

$$UA_{emitter} = A_{emitter} \cdot \left(4 \cdot h_{cv} + h_{rad}\right) \tag{6.5}$$

Figure 6.9a to 6.9e presents the balance equations for the 5 extra nodes added to the model to simulate the hot water tank volume (A and B), solar thermal collector volume (C) building heat emitters volume (D) and building indoor volume (E). The two balance nodes for the hot water tank were due to the reversibility of the water flow coming from the latent heat store. Stratification within the hot water tank is not considered due to the reduced size of the tank, as seen in figure 6.9a and 6.9b. In the buffer tank and packed bed systems, the hot water tank nodes are removed being replaced by the stratified thermal store, explained in the next section.

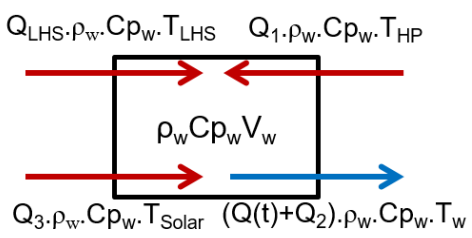

(a) hot water tank with solar

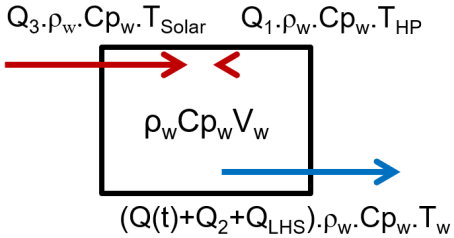

(b) hot water tank no solar

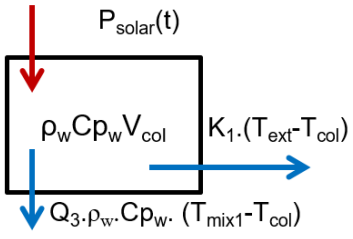

(c) solar thermal collector

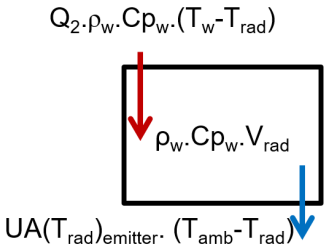

(d) heat emitters

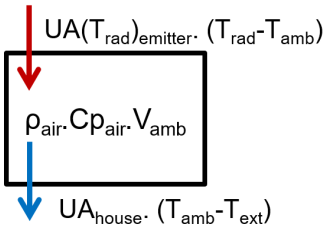

(e) indoor ambient

Figure 6.9: Nodal balance equations for the various components considered within the building model.

6.4.1 Daily carbon emissions

To calculate the daily carbon emissions associated with the heating system the grid CO_2 emissions used were those presented in figure 6.1. To determine the coefficient of performance (COP) of the heat pump, technical data sheets for Daikin Altherma V were used [29] with a 65°C outlet temperature assumed, the effect of defrost cycles was also included, as seen in figure 6.10.

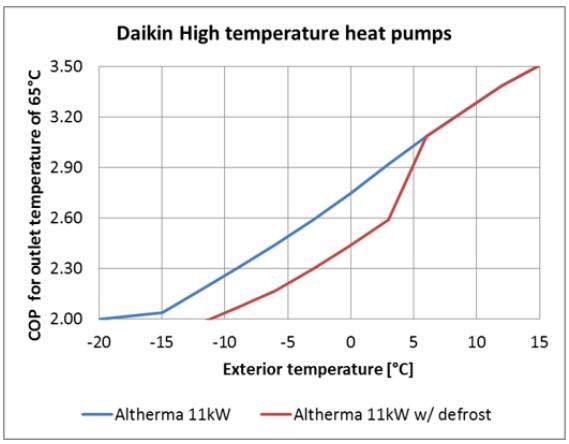

Figure 6.10: Daikin Altherma air-source heat pump COP dependency on ambient temperature, from [29].

6.4.2 Energy pricing

In order to perform an economic comparison, the gas and electricity (economy 10 [37]) prices were based on a price consultation made in January 2018 to SSE (Scottish and Southern Energy plc), presented in table below table 6.4.

Table 6.4: Energy tariffs used in the economic comparison.

Utility	Price $[£/kWh]$	Standing charge $[£/day]$
Gas	0.0372	0.148
Electricity	0.0846 (off peak price)	

6.5 The developed numerical models for domestic hot water and space heating

Two 2-dimensional finite volume models were developed in Matlab to simulate all the designed thermal energy storage systems: one for the compact latent heat stores and one for the buffer tank thermal stores (with a packed bed and without). The numerical models assumed that the thermal conductivity of the PCM was isotropic, and that no volume change occurred during phase change. To simulate the phase change of the selected PCM, heat capacity curves were experimentally determined as reported in Chapter 4.

The thermophysical properties of water (viscosity and density) used were also temperature dependent, due to its influence on convective heat transfer rates, since the Prandlt number of water varies considerably between 20°C and 70°C.

The packed bed in the simulation consisted of a specified number of horizontal layers each having a set number of spheres, illustrated in figure 6.11a. The spheres in each layer were considered to behave in the same way with identical temperatures; the model thus required that equations were solved for a single sphere in each row, as illustrated in figure 6.11b and 6.11c.

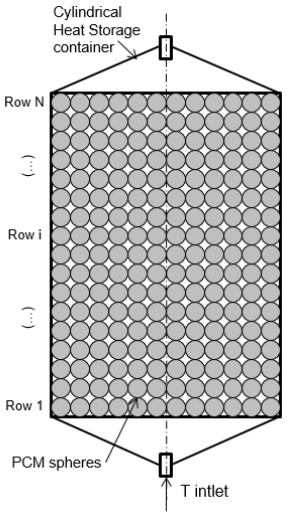

(a) longitudinal cross section

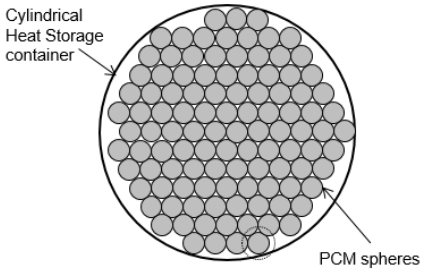

(b) transversal cross section

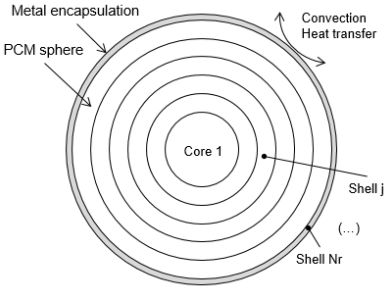

(c) PCM sphere discretization

Figure 6.11: Schematic representation of the packed bed model in longitudinal cross section, transversal cross section with possible arrangement of spheres and detailed view of the spatial divisions used within the sphere.

Charge and discharge of the container was obtained simulating a fluid flowing through the packed bed, exchanging heat by convection with the spheres. The HTF Reynolds number was calculated using equation 6.6, based on the void fraction between the spheres within the container (Ψ), and the flow length specified to be half of the cross sectional perimeter of an individual sphere. The convective heat transfer coefficient was determined using the method detailed by Wakao [183], where the average Nusselt Number is expressed in equation 6.7, and the convective heat transfer coefficient in equation 6.8.

$$Re_{\Psi} = \frac{2 \cdot \rho_{htf} \cdot \dot{Q} \cdot d_{sphere}}{\mu_{htf} \cdot D_{cont}^{2} \Psi_{htf}} \tag{6.6}$$

$$Nu = 2 + 1,1 \cdot (Re^{0,6} Pr^{0,33}) \tag{6.7}$$

$$h_{cv} = \frac{Nu \cdot \lambda_f}{D_{sphere}} \tag{6.8}$$

The compact tube-in-tube simulated comprised a long copper tube inserted into a rectangular PCM slab, as illustrated in figure 6.12a. To meet the required storage capacity, the model added numerous slabs in parallel connected through a bigger copper manifold pipe, distributing the water flow evenly throughout them, as seen in figure 6.12b. The model employed backward spatial discretization for the water flow in the HTF, and unidirectional radial and axial heat propagation within the copper tube and PCM, as presented schematically in figure 6.12c and 6.12d.

The heat loss of the container to the ambient was included at the last PCM node adjacent to the outer surface, and was determined using the insulation properties specified for the container (insulation thickness, type and ambient temperature) and divided by the number of axial nodes and strings meaning that the total heat loss of the compact thermal store would be shared in each axial section of each individual PCM slab.

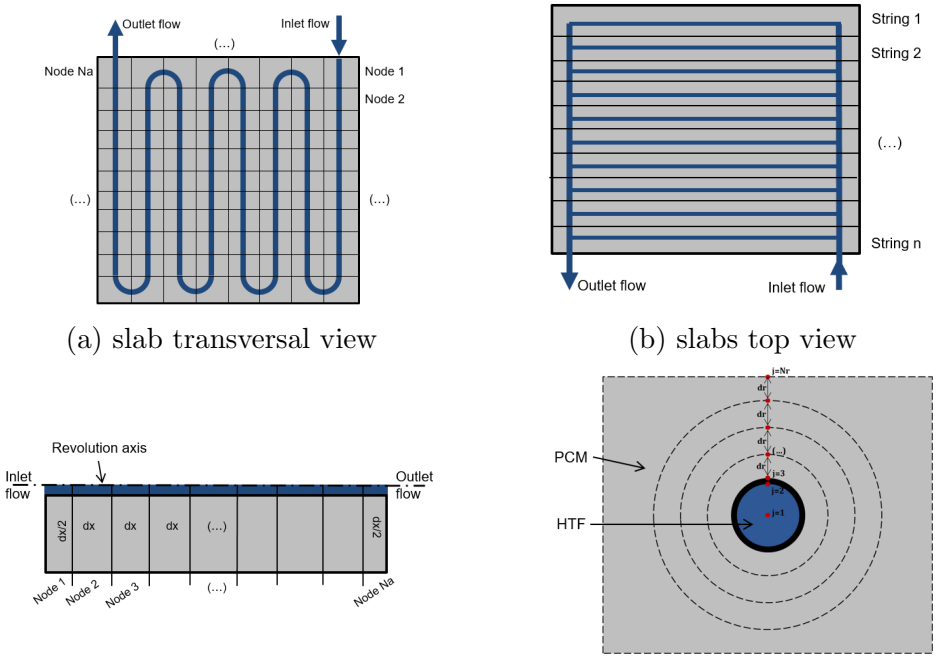

(a) slab transversal view

(b) slabs top view

(c) longitudinal discretization

(d) transversal discretization

Figure 6.12: Transversal representation of the copper tube disposition within a PCM slab, top view of the parallel of slabs in each module representation of the axial driscretization for each tube and transversal discretization in each node.

The Heat Transfer Fluid (HTF) Reynolds number was calculated using equation 6.9, for pipe flow. For laminar flows, the average Nusselt Number was obtained considering a constant wall temperature, according to the correlation of Martin [161], expressed in equation 6.10. For fully turbulent flows, with a Reynolds number above 10000, Nusselt numbers were obtained with the correlation put forward by Gnielinski [161], expressed in equation 6.13. For transitional flows, a linear interpolation according to the Reynolds number (equation 6.11) between the laminar (equation 6.12) and turbulent regimes was adopted.

$$Re = \frac{4 \cdot \rho_{htf} \cdot \dot{Q}}{\pi \cdot \mu_{htf} \cdot d_{tube}^2} \tag{6.9}$$

$$Nu_{trans} = f \cdot Nu_{lam,2300} + (1 - f) \cdot Nu_{turb,10000} \tag{6.10}$$

$$f = \frac{Re - 2300}{7700} \tag{6.11}$$

$$Nu_{lam} = \sqrt[3]{3,66 + 0,7^3 + \left(1,615\sqrt[3]{Re \cdot Pr \cdot \frac{d_{tube}}{l_{tube}}} - 0,7\right)^3 + \left(\left(\frac{2}{1 + 22 \cdot Pr}\right)^{\frac{1}{6}} \sqrt{Re \cdot Pr \cdot \frac{d_{tube}}{l_{tube}}}\right)^3} \tag{6.12}$$

$$Nu_{turb} = \frac{0,124 \cdot \zeta \cdot Re \cdot Pr}{1 + 12,7\sqrt{0,125 \cdot \zeta} \cdot \left(Pr^{\frac{2}{3}} - 1\right)} \left(1 + \left(\frac{d_{tube}}{l_{tube}}\right)^{\frac{2}{3}}\right) \tag{6.13}$$

The developed numerical model calculated new mass and transport matrices at each time step to enable the transient accounting for changes in heat capacity (phase change) and thermal conductivity of the PCM. The spatial discretization seen in figure 6.12c and 6.12d employed 9 radial nodes and 40 axial nodes giving a modelled cylinder height to thickness ratio between 125 and 170.

6.5.1 Packed bed model verification

Tanvir [30] studied a packed bed with 770 capsules containing the PCM sodium nitrate [119]. The latent heat store was charged and discharged with air 20°C above and below the PCM melting point respectively. A schematic view of their rig configuration is presented in figure 6.13a and 6.13b. The system could store a total of $1.05 kWh_{th}$ between 286°C and 326°C. Air heaters were used to maintain the charge and discharge temperatures at the required levels. The system performance was recorded by measuring the temperature throughout the experiment at 4 rows of thermocouples spaced 50.8mm axially and 25.4mm radially, as illustrated in figure 6.13b.

For representation purposes, only the modelled row 1 (at 50.8mm) and row 4 (at 203.2mm) were presented in figure 6.14.

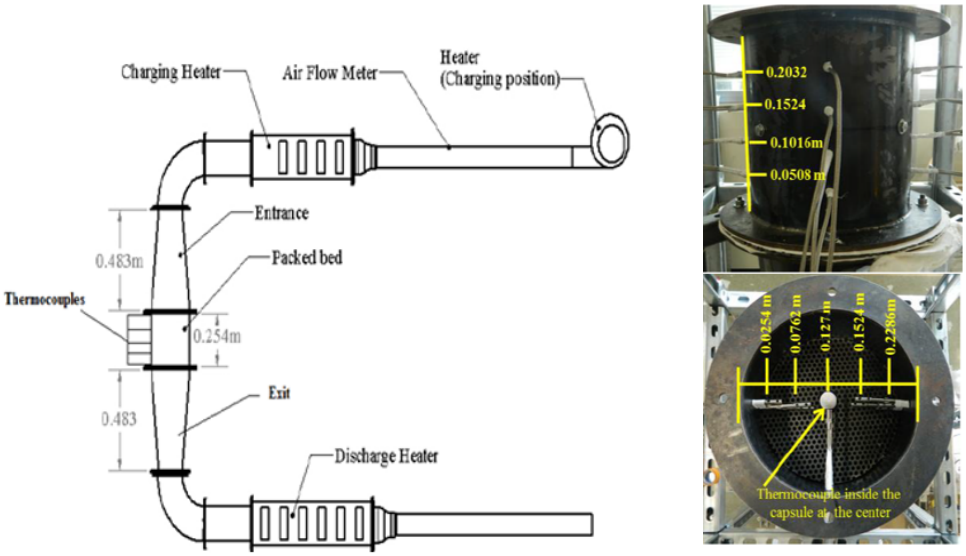

(a) experimental rig

(b) thermocouples disposition

Figure 6.13: Schematic representation of the experimental rig used and diagram of thermocouple radial and axial locations in the packed bed by Tanvir [30].

The packed bed store was formed from a 254mm length of a 114.3mm diameter carbon steel tube insulated with flexible insulation 152mm thick. The key system properties are presented in table 6.5.

Table 6.5: Store dimensions and heat transfer fluid flow properties for the experiments made by Tanvir [30].

Bed height $[mm]$	254
Bed Diameter $[mm]$	254
Total Volume of packed bed $[m^3]$	0.01287
Bed Porosity	0.35
Insulation thickness $[mm]$	152
$\lambda_{insulation}$ $[W/m.K]$	0.1
HTF:	
Flow rate $[m^3/s]$	0.0419
Reynolds Number (Re)	1293 - 1171
Prandlt (Number)	0.77
Nusselt Number (Nu)	52.3 – 49.6
Convection HT coefficient (h_{cv}) $[W/m^2.K]$	86 - 87

The model predictions using the developed Matlab model and experimental results presented by Tanvir et al. [30] are presented in figure 6.14. The predictions from the developed model are in good agreement with both the experimentally measured air and PCM temperature profiles. The abrupt temperature changes at 0 and 225 minutes are due to the higher temperature differential between the HTF inlet and the store temperatures, leading to surge in the heat transfer rate of the container, as it can be seen in figure 6.15.

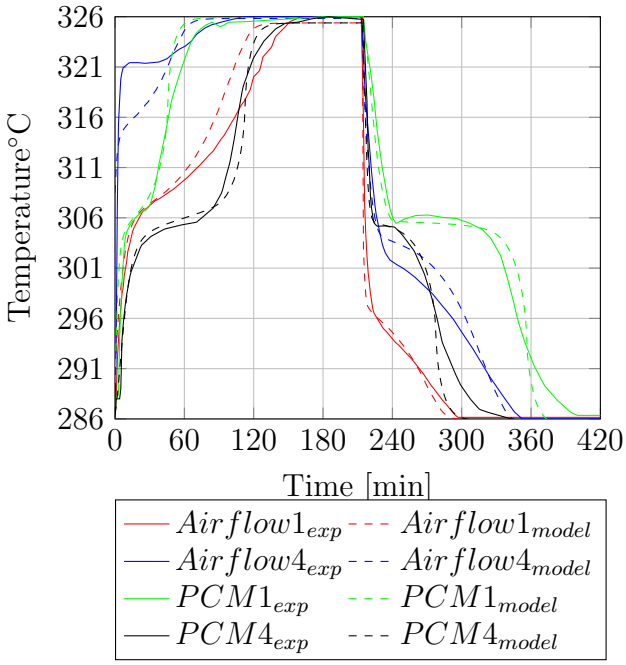

Figure 6.14: Experimentally measured [30] and model predicted values of air flow and PCM temperatures at rows 1 and 4 within the thermal store.

The slight discrepancies observed during both charging and discharging processes may be due to some geometrical irregularities within the experimental packed bed resulting from the molten PCM, leading to an uneven air flow distribution among the packed bed of spheres [30].

The predicted values for power input/output and stored energy are presented in figure 6.15. Of the $1.05kWh_{th}$ transferred to the store, only $0.98kWh_{th}$ were effectively discharged, with $0.07kWh_{th}$ lost through heat losses to ambient.

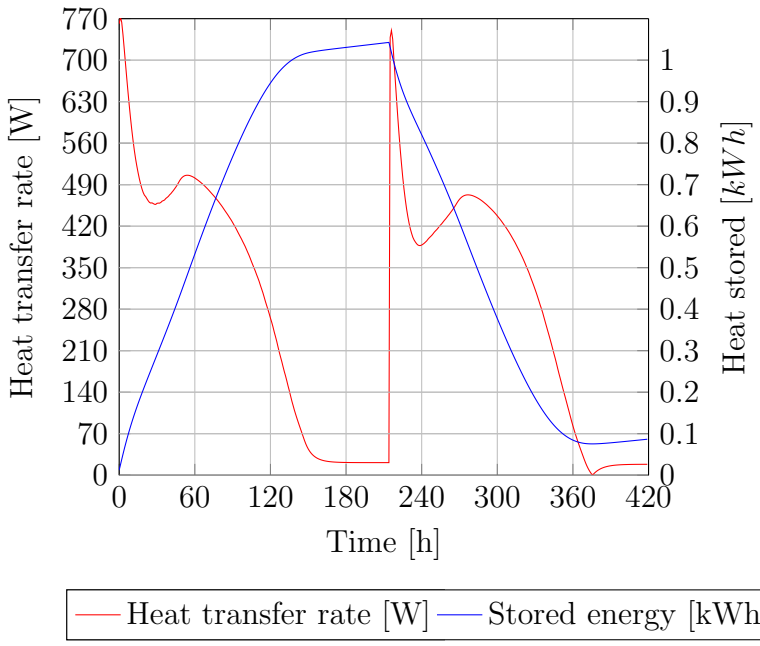

Figure 6.15: Predictions of the heat transfer input/output rates and energy stored within the PCM packed bed storage system.

6.5.2 Compact model verification

A compact latent heat storage module was developed to investigate the performance of PCMs in a rectangular container. The rectangular container was made from 3mm aluminum sheet bolted to four 37mm aluminum C profiles. A 15mm copper pipe heat exchanger was inserted within the container to exchange heat between the water flow and the PCM. The copper pipe comprised of 39 U-bends soldered to 511mm straight tube sections. Copper metal fins were soldered to the tube outer surface to improve heat transfer to the PCM to provide the charge illustrated in figure 6.16a and 6.16b. A simplified view of the experimental gravity–fed water test rig is presented in figure 6.16a.

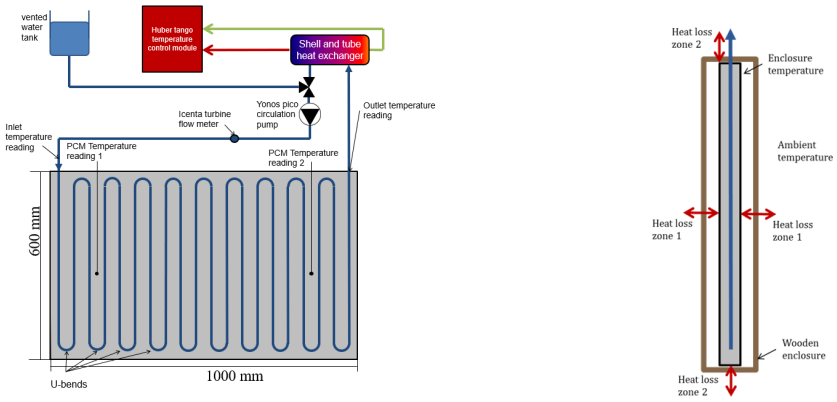

(a) experimental rig assembled (b) PCM slab section view

Figure 6.16: A schematic diagram of the experimental test rig used with the disposition of the thermocouples employed and simplified diagram demonstrating the heat balances of the thermal store tested.

The rectangular storage contained 18.3L of RT44HC [20], theoretically able to store $1.39kWh_{th}$ when heated/cycled from 20 to 70°C. The thermal store key dimensions and main characteristics are presented in table 6.6. Water was used as the heat transfer fluid, while the PCM filled the remaining volume around the tube within the rectangular container. The PCM rectangular container was inserted within a wooden enclosure 12mm thick MDF board (thermal conductivity of 0.101W/m.K) with 20mm air gaps between the container sides and the PCM rectangular enclosure. Adding 5 copper fins spaced 32mm apart soldered transversally to the copper pipe increased the total heat transfer area within the PCM by 52%.

Table 6.6: Thermal store key dimensions, heat transfer fluid flow and storage material properties for the experimental work performed.

PCM store width $[mm]$	600	Number of fins	5
PCM store length $[mm]$	950	PCM fraction [%]	89
PCM store thickness $[mm]$	37	Specific HT area $[m^2/m^3_{PCM}]$	48
Coil length $[m]$	12	Charging/Discharging error $[+-\%]$	2.37/2.55
Tube OD (ID) $[mm]$	15.86 (12.45)		
Store volume $[m3^3]$	0	PCM (RT44HC)	
PCM volume $[m^3]$	0	Hsl (37-46°C) $[kWh/m^3]$	50
		Cps (20-37°C) $[kWh/m^3.K]$	0.469+0.0045*T
HTF(average values):		Cpl (46-70°C) $[kWh/m^3.K]$	0.368+0.0027*T
Flow rate $[g/s]$	143	λ_s (20-37°C) $[W/m.K]$	0.450-0.00096*T
Re	25 504	λ_l (46-70°C) $[W/m.K]$	0.188-0.00036*T
Pr	4	β $[1/K] \times 10^{-4}$	8
Nu	155	ζ $[m^2/s] \times 10^{-6}$	9
h_{cv} $[W/m^2.K]$	7399	Pr	150-1.333*T

A Huber Unistat Tango was used to indirectly exchange heat with the gravity-fed water loop, using a programmable proportional-integral-derivative (PID) controller to maintain the set point temperature at constant values during the store charging and discharging. Thermocouples were fixed at the HTF inlet and outlet of the thermal store. The PCM temperature was monitored using thermocouples located at the 2 positions illustrated in figure 6.16a, and the flow rate was monitored by a turbine flow meter from Icenta, its signal converted to current and recorded in a compact DAQ card from National Instruments. The uncertainty of the turbine flowmeter reading is +-0.15% quoted in the supplier data sheet and the thermocouples uncertainty was already determined and reported in Chapter 5 (+-0.01°C).

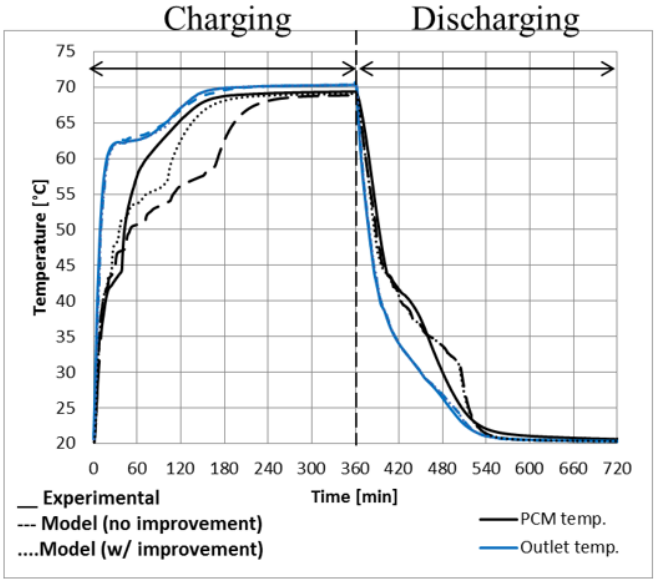

Figure 6.17: Comparison between experimental and predicted measurements for the inlet/outlet water temperatures and PCM store temperature.

The experiment was carried out in two modes: charging and discharging; and the data presented in figure 6.17 and figure 6.18 refers only to the 5^{th} cycle. In the charging mode, the initial state of the PCM was solid at room temperature of

20.3°C. The HTF was heated to the required temperature by the Huber tango heat exchanger and pumped through the copper pipe. The charging was completed when all the PCM in the tank had melted fully and its temperature stabilized around 70°C and temperature readings were taken every minute. In the discharging mode, the HTF temperature was reduced to 20°C and temperature readings continued until the PCM temperature had stabilized around 20°C. Figure 6.17 presents the experimental temperature measurements and model predictions obtained for the water flow inlet/outlet and PCM store during the charging and discharging processes. The PCM had fully melted at 180 minutes, as can be seen in figure 6.17.

Figure 6.18 presents the experimental measurements and model predictions for the heat transfer rates and stored energy. The heat transfer rate was constant at around 800W between t=30 and t=80 minutes during charging. During the discharge a lower rate of around 700W occurred between t=360 and t=460 minutes. In the model, neglecting buoyancy driven convection currents in the molten PCM led to a slower change in temperature the charging cycle, as shown in figure 6.18. This led to a lower charging rate and consequently less energy charged.

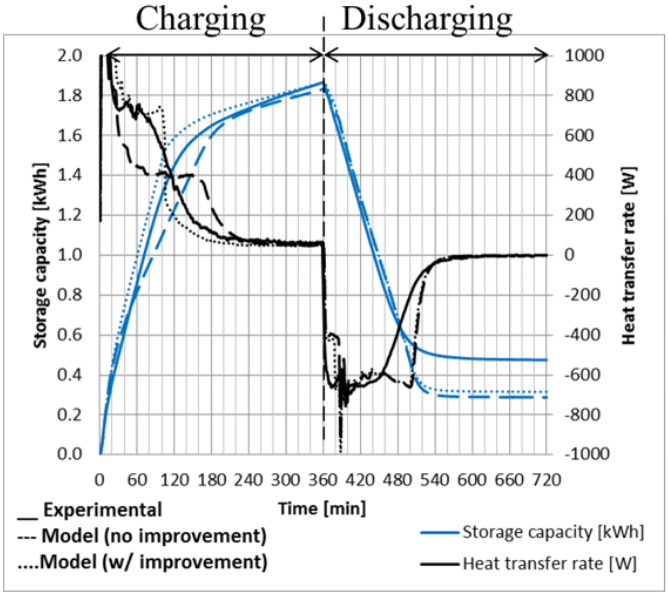

Figure 6.18: Experimental measurements and model predicted profiles of the thermal store for the heat transfer rate and storage capacity.

To improve the model accuracy for the melting process, an equivalent thermal conductivity increase to account for convection in the molten PCM was calculated based on the Rayleigh number of the temperature difference between the melting point of the PCM and the actual temperature of the PCM, expressed in equation 6.14.

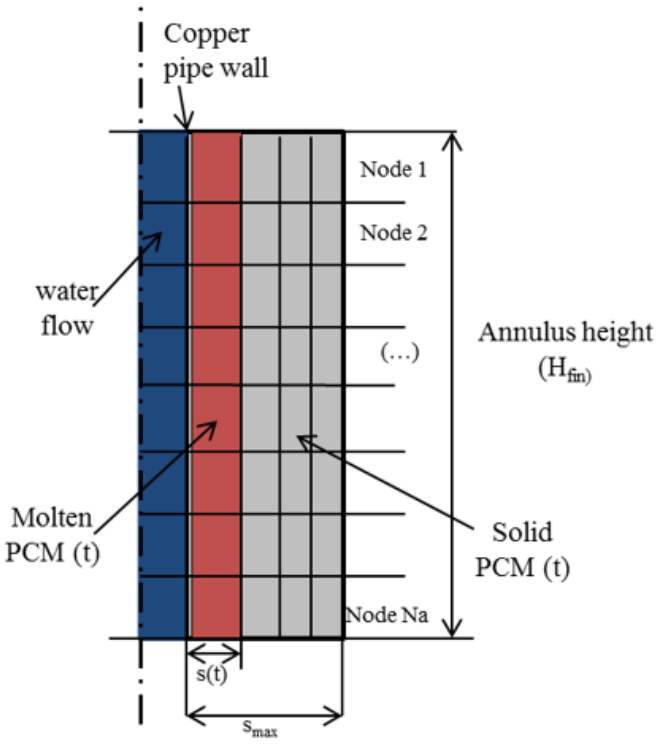

Figure 6.19: Schematic diagram of the discretization between the transversal fins used to enhance thermal conductivity within the PCM.

Based on [161], the Nusselt number was then calculated using correlations for free convection on a vertical annulus [161], displayed in equation 6.15, and applied to each PCM node. The annulus height (H_{fin}) considered was the spacing between fins and the annulus thickness (s) varied according to the fraction of molten PCM.

$$Ra_{i,j} = \frac{g \cdot \beta \cdot s_{i,j}^3 \cdot (T_{i,j} - T_m}{\zeta^2} \cdot Pr_{i,j} \tag{6.14}$$

$$Nu_{Ra_{i,j}} = \frac{0,49 \cdot Ra_{i,j} \cdot \left(\frac{H_{fin}}{s_{i,j}}\right)^2}{862 \cdot \left(\frac{H_{fin}}{s_{i,j}}\right)^4 \cdot \left(\frac{r_{tube}}{H_{fin}}\right) + \left(Ra_{i,j}\left(\frac{H_{fin}}{s_{i,j}}\right)^3\right)^{0.95} \cdot \left(\frac{r_{tube}}{H_{fin}}\right)^{0.8}} \cdot Pr_{i,j} \tag{6.15}$$

It can be seen from figure 6.17 and 6.18 that conductivity enhancement in the PCM led to a more accurate prediction of the melting process of the PCM, predicting the water flow outlet temperature more accurately when compared with the experimental measurements.

Observing the discharge profiles of figure 6.18, it can be seen that the conductivity enhancement in the PCM has negligible effect on the water flow inlet/outlet temperature difference, mainly because convection in the melt is suppressed during the freezing process, and both model predictions agree with the experimental results.

6.6 Simulation results

Using the building parameters, climate data and cumulative domestic hot water consumption profiles (space heating consumption is presented by the heat emitters temperature variation) from the high-resolution stochastic integrated domestic demand model developed by McKenna and Thomson [176, 31], a daily simulation was performed for each dwelling in Matlab, presented in figure 6.20, to be used as the reference case (with gas boiler).

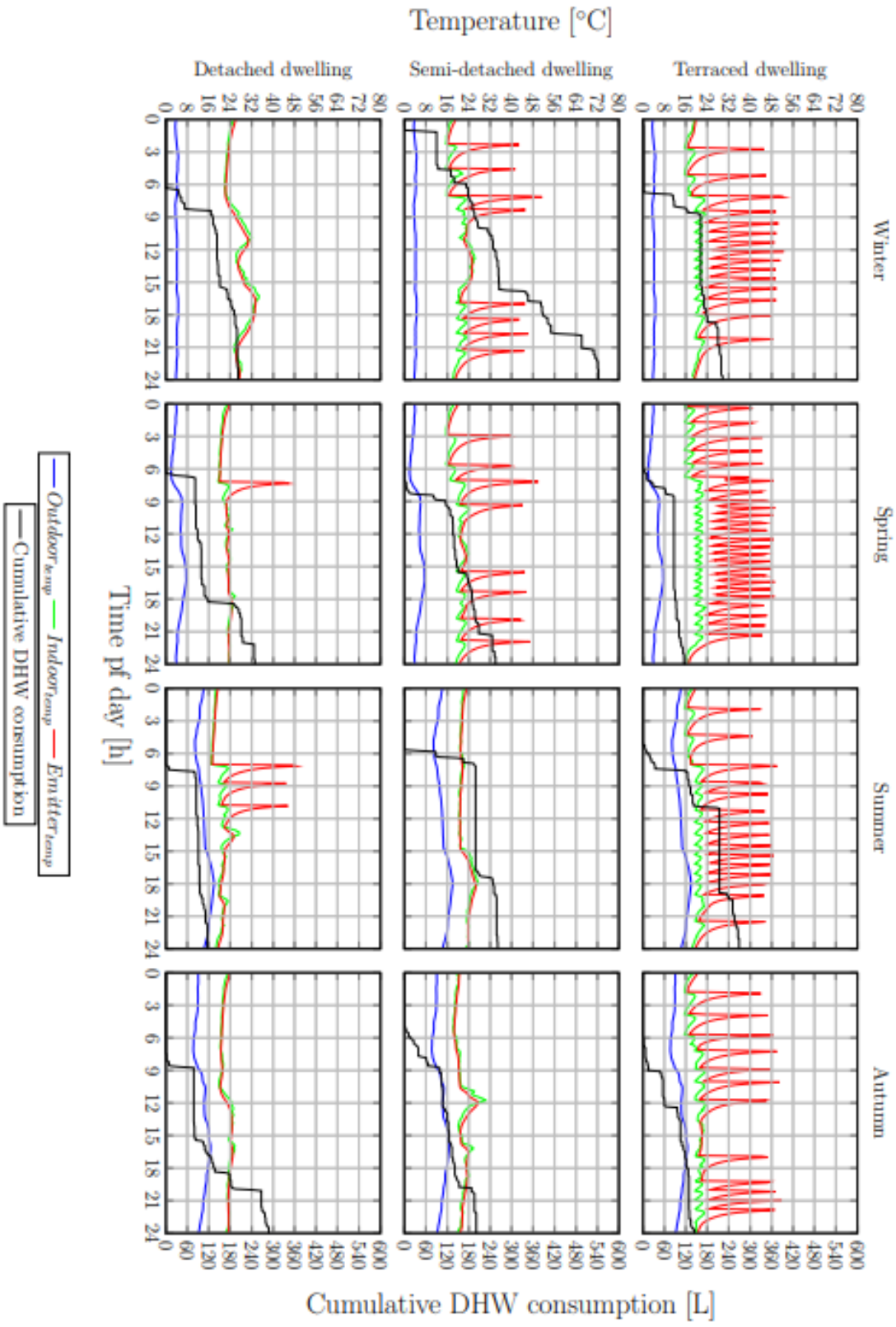

Figure 6.20: Daily model predictions for the reference case using a conventional gas boiler for each dwelling in each season, data from [31].

It can be seen from figure 6.20 that the space heating systems of all buildings modelled were more active during winter and spring months. To meet the highest

8h of space and water heating (from 05.00to 13.00) the energy consumption data obtained from the simulation predictions for the reference case were analyzed for each day and the maximum demand in each dwelling in this time interval are underlined in table 6.7. The reason for the larger daily heat use in the semi-detached dwelling is due to the higher domestic hot water consumption considered in the winter season, as seen in figure 6.20.

Table 6.7: Maximum daily heat use in each building on the studied intervals.

Household	Terraced	Semi-detached	Detached	Units
Total energy use	31.43	51.92	45.45	kWh
Used from 0.01 to 05.00	0.62	9.25	4.43	
Used from 05.01 to 13.00	15.6	20.44	15.57	
Used from 13.01 to 16.00	2.92	7.12	10.32	
Used from 16.01 to 24.00	12.29	15.11	15.13	

Solar thermal collectors were added to each dwelling to compare which system would have a better use of its solar thermal energy. The terraced dwelling was simulated with one solar collector; the semi-detached and detached dwellings were simulated with two solar flat plate collectors, all empirically selected. A fluid circulation of 2l/min and an absorber area of $2m^2$ were assumed for each collector, with an optical efficiency ($\tau\alpha$) of 78% of 0.78 and an heat loss U value of $4.87W/m^2.K$, from [31].

6.6.1 Air source heat pump with a water buffer tank

Estimating an overcapacity of 20% to cope with consumption peaks, table 6.8 presents the geometrical properties of the buffer tank system simulated in each dwelling, integrated according to figure 6.6. To obtain a cyclic temperature evolution characteristic of the chosen design day, each daily simulation modelled the same design day three times (in order to reach nominal performance parameters).

Table 6.8: Water buffer tank geometrical properties and storage capacities for each simulated hot water and space heating system.

Household	Terraced	Semi-detached	Detached	Units
Storage capacity	18.725	24.532	18.679	kWh
Tank height	1 956	2 140	1 955	mm
Tank diameter	652	713	652	
Water volume	0.653	0.856	0.652	m^3
H/D ratio	3			

Figure 6.21 presents the simulation results of each dwelling for the packed bed tank storage system; it can be seen that the tank effectively uses its thermal stratification to meet the dwelling heat demands whilst maintaining an outlet temperature nearly constant. To estimate yearly economical savings, economy 10 electricity tariffs [37] were compared with the conventional gas boiler system. Table 6.9 presents the simulation seasonal and yearly results for the heat pump and solar use, the kg CO_2 emitted in each season and their subsequent yearly reduction compared to the

gas boiler system. It can be seen that the yearly saving are around 70-73%. The predicted reduction in carbon emissions based on the current grid emission values [3, 25] for the heat pump systems with buffer tank was 48% for the terraced, 54% for the semi-detached and 52% for the detached dwelling, compared to the conventional boiler system, as presented in table 6.9.

Table 6.9: Calculated seasonal results for heat pump and solar thermal consumption and yearly CO_2 emissions reductions and savings for the buffer tank system.

Dwelling	Season	Heat pump	Solar collector	CO_2 emissions	Year reductions	
		$[kWh]$		$[kgCO_2]$	$[CO_2]$	Energy
					[%]	
Terraced	Winter	971	5	369	48	70
	Spring	662	100	230		
	Summer	320	90	99		
	Autumn	343	182	113		
Semi-detached	Winter	1315	60	495	54	73
	Spring	939	810	317		
	Summer	254	221	75		
	Autumn	298	191	107		
Detached	Winter	1286	484	758	52	71
	Spring	626	212	377		
	Summer	319	90	90		
	Autumn	306	86	86		

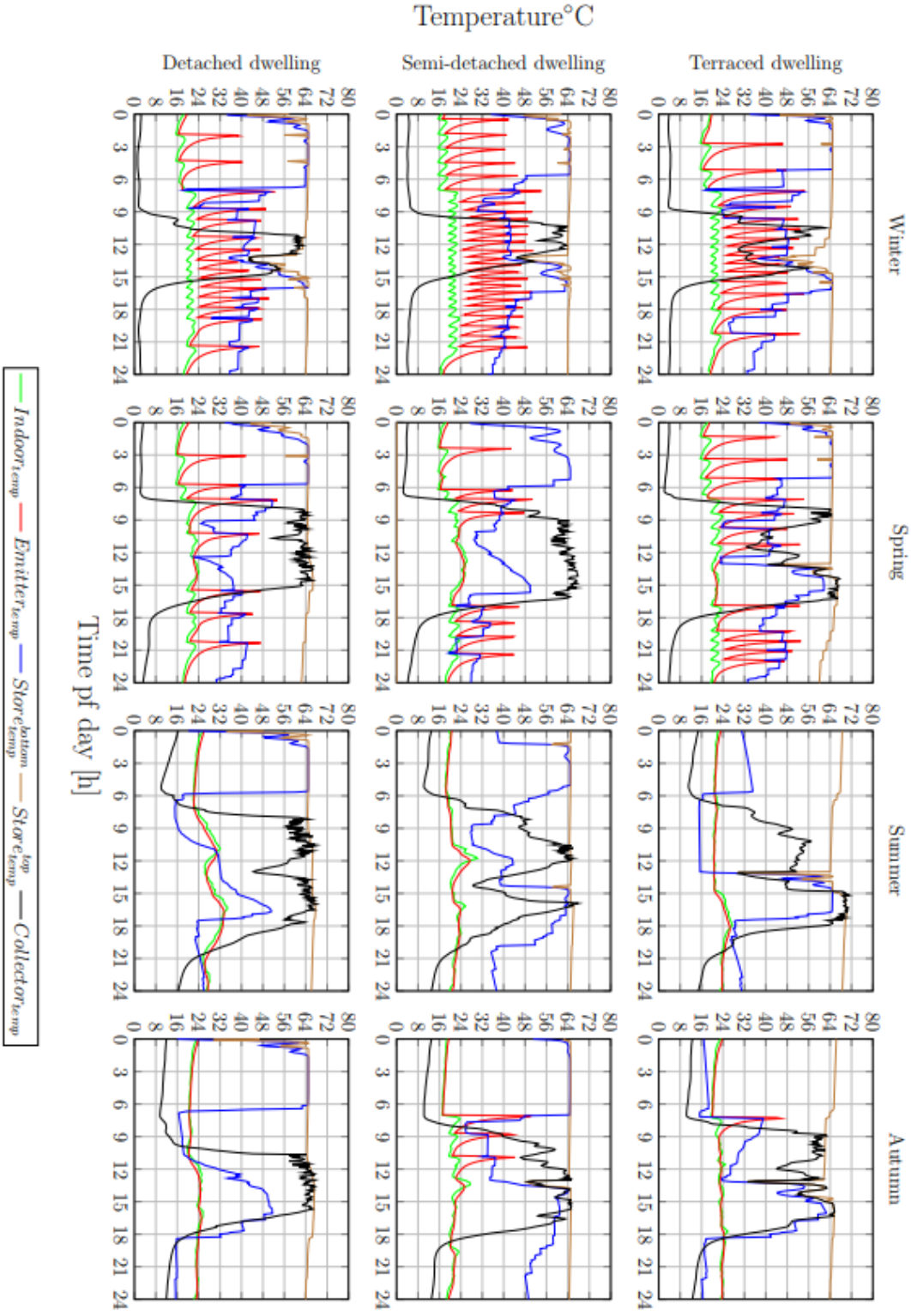

Figure 6.21: Modelled daily simulation results for all dwellings in each season using an air source heat pump with a water buffer tank.

The temperature oscillation of the solar thermal collector is due to the binary operation of the circulation pump and the intermittent behaviour of incident solar radiation.

6.6.2 Air source heat pump with a PCM packed bed buffer tank

With the eutectic mixture of magnesium nitrate hexahydrate and magnesium chloride hexahydrate (specs detailed in table 6.2) occupying around 50% of the thermal store volume, the thermal energy storage capacity was nearly doubled, when compared to the same store volume using only water, between 40 and 65°C, due to the increased heat capacity of the PCM between 56 and 62°C, as shown in figure 6.4. That lead to more compact buffer tanks, compared to the water-based tank, as presented in table 6.10. For comparison purposes, the packed bed buffer tank had the same thermal storage capacity and H/D ratio than the water buffer tank.

Table 6.10: Packed bed container properties used in the numerical model.

Household	Terraced	Semi-detached	Detached	Units
Storage capacity	18.72	24.53	18.68	kWh
Tank height	1 595	1 742	1 594	mm
Tank diameter	532	581	531	
Tank volume	0.354	0.461	0.353	m^3
N spheres	2577			
Sphere outer diameter	53.2	58.1	53.1	mm
Sphere thickness	1			
H/D ratio	3			
Overcapacity	20			%
Sphere volumetric fraction	42.7			

Table 6.11 presents the general heat transfer characteristics of the latent heat stores. The Reynolds number and convective heat transfer coefficient are presented for the minimum and maximum flows used, 2 and 20L/min respectively. The heat transfer fluid flow is laminar for all stores. It can be seen by reducing the spheres diameter, the flow Reynolds number increases, consequently increasing the convective heat transfer coefficient.

Table 6.11: Heat transfer characteristics for all packed bed latent heat storage systems modelled.

Household	Terraced	Semi-detached	Detached	Units
Heat transfer area	22.88	27.29	22.85	m^2
Specific HT area	127	115	127	m^2/m^3
Thermal storage capacity to same volume water buffer tank	1.84	1.85	1.84	kWh/kWh
Reynolds Number HTF flow	37-352	32-322	35-352	
HTF hcv	240-692	168-602	192-693	$W/m^2.K$
Storage capacity [40 to 65° C]	18.73	24.53	18.68	kWh
PCM heat storage capacity	14.1	18.54	14.06	
Water + encapsulant sensible heat storage capacity	4.63	5.99	4.62	
λ insulation	0.036			W/m.K
t insulation	80			mm

The predicted temperatures obtained from simulations using the developed numerical model for the packed bed systems are presented in figure 6.22. The modelling results demonstrate that the water tanks temperatures converged to the PCM melting point whenever there was no heat consumption from the dwelling.

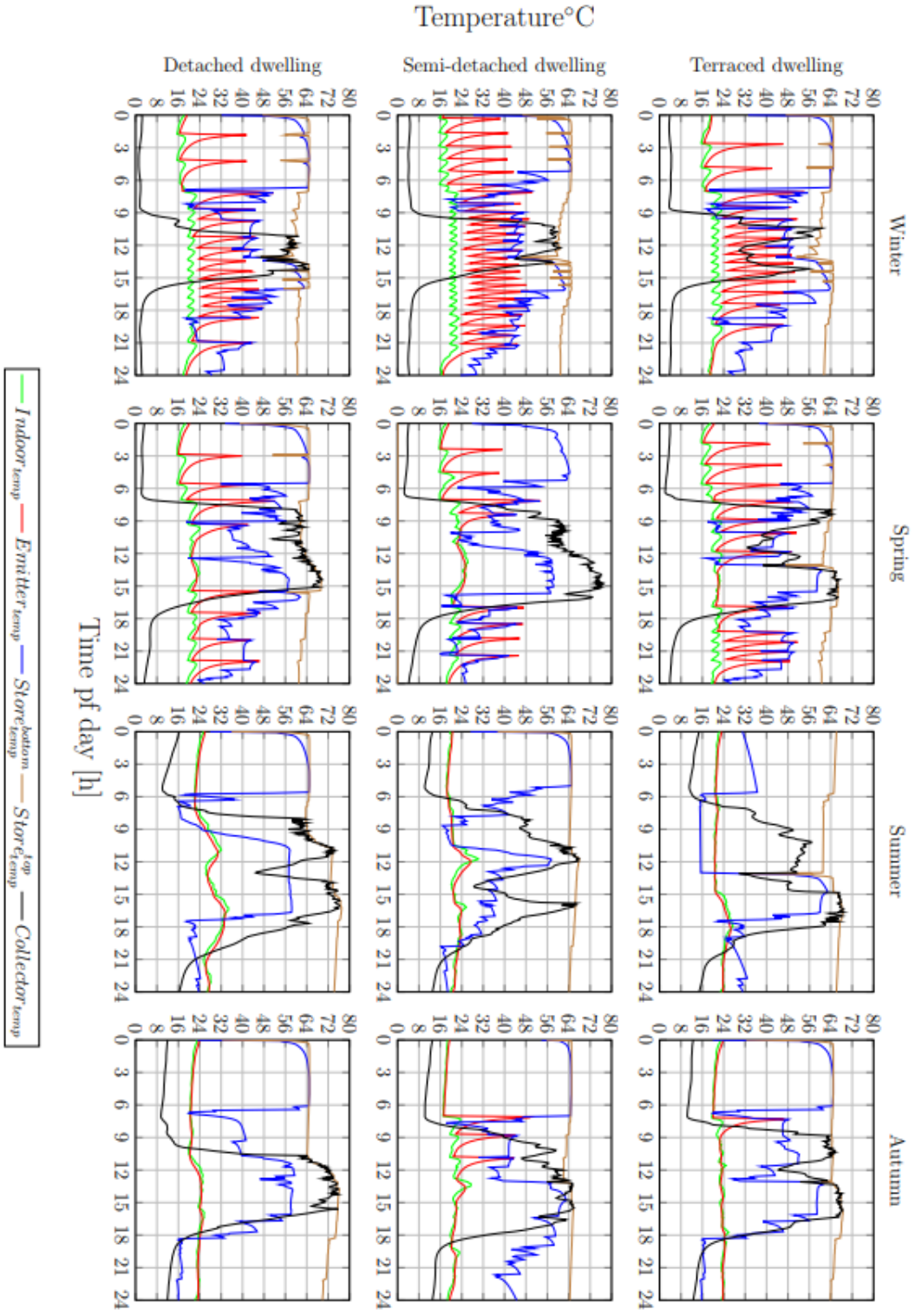

Figure 6.22: Predicted temperatures obtained using the numerical model developed with the packed bed latent heat storage system for all dwellings.

The predictions also demonstrate that the higher thermal capacity around 60°C of the PCM, allows the packed bed latent heat store to provide heat for two 8h periods (from 05.00 to 13.00 and from 16.00 to 24.00) of space heating, successfully offsetting the heat pump operation to economy 10 low tariff periods.

The predicted reduction in carbon emissions based on the current grid emission values [19], [20] for the heat pump systems with stores was higher in all dwellings when compared to the water buffer tank, as can be seen in table 6.12.

Table 6.12: Calculated seasonal results for heat pump and solar thermal consumption and yearly CO_2 emissions reductions and savings for the packed bed buffer tank.

Dwelling	Season	Heat pump	Solar collector	CO_2 emissions	Year reductions	
					CO_2	Energy
		$[kWh]$		$[kgCO_2]$	[%]	
Terraced	Winter	941	5	356	50	71
	Spring	691	98	239		
	Summer	296	95	91		
	Autumn	325	159	94		
Semi-detached	Winter	1303	64	490	53	74
	Spring	943	767	318		
	Summer	219	218	62		
	Autumn	263	184	148		
Detached	Winter	1244	150	467	53	72
	Spring	675	581	231		
	Summer	309	652	87		
	Autumn	252	421	71		

The obtained energy savings and CO_2 emissions reduction for the packed bed latent heat store were better than the buffer tank results. That was due to the lower outlet temperature of the thermal store allowing better solar fraction, and the tank temperatures convergence on the PCM melting point. The storage tank temperatures had temperature rises when no heat flow was passing through the store due to the thermal lag caused by the PCM spheres.

6.6.3 Air source heat pump with a PCM compact module next to small buffer tank

Using a compact latent heat store next to a small buffer tank lead to higher energy savings compared to the packed bed heat storage system. The full system had higher PCM volumetric ratios for the terraced and semi-detached storage containers and lower for the detached container due to the smaller size of the thermal store and the same 210L buffer tank used in the semi-detached dwelling, as seen in table 6.13. The PCM volumetric fractions of the compact thermal store without the buffer tank are higher than the packed bed thermal store, hence its reduced dimensions.

Table 6.13: Compact thermal energy storage system properties used in the numerical model.

Household	Terraced	Semi-detached	Detached	Units
Storage capacity	18.72	24.53	18.68	kWh
Container height	609	609	574	mm
Container width	855			
Container length	405	495	360	
Container volume	0.211	0.258	0.177	m^3
DHW tank volume	0.125	0.21		
Number of PCM units	9	11	8	
Tube length per unit	10.62	10.62	9.98	m
Tube outer Diameter	15.875			mm
Tube thickness	1.245			
Overcapacity	20			%
PCM volumetric fraction	55.2	48.4	40	

Comparing its heat transfer characteristics with the packed bed heat storage system, it has lower specific heat transfer area (even with the fins used to increase heat transfer area), mainly due to the higher storage density of the module, and higher convective heat transfer coefficients due to the pipe flow regime with turbulent Reynolds numbers.

Table 6.14: Heat transfer characteristics for all compact latent heat storage systems modelled.

Household	Terraced	Semi-detached	Detached	Units
Heat transfer area	7.16	8.75	6.147	m^2
Specific HT area	38.63	38.63	39.72	m^2/m^3
To water buffer tank	1.94	1.83	1.69	kWh/kWh
Reynolds Number HTF flow	651-6510	533-5330	733-7329	
HTF hcv	305-2332	288-1898	323-2050	$W/m^2.K$
Storage capacity [40 to 65°C]	18.72	24.53	18.68	kWh
PCM heat storage capacity	14.46	17.67	12.08	
Sensible heat storage capacity	4.26	6.86	6.6	
λ Insulation	0.036			W/m.K
t insulation	80			mm

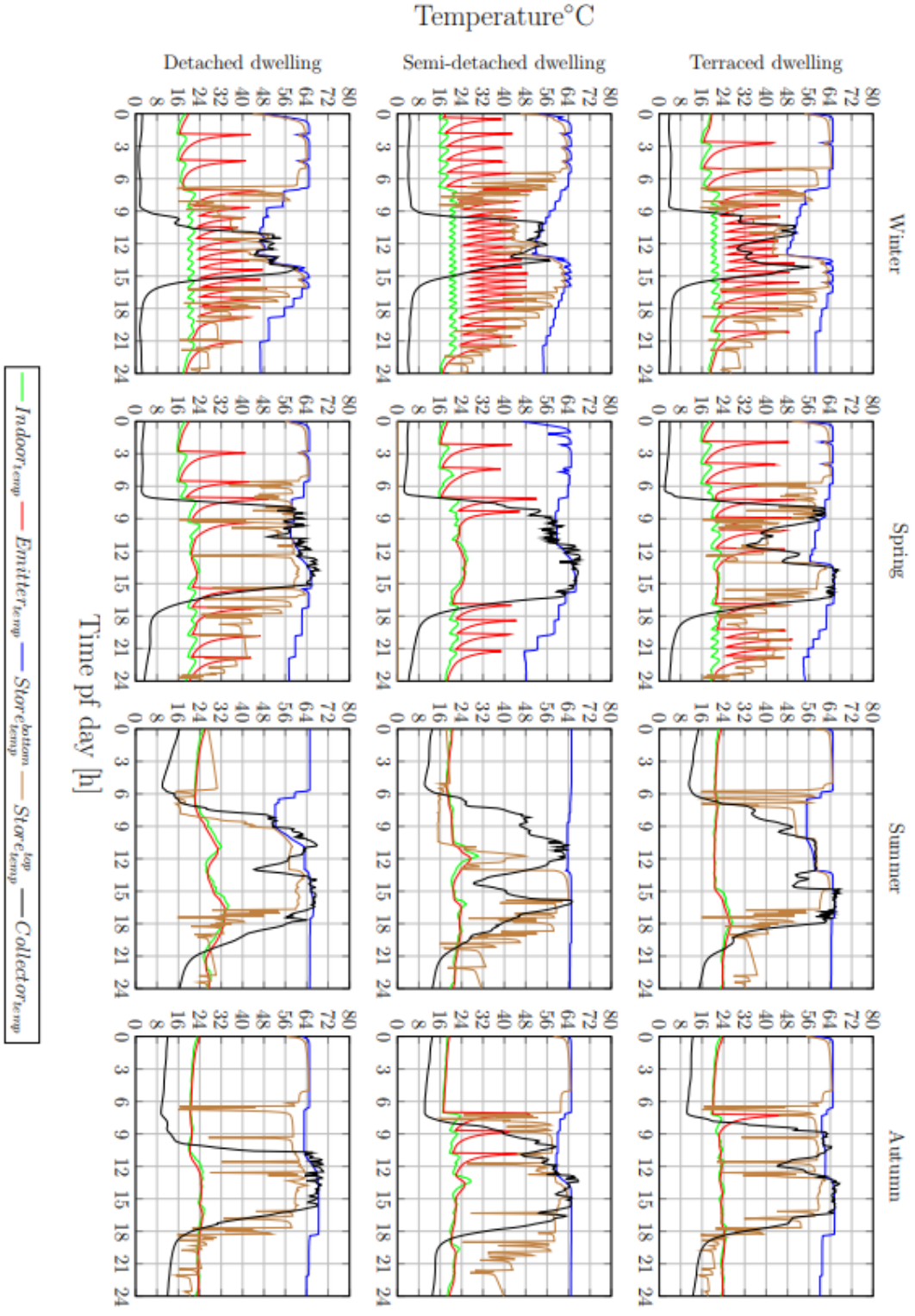

Figure 6.23: Predicted temperatures obtained from the numerical model simulating the compact latent heat storage for all dwellings.

The calculated yearly energy savings and CO_2 reduction were better than the results for the packed bed storage system mainly due to the lower outlet temperature of the buffer tank. That may be due to the larger volumetric fraction of the compact thermal store itself, allowing a larger thermal gradient to develop between the fluid

flow and the PCM, hence bigger temperature recoveries when the thermal store is idle.

Table 6.15: Calculated seasonal results for heat pump and solar thermal consumption and yearly CO_2 emissions reductions and savings for the compact latent heat store with smaller buffer tank.

Dwelling	Season	Heat pump	Solar collector	CO_2 emissions	Year reductions	
					CO_2	Energy
		$[kWh]$		$[kgCO_2]$	[%]	
Terraced	Winter	895	12	336	55	73
	Spring	624	99	215		
	Summer	272	76	80		
	Autumn	266	165	77		
Semi-detached	Winter	1269	86	472	57	75
	Spring	906	816	306		
	Summer	201	228	62		
	Autumn	268	183	81		
Detached	Winter	1229	176	456	61	78
	Spring	495	592	171		
	Summer	79	728	25		
	Autumn	172	448	48		

6.7 Economic comparison of all modelled systems

To estimate a simple payback period for a 20-year life cycle, an assessment of likely costs was made for all the required components and installation costs of the proposed systems. In terms of the heat source, table 6.16 presents the capital difference cost of installing an air-source heat pump unit with solar thermal collectors unit compared to a conventional gas boiler unit. Based on the studies performed by Najera [184], installation costs were considered 10% of the initial capital expense (CAPEX) and yearly operation and maintenance 2% of the initial CAPEX.

Table 6.16: Heating system price description by component for the 3 modelled dwellings, and total difference to a gas combi boiler system.

Prices	Component	Terraced	Semi-detached | Detached	Ref.
Solar thermal system [£]	Thermasol (TS8001) panel	300	600	[185]
	Grundfos UPS pump	89	110	[186]
	Solar control box	164		[187]
	Hydraulics (tubing+valves+filters)	150	225	[188]
	Total solar thermal system	703	1099	-
Air-source heat pump [£]	11kW Outdoor Unit (ERSQ011AV1)	2472		[29]
	11kW Hydrobox (EKHBRD011ACV1)	2985		
Combi-boiler [£]	Worcester combi boilers	996	1098	[172]
Cost difference between ASHP + solar thermal to gas boiler [£]		5164	5458	-

Table 6.17 presents a general comparison of the thermal storage costs of each modelled system. For the buffer tank pricing, a correlation based on the buffer tank water volume (in liters) was adopted by Nájera [184] was used, presented in equation 6.16.

$$C_{vol}(V) = 3E^{-8} \cdot V^3 - 4E^{-4} \cdot V^2 + 2,312 \cdot V[£]; \tag{6.16}$$

Packed bed spherical enclosures were considered to be mass produced similar to the production of polyethylene ice bags, where the molten PCM would be injected in a large polyethylene bag and a hot metal mould heat seal the plastic enclosure, producing small PCM spheres.

The compact latent heat storage system presents the lowest CAPEX, mainly due to the estimated cost of the buffer tanks. the copper tube was considered to cost $3.491£/m$ based on [188] and the tube bending was assumed to be mass produced at a cost of $1.115£/U - turn$. The packed bed heat storage system has a lower CAPEX than the buffer tank due to the cost reduction obtained by reducing the buffer tank size.

Table 6.17: Estimated storage system prices for each modelled dwelling.

Component costs [£]		Terraced	Semi-detached	Detached	Reference
Gas boiler (reference) CAPEX		996	1099		[172]
ASHP + buffer tank	ASHP + solar thermal	6160	6556		-
	Buffer tank	1348 (653L)	1705 (856L)	1346 (652L)	[184]
	CAPEX	8259	9087	8692	-
ASHP + Packed bed buffer tank	ASHP + solar thermal	6160	6556		-
	Buffer tank	770 (354L)	984 (461L)	768 (353L)	[184]
	Spherical enclosures	215			[189]
	PCM	18 (181L)	24 (238L)	18 (180L)	[177, 190]
	CAPEX	7879	8556	8312	-
ASHP + buffer tank + Compact heat storage	ASHP + solar thermal	6160	6556		-
	Buffer tank	283 (125L)	468 (210L)		[184]
	U turns	181 (162)	221 (198)	161 (144)	[188]
	Copper tube	334 (95.58m)	408 (116.82m)	279 (79.84m)	
	Soldering	46.1 (3.3h)	54.5 (3.9h)	100.6 (7.2h)	[191]
	PCM	18 (185L)	22 (227L)	15 (155L)	[177, 190]
	CAPEX	7724	8503	8338	-

Table 6.18 presents the levelized cost of heat (LCOH) for each system according to dwelling size. Equation 6.17 presents the procedure used to determine, for a lifetime of 20 years [170] and an interest rate (the "r" variable in equation 6.17) of 3.5%, the LCOH for each system (assuming a "zero-risk" investment), based on Andrew [170].

$$LCOH = \frac{\frac{CAPEX \cdot r}{1-(1+r)^{-n}} + OPEX + Q_{used} + E_{tariff}}{Heat_p roduced} \cdot 1000 \left[\frac{£}{kWh}\right] \tag{6.17}$$

Table 6.18 presents a comparison between all the systems studied in regards to their yearly operational expenses, fuel consumption and levelized cost of heat (LCOH). The LCOH for all storage systems reduces with increasing storage capacity; the compact thermal storage systems offer the lowest values of the 3 storage systems studied. The buffer tank presents the highest CAPEX of the storage systems studied; its LCOH is still higher than the other two storage systems due to its lower energy savings. Gas boilers at current gas prices are still the most economical option, however they match the LCOH of the studied compact systems if a carbon tax of $11£/ton$ is added to the fuel price, a value below that estimated by Brink [192] of around $17£/ton$ for 2016.

Table 6.18: Detailed OPEX and fuel consumption prices and LCOH for each system modelled.

Component		Terraced	Semi-detached	Detached
OPEX /Fuel $[£/year]$	Gas boiler system	36/341	31/445	31/384
	ASHP + Buffer tank system	150/249	165/293	158/269
	ASHP + Buffer tank packed bed system	143/245	156/286	151/265
	ASHP + Buffer tank + compact system	140/229	155/279	152/222
Yearly heat used $[kWh/year]$		6 559	8 942	7 546
LCOH $[£/MWh]$	Gas boiler system	70.99	66.87	71.14
	ASHP + Buffer tank system	149.45	122.69	137.69
	ASHP + Buffer tank packed bed system	143.77	116.7	132.6
	ASHP + Buffer tank + compact system	139.15	115.37	127.25

Assuming the $11£/tonCO_2$ applied to current natural gas boilers, the payback period and total return on investment (ROI) were calculated for the replacement of current natural gas heating system in each dwelling using equation 6.18 and 6.19. The calculated savings are the difference in fuel consumption costs between the reference gas boiler and the studied system.

$$ROI = \frac{Savings_{year} - OPEX - \frac{CAPEX \cdot r}{1-(1+r)^{-n}}}{\frac{CAPEX \cdot r}{1-(1+r)^{-n}} + OPEX + Q_{used} \cdot E_{tariff}} \tag{6.18}$$

$$\frac{CAPEX \cdot r}{1-(1+r)^{-n_{payback}}} = Savings_{year} - OPEX - Q_{used} \cdot E_{tariff} \tag{6.19}$$

Table 6.19 presents the ROI and payback period for all systems studied. From the analysis made, compact latent heat storage systems offer the lowest payback periods and a higher return on investment for a 20-year period for all dwellings. The values between brackets on table 6.19 represent the required CAPEX reduction to obtain an average ROI of 60% for all dwellings in each storage system. The value chosen was assuming the investment would meet the annual inflation rate of 3% over 20 years.

Table 6.19: ROI for the 20-year life cycle and projected payback period for each system, assuming a replacement for the gas boiler system used as reference.

	Component	Terraced	Semi-detached	Detached
Total ROI [%]∗	Buffer tank system (41%)	33.5	89.9	59.8
	Packed bed system (35%)	32.5	92.0	58.1
	Compact system (31%)	35.2	86.0	62.6
Payback $[years]$	Buffer tank system	24.6	14.9	18.9
	Packed bed system	21.6	13.1	16.9
	Compact system	19.5	12.7	15.1

∗ values in parenthesis correspond to the CAPEX discount applied to the whole system

6.8 Conclusions from the integration of phase change materials into domestic water heating systems

Thermal stores including phase change materials have the potential to store larger amounts of thermal energy within smaller temperature ranges when compared to water-based thermal stores. Due to the low thermal conductivity of many PCMs, poor rates of thermal diffusion within the PCM can reduce significantly the nominal storage system charge and discharge heat transfer rates.

Due to the versatility in store geometry possible with encapsulated packed bed systems they appear to be a feasible option for integrating PCMs into conventional domestic space heating systems. Inserting the PCM filled spheres into standard water buffer tanks can be achieved without major technical challenges. The lower PCM volume fraction achievable when compared to more compact store designs such as the tube in tube, can limit the increase in heat storage capacity; however, the increase in specific heat transfer area reduces the effect of having low thermal conductivity.

The numerical models developed to evaluate the replacement of conventional gas fired boilers with heat pumps coupled with a PCM thermal store to offset heat pump operation from peak electrical demand periods, predicted that CO_2 emissions for all the three dwelling studied could be reduced yearly by 51.8% using a packed bed of PCM spheres and 57.3% using the compact latent heat store with current grid emission values, as shown in table 6.20.

Table 6.20: Comparison of the results obtained for all the systems studied.

	Yearly energy used $[kWh/year]$			Yearly CO_2 emitted $[kgCO_2/year]$			Average energy savings [%]	Average CO_2 savings [%]
	Terraced	Semi detached	Detached	Terraced	Semi detached	Detached		
Reference	7717	10520	8878	1574	2146	1811		
Buffer tank system	2305	2819	2546	763	1153	939	71.5	51.2
Packed bed system	2262	2741	2489	385	606	496	72.2	51.8
Compact system	2066	2656	1985	212	346	304	74.8	57.3

Economically, the integration of PCMs into domestic hot water systems is a costly solution, using current energy prices, the best levelized cost of heat obtained with the compact latent heat storage system was $127.77£/MWh$. A carbon tax added to current natural gas consumption of $11£/tonCO_2$ is required to make the levelized cost of energy supplied using natural gas equal to that using the compact latent heat storage system, assuming a 20 years life cycle, this value is still less than the assumed $17£/tonCO_2$ by the UK government for 2016. If 31% of the initial capital expense is supported by the government, replacing current gas boilers with air source heat pumps with a compact latent heat store had an average return on investment for a 20-year cycle around 60% for all the dwellings modelled.

Shifting domestic hot water and space heating loads into off peak periods of the national grid by using compact thermal energy storage systems will allow further integration of heat pumps, so that its use does not adversely affect the electrical supply system.

Chapter 7

The potential of phase change energy storage to integrate industrial waste heat into district heating networks

District heating (DH) systems are comprised of insulated piping networks which deliver heat via steam or hot water to serve the space and water heating demands of multiple buildings [28]. They are generally seen as a convenient, economic and environmental-friendly way to supply heat to a large amount of buildings.

While the technical components of DH are relatively mature [193], their integration into the UK's space and water heating market is somewhat unsuccessful (around 2%, compared to 47% in Denmark and 55% in Sweden in 2012 [28]).

There are two main limitations to significantly scale up DH installations in the UK. First, while DH is an inherently local infrastructure, it is competing in a liberal and private market, where the main players international scope challenges the development of locally-specific systems [193]. Secondly, shifts in the role of local government, from service provision to enabling others to provide services led to an increase in public and private service providers, reducing the in-house capabilities of local authorities to plan, design and operate technically and financially viable schemes [193].

Integrating industrial waste heat into a district heating network can offer the possibility to provide cost effective hot water and space heating, improving also the industrial process efficiency, although the process industry heat source distance to the DH network often minimizes available heat and economic gains due to increased piping heat losses and costs. Phase change materials could improve the economic feasibility of such systems by providing a portable thermal storage solution, charged with industrial process waste heat and discharged to nearby DH networks.

7.1 Overview of the district heating networks in the UK

There are 81 district heating schemes implemented in the UK as of the end of 2016 according to [194]. In practical terms, a DH network should operate between 58-

82°C [195], in order to obtain relatively low flows, hence minimizing the district heating pipe cross section and its heat losses. A brief description of some of those schemes will be made in the next paragraphs.

7.1.1 Aberdeen heat and power Ltd.

Aberdeen heat and power ltd. was created in 2002 by the Aberdeen city council to develop Combined Heat and Power (CHP) schemes for the city to investigate the potential cost reductions in providing communal heat and reduce the council CO_2 emissions. It has four projects running (Seaton, Hazlehead, Stockethill and Tillydrone).

In Seaton, a gas engine sells $2.1MW_e$ to the electrical grid whilst providing $7MW_{th}$ (backed up by a gas boiler) to a district heating network composed of 14 multi-storey blocks consisting of 1243 flats, 5 public buildings and a swimming pool.

The second project installed was the Hazlehead energy centre, with a CHP producing $212kW_e$ and distributing $350kW_{th}$ to four multi-storey blocks comprising 209 flats, a sheltered housing scheme, Hazlehead academy, public swimming pool and sports pavilion. Due to the different heat profiles of the public buildings and the blocks of flats, the CHP can run throughout the year.

Stockethill energy centre has 2 steam boilers producing steam to a $212kW_e$ steam generator and distributing $300kW_{th}$ to 4 blocks with a total of 268 flats. Due to the load being only domestic flats, the steam generators do not operate 24/7 due to the heat profiles of the domestic users. The site has been extended to provide heat to 4 more blocks comprising 350 flats and a bigger generator is being installed.

7.1.2 Thameswey Energy Ltd.

Thameswey energy Ltd was created in 1999 by Woking borough council, part of the Greater London urban area. The company developed a joint venture with a Danish company to develop a CHP with DH network unit in Woking and one in Milton Keynes.

Woking CHP unit comprises a Deutz DK-TBG620 V16K gas engine providing $1.4MW_e$ and $1.4MW_{th}$ and 2 backup gas boilers with $1.5MW_{th}$ capacity, providing district heating to 2000 residential buildings and 170 commercial offices.

Milton Keynes CHP unit comprises two GE Jenbacher J624 gas engines that provide $3.2MW_e$ and $3MW_{th}$ each, and a $10MW_{th}$ backup gas boiler to supply district heating to nearly 3000 residential buildings and over 1100 commercial offices.

7.1.3 Birmingham Distric Energy Company Ltd.

In 2006, the Birmingham city council developed a partnership agreement with the energy services company ENGIE, to construct a CPH with district heating network under a 25-year "concession contract".

Birmingham district heating network comprises 3 individual schemes: Broad street scheme, Aston University and Birmingham children's Hospital. The broad street scheme comprises one CHP unit with a capacity of $3.6MW_e$ and $3.5MW_{th}$, backed up by a gas boiler with $11.8MW_{th}$ of capacity. It provides district heating to 5 public buildings, one hotel and to Cambridge and Crescent residential towers, with a total daily heat consumption of 55.6MWh.

The Eastside scheme, completed in 2009, has 2 gas engines in Aston University (one with $2.0MW_e$ and one with $1.0MW_e$) with a total electrical capacity of $3.0MW_e$ and a thermal capacity of $2.9MW_{th}$, backed up by a combined capacity of $14.3MW_{th}$ backup/top-up gas boilers (two with $3.5MW_{th}$ and one with $7.3MW_{th}$). A new energy centre was added to Birmingham children's hospital and connected to the East side heat network with a $1.6MW_e$ gas engine and two $4.5MW_{th}$ back up gas boilers. The heat network provides 4 public buildings (Aston University, Birmingham children's hospital, new Birmingham magistrate's court and Lancaster circus) and 3 clusters of buildings (Bagot street, Woodcock street and Masshouse block M), with a daily heat consumption of 54.8MWh The 2 heat networks were connected in 2015, with the addition of a new gas engine providing $1.6MW_e$ and $1.55MW_{th}$ in Birmingham new street station.

All of the example district heating networks briefly detailed in the paragraphs above are agnostic to the heat source being used; hence the indirect integration of industrial waste heat via a portable latent heat store could have some economic feasibility, and potentially avoid more CO_2 emissions by reducing the use of the backup gas boilers.

7.2 Industrial waste heat

UK industry represented 16.2% of the final energy consumption in the UK in 2016 ($23.6Mt_{oe}$), with almost 73% of its energy demand for heating purposes [3]. Most of the heat (66%, $11.37Mt_{oe}$) is used for low temperature processes (below 250°C), with medium temperature processes (between 250°C and 500°C) representing 5% and high temperature processes (above 500°C) representing 29% of the total energy used for heating purposes [196].

Within UK industry, six large sub-sectors constitute 67% of the total demand for heat and account for nearly 70% of greenhouse gas emissions from the sector, thus making them a natural focus for decarbonisation. Those industrial sub-sectors are: coke and petroleum products, food and drink, pulp and paper, basic metals, non-metallics and chemicals.

7.2.1 Coke and petroleum products

The oil refinery sector has been reducing its throughput since its 1997 peak of 97 million tonnes of crude oil. In 2012 it produced 69million tonnes of crude oil, an 8% drop compared to 2011. Around 80% of that production is petrol, diesel, jet fuel, gas oil and fuel oils.

This sub-sector, responsible for 30% of the UK's industrial CO_2 emissions, derives 75% of its energy input through firing of oil and gas, 20% from steam (derived also from oil and gas) and 5% from electricity. More than 67% of the energy input is rejected to cooling systems and therefore dissipated to the atmosphere.

The refineries tend to be heat integrated, using the high temperature process streams to pre-heat lower temperature streams before cool down. Table 7.1 presents the waste heat from the refining processes hot flue gases feasible for integration of PCM thermal energy storage for DH purposes. The total amount of waste heat from flue gases is around 31.7kWh per barrel of oil refined.

Portable thermal energy storage could potentially capture 38% of this energy source by reducing the flue gas temperature from 150°C to 100°C via a heat exchanger, charging a thermal store from 85 to 95°C.

Table 7.1: Waste flue gases form oil refineries that could be used in conjunction with portable heat storage systems.

Process Type	Unit Operation	Heat source medium	Heat supply flow [kWh/boe]	Source Temp. [$°C$]	Ref.
Distillation	Atmospheric distillation	Gas	3.3	150	[197]
	Vacuum distillation		0.9		
Coking	Delayed coking		2.7		
Cracking	Fluid catalytic cracking		7.3		
	Catalytic hydrocracking		14.3		
Combination	Catalytic reforming		3.2		

The six operational UK refineries have an average annual throughput of 12 million tonnes of oil, an estimated daily energy consumption of around 12 356 barrels of oil equivalent (boe) in each site [198]. The theoretical available waste heat from the flue gases of the atmospheric distillation, vacuum distillation and coking is around 85.25MWh/day in each site, each site having a potential of 32.8MWh/day that could be recovered by the use of an integrated portable thermal store discharged to a DH network system.

7.2.2 Food and drinks sector

The food and drinks sector presents a wide heterogeneity of processes and type of product output (sugar, beer, coffee, canned food, etc). The majority of energy used in the sector, around 75%, is for heating/cooking, baking, drying and evaporation processes. On average, more than 80% of the required heat is produced by CHP units, steam boilers and gas fired ovens.

Most of the on-site heat recovery measures such as economizers for the boilers and burners for the waste heat from fryers are available for deployment; however, due to the competitiveness of the sector, such efficiency measures are difficult to implement if the investment payback period is longer than one year. Nevertheless, their close proximity to urban areas could present opportunities for a portable latent heat storage unit, with the main waste heat sources presented in table 7.2.

Table 7.2: Industrial waste heat from the food and beverages sector that could be used in conjunction with portable heat storage systems.

Process Type	Unit Operation	Heat source medium	Heat supply flow [$kWh/kg_{endproduct}$]	Source Temp. [$°C$]	Ref.
Boilers	Atmospheric distillation	Flue gas	0.025	145	[199]
Baking	Delayed coking		0.018	170	
Drying	Fluid catalytic cracking	Hot air	0.035	125	

Of all the food industry sources of waste heat, sugar plants present the largest percentage of CO_2 emissions, due to the energy intensity of the distillation process. On average, a sugar production plant in the UK produces around 220 000 tonnes of sugar [28], with nearly $1.17kWh_{th}$ for each kg of sugar produced lost through flue gases exiting at 210°C [200].

Inserting an economizer in the tube stack to charge a thermal store could capture 31.5% of this waste heat, cooling the flue gas down to 150°C and charging a thermal store from 90 to 145°C. This would lead to a total of $222.1MWh_{th}$ of waste heat that could theoretically be retrieved by using thermal energy storage to transport heat and discharge to a DH network each day.

7.2.3 Pulp and paper sector

There are 51 pulp and paper mills operating in the UK [3], with the largest 10 sites representing 70% of the whole production. The sector has suffered a continuous decline over the past ten years; packaging materials (48%) and graphic papers (27%) form the vast majority of the sector. All the main processes operate near ambient temperature, with the exception of drying. The normal energy consumption per tonne of paper is around $1400kWh_{th}$ and $425kWh_e$.

There is some heat recovery commonly from the CHP condensates and steam boiler economizers, with limited scope for heat recovery around the wet processes prior to the paper dryers [206]. Table 7.3 presents the waste heat processes suitable to be recovered by thermal energy storage for DH networks in the sector.

Table 7.3: Industrial waste heat from the paper and pulp sector that could be used in conjunction with portable heat storage systems.

Process Type	Unit Operation	Heat source medium	Heat supply flow $[kWh/tonneofpaper]$	Source Temp. $[°C]$	Ref.
Air compressors	Vacuum production	Exhaust air	270	160	[196]

With a relatively small percentage (less than 10% of final energy demand in the sector, according to [196]) when compared to the waste heat from the drying process, the exhaust air from the compressors has an acceptable temperature to recover up to 41% of that waste heat, cooling the exhaust air of the compressors from 160 to 100°C. The annual paper production of 2015 was 3970 thousand tonnes of paper and paperboard. If the 10 largest production sites cover 70% of the total production, then an estimated daily output for each site can be determined to be around 205.6MWh of waste heat from the air compressors [201]. That would lead to 88.1MWh of available waste heat to be recovered for DH networks by cooling the exhaust air from 160 to 100°C.

7.2.4 Basic metals sector

The UK iron and steel sector can be divided into three sub-sectors: integrated (continuous process using blast furnaces), mini mills (batch-like process using electric arc furnaces) and others (comprising a large group of miscellaneous plants for annealing, re-rolling, etc.).

There are 3 integrated production sites that produced 7.5 million tonnes of crude steel in 2012. The blast furnace process blows hot air (at 900°C) from the furnace base and pours the iron ore, coke (previously carbonized from coal in a coke oven) and limestone from the top of the furnace.

Oxygen combustion from the hot air with coke producing carbon monoxide and heat removes the process oxygen from the iron ore. Then, the iron is melted, and the resulting liquid iron flows towards the basic oxygen vessel, previously charged with scrap steel. In that vessel, pressurized pure oxygen is blown, reacting with the remaining carbon, separating them from the metal and producing steel.

Table 7.4: Industrial waste heat from the steel and iron sector that could be used in conjunction with portable heat storage systems.

Process Type	Unit Operation	Heat source medium	Heat supply flow $[kWh/_{tonne of steel}]$	Source Temp. $[°C]$	Ref.
Coke ovens	Sensible heat removal	Gas	82	980	[198]
	Heat recovery from hot coke	Solid	62	800	
	Exhaust gas from blast stoves	Exhaust gas	58	200	
Blast furnaces	Heat recovery from hot slag	Solid	100	1300	
	Exhaust gas from blast stoves	Exhaust gas	82	250	
Basic Oxygen Furnaces	Heat recovery from hot off-gases	Gas	141	1700	
	Heat recovery from slag	Solid	6	1500	
Steel casting	Heat recovery from hot cast steel		352	1600	
Hot rolling	Heat recovery from hot rolled steel		1395	400	

Most of the wasted heat derived from the hot slag, hot cast and hot rolled steel is difficult to capture due to the technical barriers of directing their radiant heat to an active heat transfer device. In 2015, steel output from blast furnaces was 8.7 million tonnes and coke output from coke ovens was 2.7 million tonnes [202]. Recovering heat from processes with operational temperatures above 500°C presents some technical difficulties due to the special material requirements for the heat exchangers and the narrower selection of heat transfer fluids available (air or molten salts [203]).

Focusing on the most feasible waste heat sources, retrieving the exhaust gases from blast furnaces could generate 651.5MWh and from coke ovens 143MWh. By cooling the blast furnaces exhaust gas from 250 to 150°C and the coke ovens exhaust gas from 200 to 120°C would lead to a theoretical waste heat capacity of 283.3MWh and 63.6MWh/day, respectively.

7.2.5 Non-metallics sector

The non-metallics sector comprises two major energy users: glass and cement production sites. The UK glass industry has an annual throughput of around 4 million tonnes of glass, which can be divided into 3 different products: container flat and

domestic. Container glass such as bottles and jars accounts for 60% of UK glass production and is divided into 6 manufacturers. In the flat glass industry, 3 companies produce 32.5% of the total UK glass production.

Energy is a major consideration in the industry, representing one of the largest operational costs (36% of the gross value added). Nearly all the thermal energy is used in the melting/refining furnace. Waste heat is generally recovered from the firing process via regenerators, recovering nearly 50% of the heat from the process.

Waste heat available from furnace flue gases still has high exergetic value (316kWh per tonne of glass at 500°C), a temperature suitable for a Rankine steam power cycle. If used to charge a thermal energy storage system, it would have a theoretical 259.5MWh for each site to charge a thermal store from 90 to 145°C, cooling the flue gas from 500 to 150°C.

The UK cement sector consists of 11 production sites with a typical annual throughput of 10 million tonnes of cement. Cement production can be divided into 2 steps: clinker production and the grinding and mixing. Clinker is made in a rotary kiln at temperatures up to 1450°C, then it is ground with the other minerals (gypsum and limestone), to produce cement.

The typical cement kiln burns 50-55% coal and 35-40% of waste derived fuels (tires, sludge, bone meal, etc), and most of its CO_2 emissions are derived from the decomposition of Calcium carbonate (around 60%) [198]. Similar to the glass production sites, energy represents a huge portion of the operational costs, around 34% [19]. Main heat recovery tasks applied are using pre-heat chambers to pre-heat the raw material, although nearly 39% of the energy input is still wasted through the flue gases from the pre-heater and the pre-calciner ($417 kWh/_{tonofcement}$) at around 338°C.

By cooling that flue gas to 150°C, a theoretical 519.6MWh of waste heat could be used to charge a portable latent heat store from 85 to 145°C per production site each day via an economizer installed in the flue gases tube stack.

The ceramics industry is the last main production group in the non-metallics sector. Brick production consumes approximately half of the energy consumption in the ceramics industry. The firing process is the most energy intensive in the brick making process, usually using natural gas because of its clean burn characteristics and easier maintenance [198]. The drying process is the second largest energy user, although most of its heat is recovered from the firing kiln. A typical brick production site consumes around 694kWh of gas and 69kWh of electricity, wasting 228kWh in the flue gas from the kiln per tonne of brick made. The flue gas exit temperature is around 165°C. By cooling it down to 100°C, a theoretical 21.4MWh of waste heat could be captured by charging a thermal store from 85 to 95°C.

7.2.6 Chemicals sector

The chemicals industry comprises a variety of different products, from (in)organic bulk chemicals to small volume special products. It was the largest energy consuming industrial sub sector in 2016, responsible for 13% of the final industrial energy consumption [3]. Most chemical production facilities are already heavily heat-integrated, usually due to their close proximity with local urban areas, facilitating its integration into DH networks [198].

The UK chemical manufacturing is largely centred in the north of England and

due to the heterogeneity of the sector, the functional unit would have to be the energy input, as seen in table 7.5.

Table 7.5: Industrial waste heat from the chemical sector that could be used in conjunction with portable heat storage systems.

Process Type	Unit Operation	Heat source medium	Heat supply flow $[kWh/kWh_{input}]$	Source Temp. $[°C]$	Ref.
Curing	Processing Furnace exhaust	Exhaust gas	0.07	200	[198]
Cleaning/drying /heating	Boiler exhaust		0.08		

Due to the heterogeneity of the sector and its inherent heat integration philosophy into DH networks, portable thermal storage systems would not be used in the sector. Table 7.6 presents a compilation of the potential waste heat sources in the various industrial sectors detailed above. The focus is on flue gases from the various heat treatment processes, hence requiring the installation of an economizer on the exhaust gas outlet, prior to the chimney.

Table 7.6: Potential industrial waste heat sources that could be used in conjunction with portable latent heat storage systems.

Industry	Unit Operation	Daily heat supply capacity per site $[MWh/day]$	Source temperature band $[°C]$	Ref.
Refineries	Flue gases from the distillation and coking process	32.8	150-100	[199]
Sugar	Flue gases from the evaporator	222.1	210-145	
Pulp and paper	Exhaust air from vacuum pumps	88.1	160-100	[196]
Iron and steel	Exhaust gas from coke ovens	63.6	200-120	[198]
Iron and steel	Exhaust gas from blast furnaces	283.3	250-150	
Cement	Rotary kiln flue gases	519.6	338-150	
Glass	Furnace kiln flue gases	259.5	500-150	
Ceramics	Firing kiln flue gases	21.4	165-100	

7.3 Thermal storage system integration into a DH network

Typical district heating networks supply hot water to a set of public buildings as well as domestic clusters, usually designed in highly populated areas to maximize the heat sold and minimize circulation energy losses. To successfully integrate portable thermal energy storage system with DH it should operate at a higher temperature

band (between 200 and 90°C), providing useful heat to a DH water buffer tank indirectly through a heat exchanger.

The energy used with hot water and space heating in domestic and commercial buildings varies considerably throughout the year, with the heat consumption reaching its maximum during winter months and minimum during summer months, as seen in figure 7.1.

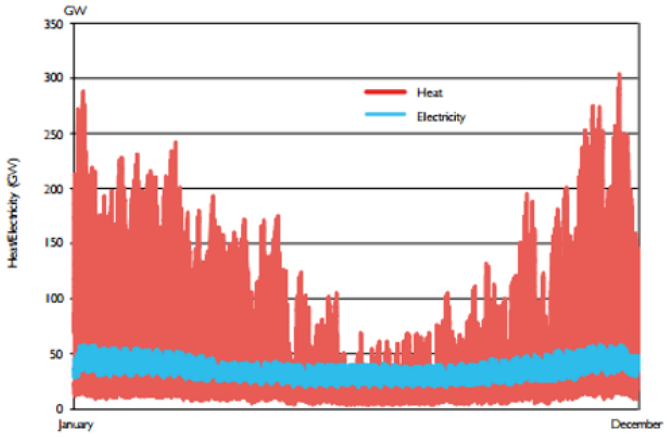

Figure 7.1: Half hourly variation of heat demand compared to the electrical demand for the domestic and commercial sectors in 2010, from [28].

Assuming that the average daily heat demand would follow a harmonic similar to the behaviour presented in figure 7.1, with its maximum values during the winter months and minimum values during the summer months, the estimated annual share of heat demand for each season is presented in table 7.7.

Table 7.7: Annual share of heat demand for each season in the UK.

	Nov-Jan	Feb-Apr	May-Jul	Aug-Oct
Annual share [%]	38.9	35.9	11.6	13.6

7.3.1 Integration of the portable latent heat store into the DH network

The indirect integration of a compact latent heat store should be made next to the water buffer tank, as seen schematically in figure 7.2. The thermal store would integrate the piping heat source of the system via a heat exchanger, charging the hot water buffer tank indirectly. The portable thermal storage system studied in this approach would comprise a set of 25-foot cargo containers being delivered constantly by road to the district heating network, further details of the whole system are reported in the economic comparison of this chapter.

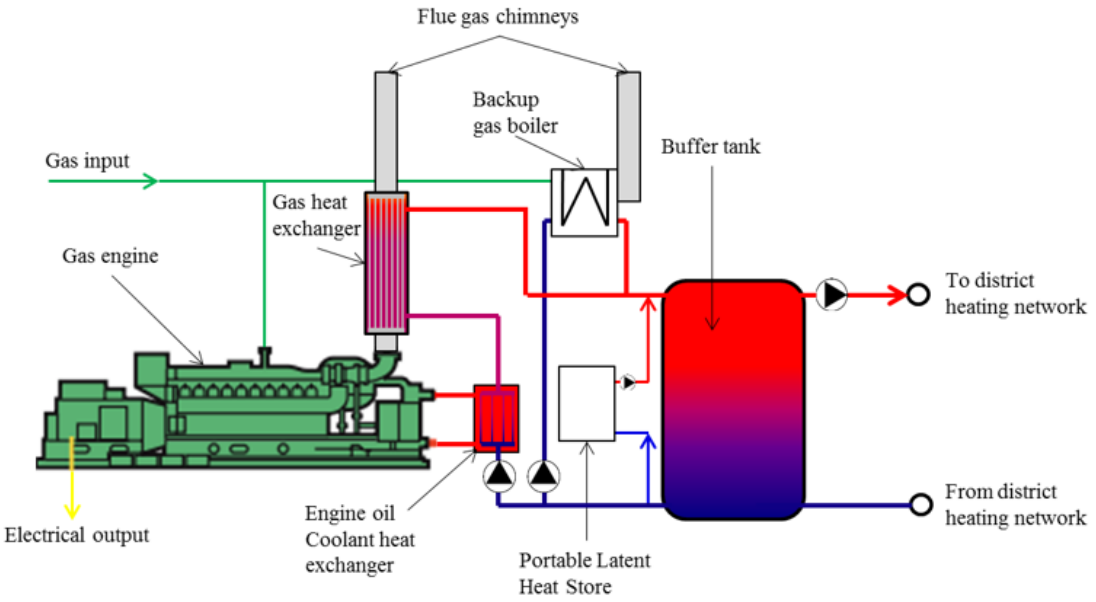

Figure 7.2: Schematic integration of a portable latent heat store in a district heating network supplied by a gas engine and a gas boiler.

To base the calculations on a practical heat demand and thermal capacity, the heat network of Milton Keynes was chosen due to the availability of heat consumption data and the mix of public and domestic buildings supplied by the district heat network.

7.3.2 Milton Keynes heat network

The heat network of Milton Keynes has two gas engines installed in 2006 each with an electrical capacity of $3.2MW_e$ and a thermal capacity of $3MW_{th}$. The energy centre also has a $10MW_{th}$ back-up/top-up boiler for peak heat demands.

The heat network comprises several residential buildings, network rail company offices, an innovation centre, some retail areas (Sainsbury's, WHS smith, Argos) and other commercial offices, as seen in table 7.8.

Table 7.8: List of buildings connected in Milton Keynes Heat network

Building type	Building Name	Annual heat demand $[MWh/_{year}]$
Offices	Luminous House	18
Offices/Residential	Moonstone House	212
Residential	Petersfield Green	240
	Petersfield Green 2	240
Offices/Residential /Commercial	Sainsbury's and Amethyst, Topaz, Jade, Sapphire, Quartz, Emerald, Jasper, Pearl and Garnet Houses	4270
Residential	Ruby House	332
	Opal House	402
Commercial /Residential	Metropolitan House	906
	Staten and Brooklyn Houses	955
	Chelsea House	1040
	Dakota House	804
	Carnegie House	1070
	Manhattan House	867
Offices	The Pinnacle/Innovation centre	2760
	The Quadrant/Network rail	4204
Total		**18310**

Combining the annual shares detailed in table 7.7 with the data from the Milton Keynes heat network presented in table 7.8, the estimated seasonal heat consumption of Milton Keynes heat network is presented in table 7.9.

Table 7.9: Annual share of heat demand for each season in the UK.

	Nov-Jan	Feb-Apr	May-Jul	Aug-Oct
Seasonal heat consumption [MWh]	7 124	6 582	2 118	2 486
Daily heat consumption [MWh]	79.16	71.54	23.03	27.31

Using the high-resolution stochastic integrated thermal-electrical domestic demand simulation tool developed by Mckenna and Thomson [31], daily heat demand profiles were determined for each design day (21^{st} January, 21^{st} March, 21^{st} June and 21^{st} December) to represent a typical day for each season. The high resolution curve from the model was adjusted (multiplied by a constant coefficient) so that its integration would represent the same daily values seen in table 7.9, obtaining the graphs presented in figure 7.3. The maximum value during the winter months is within the capacity of the heat source (16MW).

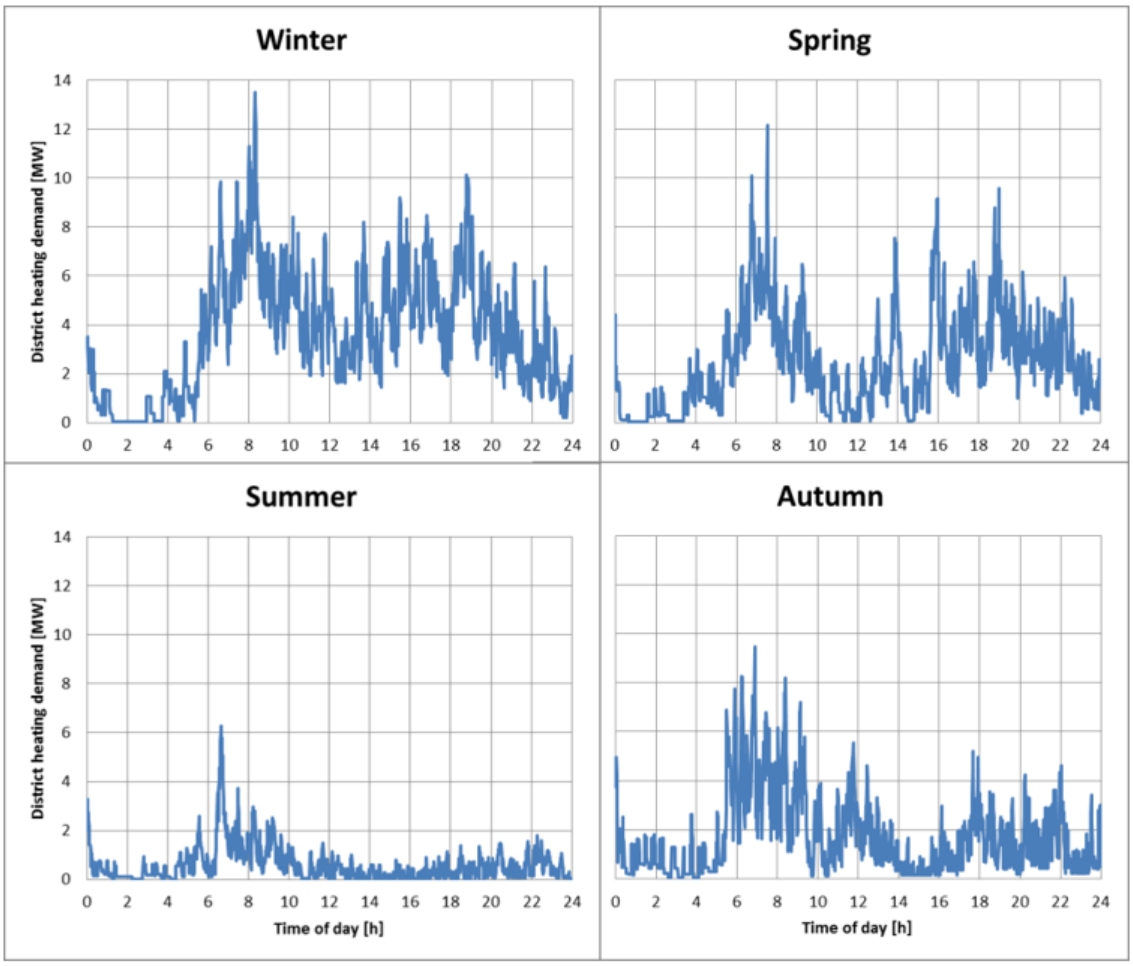

Figure 7.3: Daily heat demand profiles for the Milton Keynes district heating network for each season.

7.4 Numerical model developed

A 2D finite volume model was developed in Matlab to simulate the performance of a compact latent heat store suitable for integration in the district heating network described in figure 7.2. Similar to the algorithm developed previously for the compact latent heat store for domestic appliances, the model simulated pure diffusion only, with no volume changes during the melting process and isotropic heat propagation in the PCM.

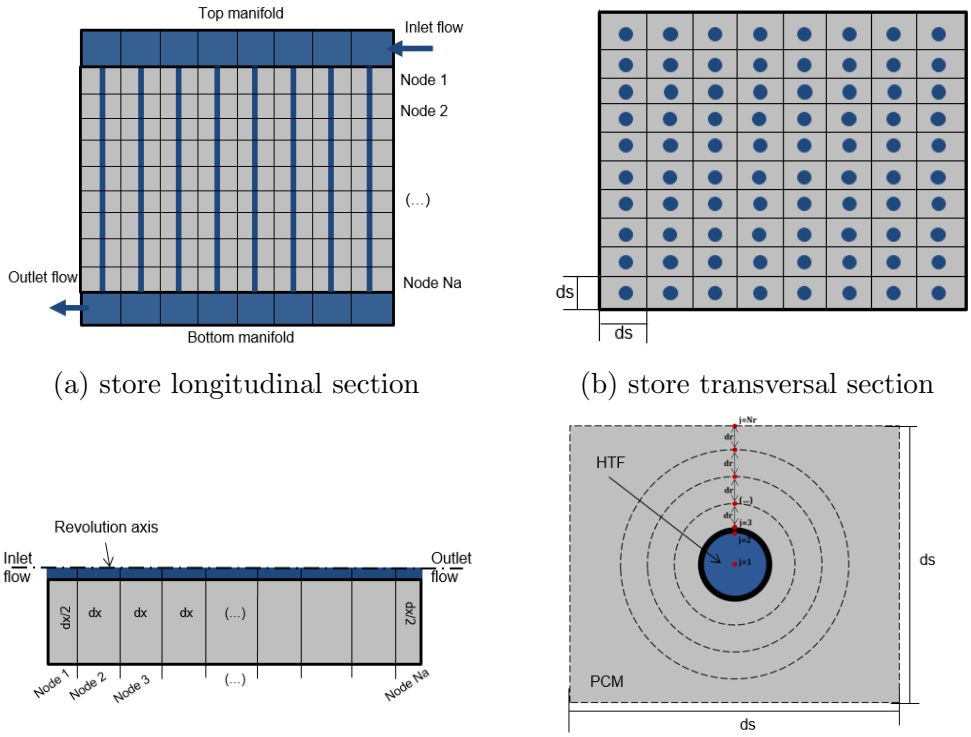

(a) store longitudinal section

(b) store transversal section

(c) tube longitudinal discretization

(d) tube transversal discretization

Figure 7.4: Modelled compact latent heat store section view, thermal store top view, longitudinal and transversal cross-section of a single tube.

The fluid flow Reynolds number used the inner diameter of the tube, with its Nusselt number, described in equation 6.12 and from VDI heat atlas [161]. For turbulent flow regimes the Gnielinski's expression was used [161], expressed in equation 6.13 and for transitional regimes the same procedure of the compact module detailed in chapter 6 was used as expressed in equation 6.10 and 6.11.

7.4.1 Storage material screening

From the PCM analysis made previously, for the given operational temperature range there were 3 candidates: Magnesium Chloride Hexahydrate, Erythritol and the eutectic mixture of urea with ammonium chloride.

The DSC analysis of magnesium chloride hexahydrate measured a melting point of 117°C with 21°C of subcooling. Using the 3-layer-calorimeter, the measured subcooling was reduced to 2°C [204].

The DSC analysis of erythritol measured a subcooling of 65°C and a shift of its initial melting point from 119°C to 107°C, due to a change of its crystal structure [74]. Hohlein measured its melting and solidification curve using the 3-layer-calorimeter and still determine 47°C subcooling. Agyenim [7] experienced lower levels of subcooling around 2°C.

Table 7.10 presents the thermal properties of the 3 candidate materials that could be used as portable latent heat stores for district heating networks. It can be seen that erythritol had the highest storage capacity ($141 kWh/m^3$ between 85°C and 125°C), although its higher bulk price makes it less competitive when compared to

magnesium chloride hexahydrate. The salt hydrate can store twice as much thermal energy in the described temperature range than water. All the quoted bulk prices were based of industrial grade materials.

Table 7.10: My caption

PCM candidates ($\%_{wt}$)	Temp. Range	Heat stored	$\Delta H/\Delta H_{H_2O}$	λ_s	λ_l	Price		Ref
	$[°C]$	$[kWh/m^3]$		$[W/m.K]$		$[£/kg]$	$[£/kWh]$	
Urea+NH_4Cl (85/15)	85-125	88	1.95	0.76	0.58	0.214	1.49	[205, 206]
$MgCl_2.(H_2O)_6$		92	2.03	0.7	0.63	0.067	0.76	[204]
Erythritol		141	3.12	0.89	0.33	3.191	14.23	

7.4.2 Thermal store designed

The compact latent heat storage system was designed to fit within a 25-foot cargo container, maximizing its storage capacity, thermal output, and minimizing its heat losses. The cargo container would have a section for the thermal store and a section for ancillary equipment (using a shell and tubes heat exchanger + circulation pumps + hydraulics) as seen in figure 7.5.

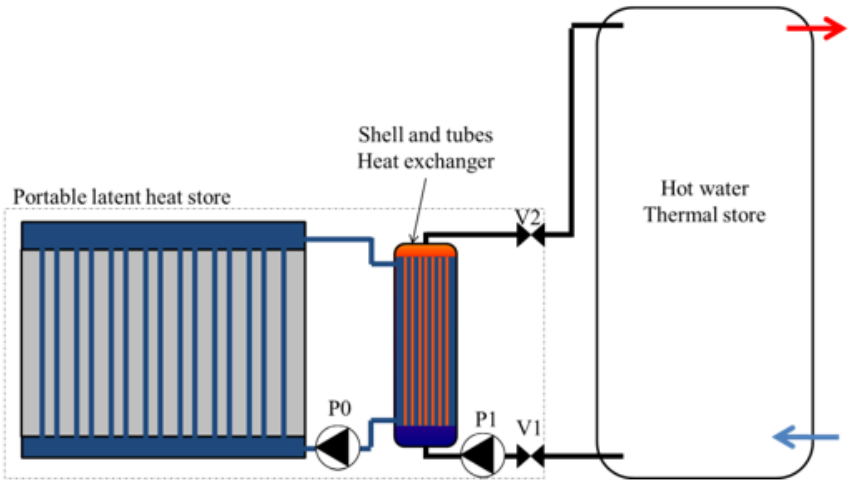

Figure 7.5: Daily heat demand profiles for the Milton Keynes district heating network for each season.

Due to the expected head loss of 100kPa in the shell and tube heat exchanger developed by EJ Bowman [207] (the PK600-3880-8), the limiting factor of the heat exchanger was the oil pump used to circulate the oil flow on the shell side. A catalogue research was made of Grundfos pumps and the TP series (the TP80-60/4 [208]) seemed to have the highest efficiency, providing the required head and flow rates for the complete discharge of the portable $2MWh_{th}$ in 6h.

Three sets of simulations were carried out testing the charging and discharging process of the thermal store, aiming for a charging/discharging time of 6h, followed by a standby test of 12h to determine its parasitic losses. Two of the thermal stores tested had a higher PCM volumetric ratio, one with no fins (A) and one with 43 transversal fins (B). The last thermal store tested (C) had a lower PCM volumetric

fraction, with the same specific heat transfer area compared to the store with fins. Table 7.11 details the properties of each thermal store studied. All of the systems could store more than 2000kWh in the temperature range from 85 to 125°C, using magnesium chloride hexahydrate (with a melting point of 116°C).

Table 7.11: Geometrical properties of the 2 designed compact thermal stores.

Parameter	A	B	C
Thermal store capacity $[kWh]$	2251		2046
Store length $[mm]$	6400		
Store width $[mm]$	2300		2308
Store height $[mm]$	2200		
Transversal tubes	42		68
Longitudinal tubes	124		200
Tube spacing $[mm]$	50		31
Number of axial fins	0	43	0
Specific HT area $[m^2/m^3_{PCM}]$	21.52	64.52	
Area increase [%]	0	300	0
Number of tubes	5 208		13 600
Tube ID/OD $[mm]$	13.31/15.79		
Modelled store Volume $[m^3]$	26.040		26.139
PCM volume $[m^3]$	24.002		20.816
PCM fraction [%]	92.17		79.64
Insulation conductivity $[W/m.K]$	0.040		
Insulation thickness $[mm]$	100		

Figure 7.6a and 7.6b presents the simulated results for the designed thermal store A (without fins), B (with fins) and C (without fins but same specific heat transfer area than store B). The model started by a discharge process of the thermal store from 125°C to 85°C in 6h, followed by a 6h charging process up to 125°C and then a 12h standby process, where the flow-rate was maintained and the store outlets connected.

Using magnesium chloride hexahydrate as the PCM, the storage charging process would be more prolonged than the discharging process, due to the closer proximity of the melting point of the PCM (116°C) to the maximum temperature (125°C). That would eventually lead to a higher discharging heat transfer rate due to the larger temperature range available from the melting point of the PCM to the DH temperature of 85°C.

The thermal stores with higher PCM volumetric fraction did not manage to fully charge within the 6h time interval. The thermal store with the lowest PCM fraction had the highest charging and discharging heat transfer rates and the quickest temperature changes within the PCM, hence obtaining the best performance parameters of the three stores studied.

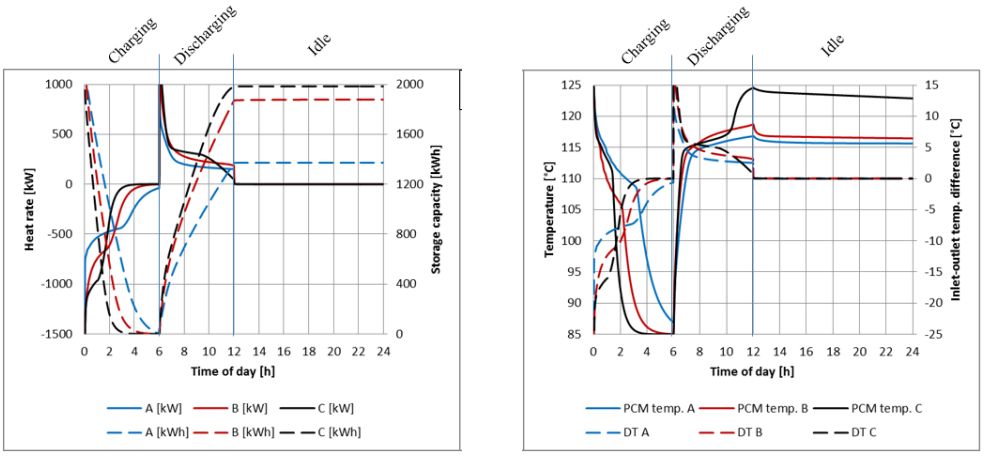

(a) heat transfer rate storage capacity

(b) thermal store temperature readings

Figure 7.6: Simulation predictions of the three storage configurations studied for their heat transfer rate and thermal storage capacity and for the PCM temperature and thermal store inlet/outlet temperature difference with time.

Table 7.12 presents the performance results for the simulation of the thermal stores. The average heat transfer rate was measured including only values above 50kW. None of the thermal stores managed to fully recharge in 6h. The fastest discharging time was achieved for store C, 4.11h. Between the thermal stores with larger PCM fraction, the inclusion of the 43 transversal fins increased the thermal energy charged in 6h from 1300 to $1800kWh_{th}$, although it did not fully charge the thermal store, as seen in figure 7.6a.

Table 7.12: Fluid flow properties and thermal performance results obtained for the 3 thermal stores studied.

Thermal store	A	B	C
Storage capacity $[kWh]$	2251		2046
Temperature range $[°C]$	85-125		
HTF mass rate $[kg/s]$	9.95		
HTF pipe velocity $[m/s]$	0.017		0.006
HTF Reynolds	41		16
HTF convective heat transfer $[W/m^2.K]$	46		39
Average discharging rate $[kW]$	333	476	559
Average charging rate $[kW]$	155	229	247
Charging/Discharging time $[h]$	6/6+	5.1/6	4.11/6
Charging capacity in 6h [%]	48.18	64.11	75.29
Self- discharge rate $[W]$	182	655	954

From the numerical results obtained, latent heat store C was chosen due to the better thermal performance obtained: fastest discharging time and highest discharging rate. Thermal store C had the highest self-discharging rate of 954W, although it is still negligible compared to the storage capacity (around 0.57% heat lost in 12h). The store had also a lower flow Reynolds number due to the larger number

of tubes. The inefficiencies of the thermal stores A and B were due to their wider tube spacing among the PCM (50mm).

7.5 Predicted daily performance in each season

Using the thermal demand profile detailed in figure 7.3, the portable latent heat store was integrated into the modelled Milton Keynes district heating network. The model included 3 hot water buffer tanks with a capacity of $160m^3$ each, providing a hot outlet of 85°C and receiving a cold inlet from the heat network of 55°C, a temperature range commonly used by commercial district heating plants [50].

A series of portable latent heat stores could be charged at a nearby cement plant located in Rugby, 40 miles away from the energy centre. They could be discharged to the hot water buffer tanks, being rotated every 6 hours. Three sets of storage systems can work continuously between the energy centre and the cement factory, with 2 sets at the cement plant charging and a set at the energy centre discharging. This would allow a period of 12h for charging and 6h for discharging for each set. With 2 thermal stores at any given time in the cement plant would allow the flue gas heat exchanger from cement plant to operate at a constant heat flow. Figure 7.7a and 7.7b present a general view of the portable latent heat store designed.

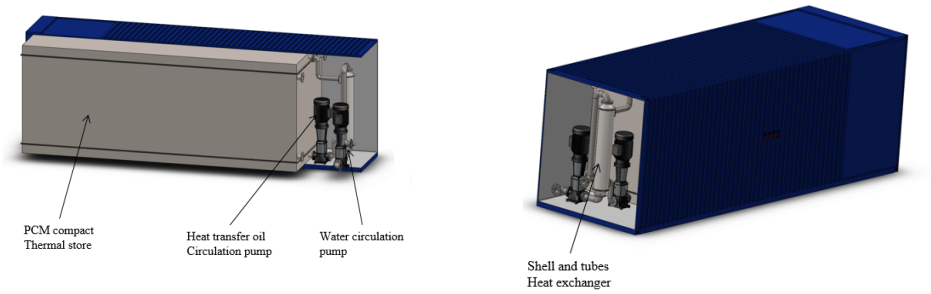

(a) section view

(b) isometric view

Figure 7.7: Schematic representation of a $2000kWh_{th}$ portable latent heat store within a 25-foot cargo container.

Three different scenarios were assessed: none, one and three portable thermal stores; to evaluate the potential reduction in the gas boiler use for each scenario. The gas boiler is activated when the water tanks thermal storage capacity goes below 40% and is deactivated when it reaches 65%. The CHP was activated during peak hours (from 07.00 to 22.00) and deactivated if the water tanks reach 80% storage capacity. The portable latent heat storage set would operate until the thermal storage capacity of the tank reaches 90% and be replaced when its outlet temperature drops below 100°C.

Table 7.13 presents the yearly energy consumption for each heat source in each case studied. The obtained reduction in gas boiler use increases with increasing number of portable latent heat stores, reducing the CHP unit operating time.

Table 7.13: Yearly boiler, CHP unit and latent heat store system (LHS) thermal energy supply.

System	No LHS	1 LHS	3LHS
Boiler use $[MWh_{th}/year]$	5497	4 111	2 826
CHP use $[MWh_{th}/year]$	12 806	11 407	9 159
CHP use $[MWh_e/year]$	13 659	12 168	9 770
LHS use $[MWh_{th}/year]$	0	3 410	9 417

Figure 7.8 presents the daily temperature profiles for each season for the PCM and the water buffer tanks top and bottom temperatures in each case studied. The hot water tanks temperature gradient is nearly identical in all cases, and there are moments in the case using 3 portable latent heat stores simultaneously where the portable latent heat storage system is deactivated due to lower heat consumption from the district heating network. In both cases employing portable thermal stores, the PCM temperature does not diverge much from the compact latent heat store flow outlet temperature, indicating a good heat exchange between the PCM and the heat transfer oil.

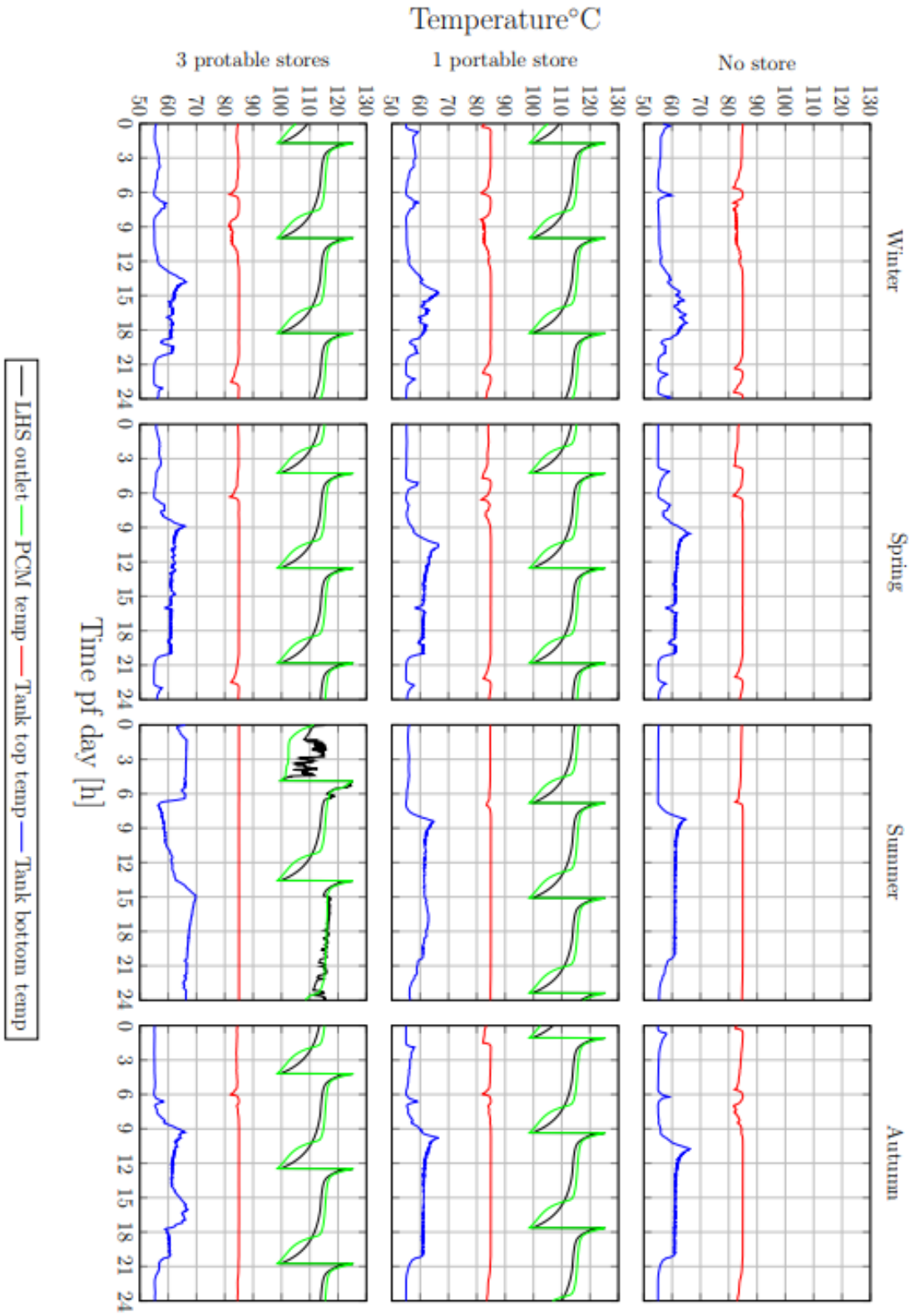

Figure 7.8: Daily predictions of the buffer tank top and bottom and PCM average temperature for the 3 cases modelled: no portable thermal store, with 1 and with 3 portable stores discharging simultaneously.

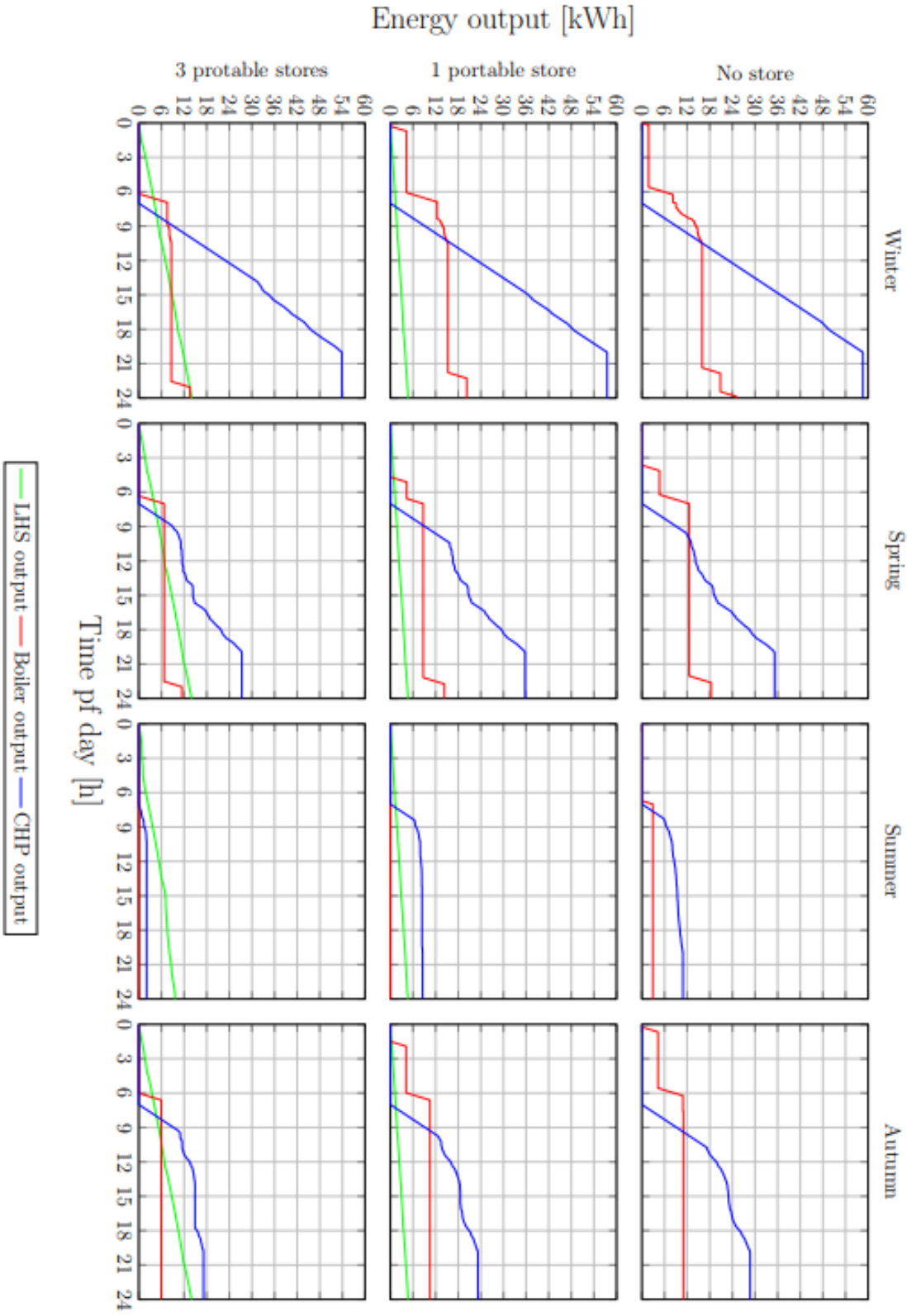

Figure 7.9: Daily cumulative heat output profiles for the 3 scenarios simulated: no portable thermal store, with 1 and with 3 portable stores discharging simultaneously.

Figure 7.9 presents the thermal energy delivered by the boiler, CHP unit and portable latent heat stores in each case studied. The number of actuations from the

gas boiler clearly reduces with the introduction of a portable latent heat store, with the storage daily contribution surpassed when 3 portable latent heat stores are used simultaneously.

The cement plant located in Rugby has a waste heat potential from its rotary kiln flue gases of 519.6MWh/day as seen on table 7.6, assumptions made estimating a daily throughput of 2490 tonnes of cement [28]. Using 1 portable latent heat store reduced gas consumption by 10.8% and the gas boiler consumption by 21.32%, using only 0.89% of the daily waste heat of the plant. When using 3 portable latent heat stores simultaneously, the system gas consumption reduction was 31.11%, the boiler had a more pronounced reduction in use of 45.92% achieved using 2.48% of the daily waste heat available from the Cement plant.

7.6 Economic comparison of all modelled systems

A general price assessment of the whole system cost was made to assess the levelized cost of energy of the 3 scenarios studied. In the portable latent heat store cases, a slow charging period at the cement plant was considered, with 2 thermal stores constantly charging and 1 store at the DH network discharging. The number of portable stores reported previously refers to the number of sets used simultaneously.

Table 7.14 presents the initial capital expense (CAPEX) and operational expense (OPEX) costs for the 3 cases studied. Regarding the costing of the PCM, the database of materials presented in Chapter 4 was used. For Rock-wool insulation, an indicative cost of $4.98£/m^2$ store external area was used, based on [209].

The stainless steel tubes were the most expensive component of the portable latent heat storage system, representing 93.9% of its whole cost. Their price of $8.633£/m$ was based on Metals4U indicative prices [210]. The enclosure cost assumed the same insulation area and a 3mm stainless steel sheet, with a price of $117.6£/m^2$ [211].

The circulation pumps were selected from GRUNDFOS [208] because they meet the operational flow rate and have a pumping pressure lift of around 1bar. The price was $1430£$ for each unit, based on [212]. The shell and tube heat exchanger selected, based on the EJ Bowman PK600-8 [207], had an indicative price of $5000£$. The economizer to be installed at the cement production unit to charge the portable latent heat stores was assumed to cost $10000£$, giving a specific power cost of $16.7£/kW_{th}$.

For the 25-foot cargo container, [213] indicated $200£/unit$ as a reference price. The heat transfer oil used in the simulation was shell S2 heat transfer fluid, with a price of $2.83£/L$ when sold in 209L barrels [214]. The yearly transportation costs of replacing the LHS units accounted for the 72km distance from the energy centre to the cement unit, with a truck fuel consumption of 45L/100km at 50km/h and a driver hourly rate of $10£/h$.

For the cost analysis of the gas boiler unit, an indicative price of $0.08e/W_{th}$ was used, based on [215]. For the CHP unit, a specific price of $32£/kW_{el}$ was used , based on [216]. The water buffer tank capital cost, an indicative price of $962£/m^3$ was used based on [217]. System installation costs were assumed 5% of the initial CAPEX [168]. Operation and maintenance costs were assumed 5% of the CAPEX for the gas boiler and buffer tanks, and 1% for the CHP unit, in accordance with [216]. The heat network operation and maintenance costs were based on [217],

assuming a total of $30£/MWh_{th}$ produced. For the standard gas tariff, a price of $3.2£/kWh$ provided by Npower was used.

Table 7.14: CAPEX and OPEX costs comparison for the systems studied.

System		No portable store	1 LHS	3 LHS	Ref.
Thermal store	PCM cost (volume)		6 715 ($62.4m^3$)	20 146 ($187.3m^3$)	[90]
	Insulation cost (area)		1 014 ($203.6m^2$)	3 041 ($610.7m^2$)	[209]
	Tubes cost		704 480 (40 800)	2 113 440 (122 400)	[210]
	Enclosure cost (area)		47 880 ($203.6m^2$)	143 641 ($610.7m^2$)	[211]
	TP 80-60/4 pump		8 580	25 740	[212]
	PK600-8 heat exchanger		15 000	45 000	[207]
	25-foot container		6 000	18 000	[213]
	Economizer		10 000	10 000	[207]
	HT oil		32 107 (11 346L)	96 320 (34 038L)	[214]
	Total [£]	0	792 283	2 359 848	
10MW Gas boiler		531 361			[215]
3.2MW Gas engine		146 073			[216]
$3 \times 160m^3$ water buffer tanks		461 760			[217]
Heat connections		457 500			
Heat network		2 745 00			
CAPEX		4 341 694	5 173 470	6 817 022	
OPEX	OM boiler + CHP + water tank	66 452			[231]
	OM LHS system	0	8318	24753	
	Gas consumption cost	972221	885969	696130	
	LHS yearly replacement cost	0	118336	98614	
	OM heat network	550 830			[217]
	Total [$£/year$]	1 549 661	1 552 570	1 436 979	

The main capital component in the CAPEX of the system is the respective heat network and subsequent heat-metered connections (representing 83% of the initial capital cost in the case with no portable store, 68% in the case with 1 store and 51% in the case with 3 portable thermal stores) as seen in table 7.14.

The levelized cost of energy (LCOE) for each system was calculated using equation 7.1, from [170]. It considered both the thermal energy and electricity produced by the system.

$$LCOE = \frac{\frac{CAPEX \cdot r}{1-(1+r)^{-n}} + OPEX}{E_{produced}} \left[\frac{£}{kWh}\right] \tag{7.1}$$

Table 7.15 summarizes the yearly results obtained with each system studied in regards to the energy used in the gas boiler, the CHP unit and by the portable thermal energy storage system. For a 20-year cycle and considering an annual interest rate of 3.5% the LCOE obtained for each system are presented in table 7.15. The system with no portable latent heat store presents the lowest LCOE, with the difference to the systems with latent heat store being relatively small due to the high CAPEX cost of the heat network itself, as seen in table 7.15.

Table 7.15: Energy provided by each source in each system, and its respective levelized cost of energy, for a 20-year life-cycle.

System	No portable store	1 LHS	3 LHS
Boiler use $[MWh_{th}/year]$	5 225	4 111	2 826
CHP use $[MWh_{th}/year]$	12 173	11 407	9 159
CHP use $[MWh_{el}/year]$	12 984	12 168	9 770
LHS use $[MWh_{th}/year]$	0	1 704	4 706
LCOE $[£/MWh_{energy}]$	62.37	67.94	70.12

The integration of portable latent heat stores and their priority over the other heat sources led to a decrease in the CHP unit operation time, reducing also the yearly electricity produced. That reduction provided a lower value of energy produce throughout the year, increasing the cost of energy of the latent heat stores.

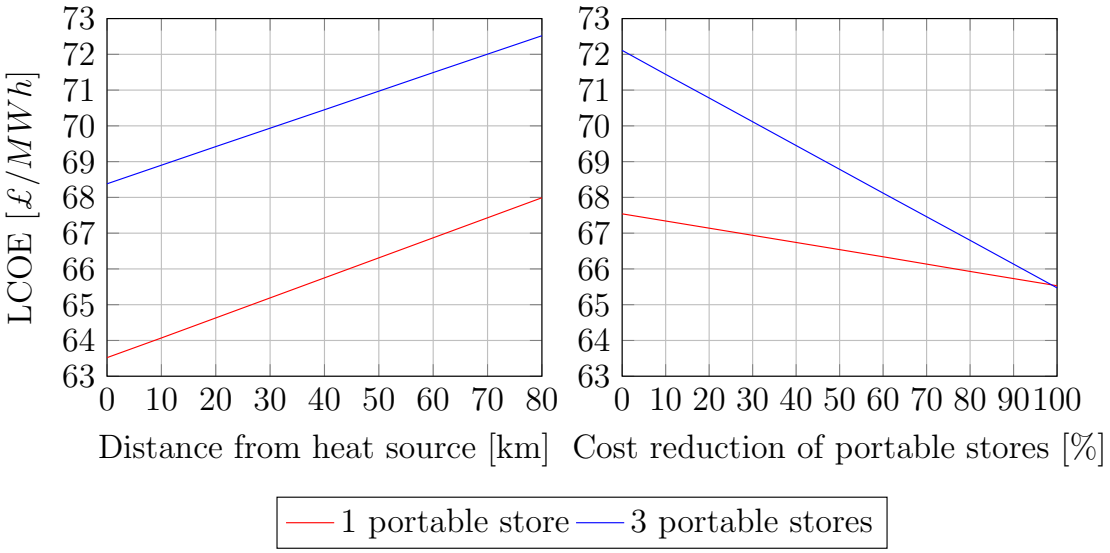

Figure 7.10: -Impact of the distance and of the cost reduction on the LCOE for the portable latent heat storage systems studied.

Figure 7.10 presents the impact of the distance to the heat source and cost reduction of the portable heat store on the LCOE of the system. For the system with 1 portable heat store there is a bigger impact on the distance of the heat source whilst on the system with 3 portable heat stores delivered continuously, the cost reduction of the thermal stores has a greater impact. In none of the cases studied the LCOE could be matched to the reference case.

7.7 Conclusions from the integration of industrial waste heat into district heating networks with portable phase change energy storage

The adoption of district heating networks in the UK requires strong local governments to involve and aware local communities of the economic potential of centralized heating solutions. Due to the flexibility of connecting any heat source to the

district heating network, the integration of industrial waste heat does not impose any major technical obstacles.

The UK industry sector possesses various continuous thermal processes suitable for integration into district heating networks, mainly in the refineries flue gases from the distillation and coking processes, flue gases from sugar evaporators, exhaust air from vacuum pumps in the pulp and paper sector and flue gases from the various kilns used in the cement, glass and ceramic producers.

Some of these intensive energy users are located more than 20km from local district heating networks, where the continuous supply of portable latent heat stores by road might be more economically feasible than connecting them to the district heating pipe network.

A 25-foot cargo container with $26.139m^3$ of magnesium chloride hexahydrate charged at 125°C and discharged to 85°C using a heat transfer oil can store around $2MWh_{th}$, in the ideal temperature band for an indirect discharge to a hot water buffer tank in a district heating network. A string of these containers being constantly charged at a nearby cement factory and discharged 72km away has been studied and found to have a relatively small economic impact on the Milton Keynes district heating network, successfully reducing the gas boiler use by 21%, while increasing its cost of energy by $2£/MWh$ to $64.07£/MWh$, an overall system yearly decarbonisation potential of 10.8%.

To obtain better levelized costs of energy, the CHP unit should have priority to operate at specific times, hence maintaining its electricity production. The utilization of electric vehicles to transport the portable stores could also improve to further decarbonize this storage solution.

Chapter 8

Conclusions

Phase change materials can store larger amounts of thermal energy within a smaller temperature range when compared to common sensible heat storage materials. Due to the low thermal conductivity of PCMs, poor rates of thermal diffusion within the PCM can seriously affect the storage system charge and discharge heat transfer rates that can be achieved.

From the literature review made, organic compounds and salt hydrates are the most promising materials below 100°C due to their relative low bulk price and high thermal storage energy density $[kWh/m^3]$. The eutectic mixtures of urea seem promising in the temperature band from 80 to 110°C, and eutectic mixtures of nitrate salts appear promising in the range from 130°C up to 250°C. The utilization of encapsulated PCMs offers the versatility of integration into any existing thermal storage system with no major technical constraints. The lower PCM volume ratio that encapsulated thermal storage systems have provides them with higher specific heat transfer areas $[m^2/m^3_{PCM]}$ when compared to more compact geometries, minimizing the impact on heat transfer of the PCM inherent low thermal conductivity. More compact systems do offer larger constant temperature output periods; however heat transfer enhancement within the PCM is critical to achieve reasonable thermal power output rates, since PCMs thermal conductivity can be a major issue. In general terms, increasing the specific heat transfer area of any given thermal storage volume to its heat transfer fluid flow will increase its heat transfer rates, however it reduces the PCM volumetric fraction, making the thermal store less energy dense.

From the thermal analysis made, 11 promising PCMs were identified and 3 were selected for three different applications: space cooling (5 to 25°C), domestic heating (40 to 65°C) and district heating (50 to 85°C). The decarbonisation potential and economic feasibility of the integration of phase change materials was theoretically analyzed for these three applications.

In office space cooling systems, using extra air ventilation or night time ambient cooling can contribute to the decarbonisation of current office HVAC systems through electricity consumption reduction, however that reduction is more attractive with night time ambient cooling via a thermal store. Shifting daily cooling loads with electrical off peak cooling using a heat pump has a lower decarbonisation potential, although it successfully shifted 37% of the daily cooling demand into off peak times. Shifting daily cooling loads into off peak times can have a significant impact on the peak grid demand because building cooling loads can be met with night time renewable generation such as wind, wave or hydro power, hence consuming low

carbon electricity.

Shifting office space cooling demands with latent heat stores is an expensive solution compared to increasing the building fresh air intake only (with a levelized cost of energy of $84.45£/MWh$), and the thermal stores parasitic heat losses to ambient minimize the electricity savings of storing cooling loads during the night, those losses being very dependent on the type of storage geometry used. The most feasible thermal storage solution was using night time ambient cooling to charge the thermal store and obtained a levelized cost of energy of $120.66£/MWh$ and the highest overall decarbonisation of 27% of the heating and cooling system of the building.

For domestic heating applications, packed bed buffer tanks present a promising solution to increase the thermal storage capacity of a water buffer tank, as well as to improve its thermal stratification. Its successful implementation relies on the assumption that affordable small spherical or cylindrical enclosures (50-70mL volume) will not be a constraint.

The results show that shifting domestic hot water and space heating demands using PCMs is more economically feasible than using larger water buffer tanks due to the reduction in storage volume achieved, although using gas boilers is still the most cost effective solution. Integrating PCM spherical capsules into the buffer tank reduces the required storage volume by 46%, and the levelized cost of heat by $5.65£/MWh$ to $131.39£/MWh$. Coupling a compact latent heat store next to a smaller buffer tank obtained the lowest levelized cost of heat of $127.77£/MWh_{th}$ and an overall decarbonisation of 57.3% of the domestic hot water and space heating system.

The integration of a compact PCM module next to a buffer tank presents the highest solar fraction mainly due to the lower temperature that the compact PCM module can operate at benefitting the highest thermal stratification. The storage system presented large temperature drops upon high heat demands (when DHW was needed by the household). To minimize this problem, these storage containers would perform better when there is laminar flow within the heat transfer fluid flow.

The reduction of district heating loads can be made via portable latent heat stores and still provide a cost-effective solution when an industrial surplus of heat is located relatively far from the district heating network. The main economic limitations of the portable storage systems proposed is the relatively high cost of the tube-in-tube configuration, the tubes being responsible for 89% of the total portable thermal store cost.

To meet the UK's 80% carbon emissions reduction targets by 2050, the decarbonisation of the heating and cooling sector must continue. The main conclusions of this thesis are related to the decarbonization potential of latent heat thermal energy storage system in the heating and cooling sector and can be summarized in the following points:

- Shifting office cooling loads using a thermal storage system charged with nigh time ambient cooling can reduce the electricity used for cooling by 40% (meeting most of the daily cooling loads in spring, winter and autumn months and part of cooling loads during summer months) in highly glazed office buildings (50% glazing area);

- Shifting domestic hot water and space heating demand into economy 10 elec-

tricity tariff periods and a solar thermal system can decarbonize the heating system by up to 57.3% (when replacing a gas boiler with air source heat pump) when using a buffer tank next to a compact PCM module;

- The integration of industrial waste heat into a remote district heating network made via a continuous delivery of portable latent heat storage systems can reduce the use of peak gas boilers up to 46%;

Thermal energy storage can provide the ability to shift peak heating and cooling loads along with further integration of heat pumps, potentially reducing electrical peak loads and the need for backup ancillary services such as coal and combined cycle gas turbines required to meet that demand. Further decarbonisation of the UK electrical grid, already achieving 15% emissions reduction from 2015 to 2016, will have a larger impact if heating and cooling systems are further electrified.

The algorithms developed demonstrated that for a successful integration of PCMs into any given application, the minimization of heat losses, optimization of the heat transfer and overall cost are the three main parameters. The flexibility of the developed algorithms to simulate both the thermal store fluid flow as well as the heat propagation within the storage material provided a useful tool to determine the energy performance of selected geometries with relative ease for any given heat generation or demand profile. This offers a valuable tool to compare thermal energy storage technologies for any given heating or cooling application.

The contributions to knowledge from this research can then be summarized in the numerical domain:

- Development of numerical models to predict the thermal performance of different store geometries:
  - Parallel slabs;
  - Staggered cylinders;
  - Packed beds in buffer tanks;
  - Compact vertical tube in tube;
- Stratification modelling by accounting flow reversion within fluid flow;
- Integration of thermal stores into heating/cooling networks:
  - Office space cooling;
  - Domestic hot water and space heating;
  - District heating networks;

In the material domain:

- Novel shape stabilization technique using a polymeric adsorbent (composite adsorbent developed by [162]);

In the systems domain:

- Fast transient analysis to predict energy efficiency gains and emissions reduction (based on climate data) for a building by integrating any of the discussed above thermal storage geometries;

8.1 Recommendations for further work

The following recommendations are suggested for further research linked to the 3 thermal energy storage systems analyzed in this research. For office space cooling applications:

- The experimental thermal stores constructed for ventilated appliances were not designed for high power outputs in the 10-50kW range. The development of a larger and optimized parallel slab thermal store should be made adopting the heat transfer enhancement suggested for the air flow of introducing corrugated metal sheets operating as fins to determine their thermal behaviour.

- Using the solid-liquid latent heat energy of water might be a promising storage technology due to the storage material low cost and high storage density. Further research should be made on the design of storage geometries that accommodate volumetric expansions during the freezing process and how to tackle the cooling capacity limitation of heat pumps, in order to charge larger amounts of ice in off-peak times. Direct contact heat exchangers could offer a cost-effective heat transfer approach to be used within ice tanks, increasing convective flow in the liquid water.

- The integration of solar thermal into large space cooling systems is usually made supplying part of heat required by absorption chillers. Compact latent heat stores could increase the solar gain in such systems by maintaining the heat source at 90-120°C whilst increasing thermal storage capacity 3-5 times compared to current oil based buffer tanks within that temperature band.

For the integration into domestic hot water and space heating applications:

- The impact on thermal storage capacity and thermocline degradation within domestic-scale water buffer tanks could be investigated with and without encapsulated PCM.

- A compact module could also be tested in low fluid flow regimes or even within a solar thermal system in closed loop, exchanging heat indirectly with a hot water tank via a shell and tube heat exchanger. This would maximize the energy provided by solar thermal collectors by maintaining the compact thermal store at a lower temperature around 25-35°C. Using a lower temperature thermal store would also require the use of low temperature convector radiators or even underfloor heating, maximizing the COP of the heat pump.

For the integration of thermal energy storage into district heating networks:

- The increase in thermal storage capacity of current water buffer tanks by the direct integration of PCM capsules to the tank should be studied within the 55-85°C working temperature range to determine their thermal behaviour.

- Large compact thermal energy stores offer the possibility to transport heat into nearby integrated heat networks. The theoretical system studied in this research of a high power latent heat store relied on the assumption that the heat transfer fluid flow would distribute itself evenly throughout all the tubes. An experimental prototype could be developed to measure the inefficiencies

of the fluid flow distribution and to determine where parasitic heat losses are more likely to occur.

Other potential applications that could benefit from latent heat storage could be electrical ancillary services such as nuclear power plants, allowing them to flex some of its daily heat production according to the required demand:

- Pressurized water-cooled nuclear reactors operate around the 290-330°C temperature band and are a potential candidate to decarbonize the electrical supply. Allowing their electrical production to be more flexible whilst maintaining a near constant heat output could be made possibly via large thermal storage containers using molten salts. Using encapsulated PCMs within those molten salt tanks could increase thermal storage capacity around 4-6 times over the operating temperature range, potentially making more cost effective storage solutions possible.

- Sodium-cooled fast reactors are considered a promising recycling solution for used nuclear fuel. Flexing their electrical output by integrating large molten salt tanks is also an option to be considered, but due to the larger temperature band available between 320 and 475°C, using encapsulated PCMs can only increase the thermal storage capacity by 60%.

The characterization of other key material properties during phase change (mainly viscosity, density and thermal diffusivity) should also be made for the promising PCMs studied. That would allow a more detailed theoretical analysis to calculate the velocities due to buoyancy effects in the molten PCM, since it has a great impact on the thermal behaviour within the storage material.

Enhancement techniques such as the shape stabilization are promising solutions to improve thermal performance of organic PCMs below 100°C due to the feasibility of currently used adsorbents and their bulk thermal conductivity can be increased 50-100% with a relatively low mass fraction of bulk graphite ($5\%_{wt}$). Novel thermal storage containers with these shape stabilized materials could be more accurately optimized to the required heating or cooling profiles of a specific application using the algorithms developed since there would be no molten PCM within the container and only thermal diffusion would occur. After being validated for the respective application, these algorithms could be implemented into the thermal storage system control unit to provide real-time predictions of the thermal storage capacity and allow the heating or cooling system to adapt its operation more accordingly to the actual demand.

Bibliography

[1] Robert Levy. Nasa earth observatory: Home at *http://earthobservatory.nasa.gov/*, 2018.

[2] Heriot-Watt University. Bp statistical review of world energy june 2017. Technical report, BP at *https://www.bp.com/content/dam/bp/en/corporate/pdf/energy-economics/statistical-review/bp-stats-review-2018-full-report.pdf*, 2017.

[3] Kevin Harris, Anwar Annut, and I MacLeay. Digest of united kingdom energy statistics 2017. Technical report, Department for Business, Energy and Industrial Strategy at *https://www.gov.uk/government/statistics/digest-of-uk-energy-statistics-dukes-2017-main-report*, 2017.

[4] Herbert Zondag, Benjamin Kikkert, Simon Smeding, Robert de Boer, and Marco Bakker. Prototype thermochemical heat storage with open reactor system. *Applied Energy*, 109:360–365, sep 2013.

[5] S. Jegadheeswaran and Sanjay D. Pohekar. Performance enhancement in latent heat thermal storage system: A review. *Renewable and Sustainable Energy Reviews*, 13(9):2225–2244, 2009.

[6] Koichi Nakaso, Hirofumi Teshima, Akito Yoshimura, Seiichi Nogami, Yuichi Hamada, and Jun Fukai. Extension of heat transfer area using carbon fiber cloths in latent heat thermal energy storage tanks. *Chemical Engineering and Processing: Process Intensification*, 47(5):879–885, 2008.

[7] Francis Agyenim, Philip Eames, and Mervyn Smyth. Experimental study on the melting and solidification behaviour of a medium temperature phase change storage material (Erythritol) system augmented with fins to power a LiBr/H2O absorption cooling system. *Renewable Energy*, 36(1):108–117, 2011.

[8] Weilong Wang, Xiaoxi Yang, Yutang Fang, Jing Ding, and Jinyue Yan. Preparation and thermal properties of polyethylene glycol/expanded graphite blends for energy storage. *Applied Energy*, 86(9):1479–1483, 2009.

[9] Shaopeng Guo, Jun Zhao, Weilong Wang, and Guang Jin. Experimental study on solving the blocking for the direct contact mobilized thermal energy storage container. *Applied Thermal Engineering*, 78:556–564, mar 2015.

[10] Marco Deckert, Rainer Scholz, Samir Binder, and Andreas Hornung. Economic Efficiency of Mobile Latent Heat Storages. *Energy Procedia*, 46:171–177, 2014.

[11] Luisa F Cabeza, Manuel Ibanez, Cristian Sole, Joan Roca, and Miquel Nogues. Experimentation with a water tank including a pcm module. *Solar Energy Materials and Solar Cells*, 90(9):1273–1282, 2006.

[12] A. Felix Regin, S. C. Solanki, and J. S. Saini. An analysis of a packed bed latent heat thermal energy storage system using PCM capsules: Numerical investigation. *Renewable Energy*, 34(7):1765–1773, 2009.

[13] A.H. Mosaffa, L. Garousi Farshi, C.A. Infante Ferreira, and M.A. Rosen. Energy and exergy evaluation of a multiple-PCM thermal storage unit for free cooling applications. *Renewable Energy*, 68:452–458, aug 2014.

[14] Pradip Majumdar. *Computational Methods for Heat and Mass Transfer*. CRC Press, 1^{st} edition edition, September 2005.

[15] Aran Solé, Laia Miró, Camila Barreneche, Ingrid Martorell, and Luisa F. Cabeza. Review of the T-history method to determine thermophysical properties of phase change materials (PCM). *Renewable and Sustainable Energy Reviews*, 26:425–436, 2013.

[16] Jyh-Chau Liou and Neng-Chuan Tien. Estimation of the thermal conductivity of granite using a combination of experiments and numerical simulation. *International Journal of Rock Mechanics and Mining Sciences*, 81:39–46, jan 2016.

[17] Mohammad Ahadi, Mehdi Andisheh-Tadbir, Mickey Tam, and Majid Bahrami. An improved transient plane source method for measuring thermal conductivity of thin films: Deconvoluting thermal contact resistance. *International Journal of Heat and Mass Transfer*, 96:371–380, 2016.

[18] Murat M. Kenisarin. Thermophysical properties of some organic phase change materials for latent heat storage. A review. *Solar Energy*, 107:553–575, 2014.

[19] Crodatherm international Plc. Croda at *https://www.crodatherm.com/en-gb*, 2018.

[20] Rubitherm Technologies GmbH. Rubitherm gmbh at *http://www.rubitherm.eu/*, 2018.

[21] Tao Wang, Divakar Mantha, and Ramana G. Reddy. Novel low melting point quaternary eutectic system for solar thermal energy storage. *Applied Energy*, 102:1422–1429, 2013.

[22] Research Team, Verco, and GFK. Building energy efficiency survey 2014-15: Overarching report. Technical report, Department of Business, Energy & Industrial Strategy at *https://www.gov.uk/government/publications/building-energy-efficiency-survey-bees*, 2016.

[23] I Korolija, Y Zhang, L Marjanovic-Halburd, and VI Hanby. Selecting hvac systems for typical uk office buildings. In *The 6th International Symposium on Heating, Ventilating and Air Conditioning*, pages 388–396. ISHVAC 2009, 2009.

[24] D. B Crawley, C. O. Pedersen, and L.K. Lawrie. Energy plus: Energy simulation program. *ASHRAE Journal*, 42(4):49–56, 2000.

[25] A.D. Hawkes. Estimating marginal CO2 emissions rates for national electricity systems. *Energy Policy*, 38(10):5977–5987, oct 2010.

[26] National Grid. National Grid. *Interconnector TEC Register*, 2016.

[27] Melanie Dawes CB. English housing survey, headline report 2016-17. Technical report, Ministry of Housing, Communities and Local Government at *https://www.gov.uk/government/collections/english-housing-survey*, 2017.

[28] Her Majesty's Stationery Office. The future of heating: A strategic framework for low carbon heat in the uk. Technical report, Department of Energy and Climate Change at *https://www.gov.uk/government/publications/the-future-of-heating-a-strategic-framework-for-low-carbon-heat*, 2012.

[29] Daikin technical team. Daikin altherma high temperature heat pumps.

[30] E. Alam Tanvir, Jaspreet Dhau, D. Y. Goswami, M. M. Rahamn, and Elias Stefankos. Experimental investigation of a packed bed latent heat thermal storage system with encapsulated phase change material, 2014.

[31] Eoghan McKenna and Murray Thomson. Crest demand model at *https://figshare.com/articles/CREST˙Demand˙Model˙v2˙0/2001129*, 2015.

[32] European Commission. Emission database for global atmospheric research (edgar), release version 4.3.2. at *http://edgar.jrc.ec.europa.eu/*, 2017.

[33] United Nations. Kyoto protocol to the united nations framework convention on climate change. Technical report, United Nations at *http://unfccc.int/resource/docs/convkp/kpeng.pdf*, 1998.

[34] Laura Cozzi and Tim Gould. World energy outlook 2017. Technical report, International Energy Agency at *https://www.iea.org/weo2017*, 2017.

[35] Shuo Liu, Andreas Wilkes, and Yu'e Li. Contribution of different sectors to developed countries' fulfillment of GHG emission reduction targets under the first commitment period of the Kyoto Protocol. *Environmental Science & Policy*, 61:143–153, 2016.

[36] Shafiqur Rehman, Luai M. Al-Hadhrami, and Md Mahbub Alam. Pumped hydro energy storage system: A technological review. *Renewable and Sustainable Energy Reviews*, 2015.

[37] Nicolas J. Kelly, Paul G. Tuohy, and Adam D. Hawkes. Performance assessment of tariff-based air source heat pump load shifting in a UK detached dwelling featuring phase change-enhanced buffering. *Applied Thermal Engineering*, 71(2):809–820, oct 2014.

[38] Hamidreza Mozayeni, Michael Negnevitsky, Xiaolin Wang, Feng Cao, and Xueyuan Peng. Performance Study of an Advanced Adiabatic Compressed Air Energy Storage System. *Energy Procedia*, 110:71–76, 2017.

[39] Wei He, Xing Luo, and David Evans. Exergy storage of compressed air in cavern and cavern volume estimation of the large-scale compressed air energy storage system. *Applied Energy*, 2017.

[40] Samuel Wicki and Erik G. Hansen. Clean energy storage technology in the making: An innovation systems perspective on flywheel energy storage. *Journal of Cleaner Production*, 162:1118–1134, sep 2017.

[41] J. P. Douady, S. Fouache, and J. F. Sarrau. *Lead-Acid Batteries for Future Automobiles*. Elsevier, 2017.

[42] Massaki Yoshio, Ralph J. Brodd, and Akiya Kozawa. *Lithium-Ion Batteries*. Springer Berlin Heidelberg, 2 edition, 2010.

[43] K M Abraham. Rechargeable sodium and sodium-ion batteries. In *Lithium Batteries*, 2013.

[44] Haisheng Chen, Thang Ngoc Cong, Wei Yang, Chunqing Tan, Yongliang Li, and Yulong Ding. Progress in electrical energy storage system: A critical review. *Progress in Natural Science*, 19(3):291–312, mar 2009.

[45] Adam Z. Weber, Matthew M. Mench, Jeremy P. Meyers, Philip N. Ross, Jeffrey T. Gostick, and Qinghua Liu. Redox flow batteries: A review, 2011.

[46] J.K. Kaldellis and D. Zafirakis. Optimum energy storage techniques for the improvement of renewable energy sources-based electricity generation economic efficiency. *Energy*, 32(12):2295–2305, dec 2007.

[47] Lidia Navarro, Alvaro de Gracia, Dervilla Niall, Albert Castell, Maria Browne, Sarah J McCormack, Philip Griffiths, and Luisa F Cabeza. Thermal energy storage in building integrated thermal systems: A review. Part 2. Integration as passive system. *Renewable Energy*, 85:1334–1356, 2016.

[48] U Stritih, V V Tyagi, R Stropnik, H Paksoy, F Haghighat, and M Mastani Joybari. Integration of passive PCM technologies for net-zero energy buildings. *Sustainable Cities and Society*, 41:286–295, 2018.

[49] S.M. Hasnain. Review on sustainable thermal energy storage technologies, Part II: cool thermal storage. *Energy Conversion and Management*, 39(11):1139–1153, aug 1998.

[50] Francesco Colella, Adriano Sciacovelli, and Vittorio Verda. Numerical analysis of a medium scale latent energy storage unit for district heating systems. *Energy*, 45(1):397–406, sep 2012.

[51] Igengard Johansson. AMIDES , Fatty Acid. *Kirch-Othmer Encyclopedia of Industrial Chemistry*, 2, 2000.

[52] A. Raemy and T. F. Schweizer. Thermal behaviour of carbohydrates studied by heat flow calorimetry. *Journal of Thermal Analysis*, 28:95–108, 1983.

[53] Hubert Schiweck, Albert Bär, and Roland Vogel. Sugar Alcohols. In *Ullmann's Encylcopedia of Industrial Chemistry*, pages 2–32. Wiley-VCH Verlag GmbH & Co. KGaA, 2012.

[54] Boy Cornils and Peter Lappe. Dicarboxylic acids. Aliphatic. In *Ullmann's Encyclopedia of Industrial Chemistry*. Wiley-VCH Verlag GmbH & Co. KGaA, 2008.

[55] D. H. Kerridge. The chemistry of molten acetamide and acetamide complexes. *Chemical Society Reviews*, 17:181, 1988.

[56] Ivo Mavrovic, a. Ray Shirley, and G. R. Coleman. Urea. *Kirk-Othmer Encyclopedia of Chemical Technology*, 2:1–21, 2010.

[57] D. Haillot, T. Bauer, U. Kröner, and R. Tamme. Thermal analysis of phase change materials in the temperature range 120-150 °C. *Thermochimica Acta*, 513(1-2):49–59, 2011.

[58] Alibaba Group. Alibaba at *www.alibaba.com*, 2018.

[59] Nicholas R. Jankowski and F. Patrick McCluskey. A review of phase change materials for vehicle component thermal buffering. *Applied Energy*, 113:1525–1561, 2014.

[60] Arthur P. Miller. Lange's Handbook of Chemistry. *American Journal of Public Health and the Nations Health*, 31(12):1324, 1941.

[61] Sivasankaran Harish, Daniel Orejon, Yasuyuki Takata, and Masamichi Kohno. Thermal conductivity enhancement of lauric acid phase change nanocomposite with graphene nanoplatelets. *Applied Thermal Engineering*, 80:205–211, apr 2015.

[62] Yanping Yuan, Nan Zhang, Wenquan Tao, Xiaoling Cao, and Yaling He. Fatty acids as phase change materials: A review, 2014.

[63] Fang Tang, Lei Cao, and Guiyin Fang. Preparation and thermal properties of stearic acid/titanium dioxide composites as shape-stabilized phase change materials for building thermal energy storage. *Energy and Buildings*, 80:352–357, sep 2014.

[64] Mohammed M. Farid, Amar M. Khudhair, Siddique Ali K Razack, and Said Al-Hallaj. A review on phase change energy storage: Materials and applications. *Energy Conversion and Management*, 45:1597–1615, 2004.

[65] Mahyar Silakhori, Hadi Fauzi, Mohammad R. Mahmoudian, Hendrik Simon Cornelis Metselaar, Teuku Meurah Indra Mahlia, and Hossein Mohammad Khanlou. Preparation and thermal properties of form-stable phase change materials composed of palmitic acid/polypyrrole/graphene nanoplatelets. *Energy and Buildings*, 99:189–195, jul 2015.

[66] Francis Agyenim, Philip Eames, and Mervyn Smyth. Heat transfer enhancement in medium temperature thermal energy storage system using a multitube heat transfer array. *Renewable Energy*, 35(1):198–207, 2010.

[67] J.G. Dunn, H.G. Smith, and R.L. Willix. The supercooling of acetamide. *Thermochimica Acta*, 80(2):343–353, oct 1984.

[68] B. Tong, Z. C. Tan, J. N. Zhang, and S. X. Wang. Thermodynamic investigation of several natural polyols (III): Heat capacities and thermodynamic properties of erythritol. *Journal of Thermal Analysis and Calorimetry*, 95(2):469–475, 2009.

[69] Kinga Pielichowska and Krzysztof Pielichowski. Phase change materials for thermal energy storage. *Progress in Materials Science*, 65:67–123, 2014.

[70] Peter Lorz, Friedrich Towae, Walter Enke, Rudolf Jäckh, Naresh Bhargava, and Wolfgang Hillesheim. Phthalic acid and Derivates. In *Ullmann's Encyclopedia of Industrial Chemistry*, pages 35–154. Wiley-VCH Verlag GmbH & Co. KGaA, 2012.

[71] Takao Maki and Kazuo Takeda. Benzoic acid and derivatives. In *Ullmann's Encyclopedia of Industrial Chemistry*, volume 60, pages 329–342. John Wiley & Sons, 2012.

[72] Tomas Hasl and Ivo Jiricek. The prediction of heat storage properties by the study of structural effect on organic phase change materials. *Energy Procedia*, 46:301–309, 2014.

[73] Guido Barone, Giuseppe Della Gatta, Daniela Ferro, and Vincenzo Piacente. Enthalpies and entropies of sublimation, vaporization and fusion of nine polyhydric alcohols. *Journal of the Chemical Society, Faraday Transactions*, 86(1):75, 1990.

[74] Aran Solé, Hannah Neumann, Sophia Niedermaier, Luisa F. Cabeza, and Elena Palomo. Thermal stability test of sugar alcohols as phase change materials for medium temperature energy storage application. *Energy Procedia*, 48:436–439, 2014.

[75] G Krishna Bama, R Anitha, and K Ramachandran. On the thermal properties of aqueous solution of D-mannitol. *Nondestructive Testing and Evaluation*, 25(1):67–75, oct 2009.

[76] Antoni Gil, Eduard Oró, and Luisa F. Cabeza. Experimental analysis of hydroquinone used as phase change material (PCM) to be applied in solar cooling refrigeration. *International Journal of Refrigeration*, 39:95–103, mar 2014.

[77] Wilhelm Riemensschneider and Minoru Tanifuji. Oxalic Acid. In *Ullmann's Encyclopedia of Industrial Chemistry*, pages 543–600. Wiley-VCH Verlag GmbH & Co. KGaA, 25 edition, 2012.

[78] Murat Kenisarin and Khamid Mahkamov. Salt hydrates as latent heat storage materials:Thermophysical properties and costs. *Solar Energy Materials and Solar Cells*, 145:255–286, 2016.

[79] George A. Lane. Phase change materials for energy storage nucleation to prevent supercooling. *Solar Energy Materials and Solar Cells*, 27:135–160, 1992.

[80] G. M. Habashy and G. A. Kolta. Thermal decomposition of the hydrates of barium hydroxide. *Journal of Inorganic and Nuclear Chemistry*, 34(1961):57–67, 1972.

[81] William E. Acree. Thermodynamic properties of organic compounds: enthalpy of fusion and melting point temperature compilation. *Thermochimica Acta*, 189:37–56, 1991.

[82] Fernanda Coen Porisini. Salt hydrates used for latent heat storage: Corrosion of metals and reliability of thermal performance. *Solar Energy*, 41(2):193–197, 1988.

[83] B Zalba. Review on thermal energy storage with phase change: materials, heat transfer analysis and applications. *Applied Thermal Engineering*, 23(3):251–283, 2003.

[84] Murat Kenisarin and Khamid Mahkamov. Passive thermal control in residential buildings using phase change materials. *Renewable and Sustainable Energy Reviews*, 55:371–398, 2016.

[85] M Hadjieva, R Stoykov, and Tz Filipova. Composite salt-hydrate concrete system for building energy storage. *Renewable Energy*, 19(1-2):111–115, jan 2000.

[86] B. Sandnes and J. Rekstad. Supercooling salt hydrates: Stored enthalpy as a function of temperature. *Solar Energy*, 80(5):616–625, may 2006.

[87] Jakob Berg Johansen, Mark Dannemand, Weiqiang Kong, Jianhua Fan, Janne Dragsted, and Simon Furbo. Thermal Conductivity Enhancement of Sodium Acetate Trihydrate by Adding Graphite Powder and the Effect on Stability of Supercooling. *Energy Procedia*, 70:249–256, may 2015.

[88] Pradyot Patnaik. *Handbook of Inorganic Chemicals*. McGraw-Hill, 2003.

[89] Liu Zhongliang, Ma Chongfang, and Li Jing. An experimental study on the stability and reliability of the thermal properties of barium hydroxide octahydrate as a phase change material. *Proceedings of 7th Expert Meeting and Workshop of IEA Annex 17 on Advanced Thermal Energy Storage trough Phase Change Materials and Chemical Reactions – Feasibility Studies and Demonstration Projects*, pages 63–69, 2004.

[90] Radim Pilar, Ladislav Svoboda, Pavla Honcova, and Lucie Oravova. Study of magnesium chloride hexahydrate as heat storage material. *Thermochimica Acta*, 546:81–86, 2012.

[91] Maria Telkes. Thermal energy storage in salt hydrates. *Solar Energy Materials*, 2(4):381–393, 1980.

[92] J P Howe and R R Katucki. Heat storage material [Patent US2706716], apr 1955.

[93] T Bauer, D Laing, and R Tamme. Recent progress in alkali nitrate/nitrite developments for solar thermal power applications. In *Molten Salts Chemistry and Technology*, pages 1–10, June 2011.

[94] Judith C. Gomez, Nicolas Calvet, Anne K. Starace, and Greg C. Glatzmaier. Ca(NO3)2 —NaNO3 —KNO3 Molten Salt Mixtures for Direct Thermal Energy Storage Systems in Parabolic Trough Plants. *Journal of Solar Energy Engineering*, 135(May 2013):021016, 2013.

[95] Joseph G. Cordaro, Nicholas C. Rubin, and Robert W. Bradshaw. Multicomponent Molten Salt Mixtures Based on Nitrate/Nitrite Anions. *Journal of Solar Energy Engineering*, 133(February 2011):011014, 2011.

[96] M. Yamada, M. Tago, S. Fukusako, and A. Horibe. Melting point and supercooling characteristics of molten salt. *Thermochimica Acta*, 218:401–411, may 1993.

[97] Yuan Yanping, Tao Wenquan, Cao Xiaoling, and Bai Li. Theoretic prediction of melting temperature and latent heat for a fatty acid eutectic mixture. *Journal of Chemical and Engineering Data*, 56(6):2889–2891, 2011.

[98] J.S Rowlinson. *Molecular thermodynamics of fluid-phase equilibria*. Prentice Hall, 3^{rd} edition edition, 1998.

[99] Jürgen Gmehling, Jiding Li, and Martin Schiller. A modified UNIFAC model. 2. Present parameter matrix and results for different thermodynamic properties. *Industrial & Engineering Chemistry Research*, 32(1):178–193, 1993.

[100] Atul Sharma, V. V. Tyagi, C. R. Chen, and D. Buddhi. Review on thermal energy storage with phase change materials and applications. *Renewable and Sustainable Energy Reviews*, 13:318–345, 2009.

[101] Gülseren Baran and Ahmet Sari. Phase change and heat transfer characteristics of a eutectic mixture of palmitic and stearic acids as PCM in a latent heat storage system. *Energy Conversion and Management*, 44(20):3227–3246, dec 2003.

[102] Rene I. Olivares and William Edwards. LiNO3-NaNO3-KNO3 salt for thermal energy storage: Thermal stability evaluation in different atmospheres. *Thermochimica Acta*, 560:34–42, 2013.

[103] F. Roget, C. Favotto, and J. Rogez. Study of the KNO3-LiNO3 and KNO3-NaNO3-LiNO3 eutectics as phase change materials for thermal storage in a low-temperature solar power plant. *Solar Energy*, 95:155–169, 2013.

[104] B. Yu. Gamataeva, R. M. Bagomedova, and A. M. Gasanaliev. Differentiation of the Li,Na,K‖NO2,NO3 quaternary reciprocal system and phase formation in its stable partitioning tetrahedron LiNO2-NaNO2-KNO2-KNO3. *Russian Journal of Inorganic Chemistry*, 59(2):134–140, 2014.

[105] George J. Janz and R. P. T. Tomkins. Molten Salts: Volume 5, Part 2. Additional Single and Multi-Component Salt Systems. Electrical Conductance, Density, Viscosity and Surface Tension Data, 1983.

[106] Abdulla M Gasanaliev and Bariyat Yu Gamataeva. Heat-accumulating properties of melts. *Russian Chemical Reviews*, 69:179–186, 2007.

[107] Leonesi Dante, Braghetti Mario, Cingolani Augusto, and Franzosini Paolo. Molten Mixtures of K, Na Formates with Alkali Halides. Note I, 1970.

[108] Murat M. Kenisarin. High-temperature phase change materials for thermal energy storage. *Renewable and Sustainable Energy Reviews*, 14:955–970, 2010.

[109] George J. Janz and R. P. T. Tomkins. Molten Salts: Volume 5, Part 1 Additional Single and Multi-Component Salt systems. Electrical Conductance, Density, Viscosity and Surface Tension Data, 1980.

[110] Bing-chen Zhao, Mao-song Cheng, Chang Liu, and Zhi-min Dai. System-level performance optimization of molten-salt packed-bed thermal energy storage for concentrating solar power. *Applied Energy*, 226:225–239, 2018.

[111] Murat M. Kenisarin and Kamola M. Kenisarina. Form-stable phase change materials for thermal energy storage. *Renewable and Sustainable Energy Reviews*, 16(4):1999–2040, 2012.

[112] Jungwook Shon, Hyungik Kim, and Kihyung Lee. Improved heat storage rate for an automobile coolant waste heat recovery system using phase-change material in a fin–tube heat exchanger. *Applied Energy*, 113:680–689, jan 2014.

[113] A. Sciacovelli, F. Gagliardi, and V. Verda. Maximization of performance of a PCM latent heat storage system with innovative fins. *Applied Energy*, 137:707–715, jan 2015.

[114] Weilong Wang, Shiquan He, Shaopeng Guo, Jinyue Yan, and Jing Ding. A combined experimental and simulation study on charging process of Erythritol–HTO direct-blending based energy storage system. *Energy Conversion and Management*, 83:306–313, jul 2014.

[115] Liguang Xiao, Rui Ding, Hao Sun, and Fujun Wang. A new kind of shape-stabilized phase change materials. *Journal of Wuhan University of Technology-Mater. Sci. Ed.*, 26(2006):491–494, 2011.

[116] Cemil Alkan and Ahmet Sari. Fatty acid/poly(methyl methacrylate) (PMMA) blends as form-stable phase change materials for latent heat thermal energy storage. *Solar Energy*, 82(2):118–124, 2008.

[117] Neil J Hewitt. Heat pumps and energy storage – The challenges of implementation. *Applied Energy*, 89(1):37–44, jan 2012.

[118] E. Osterman, V. Butala, and U. Stritih. PCM thermal storage system for 'free' heating and cooling of buildings. *Energy and Buildings*, 106:125–133, nov 2015.

[119] A. Barba and M. Spiga. Discharge mode for encapsulated PCMs in storage tanks. *Solar Energy*, 74(February):141–148, 2003.

[120] Anica Trp. An experimental and numerical investigation of heat transfer during technical grade paraffin melting and solidification in a shell-and-tube latent thermal energy storage unit. *Solar Energy*, 79(6):648–660, dec 2005.

[121] M N a Hawlader, M S Uddin, and H J Zhu. Encapsulated phase change materials for thermal energy storage: Experiments and simulation. *International Journal of Energy Research*, 26(January 2001):159–171, 2002.

[122] Feifei Jiao and Peng Xu. Simulation and Feasibility Analysis of PCM Based Passive Cooling Technique in Residential House. *Procedia Engineering*, 121:1969–1976, 2015.

[123] A. Reyes, L. Henríquez-Vargas, R. Aravena, and F. Sepúlveda. Experimental analysis, modeling and simulation of a solar energy accumulator with paraffin wax as PCM. *Energy Conversion and Management*, 105:189–196, nov 2015.

[124] M. J. Huang, P. C. Eames, S. McCormack, P. Griffiths, and N. J. Hewitt. Microencapsulated phase change slurries for thermal energy storage in a residential solar energy system. *Renewable Energy*, 36:2932–2939, 2011.

[125] L.F. Cabeza, I. Martorell, L. Miró, A.I. Fernández, and C. Barreneche. Introduction to thermal energy storage (TES) systems. In *Advances in Thermal Energy Storage Systems*, pages 1–28. Elsevier, 2015.

[126] Frank P Incropera, David P DeWitt, Theodore L Bergman, and Adrienne S Lavine. *Fundamentals of Heat and Mass Transfer*, volume 6th of *Dekker Mechanical Engineering*. John Wiley & Sons, 2007.

[127] Giovanni Angrisani, Michele Canelli, Carlo Roselli, and Maurizio Sasso. Calibration and validation of a thermal energy storage model: Influence on simulation results. *Applied Thermal Engineering*, 67(1-2):190–200, 2014.

[128] V Alexiades. *Mathematical Modeling Of Melting And Freezing Processes*. Taylor & Francis, 1992.

[129] Yvan Dutil, Daniel R. Rousse, Nizar Ben Salah, Stéphane Lassue, and Laurent Zalewski. A review on phase-change materials: Mathematical modeling and simulations. *Renewable and Sustainable Energy Reviews*, 15(1):112–130, jan 2011.

[130] Josef Stefan. Über einige Probleme der Theorie der Wärmeleitung. *Wien. Ber.*, 98:473–484, 1888.

[131] Shimin Wang, Amir Faghri, and Theodore L. Bergman. A comprehensive numerical model for melting with natural convection. *International Journal of Heat and Mass Transfer*, 53(9-10):1986–2000, apr 2010.

[132] Suhas Patankar. *Numerical heat transfer and fluid flow*. CRC Press, 1^{st} edition edition, January 1980.

[133] B. Nedjar. An enthalpy-based finite element method for nonlinear heat problems involving phase change. *Computers & Structures*, 80(1):9–21, jan 2002.

[134] S. Jana, S. Ray, and F. Durst. A numerical method to compute solidification and melting processes. *Applied Mathematical Modelling*, 31(1):93–119, jan 2007.

[135] M. Costa, A. Oliva, C.D.Férez Segarra, and R. Alba. Numerical simulation of solid-liquid phase change phenomena. *Computer Methods in Applied Mechanics and Engineering*, 91(1-3):1123–1134, oct 1991.

[136] H. Rieger, U. Projahn, and H. Beer. Analysis of the heat transport mechanisms during melting around a horizontal circular cylinder. *International Journal of Heat and Mass Transfer*, 25(1):137–147, jan 1982.

[137] Peter Krupa and Svetozr Malinaric. Using the transient plane source method for measuring thermal parameters of electroceramics. *International Journal of Mechanical and Mechatronics Engineering*, 1(5):245, 2014.

[138] Thermofischer scientific at *www.fishersci.co.uk*. Fischer scientific, 2016.

[139] Merck KGaA. Sigma-aldrich at *http://www.sigmaaldrich.com/*, 2016.

[140] Jose Pereira da Cunha and Philip Eames. Thermal energy storage for low and medium temperature applications using phase change materials – a review. *Applied Energy*, 177:227–238, 2016.

[141] TA Instruments. Discovery ta intruments brochure at *http://www.tainstruments.com/wp-content/uploads/BROCH-PRODUCT-GUIDE-2017-EN.pdf*, 2015.

[142] Atul Sharma, S.D Sharma, and D Buddhi. Accelerated thermal cycle test of acetamide, stearic acid and paraffin wax for solar thermal latent heat storage applications. *Energy Conversion and Management*, 43(14):1923–1930, sep 2002.

[143] B. Tong, Z. C. Tan, Q. Shi, Y. S. Li, and S. X. Wang. Thermodynamic investigation of several natural polyols (II): Heat capacities and thermodynamic properties of sorbitol. *Journal of Thermal Analysis and Calorimetry*, 91:463–469, 2008.

[144] Camila Barreneche, Antoni Gil, Falguni Sheth, a. Inés Fernández, and Luisa F. Cabeza. Effect of d-mannitol polymorphism in its thermal energy storage capacity when it is used as PCM. *Solar Energy*, 94:344–351, 2013.

[145] A.A. El-Sebaii, S. Al-Heniti, F. Al-Agel, A.A. Al-Ghamdi, and F. Al-Marzouki. One thousand thermal cycles of magnesium chloride hexahydrate as a promising PCM for indoor solar cooking. *Energy Conversion and Management*, 52(4):1771–1777, apr 2011.

[146] K Nagano, K Ogawa, T Mochida, K Hayashi, and H Ogoshi. Thermal characteristics of magnesium nitrate hexahydrate and magnesium chloride hexahydrate mixture as a phase change material for effective utilization of urban waste heat. *Applied Thermal Engineering*, 24(2–3):221–232, feb 2004.

[147] E J Griffith. Double nitrate salts and methods for their preparation [patent us3173756], mar 1965.

[148] Xuejun Zhang, Kangcheng Xu, and Yici Gao. The phase diagram of LiNO 3 – KNO 3. *Thermochimica Acta*, 385(July 2001):81–84, 2002.

[149] Christoph Rathgeber, Henri Schmit, and Luisa F. Cabeza. Enthalpy-temperature plots to compare calorimetric measurements of phase change materials at different sample scales. *Journal of Energy Storage*, 15:32–38, feb 2018.

[150] Alejandro Prieto, Ulrich Knaack, Tillmann Klein, and Thomas Auer. 25 Years of cooling research in office buildings: Review for the integration of cooling strategies into the building façade (1990–2014). *Renewable and Sustainable Energy Reviews*, 71:89–102, 2017.

[151] European Commission. Eurostat energy database at *https://ec.europa.eu/eurostat/web/energy/data/database*, 2017.

[152] European Comission. 2002/91/ec - energy efficiency: energy performance of buildings, 2002.

[153] Derrik Braham. Cibse guide a: Environmental design. In *CIBSE Publications*. CIBSE, 2015.

[154] D. P. Jenkins, H. Singh, and P. C. Eames. Interventions for large-scale carbon emission reductions in future UK offices. *Energy and Buildings*, 2009.

[155] Her Majesty's Stationery Office. The building regulations 2010 - part l. Technical report, Department of Communities and Local Government at *http://www.legislation.gov.uk/uksi/2010/2214/regulation/23/made*, 2010.

[156] National Renewable Energy Laboratory. Energyplus: Engineering reference. Technical report, US Department of Energy at *https://energyplus.net/documentation*, 2010.

[157] Jitka Mohelníková and Hasim Altan. Evaluation of Optical and Thermal Properties of Window Glazing. *WSEAS TRANSACTIONS on ENVIRONMENT and DEVELOPMENT*, 5(1):86–93, 2009.

[158] John A. Duffie and William A. Beckman. *Solar Engineering of Thermal Processes: Fourth Edition*. John Wiley & Sons, 2013.

[159] Daikin. Esie05-04 service manual r-410a sky-air indoor unit at *http://www.daikintech.co.uk/Data/Split-Sky-Air-Outdoor/RZQ-BW/2005/RZQ-B7W1B/RZQB7W1B˙SM.pdf*, 2005.

[160] S. B. Riffat. A thermochemical/compressor heat pump using 'economy 7' tariff electricity. *International Journal of Energy Research*, 1988.

[161] Wolfgang Wagner. *VDI Heat Atlas*. Springer-Verlag Berlin Heidelberg, 2^{nd} edition edition, 2010.

[162] Ian Biggin. Phase energy ltd at *http://phase-energy.com/*, 2017.

[163] Robin Hogan. How to combine errors. Technical report, Department of Metereology, University of reading, 2006.

[164] William Cory. *Fans and Ventilation*. Elsevier Ltd, 2005.

[165] SODECA. Sodeca, efficient work fans www.sodeca.com, 2017.

[166] Yuu Gao. High frequency welded longitudinal spiral fin tube at *https://www.alibaba.com/product-detail/High-Frequency-Welded-longitudinal-spiral-fin˙60799306849.html?spm=a2700.7724838.2017115.1.107943f0PeTxCK*, 2017.

[167] Ltd. Wuxi Raymond Steel Co. Hot dipped galvanized steel sheet at *https://www.alibaba.com/product-detail/Hot-Dipped-Galvanized-Steel-Sheet-Sheets_60630874458.html?spm=a2700.7724857.main07.269.42adbc51WA5teT*, 2017.

[168] Ahmet Teke and Oguzkan Timur. Assessing the energy efficiency improvement potentials of HVAC systems considering economic and environmental aspects at the hospitals. *Renewable and Sustainable Energy Reviews*, 33:224–235, may 2014.

[169] K Nissinen, P Takkunen, and H Ito. Maintenance and repair cost of office buildings in japan. In *Durability of Building Materials and Components 7*. Routledge, 2014.

[170] Andrew Smallbone, Verena Jülch, Robin Wardle, and Anthony Paul Roskilly. Levelised Cost of Storage for Pumped Heat Energy Storage in comparison with other energy storage technologies. *Energy Conversion and Management*, 152(Supplement C):221–228, 2017.

[171] Insulation Express. Eps 70 polystyrene insulation board at *https://www.insulationexpress.co.uk/stylite-eps-70-polystyrene-insulation-board-sdn*, 2017.

[172] Orion air. Daikin air conditioning rooftop packaged unit uatyq700cy1 at *www.orionairsales.co.uk*, 2017.

[173] Her Majesty's Stationery Office. Climate change act 2008. Technical report, Department of Energy and Climate Change at *https://www.legislation.gov.uk/ukpga/2008/27/contents*, 2008.

[174] Rajat Gupta and Matt Gregg. Empirical evaluation of the energy and environmental performance of a sustainably-designed but under-utilised institutional building in the UK. *Energy and Buildings*, 128:68–80, 2016.

[175] Arash Beizaee, David Allinson, Kevin J. Lomas, Ehab Foda, and Dennis L. Loveday. Measuring the potential of zonal space heating controls to reduce energy use in UK homes: The case of un-furbished 1930s dwellings. *Energy and Buildings*, 92:29–44, apr 2015.

[176] Eoghan McKenna and Murray Thomson. High-resolution stochastic integrated thermal–electrical domestic demand model. *Applied Energy*, 165:445–461, mar 2016.

[177] Alibaba Group. Magnesium chloride hexahydrate at *https://www.alibaba.com/product-detail/Magnesium-Chloride-Hexahydrate-98-_49572830O.html?spm=a2700.7724838.0.0.xCJ2OM&s=p*, 2017.

[178] Alibaba Group. Plastic rubber cosmetic grade/stearic acid at *https://www.alibaba.com/product-detail/Plastic-Rubber-Cosmetic-Grade-Stearic-Acid_50032253807.html?spm=a2700.7724838.0.0.gqR1ME*, 2017.

[179] Neven Ukrainczyk, S Kurajica, and J Šipušiæ. Thermophysical comparison of five commercial paraffin waxes as latent heat storage materials. *Chemical & Biochemical Engineering Quarterly (cabeq@pbf.hr)*, 24:129–137, jul 2010.

[180] Alibaba Group. Refined & semi refined paraffin wax 58/60at *https://www.alibaba.com/product-detail/Refined-Semi-Refined-Paraffin-Wax-58_50033585100.html?spm=a2700.7724838.0.0.pUWhgk*, 2017.

[181] K.J. Chua, S.K. Chou, and W.M. Yang. Advances in heat pump systems: A review. *Applied Energy*, 87(12):3611–3624, 2010.

[182] Ana Maria Silva and Rui Rosa. Radiative environment inside a greenhouse. *Agricultural and Forest Meteorology*, 33(4):339–346, 1985.

[183] N. Wakao, S. Kaguei, and T. Funazkri. Effect of fluid dispersion coefficients on particle-to-fluid heat transfer coefficients in packed beds. *Chemical Engineering Science*, 34(3):325–336, 1979.

[184] Mario Nájera-Trejo, Ignacio R. Martin-Domínguez, and Jorge A. Escobedo-Bretado. Economic feasibility of flat plate vs evacuated tube solar collectors in a combisystem. *Energy Procedia*, 91:477–485, jun 2016.

[185] J F Kreider and F Kreith. *Solar heating and cooling: engineering, practical design, and economics*. McGraw-Hill Book Company,New York, jan 1975.

[186] Niels D Jensen, Horst Komossa, and Kurt F Nielsen. Circulating pump unit, mar 1984.

[187] Solar supplies UK. Solar thermal controller at *https://solarsuppliesuk.co.uk/product/solar-thermal-controller/*, 2017.

[188] Screwfix Direct Ltd. Screwfix at *http://www.screwfix.com/*, 2017.

[189] EBay Inc. Plain white tennis balls at *http://www.ebay.co.uk/itm/New-pack-of-12PCS-Ping-Pong-Plain-White-Table-Tennis-Sports-Balls-Set-40mm-DM/331866115606*, 2017.

[190] Handong Wang. A steady-state empirical model for evaluating energy efficient performance of centrifugal water chillers. *Energy and Buildings*, 154(Supplement C):415–429, 2017.

[191] Payscale Inc. Soldering technician salary at *http://www.payscale.com/research/US/Job=Soldering_Technician/Hourly_Rate*, 2017.

[192] Ralf Martin, Laure B de Preux, and Ulrich J Wagner. The impact of a carbon tax on manufacturing: Evidence from microdata. *Journal of Public Economics*, 117(Supplement C):1–14, 2014.

[193] David J C Hawkey. District heating in the UK: A Technological Innovation Systems analysis. *Environmental Innovation and Societal Transitions*, 5(Supplement C):19–32, 2012.

[194] Modassar Chaudry, Muditha Abeysekera, Seyed Hamid Reza Hosseini, Nick Jenkins, and Jianzhong Wu. Uncertainties in decarbonising heat in the UK. *Energy Policy*, 2015.

[195] Daniele Basciotti and R R Schmidt. Peak Reduction in District Heating Networks: a Comparison Study and Practical Considerations. In *14th International Symposium on District Heating and Cooling*, 2014.

[196] G. P. Hammond and J. B. Norman. Heat recovery opportunities in UK industry. *Applied Energy*, 2014.

[197] Joan L Pellegrino, Nancy Margolis, Mauricio Justiniano, Melanie Miller, and Arvind Thedki. Energy Use, Loss and Opportunities Analysis: US Manufacturing and Mining. *DOE/ITP (U.S. Department of Energy's Iindustrial Technologies Program)*, 2004.

[198] Dr. Robert Hyde Element Energy, Ecofys, Imperial College, Dr. Paul Stevenson. The potential for recovering surplus heat from industry. Technical report, Department of Energy and Climate Change, London TW9 4DU, UK, 2014.

[199] J. N.W. Chiu, J. Castro Flores, V. Martin, and B. Lacarrière. Industrial surplus heat transportation for use in district heating. *Energy*, 2016.

[200] S D MADNAIK and M G JADHAV. Waste Heat Recovery Systems in the Sugar Industry: An Indian Perspective. *Energy Sources*, 18(3):333–343, apr 1996.

[201] Confederation of European Paper Industries. Pulp and paper industry definitions: Definitions and concepts. *chemical society of America*, 2014.

[202] International Statistics Bureau. Key statistics 2016, UK Steel. Technical report, ISSB Limited, Croydon, 2016.

[203] Thomas Bauer, Nicole Pfleger, Nils Breidenbach, Markus Eck, Doerte Laing, and Stefanie Kaesche. Material aspects of Solar Salt for sensible heat storage. *Applied Energy*, 111:1114–1119, nov 2013.

[204] Stephan Höhlein, Andreas König-Haagen, and Dieter Brüggemann. Thermophysical Characterization of MgCl2·6H2O, Xylitol and Erythritol as Phase Change Materials (PCM) for Latent Heat Thermal Energy Storage (LHTES), 2017.

[205] Robert Ruehrwein and Hugh Huffman. Thermal data; the heat capacity, entropy and free energy of urea. *Journal of the American Chemical Society*, 68:1759–1761, 1946.

[206] Charles W. Weston, John R. Papcun, and Maurice Dery. Ammonium compounds. In Inc. John Wiley & Sons, editor, *Kirk. Othmer Encyclopedia of Chemical Technology*, volume 2. Wiley Online Library, 2000.

[207] E. J. Bowman. Bowman heat hexchangers at *www.ejbowman.co.uk*, 2018.

[208] Grundfos. Grundfos product center at *product-selection.grundfos.com*, 2018.

[209] Building Materials Nationwide Ltd. Rockwool 100mm acoustic slab at *www.buildingmaterials.co.uk*, 2018.

[210] Metals4U Ltd. 5/8"odx1.2mm stainless steel 304l tube at *www.metals4u.co.uk*, 2018.

[211] The Metals Wharehouse. Stainless steel sheet at *http://www.metalswarehouse.co.uk*, 2018.

[212] Anchor Pumps. Tp 80-60/4 0.75kw single stage in line 4 pole 240v at *www.anchorpumps.com*.

[213] Containers Direct. Shipping container prices online at *www.shippingcontainersuk.com*, 2018.

[214] Olieonline. Shell heat transfer oil s2 at *www.olieonline.co.uk*, 2018.

[215] O. Gudmundsson, J. E. Thorsten, and L. Zhang. Cost Analysis Of District Heating Compared To Its Competing Technologies. *Transactions on Ecology and The Environment*, 176(1):17, 2013.

[216] U.S. Environmental Protection Agency (EPA). dCHPP (CHP Policies and Incentives Database), 2016.

[217] Her Majesty's Stationery Office. Assessment of the costs, performance, and characteristics of uk heat networks. Technical report, Department of Energy & Climate Change, London SW1A, 2AW, UK, 2015.